Mesoporous calcium carbonate crystals as novel vectors for *in ovo* delivery

Jack Charlie Campbell

A thesis submitted in partial fulfilment of the requirements of
Nottingham Trent University for the degree of
Doctor of Philosophy

February 2023

Acknowledgements

Abstract

The continuing increase in population demands for an affordable food and protein source, farmed poultry provides a means to combat this. Current growth rates within modern broiler lines have continually increased due to intense genetic selection; due to this, the developing embryo cannot solely rely on the contents of the egg for its successful growth. *In ovo* feeding (IOF) is the nutrient supplementation of the egg and acts to improve the energy-status of late-term chick embryos. Current methodologies to provide IOF are based upon mechanical injection, which can result in the reduced structural integrity of the eggshell and leaves the developing embryo susceptible to bacterial infection. Moreover, delivered nutrients are unprotected, and there is a lack of protective delivery vectors.

The permeation of food-grade carrier gels is proposed as an alternative approach to IOF via injection. An investigation into the surface properties of the eggshell is presented, focusing on shell permeability and porosity. This permeation is dependent upon the polarity of the carrier gel. With this, an injection-free delivery method is proposed utilising the spontaneous permeation of polypropylene glycol (PPG) through the eggshell. IOF is demonstrated through the delivery of fluorescently labelled model bioactives. Delivery vectors dispersed throughout the PPG carrier gel act as hosts and an approach to protect sensitive bioactive material.

Both vaterite $CaCO_3$ crystals and their layer-by-layer templated microgels are novel inorganic and organic structures which have attracted significant scientific interest as drug delivery vectors owing to their biological relevance, low-cost production, and highly tuneable properties. This work seeks to develop delivery vectors based on vaterite crystals and biopolymer microgels for non-invasive IOF, and to aid in the delivery of micro- and nano-encapsulated nutrients or other compounds of interest.

Vaterite crystals (diameter of 0.5-20 μm) can be loaded with model nutrients such as food-grade macromolecular dextrans and small molecule cobalamin (vitamin B12) via co-synthesis, reaching up to 8 and 1% w/w, respectively. Neutral dextran (DEX) and its charged derivatives (carboxymethyl- (CM) and diethylaminoethyl (DEAE)-DEX) were utilised. The molecular weight and charge of DEX does not affect the crystal size, but drastically influence the crystal porosity. Neutral and CM-DEX can stabilise vaterite against the recrystallisation to non-porous calcite. Vitamin B12 does not affect the vaterite morphology.

The formulation of sixteen types of vaterite-templated biopolymer-based microgels is investigated utilising four polycations (poly-L-lysine (PLL), protamine (PR), dextran amine (DA) and collagen (COL)) and four polyanions (hyaluronic acid (HA), chondroitin sulfate (CS), dextran sulfate (DS) and heparin sulfate (HS)). Stable microgels are formed from all polyanions paired with PLL and PR, whereas those paired with DA and COL undergo dissolution or disaggregation. Formation of the microgels has been correlated with the stability of the respective polyelectrolyte complexes at increased ionic strength. All formed microgels shrink upon template dissolution and the degree of shrinkage increased in the series of polyanions HS < DS < CS < HA. The same trend is observed for the adhesion of microgels to the surface upon which they are formed. The biopolymer molecular weight and charge also governs the microgel stability and internal structure. Neutral and charged DEX, as well as silver nanoparticles (AgNPs) can be encapsulated into microgels via pre-loading (co-synthesis with vaterite templates) or post-loading (adsorption to formed microgels). The loading mechanism is governed by the mechanical entrapment of cargo, as well as electrostatic interactions, where the components of charge and the capping agent of AgNPs play a role.

The findings of this thesis open new routes for the design of, and encapsulation within, $CaCO_3$-based vectors. Such vectors may aid in the preservation of activity, protection, and the controlled release of necessary bioactive compounds for chick development. The novel permeation-based IOF approach demonstrates the universal delivery of bioactive compounds - both free and encapsulated - and its potential to replace IOF via injection.

Statement of novelty

The study presented within this thesis provides novelty directly through its primary aim - the injection-free permeation-based approach of IOF has not been previously reported within the literature, nor has the delivery of porous vaterite carriers *in ovo*. The thesis also explores the characterisation, controlled growth and re-crystallisation of both micron and submicron DEX/vaterite hybrids at physiological conditions, and, in view of biomedical carriers, has not been previously investigated. Further, the production of biopolymer-based microgels is an aspect widely discussed within the literature, however a comparative study between microgels formed of different biopolymers has not been performed and is an important milestone in their development and is explored within this work.

Declaration

The work described in this thesis was carried out by myself and, where indicated, in collaboration with colleagues. The data analysis and interpretation is my own work. This thesis has been written entirely by myself.

Jack C. Campbell

Contents

Contents

Contents

Contents

List of Figures

List of Tables

Abbreviations

AgNPs Silver nanoparticles

ALG Alginate

ATP Adenosine triphosphate

ATR Attenuated total reflectance

BET Brunauer-Emmett-Teller

BL Bilayer

BJH Barret-Joyner-Halenda

BSA Bovine serum albumin

CAR Carrageenan

CHI Chitosan

CLSM Confocal laser scanning microscopy

CM Carboxymethyl

CMC Carboxymethylcellulose

CNT Carbon nanotube

COL Collagen

CS Chondroitin sulfate

DA Dextran amine

DDAB Didodecyldimethylammonium bromide

DEAE Diethylaminoethyl

DEX Dextran

DEX-HEMA Dextran hydroxyethylmethacrylate

DLS Dynamic light scattering

DOX Doxorubicin

DS Dextran sulfate

EDC 1-ethyl-3-(3-dimethylaminopropyl)carbodiimide

EDTA Ethylenediaminetetraacetic acid

EDX Energy dispersive X-ray

ELR Elastin-like recombinamer

FC Fucoidan

FG2 Basic fibroblast growth factor

FITC Fluorescein isothiocyanate

FT-IR Fourier transform infrared

FT-SPR Fourier transform-surface plasmon resonance

FRAP Fluorescence recovery after photobleaching

FRET Forster resonance energy transfer

GA Glutaraldehyde

HA Hyaluronic acid

Hgb Hemoglobin

HPMC Hydroxypropylmethylcellulose

HS Heparin sulfate

ICP-MS Inductively coupled plasma-mass spectrometry

IgY Egg yolk immunoglobulin

IOF *in ovo* feeding

LbL Layer-by-Layer

LF Lactoferrin

LS Lignosulfonate

MC Methylcellulose

MF Melamine formaldehyde

MNP Magnetic nanoparticle

MS Mesoporous silica

NHS N-hydroxysuccinimide

NP Nanoparticle

OCT Optical coherence tomography

OWRK Owens-Wendt-Rabel-Kalble

PAA Poly(acrylic acid)

PAH Poly(allylamine hydrochloride)

pARG Poly(arginine)

pASP Poly(aspartic acid)

PDADMAC Poly(diallyldimethylammonium chloride)

PEC Polyelectrolyte complex

PEG Poly(ethylene glycol)

PEM Polyelectrolyte multilayer

PEMC Polyelectrolyte multilayer capsule

PDMS Polydimethylsiloxane

PG Propylene glycol

pGLU Poly(glutamic acid)

PLL Poly-L-lysine

PLL-bp Phenylboronic modified poly(lysine)

PNIPAM Poly(N-isopropylacrylamide)

pONT Poly(ornithine)

PPG Poly(propylene glycol)

PR Protamine sulfate

PS Polystyrene

PSS Poly(styrene sulfonate)

PVP Poly(vinylpyrrolidone)

RFU Relative fluorescence units

RhoB Rhodamine B

SC Shrinkage coefficient

SD Standard deviation

SEM Scanning electron microscopy

SP Spermidine

TA Tannic acid

TEM Transmission electron microscopy

TGA Thermal gravimetric analysis

TIRF Total internal reflection fluorescence

TMR-D Tetramethylrhodamine-modified dextran

TRITC Tetramethylrhodamine

XRD X-ray diffraction

Chapter 1

Introduction

1.1   Thesis motivation

There is a growing demand for an affordable food and protein source for the growing population; farmed chicken presents itself as an appropriate means to combat this. For instance, there has been an increase of ∼470,000 tonnes of broiler meat production since the year 2000 in the UK alone [1]. Modern broiler lines are of those selected with a higher growth rate, and as such, chick embryos hold a greater need for energy and nutrients that are typically depleted in modern chicks. IOF presents itself as a method to overcome this and improve the energy status of late-term chicken embryos [2]. IOF is the delivery of key nutrients to the developing embryo and promotes the early development of the gastrointestinal tract, of which, is vital for the utilisation of the provided nutrients, and hence is required for the optimisation of the overall growth performance of the chick, as well as the potential improvement of hatchability, immunity, and overall gut health [2–4].

During embryogenesis, the contents of the egg are responsible for providing the energetic and nutritional value necessary for chick growth and play a major role in the development of the chicken embryo from fertilisation [5]. Moreover, during the prolonged hatching window of the chick, and, owing to the current operation at hatcheries, the chick undergoes a fasting period of 48-72 hours and relies solely on the nutritional value received from the contents of the egg during the pre-hatch stage [3]. Due to this, chicks may have delayed gut development and increased mortality [6]. IOF can ensure the sufficient nutrients are present during this early embryonic developmental stage, as well as the neonatal period [2]. Despite these developments in IOF, current methodologies to provide IOF depend upon the mechanical injection through the eggshell itself. Such injection is performed automatically, and typically does not support amniotic injection due to imprecision [7], and can result in the reduced structural integrity of the eggshell, as well as leaves the developing embryo susceptible to bacterial infection if not sealed correctly. Depending upon the time and site of the injection, the embryo may be traumatised, and not result in the desired effect on the hatchling [8, 9]. More-

over, each incubated embryo uses and/or rearranges the compartments of the egg at the latter stages of development (i.e. the allantonic sac, yolk sac, amniotic sac and the air cell) [7].

Beneficial here, are non-invasively delivered vectors with encapsulated nutritional cargo and programmable release mechanisms to direct chick growth and post-hatch performance, whilst also acting to protect potential sensitive nutrients during their delivery. Hence, the paramount motivation for this project is the lack of developed IOF vectors and non-injectable delivery approaches within poultry production, as well as within the field of early nutritional programming. Indeed, such delivery vectors are not solely limited to feeding, but may be applicable to *in ovo* vaccination, stimulation and to improve embryo viability in various species.

Already FDA-approved materials draw great attention for such applications. Here, calcium carbonate ($CaCO_3$) presents itself as a potential material owing to its low-cost and ease of production, biodegradability, and versatility [10–13]. Moreover, $CaCO_3$ is responsible for $\sim95\%$ of the dry weight of the eggshell itself [14], offering a potential recyclable material following hatching. $CaCO_3$ is also widely used as a filler in construction materials [15, 16], and has seen significant use within carbon capture [17]. Notwithstanding its industrial use, it also has clear biological applications; naturally occurring, $CaCO_3$ crystals have attracted significant attention as drug delivery vehicles [18–21]. In its vaterite polymorph, the porosity of the crystals is beneficial for the hosting of nutrients [22–24] and for the formation of $CaCO_3$-based capsules or microgels [25, 26]. The work presented in this thesis seeks to develop and apply suitable vectors utilising these materials as novel vectors for non-invasive *in ovo* delivery.

1.2 Thesis aims and outline

As aforementioned, there is a lack of developed micro- or nano-delivery systems for IOF. Currently employed IOF approaches only rely on the mechanical injection of unprotected nutrients through the eggshell to the target location. In attempt to improve

current IOF technologies, the aim of this work is to formulate novel $CaCO_3$-based vectors for the delivery of nutrients in order to be delivered non-invasively, *in ovo*.

This thesis is divided into four main sections; the background and current technologies utilised within Chapter 2, the experimental methodologies employed within Chapter 3, results and discussion within Chapters 4, 5 and 6, as well as conclusions and future work within Chapter 7.

As such, the thesis is divided as the below:

- Chapter 2 is devised as an introduction to the formation and properties of $CaCO_3$ and $CaCO_3$-templated capsules and microgels. This is followed by the exploration of current IOF approaches and the typical nutrients delivered and their effect on the chick post-hatch.

- Chapter 3 contains the experimental methodologies utilised throughout this work.

- Chapter 4 marks the beginning of the results section for this thesis. This first results chapter discusses the design of the novel $CaCO_3$-based vectors that have been formulated.

- Chapter 5 provides the encapsulation capabilities of the developed vectors, providing knowledge into the key mechanisms of encapsulation of model bioactive materials.

- Chapter 6 details the *in ovo* delivery of bioactive materials and explores the delivery of the newly developed vectors, whilst exploring key surface and structural properties of the eggshell.

- Chapter 7 draws on the key conclusions made throughout this thesis and explores potential directions for future work.

1.3   Publications

Publications attained during the PhD are chronologically listed below.

1. **Campbell, J**., Kastania, G. and Volodkin, D., 2020. Encapsulation of low-molecular-weight drugs into polymer multilayer capsules templated on vaterite $CaCO_3$ Crystals. Micromachines, 11(8), p.717.

2. **Campbell, J**. and Vikulina, A.S., 2020. Layer-by-layer assemblies of biopolymers: Build-up, mechanical stability and molecular dynamics. Polymers, 12(9), p.1949.

3. Kastania, G., **Campbell, J**., Mitford, J. and Volodkin, D., 2020. Polyelectrolyte multilayer capsule (PEMC)-based scaffolds for tissue engineering. Micromachines, 11(9), p.797.

4. Yola, A.M., **Campbell, J**. and Volodkin, D., 2021. Microfluidics meets layer-by-layer assembly for the build-up of polymeric scaffolds. Applied Surface Science Advances, 5, p.100091.

5. **Campbell, J**., Abnett, J., Kastania, G., Volodkin, D. and Vikulina, A.S., 2021. Which biopolymers are better for the fabrication of multilayer capsules? A comparative study using vaterite $CaCO_3$ as templates. ACS applied materials & interfaces, 13(2), pp.3259-3269.

6. Vikulina, A.S. and **Campbell, J**., 2021. Biopolymer-Based Multilayer Capsules and Beads Made via Templating: Advantages, Hurdles and Perspectives. Nanomaterials, 11(10), p.2502.

7. Zafar, B., **Campbell, J**., Cooke, J., Skirtach, A.G. and Volodkin, D., 2022. Modification of Surfaces with Vaterite $CaCO_3$ Particles. Micromachines, 13(3), p.473

8. **Campbell, J**., Ferreira, A.M., Bowker, L., Hunt, J., Volodkin, D. and Vikulina, A., 2022. Dextran and Its Derivatives: Biopolymer Additives for the Modulation of Vaterite $CaCO_3$ Crystal Morphology and Adhesion to Cells. Advanced Materials Interfaces, 9(31), p.2201196.

9. Kotoulas, K.T., **Campbell, J**., Skirtach, A.G., Volodkin, D. and Vikulina, A., 2022. Surface Modification with Particles Coated or Made of Polymer Multilayers. Pharmaceutics, 14(11), p.2483.

10. **Campbell, J**., Taghavi, A., Preis, A., Martin, S., Skirtach, A.G., Franke, J., Volodkin, D. and Vikulina, A., 2022. Spontaneous shrinkage drives macromolecule encapsulation into layer-by-layer assembled biopolymer microgels. Journal of Colloid and Interface Science, 635, p.12-22.

1.4   Conference proceedings

1.4.1   Oral presentations

1. **Campbell, J**., Vikulina, A., Cave, G., and Volodkin, D. Self-shrinking natural polymer-based microgels: assemblage and potential applications, 15th International Conference on Materials Chemistry, 12-15 July 2021, online, O77. Presenting author.

2. Zafar, B., **Campbell, J**., Wulf, A., Cave, G., and Volodkin. D. Metal nanoparticles meet multilayer capsules: pros and contras of pre-loading and post-coating approaches, ACS Spring Meeting, 5-30 April 2021.

3. **Campbell, J**., Vikulina, A., and Volodkin, D. Spontaneous annealing of biopolymer multi-layered vehicles: fundamental aspects and a new route for drug delivery via physical trap, Dynamic self-assembly and quorum effects in chemistry and biology predicted by non-linear modelling algorithms workshop, 20-23 October 2019 Liverpool, UK, O19. Presenting author.

4. **Campbell, J**., Vikulina, A., and Volodkin, D. Dextran encapsulation via the annealing of multilayer capsules at physiological conditions, Patient-tailored biomaterials for tissue regeneration, combating microbial contamination and drug delivery symposium, 2-5 October 2019, Lancaster, UK, O14. Presenting author.

5. **Campbell, J**., Vikulina, A., and Volodkin, D. Can multilayer bio-capsules shrink at ambient conditions? The fundamentals and potential applications, Biomaterials Symposium, 11-12 February 2019, Lancaster, UK, O31. Presenting author.

1.4.2   Poster presentations

1. **Campbell, J**., Vikulina, A., Cave, G., Liang, H. and Volodkin, D. Hybrid $CaCO_3$ crystal-based vectors for *in ovo* feeding, 16th European Symposium on Controlled Drug Delivery, 12-15 April 2022, Egmond ann Zee, The Netherlands. Presenting author.

2. **Campbell, J**., Rothfelder, R., Wittmann, A., Schmidt, M., Volodkin, D. and Vikulina, A. Biopolymer-based microgels as carriers for surface functionalisation, 16th European Symposium on Controlled Drug Delivery, 12-15 April 2022, Egmond ann Zee, The Netherlands.

3. **Campbell, J**., Vikulina, A., and Volodkin, D. Self-annealing Layer-by-Layer assembled biopolymer microgels: formulation and encapsulation via mechanical trap, RSC Materials Chemistry Division Poster Symposium, 20 January 2021, online. Presenting author.

4. **Campbell, J**., Vikulina, A., Cave, G., and Volodkin, D. Self-shrinking biopolymer microgels as drug delivery vehicles: fabrication and encapsulation, UK-Poland Bioinspired Materials Conference, 23-24 November 2020, online, P5. Presenting author.

5. **Campbell, J**., Kastania, G., Abnett, J., Volodkin, D., and Vikulina, A. Multilayer capsules made of biopolymers. Stability prediction and encapsulation capability by mechanical trap, 2nd International Conference on Materials Research and Nanotechnology, 10-12 June 2019, Rome, Italy, P24.

6. Ferreira, A., **Campbell, J**., Polytarchou, C., Volodkin, D., Vikulina, A. $CaCO_3$ crystals as promising vectors for intracellular delivery via pH-mediated recrystal-

lization, 2nd International Conference on Materials Research and Nanotechnology, 10-12 June 2019, Rome, Italy.

7. **Campbell, J**., Ali, R., Vigneswaran, V., Volodkin, D. and Vikulina, A. The fabrication of self-shrinking multilayer bio-capsules templated on $CaCO_3$ vaterite crystals, 22nd Global Congress on Biotechnology, 28 February - 02 March 2019, Berlin, Germany (best poster prize).

8. **Campbell, J**., Vikulina, A. and Volodkin, D. Multilayer biopolymer-based capsules made using vaterite $CaCO_3$ crystals, MERCIA Annual Meeting, 12 December 2018, Manchester UK, P28. Presenting author.

9. Vikulina, A., **Campbell, J**. and Volodkin, D. Multilayer biopolymer-based capsules made using vaterite $CaCO_3$ crystals, 19th Global Congress on Materials Science and Engineering, 11-13 June 2018, Barcelona, Spain.

Chapter 2

Literature Review

2.1 Introduction

This chapter first discusses CaCO$_3$, exploring its formation, properties, and use as a drug delivery vector. Following this, the principals of Layer-by-Layer (LbL) assembly are presented for both 2D and 3D films and structures; here, film growth mechanisms and application in drug delivery are discussed in detail, focusing on biopolymers as their constituents. Finally, the current approaches to IOF are introduced; including the nutrients typically delivered *in ovo* and their effect on the chick post-hatch. Of note, part of the research presented in this Chapter has been published as references (1), (2), (6), and (8), as listed in Section 1.3.

2.2 CaCO$_3$ crystals

2.2.1 CaCO$_3$ and its polymorphs

CaCO$_3$ is highly versatile and is used within a variety of applications and industries, including use as a filler for coatings, paper and paints [27–30], as well as a key component in construction materials and widely used within the food and pharmaceutical sectors (e.g. for acidity regulation and colouring, for instance) [31–33]. CaCO$_3$ naturally occurs as six polymorphic forms, including two hydrated crystalline forms (hexahydrate ikaite and monohydrocalcite), an amorphous form, and three crystalline anhydrous forms (aragonite, vaterite and calcite) [34–36]. In terms of the stability of the polymorphs, the hydrated and amorphous polymorphs typically transform to the anhydrous polymorphs. Despite this, the anhydrous aragonite and vaterite forms are metastable and will likely convert to the more thermodynamically stable calcite when present in an aqueous environment [37, 38]. Indeed, this results in the vaterite and aragonite polymorphs occurring much more rarely than the calcite form [39]; nevertheless, vaterite can be found present as a natural biomineral in various species (e.g. gastropods, mollusc pearls and ascidians) [39, 40]; where aragonite can be found in marine and terrestrial environments due to the increased pressure that is required for

it to form [38]. Calcite is typically rhombohedral in its morphology, where aragonite and vaterite are present as needle-like and spherical in shape, respectively, as shown in Figure 2.1 [10, 41]. Despite this, the morphologies can be significantly altered by varying the conditions used to synthesise CaCO$_3$.
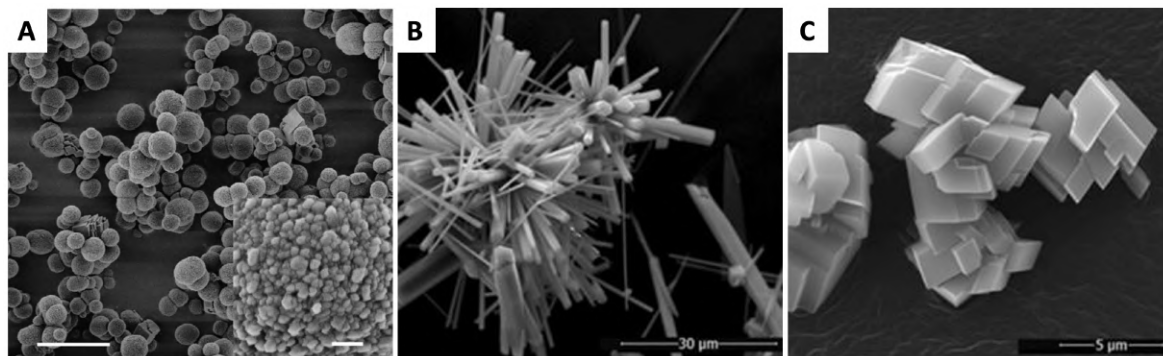
Figure 2.1: Representative SEM images of (A) vaterite, (B) aragonite, and (C) calcite. Reprinted with permission from references [42] Copyright © 2022 John Wiley and Sons Ltd. (A) and [43] Copyright © 2017 Springer (B,C).

2.2.2 Approaches to CaCO$_3$ synthesis

A variety of synthesis methods have been implemented to produce CaCO$_3$ crystals of varying polymorphs and morphologies. The most popular and simple approach to synthesise such particles is via the precipitation or solution method, which involves the mixing of two supersaturated solutions of salts containing Ca^{2+} and CO$_3^{2-}$ (e.g. CaCl$_2$ and Na$_2$CO$_3$) to result in the spontaneous precipitation of CaCO$_3$ [44, 45]. Besides the precipitation method, alternate methods for CaCO$_3$ synthesised used throughout the literature include carbonation approaches (i.e. slow carbonation and CO$_2$ bubbling) and the reverse emulsion synthesis [46, 47]. The carbonation approaches typically involves the production of CO$_3^{2-}$ ions upon the dissolution of CO$_2$ in water or through the hydrolysis of compounds such as ammonium carbonate and dimethyl carbonate under alkaline conditions [46, 48, 49]. Reverse emulsion involves the dispersion of aqueous solutions of Ca^{2+} and CO$_3^{2-}$ within a hydrophobic continuous phase, and, driven by surfactant self-assembly, a microemulsion is formed. The micelles act as micro- or nano-reactors and collide under agitation, resulting in the controlled nucleation and growth

of CaCO$_3$ crystals [50, 51]. Indeed, the synthesis parameters of these approaches can be altered in order to control the size, morphology and polymorph of the CaCO$_3$ crystals formed.

2.2.3 Vaterite CaCO$_3$ formation and recrystallisation

Upon the mixing of two salt solutions containing Ca^{2+} and CO$_3{}^{2-}$ ions, amorphous CaCO$_3$ is first formed, of which is able to transform into an anhydrous CaCO$_3$ polymorph, eventually resulting the formation of calcite [52]. Rodriguez-Blanco *et al.* (2011) [53] has suggested the amorphous CaCO$_3$ rapidly dehydrates, followed by an internal structural rearrangement and local ordering of the amorphous structure within individual nanoparticles to give rise to the spherulitic growth of crystalline vaterite CaCO$_3$, of which continues as the remaining amorphous CaCO$_3$ solubilises. The resultant vaterite crystals continue to grow via Ostwald ripening, arising from the difference in solubility between small and large particles. Upon the lengthened incubation of vaterite CaCO$_3$ within aqueous solutions, the transformation from the porous vaterite polymorph to the non-porous calcite polymorph can take place over a few hours-to-days, hence bare-vaterite should be handled quickly when in the presence of water [53]. This, however, can be beneficial for the release of encapsulated cargo, via a recrystallisation mechanism [18, 54]. This transformation occurs due to the difference in solubility between both vaterite (K$_{sp}$ of 10$^{-7.913}$) and calcite (K$_{sp}$ of 10$^{-8.480}$) [53]; the solution will remain supersaturated with respect to calcite, driving the precipitation of this polymorph. This process is a dissolution-reprecipitation mechanism and is dependent upon the surface area of calcite present in solution; where vaterite undergoes dissolution and releases Ca^{2+} and CO$_3{}^{2-}$ into solution, which reprecipitates on the surface of growing calcite crystals [10, 53, 55]. Although such properties may be beneficial for some medical applications, e.g. pH-triggered release in tumor sites [56, 57], many other applications require the stabilisation of vaterite and the suppression of its recrystallisation. This is especially important for the use of vaterite in implantable drug delivery systems, tissue engineering platforms, food/cosmetic additives, and storage

materials, of which are designed for prolonged action.

The most widely used approach to control recrystallisation of the carbonates is the use of polymer matrices, which stabilise the vaterite nanocrystallites and suppress the transportation of ions from the crystal surface. Previously, mucin acted to hamper the recrystallisation rate of vaterite to calcite, in which the vaterite-to-calcite transformation acted as the mechanism of doxorubicin (DOX) release and was attributed to the reduced ion mobility in aqueous solution in the presence of mucin [54]. Poly(N-vinyl-2-pyrrolidone) (PVP) has acted to increase the recrystallisation rate of vaterite to calcite, owing to the lower solubility of calcite compared to vaterite [58]. Besides these, some known examples of polymeric matrices to control vaterite recrystallisation include: polycarboxylate-type superplasticizers [59], poly(aspartate) [60], poly(amidopamine) [61], carboxymethylinulin [62] and lentinan [63], for instance. Such matrices may be encapsulated within the vaterite CaCO$_3$ crystals via various loading approaches. Such bioactive-loaded vaterite CaCO$_3$ crystals have already been implemented for therapeutic, diagnostic, and theranostic uses both *in vitro* and *in vivo* [11, 64–67]. There are various approaches to encapsulate such an array of bioactives, and these will be discussed below.

2.2.4 Encapsulation approaches

Adsorption

This approach is based on the simple adsorption of bioactives to the CaCO$_3$ crystal surface (both the crystal surface and within the pores); this is dependent upon the extent of molecular interactions and affinity (i.e. van der Waals and electrostatic interactions) between the bioactive and CaCO$_3$ surface [68]. It is typically performed via the agitation of CaCO$_3$ crystals within a solution containing the bioactive of interest [69, 70]. This approach is better-suited to larger macromolecular compounds due to the larger pore sizes of the CaCO$_3$ crystals, of which are typically a hindrance to low-molecular-weight drugs [71]. Indeed, inter-bioactive interactions have shown to dictate

the extent of loading into the crystal pores, e.g. the formation of protein aggregates in solution are able to alter the diffusion of proteins into the CaCO$_3$ crystal pores, resulting in varying loading capacities for different proteins adsorbed [72], as well as vary their respective bioactivities [22]. Despite the larger pore sizes hindering small molecule adsorption, the presence of a pre-encapsulated matrix within the CaCO$_3$ crystal can act to significantly enhance the degree of adsorption of bioactives of interest, if the matrix itself holds affinity to both the CaCO$_3$ and the drug. For instance, Balabushevich *et al.* (2019) [54] demonstrated the uptake of DOX within mucin-doped CaCO$_3$ vaterite crystals, reporting a significant increase in the efficiency of loading DOX compared to that of bare CaCO$_3$, due to DOX-mucin electrostatic interactions. Similarly, Shi *et al.* (2019) [73] demonstrated the increased lysozyme uptake within heparin sulphate-doped CaCO$_3$ crystals due to the electrostatic interactions between the polysaccharide and protein.

Infiltration

Infiltration is performed via the mixing of porous vaterite CaCO$_3$ crystals with the bioactive of interest whilst decreasing the solubility of the bioactive, causing it to precipitate within the pores of the vaterite crystal to a large extent. For instance, insulin was incubated with CaCO$_3$ crystals at pH 9.5, where CaCO$_3$ is insoluble and insulin is soluble, the pH is then slowly reduced to pH 5.2; during this decrease, insulin solubility is reduced and precipitates within the crystal pores [74, 75]. This may also be performed via the evaporation of the surrounding solvent, forcing the precipitation of the bioactive into the crystal pores. Moreover, the infiltration approach can be used to synthesise beads formed fully of the bioactive of interest. These particulate structures are formed via the loading of the respective molecule into a porous template via infiltration, followed by cross-linking and elimination of this template - resulting in the formation of a pure polymeric particle, of which is an inverted replica of the template utilised [76]. Moreover, dependent upon the physiochemical properties of the biopolymer used and the extent of cross-linking, varying resultant properties in the final

particles are seen, for instance, if strong inter-polymer interactions or a high degree of cross-linking occurs, free-standing porous particles are produced. Where there are weaker interactions, the particles may collapse to non-porous beads to minimise their contact with surrounding water [77]. CaCO$_3$-templated particulate beads have been formed via use of BSA [78], poly(N-isopropylacrylamide) (PNIPAM) [79], and gelatin [80], amongst others.

Freezing-induced

Similarly to infiltration, the vaterite CaCO$_3$ crystals are incubated with the bioactive of interest and the suspension undergoes freezing. Upon freezing, during water crystallisation, both the bioactive and the CaCO$_3$ crystals concentrate in a given microvolume and the bioactive is embedded within the CaCO$_3$ crystals due to growing pressure from the crystallisation of the surrounding water [81]. This has been demonstrated with the freezing-induced loading of TiO$_2$ nanoparticles [82] and barnase [83]. Besides this, the bioactive and CaCO$_3$ crystals may be frozen under constant agitation, and, dependent upon the number of freeze/thaw cycles, the bioactive can be encapsulated to various mass contents [81].

Co-synthesis

The co-synthesis of bioactives into vaterite CaCO$_3$ crystals is performed via the mixing of the bioactive of interest with the precursor salt solutions prior to CaCO$_3$ precipitation. This results in the bioactive being entrapped within the vaterite crystal interior and can result in encapsulation to very large extents compared to adsorption [83, 84]. Lysozyme, for instance, can be loaded up to 500 ± 128 mg/g CaCO$_3$ within sub-micron crystals [85], and superoxide dismutase can reach up to 240 ± 8 mg/g CaCO$_3$ within crystals of $\simeq 4 \, \mu$m [18]. Despite these high loading capacities, the co-synthesis of bioactives may alter the nucleation and growth process of CaCO$_3$ crystals; for instance, in the presence of polylysine, both calcite and vaterite were formed, where in the pres-

ence of polyaspartic acid only calcite was produced [86]. Moreover, the encapsulation of large, highly sensitive macromolecules is possible due to the ability to form and load vaterite at close-to-physiological conditions [18], maintaining the bioactivity of such materials [70]. Due to these significant load capacities from a range of loading techniques, its versatility, and owing to its biodegradability and biocompatibility, vaterite $CaCO_3$ presents itself as an ideal template for the formation of templated LbL polymer capsules. The principals of capsule assembly and the various templates will be explored in the following section.

2.3 Layer-by-layer assembly

2.3.1 Principles of layer-by-layer assembly

The LbL assembly of oppositely charged polyelectrolytes originated in the early 1990s, and since that time, it has gained considerable interest due to its versatility and ability to modulate nanometer control over the film properties [87, 88]. The broad spectrum of usable materials and a choice of coating both flat and particulate substrates provoked exponential growth of research in this field, that has demonstrated the potential of LbL technology for various applications. Particularly, LbL technology presented several advantages for biomedicine: (i) deposition of homogeneous films with controlled thickness, (ii) high loading capacities and controlled release of biomolecules/drugs of various nature and (iii) coating stability under physiological conditions. This made the LbL method one of the most rapidly growing strategies for generating thin film coatings of biomedical scaffolds [89–91], patterned surfaces [92, 93], medical devices [94, 95] and implants [96, 97], while multilayer capsules became promising nano- and micro-carriers for drug delivery applications [69, 87, 98–103].

Generally, LbL fabrication is based on the alternating exposure of a substrate (of nearly any geometry) to positively and negatively charged polyelectrolytes (Figure 2.2). The three classical methods for applying LbL coatings (i.e. polyelectrolyte mul-

tilayers (PEMs)) consist of dip coating, spraying, and spin coating. Each method has distinct advantages and disadvantages that are discussed elsewhere. In brief, alternating dipping of the substrate into the solutions of polyelectrolytes is the most widely used method for LbL deposition. This method is the most simple, robust and versatile amongst the three methods proposed. However, it is also the most time consuming and leaves abundant residual polyelectrolyte from each deposition step, of which obstacles its commercialisation. Spin coating is based on the rapid evaporation of the solvent from the coating material. Notably, polymer dynamics in spin-assisted PEMs is inhibited due to the stronger binding between spin-deposited polyelectrolytes [104]. Such films are generally thicker than those resulting from the dipping technique, however, spin coating of peculiar 2D substrates and 3D substrates is technically challengeable. In its turn, spray coating is devoid of these shortcomings, although some reports indicate that sprayed samples are more labile to variable external microenvironments [105]. Recently, microfluidics has also been adapted for LbL assembly within microchannels [92].
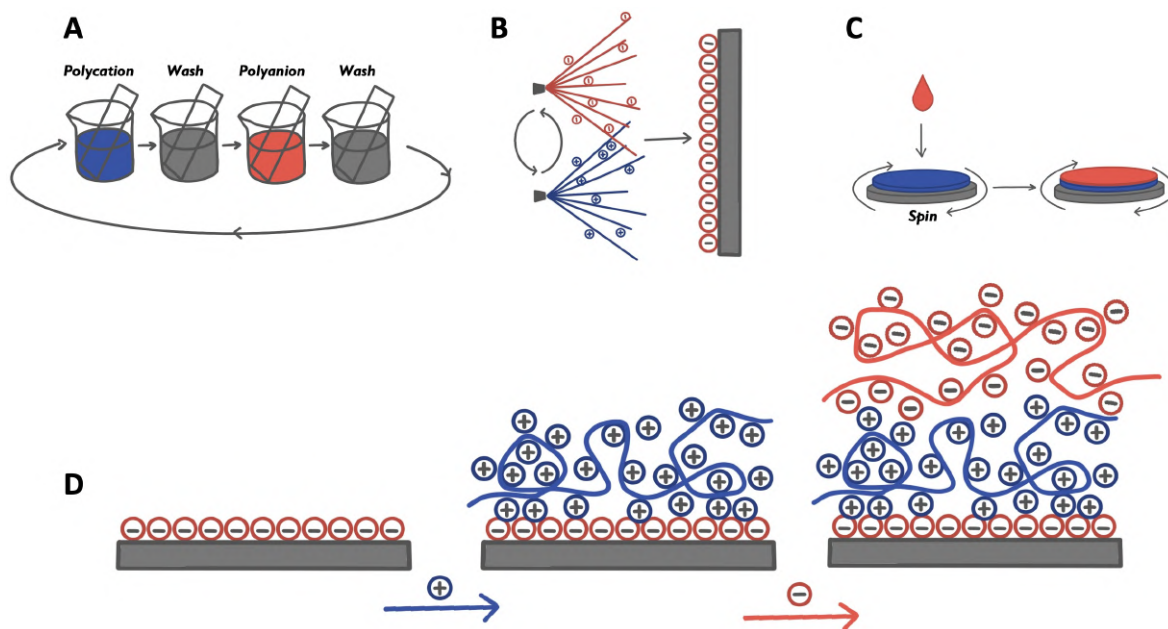
Figure 2.2: Schematic of classical approaches to form LbL films: (A) dip-coating, (B) spray-coating, and (C) spin-coating; (D) schematic of the build-up of LbL films upon a negatively charged substrate. Blue: polycation, red: polyanion. Reprinted with permission from reference [106].

Depending on the nature of the polyelectrolytes, PEMs can be been assembled from synthetic, from naturally occurring polymers, or from their mixture. The most important examples of synthetic polyelectrolytes that are utilised for LbL assemblies and generate cations are poly(allylamine hydrochloride) (PAH) and poly(diallyldimethylammonium chloride) (PDADMAC); typical synthetic polyanions are poly(acrylic acid) (PAA) and poly(styrene sulfonate) (PSS).

Natural polyelectrolytes, such as components of the extracellular matrix (HA, COL, elastin, fibronectin, laminin), proteins (PR, gelatin), nucleic acids (DNA and RNA) and polysaccharides (which are the most abundant family of natural polymers), have also gained considerable attention as the building blocks for the multilayers [13]. PEMs fabricated from such biogenic polyelectrolytes hold specific bioactivities (e.g. antinflammatory [107, 108] and osteogenic activities [109]), useful for a variety of bioapplications. In some studies, self-assembled structures such as liposomes and micelles were also used as the building blocks for LbL deposition [110]. Recent trends in LbL technology include the assembly of hybrid structures composed from polymers, lipids, and nanoparticles [111–115].

Biopolyelectrolytes are intrinsically labile and more difficult to handle than synthetic polyelectrolytes; it makes the design of LbL structures made of biopolymers more challengeable [87]. However, obvious benefits of the use of biopolymers (such as their intrinsic unique biocompatibility, biodegradation, no-to-low toxicity, high loading capacities and mimicking of the natural cellular microenvironment) [116, 117] boost the use of biopolymer-based PEMs for biomedical applications and in other fields such as bioelectronics [118, 119], bio-energy [120, 121], food packaging/storage [122], etc.

Regardless of the nature of the polyelectrolytes, the most predominant interaction in LbL multilayer formation is the electrostatic interaction between oppositely charged polyelectrolytes. In a review [123], it is reported that there is a charge threshold, of which the previously deposited layer on the surface of the template must hold a certain charge density and charge distribution for adsorption to occur. However, additional interactions also contribute to multilayer formation. Generally, the anionic polyelec-

trolytes employed are composed of a hydrophobic hydrocarbon backbone, with the side groups containing charged groups, therefore, the polymers hold some amphiphilic character so hydrophobic interactions [124] must also be taken into account for film formation. It has been reported that, from Gibbs free energy of multilayer formation, for increased numbers of polyelectrolyte pairs, hydrophobic interactions are essential for formation of the multilayers. Furthermore, depending upon the polymers used, hydrogen bonding may also be a decisive factor, especially for use of neutral polymers. All these interactions determine the dynamics of biopolymers in the PEMs. It is commonly accepted to distinguish between the dynamics of polymer molecules that may diffuse inside or in/out the PEMs and the dynamics of polymer chains or binding sites

2.3.2 Polymer dynamics and multilayer growth

The growth of PEMs is something that has been widely discussed in the literature. Typically, two different growth regimes are observed when assembling PEMs; these are the linear and non-linear (exponential) growth regimes. The former involves a film which grows linearly with each additional polymer deposition step i.e. the thickness increment by which the PEM increases by remains constant throughout the multilayer build-up. The latter involves a film thickness that increases exponentially with each polymer deposition step. Many synthetic polymers form linearly growing PEMs, one extensively studied pair is the PSS/PDADMAC system [125, 126]. Linear growth can only take place if the charge of the newly added polyelectrolyte overcompensates that of the surface it is adsorbed upon [127]; this may occur if there is some additional affinity the freshly added polymer has to the pre-adsorbed polyelectrolyte at the surface, such as hydrophobic interactions or van der Waals forces.

The exponential growth of PEMs is much more dependent upon the polymer dynamics within the multilayer, it is shown that even PSS/PDADMAC PEMs exhibit exponential growth at higher ionic strengths, where the PEM behaves similar to a fluid rather than a glassy solid [127]. It is widely thought that the mechanism in which exponential

growth occurs involves the whole of the PEM. Exponential growth can only occur if at least one of the polymers constituting the PEM is able to diffuse in and out of the film [128, 129]. For example, if the polycation is the diffusive species within the PEM, it will be able to diffuse out of the film when the film is in contact with polyanion-containing solution, and form complexes with the polyanion chains at the surface (forming a new layer). Therefore, the thickness increment added can be said to be proportional to the number of polycation chains able to diffuse out of the PEM when in contact with polyanion-containing solution; which is also proportional to the total PEM thickness - this leads to the exponential growth regime. This was first shown by Picart *et al.* (2002) [130], demonstrating that within HA/PLL PEMs, PLL was able to diffuse throughout the whole PEM to interact with HA at the surface to form polyelectrolyte complexes, contributing to a new layer - leading to an exponential increase in PEM thickness. Later, it was demonstrated that the distribution of PLL within PEMs depends on its dynamics that are correlated with the degree of its polymerisation (Figure 2.3) [131].
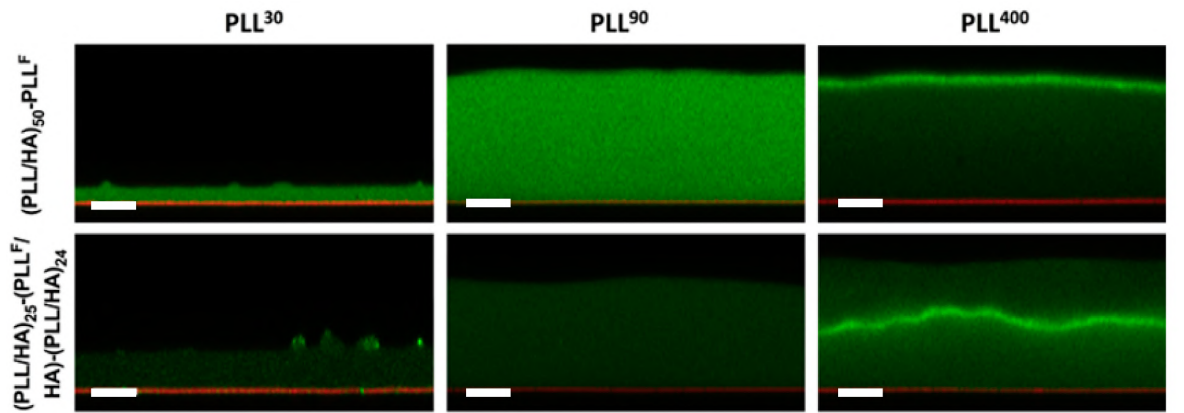
Figure 2.3: Examining PLL mobility within $(PLL/HA)_{50}$ films using confocal laser scanning microscopy (CLSM) and fluorescence recovery after photobleaching (FRAP) experiments: cross-sectional CLSM images of $(PLL/HA)_{50}$-PLLF (top) and $(PLL/HA)_{25}$-(PLLF/HA)-$(PLL/HA)_{24}$ films (bottom) assembled with PLL^{30}, PLL^{90}, and PLL^{400} (left to right). Green indicates PLLF and red indicates the glass substrate. The scale bar is 10 μm. Figure reprinted with permission from reference [131], Copyright © 2019 John Wiley and Sons Ltd.

The charge densities of biopolyelectrolytes play a profoundly important role within stable PEM formation. Two different types of PEM charge compensation are typically observed: extrinsic and intrinsic charge compensation. Extrinsic charge compensation

refers to any excess polyelectrolyte charge being compensated via counter ions arising from salt (i.e. Na$^+$ and Cl$^-$), where intrinsic charge compensation refers to the balance of charge between pre-existing polyelectrolytes within the PEM [132]. Due to their inherently low charge densities, one can expect that the majority of biopolymer-based PEMs will exhibit exponential growth, making extrinsic charge compensation much more important within these systems. Many studies have depicted the growth regimes of biopolymer 2D PEMs; multiple studies are present on, arguably, the most studied biopolymer PEM, the exponentially growing HA/PLL system; which typically forms a viscous, hydrogel-like film [133]. Others include PEMs such as the highly studied CHI and PLL systems, both of which have been previously paired with HA [92, 134]; alginate (ALG) [135, 136]; HS [137, 138], CS [139, 140] and poly(glutamic acid) (pGLU) [141]. Each of these systems have been shown to grow exponentially. Lundin *et al.* (2009) [142] has demonstrated that CHI is able to diffuse throughout the whole film (7 bilayer film), through forster resonance energy transfer (FRET) and total internal reflection fluorescence (TIRF) approaches, when in combination with HS. Furthermore, Mutschler *et al.* (2017) [143] conducted a systematic study comparing the exponential character of poly(arginine) (pARG) paired with ALG, CS, HA, HS, pGLU and PSS within PEMs. It was observed all combinations resulted in the exponential growth regime, apart from PSS. Therefore, it can be said the exponential character of the film increases with decreasing polyion-polyion interaction. The HA/pARG reaction enthalpy was endothermic, and hence held the weakest interaction - this suggests a strongly exponential-like growth regime, as demonstrated by Laugel *et al.* (2006) [144]. It can be said, the weaker the interaction between the two polyelectrolytes, the easier the diffusion is throughout the film, which is the cause of exponential growth. A strong exothermic interaction between two polyelectrolytes will result in a much more favourable interaction for the polymers, and hence a tightly knit polymer network within the PEM; leading to the linear growth observed for PSS/pARG, PSS/PDADMAC [126], PSS/PAH [145], and other synthetic systems. However, biopolymer pairs which possess linear growth regimes are possible; Radeva *et*

al. (2006) [146] reported linearly growing CHI/carboxymethylcellulose (CMC) PEMs, when formed using highly charged CHI and weakly charged CMC at low ionic strengths; the effect of which will be discussed later. Besides these studies, it can be relatively difficult to obtain a stable biopolymer PEM, as their lower inherent charge densities may result in too weak an interaction for biopolymer-based PEMs to form at all, especially at physiological conditions. For example, HA has been previously paired with COL [147], but the PEM proved to be unstable at physiological pH due to protein reorganisation and changes to the degree of ionisation of HA at these conditions. However, the film became stable upon cross-linking the polymers within the film.

However, there comes a point during PEM build-up in which the exponential growth switches to linear. How this transition occurs is still debated within the literature. An island model has been proposed, where, firstly, islands grow upon a substrate (their growth is exponential); eventually they will coalesce and form a uniform film across the substrate [148]. A model based on the dendritic-nature of linear polymers was also suggested, at which the transition point occurs due to steric hindrance of the polymer chains during the exponential build-up, finally resulting in a constant number of binding sites [149] (Figure 2.4). A model proposed by Hübsch *et al.* (2004) [145], stated that once the PEM reaches a critical thickness at which neither of the polymers are able to diffuse through the whole PEM when in contact with the alternate polymer solution, the diffusive species that will contribute further towards the growth of the PEM will be the zone just below the PEM-solution interface. Therefore, the number of polymer chains able to diffuse in and out of the PEM becomes constant as this zone will remain a constant thickness upon further addition of new polymer layers - leading to the linear growth regime. Salomäki *et al.* (2005) [150] proposed a similar model, proposing a diffusion-limited mechanism also, where the PEM reaches a thickness at which the rate of diffusion is too low for exponential growth to continue. Moreover, it is put forward that as the PEM thickness increases, a restructuration zone develops due to the rearrangement of polymer chains as the build-up continues (Zone II in Figure 2.4). This zone holds a much higher polymer density compared to the rest of

the film, in which polymer diffusion is greatly limited. This was first developed by
Porcel *et al.* [151, 152], in which, as the exponential build-up continues, eventually this
restructuration zone will develop, within which polymer diffusion is so hindered that
the part of the film contributing to PEM growth reaches a constant thickness (Zone
III in Figure 2.4).
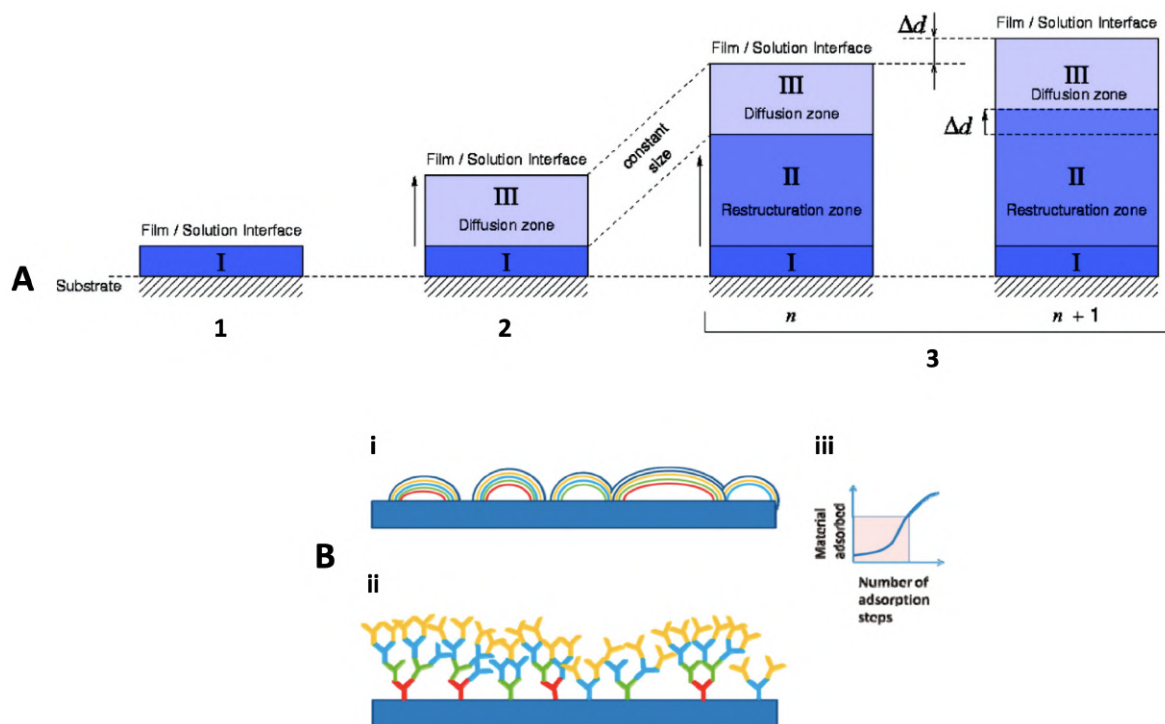
Figure 2.4: Models of film build up. (A) Model of the restructuration zone; (1) initial
film build-up upon the substrate, (2) the development of the diffusion zone within the
film, and (3) the formation of the re-structuration zone, including the case where the
number of deposition steps increases from n to n + 1. Reprinted with permission from
reference [151], Copyright © 2007 American Chemical Society. (B) The substrate for
film fabrication is shown as a horizontal slab. The film resulting from successive poly-
mer adsorption steps is shown via different colours, each representing a polymer layer.
(i) Island model, (ii) Dendritic model, and (iii) Approximate growth of material de-
posited. Reprinted with permission from reference [149], Copyright © 2011 American
Chemical Society.

From this point on, the film grows linearly with deposition steps. HA/PLL films have
been shown to exhibit an exponential-to-linear transition point between twelve and
eighteen bilayers [151], and CHI/pGLU have been reported to transition around nine
deposition cycles [141]. However, this number may vary with build-up conditions able
to alter the diffusion of polyelectrolytes through the PEM.

Certain microenvironmental changes can drastically influence the growth and build-up regimes of PEMs. This is one of the reasons why biopolymer-based multilayer films have become attractive drug delivery/reservoir systems; due to their ease of tunability and respective properties. As aforementioned, biopolymers are much more dynamic and possess low charge densities - making biopolymer-based PEMs highly sensitive to their microenvironment. This gives us the opportunity to alter the microenvironment during PEM build-up in order to tune their growth dynamics. In this review, we consider three main factors - the temperature, the pH and the ionic strength - that influence the growth of PEMs.

Effect of temperature

In the study [153], the effect of temperature on the transition point from exponential-to-linear growth of HA/PLL PEMs has been investigated. It was found the transition point could be shifted from 12 to 21 bilayers. The increase in preparation temperature (to a maximum of 85°C) increased the polymer mobility, and therefore the diffusion rate of PLL, allowing PLL to diffuse through the entire PEM even when the total PEM thickness was increased. It is also inferred that these multilayers grown at higher temperatures are more porous, allowing for less-hindered diffusion. This was demonstrated through temperature changes during PEM build-up at 21 bilayers, either from 25°C to 65°C, or vice versa (Figure 2.5). When increasing the temperature during PEM build-up, the film grows slower compared to when it is fully grown at a higher temperature to begin with. One can expect a difference in PEM structure as the temperature changes through initial build-up stages as the polymers will have higher thermally induced motion, and as such the polyion-polyion interactions will be weakened and the film is more porous. For instance, it has been shown that even in synthetic PEMs that an increase in temperature can alter the growth regime of the film, extending the exponential growth region at the beginning of film build-up, when using the polymer pairs PSS/PDADMAC and PSS/PAH, with an increase in deposited bilayer mass [150].
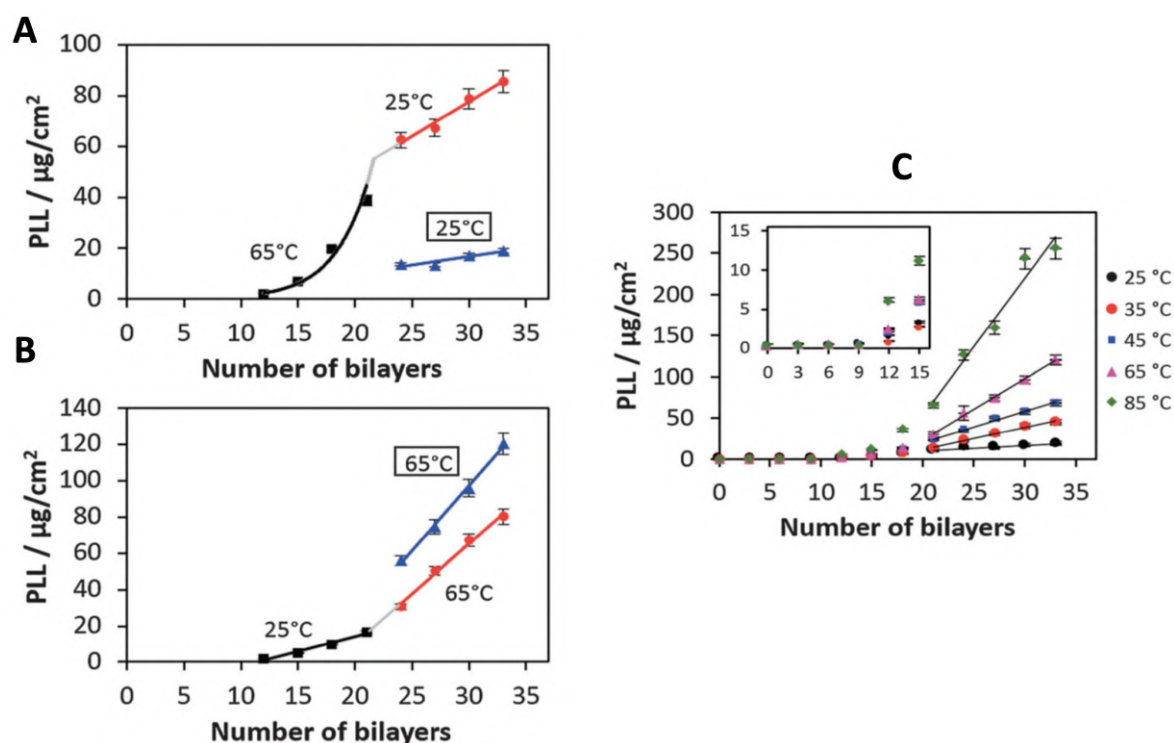
Figure 2.5: (A) Temperature change from 65°C to 25°C; (B) Temperature change from 25°C to 65°C at the 21st bilayer. The blue triangles represent film preparation at 25°C and 65°C without the temperature change after 21 bilayers. (C) Mass coverage of PLL in the HA/PLL film formed at different temperatures. The inset shows the enlarged growth profile until 15 bilayers. Reprinted with permission from reference [153], Copyright © 2016, published by the PCCP Owner Societies.

Effect of pH

Controlling the pH during PEM build-up is also of crucial importance; especially for weak polyelectrolytes in which their charge densities can be easily tuned. Yuan *et al.* (2007) [154] reported the effect of build-up pH upon CHI/ALG multilayer films; the pH of the ALG solution was altered whilst CHI remained constant at pH 3. The thickness of ALG layers decreases with increasing pH, this is due to the increased ionisation of the ALG chain, causing the chain to become more extended, to give thinner layers. Changing the polyion solution pH also gives the opportunity to tune the surface composition; In the same study, Yuan *et al.* demonstrated that increasing the ALG solution pH changes the conformation of the CHI layer on which it is deposited upon, inducing more globular complexation between the two polyions, as well as aggregation of the CHI molecules due to less intra-chain repulsion at higher pHs. This change in

conformation also resulted in the increase in relative thickness of the neighbouring CHI layer. These results both support and build upon the results of Bieker and Schönhoff (2010) [155], in which the thickness of the PEM of two weak polyelectrolytes was significantly altered within a narrow pH range. It was found, at either low or high pH, where one of the polyions is more ionised than the other, interpenetration between polymer layers occurs and the growth becomes exponential. This is opposed to a relatively equal ionisation degree between the two polymers at an intermediate pH, which gives very defined layers, and hence, the linear growth regime. However, at pHs where there is a dramatic difference in ionisation degrees, this interpenetration stops and asymmetric growth occurs, causing the PEMs to grow linearly again. Indeed, the resulting growth behaviours are governed by the degree of ionisation of polyelectrolytes at certain pHs [156]; depositing each layer at pHs where the polyelectrolytes are partially ionised and in coiled conformations (close to their pKa) i.e. HA (pH 2.9) and PLL (pH 9.5), will result in thicker layers being deposited [157]. Again, Burke *et al.* (2003) [158] reported the build-up of HA/PLL films at different pHs; pH 7 resulted in the thinnest PEMs where pH 9 gave the thickest. This was due to the partially ionised and coiled conformation of PLL, in comparison to HA at pH 9, resulting in higher adsorbed quantities of PLL; where, at pH 7, both polyelectrolytes are almost fully ionised, resulting in flatter conformations. This observation was also noted by Barrantes *et al.* (2012) [159], in which it is proposed PLL and HS adopt a flat conformation at more acidic conditions (pH 5.5), and PLL is thought to adopt an α-helical structure at higher pHs (7-8.5, depending on the substrate used for deposition) due to its reduced charge density. This results in the exponential growth of HS/PLL PEMs as the lower charge density of PLL allows for easier diffusion through the entire film. Moreover, Rocha Neto *et al.* (2019) [134] observed the opposite effect, reporting thinner deposited layers of both HA and CHI at pH 5 due to the high charge densities, and hence, rigid conformations of both polyelectrolytes. This results in lower surface roughness of the film due to a lower concentration of randomly coiled HA and CHI chains penetrating the surface. The effect of pH upon the incremental bilayer thickness at different ionic strengths has also

been studied within HS/CHI PEMs. As the pH of CHI approaches its pKa (6.46-7.32 for NH_2 groups) from a more acidic pH, it becomes increasingly less ionised, as such it adopts are more coiled conformation upon the pre-adsorbed HS surface, as well as adsorbs in higher quantities. Therefore, with increasing pH from 4.6 to 5.8, there is an increase in bilayer thickness at all ionic strengths studied [160], as seen in Figure 2.6. The authors attributed the increasing HS layer adsorption with increased pH to the increasing mass of CHI adsorbed, so a larger amount of HS is needed for charge reversal.
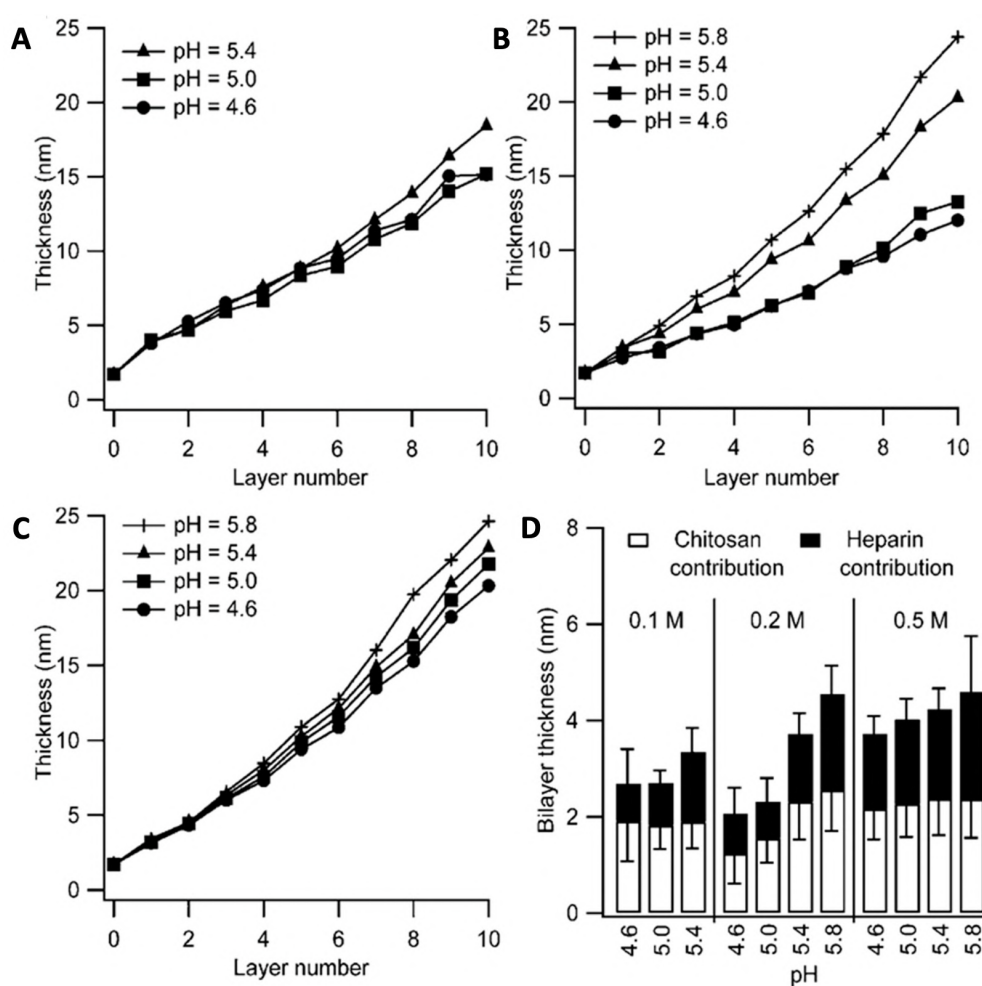
Figure 2.6: PEM thickness obtained from *in situ* Fourier transform-surface plasmon resonance (FT-SPR) data as a function of layer number and pH for 0.1 M buffer (A), 0.2 M buffer (B), and 0.5 M buffer (C). Odd numbered layers are CHI and even-numbered layers are HS. (D) Average incremental bilayer thickness of PEM at different buffer conditions as a function of pH. Reprinted with permission from reference [160], Copyright © 2008 American Chemical Society.

Effect of ionic strength

The ionic strength of the solution can profoundly affect the assembly of PEMs, especially those in which extrinsic charge compensation is of great importance (i.e. biopolymers). Boddohi *et al.* (2008) [160] reported an increase in HS/CHI film thickness with increasing ionic strength within the polyelectrolyte dipping solutions, this was attributed to the effective electrostatic screening of charges along the HS and CHI chain. This will give rise to less intra-chain repulsion and result in more coiled conformations of polymers resulting in thicker deposited layers, as seen in Figure 2.6. Moreover, Lundin *et al.* (2011) [161] reported similar results, and observed the exponential growth regime of PEMs regardless of the ionic strength used. Interestingly, Richert *et al.* (2004) [162] demonstrated the transition from exponential to linear growth when decreasing the ionic strength from 0.15 M to 10^{-4} M, and linear growth for a $(HA/CHI)_8$ film (built at 10^{-4} M) built atop an exponentially growing $(HA/CHI)_9$ film (built at 0.15 M). At concentrations of 10^{-4} M, only PEM islands of HA/CHI films could grow upon the substrate but appeared to grow linearly. At higher ionic strengths (0.15 M), the islands were only present for the first deposition steps, until they coalesce to form a uniform film - the higher the salt concentration, the earlier this coalescence. The increased ionic strength screens the charges along the polyelectrolyte chain, reducing HA-CHI interaction and allowing for easier diffusion of CHI through the entire film compared to lower ionic strengths (where only islands may form), resulting in the final thicker PEM.

2.3.3   3D assembled layber-by-layer structures

A plethora of sacrificial templates are utilised to form such 3D structures (i.e. polyelectrolyte multilayer capsules (PEMCs)), and all host a variety of properties related to the final capsule structure, stability, and application. The variation in capsule internal structure is dependent on both the porosity of the template, as well as the size of the biopolyelectrolytes utilised for multilayer coating [100]. Templates may be categorised

as porous; for instance, carbonates (i.e. calcium [68, 163] and manganese [164, 165] carbonates), mesoporous silica (MS) [166–168], and potentially calcium phosphate [169], or non-porous templates; for instance, polystyrene latex (PS) [170, 171] and melamine formaldehyde (MF) [172]. Biological entities (e.g. erythrocytes [173, 174] or bacteria (*Escherichia coli* (*E. coli*) for instance [175, 176])) are also utilised as templates.

When utilising a porous template, varying capsule structures are yielded. If the pore diameters are larger than that of the biopolymers used, during the initial deposition stages of LbL assembly the biopolymers adsorb to the template surface, however, in this case the polymers are also able to permeate the template internal structure through surface pores and form an internal polymeric matrix [25]. Once the desired number of deposition stages is achieved, the template undergoes dissolution, leaving a capsule with an internal gel-like matrix; this capsule is coined a matrix-type capsule, or microgel [25, 177] (Figure 2.7). During LbL deposition upon a non-porous template, the polyelectrolytes adsorb to the template surface, following this, the template is eliminated, leaving a polymeric shell and a hollow lumen - these are known as hollow-type capsules. These shells may also form if no polymer is able to permeate the pores of a porous template, as illustrated in Figure 2.7, using vaterite $CaCO_3$ as an example template. Moreover, the control over the capsule internal structure allows to control the capsule release properties; a burst or sustained release can both be achieved with hollow- and matrix-type capsules, respectively [25].
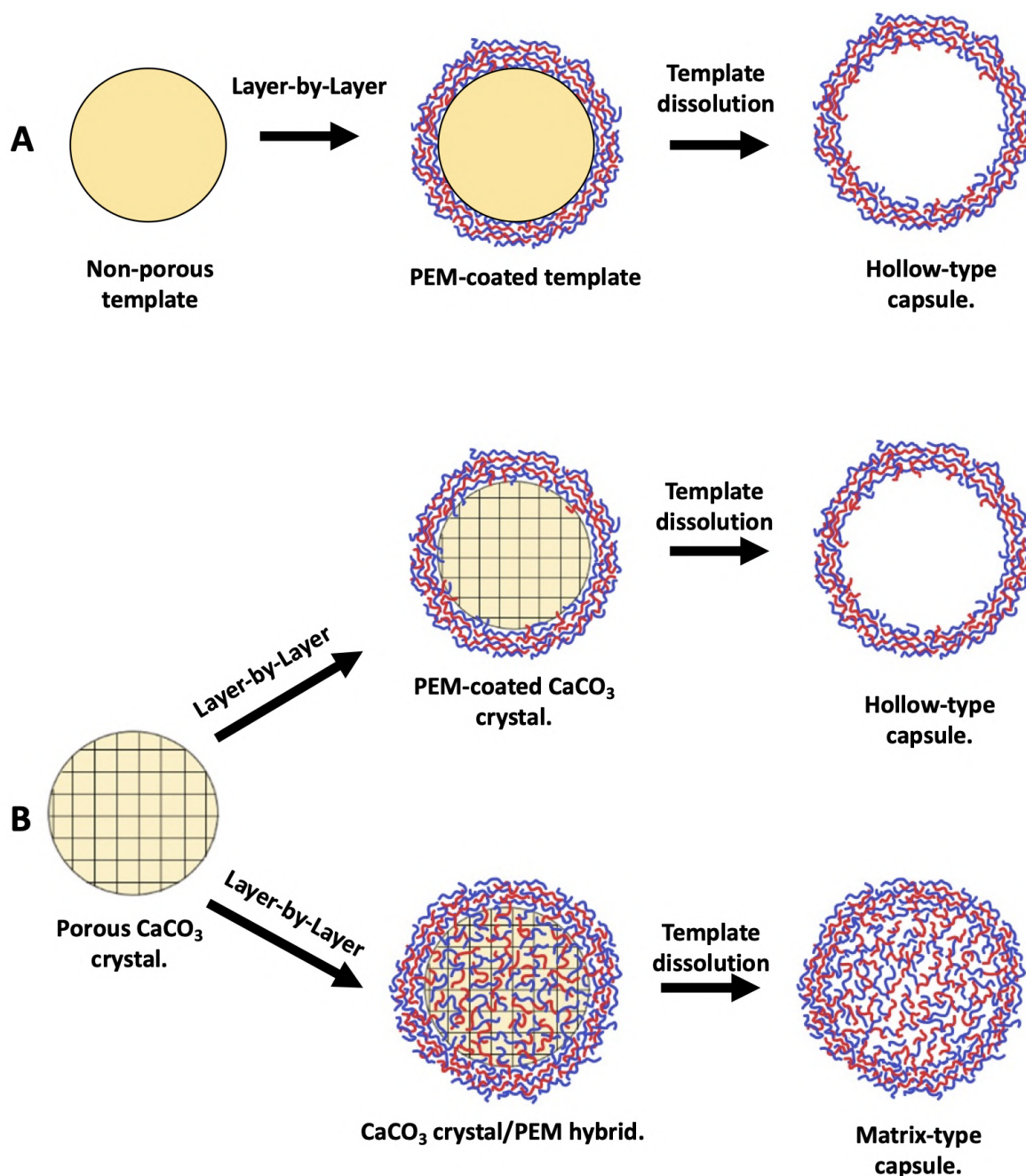
Figure 2.7: (A) The formation of hollow-type PEMCs upon a non-porous template. (B) The formation of hollow- and matrix-type PEMCs via either the formation of a polymer shell or CaCO$_3$/PEM hybrid, respectively. Reprinted with permission from reference [106].

For stable biopolymer-based capsules to form, a sacrificial core that undergoes dissolution at mild conditions and gives rise to the minimal amount of osmotic pressure upon dissolution is required to prevent the rupture of multilayers during dissolution. However, many sacrificial cores possess specific drawbacks typically related to dissolution conditions and their toxicity *in vivo*. For example, MF cores undergo dissolution at

low pHs [178] and are hence not physiologically relevant, but upon dissolution there is an increase in osmotic pressure within the capsule, leading to high degrees of swelling and sometimes capsule rupture; and if the capsule is able to form, residues of MF often remain within [179]. The carbonates, $MnCO_3$ and $CaCO_3$, are particularly attractive; the vaterite polymorph of $CaCO_3$ holds a well-developed porous structure [10], with pore sizes in the typical range of 5-35 nm that can be further manipulated to control capsule internal structure [100]. It is biocompatible, of low cost production [44] and undergoes dissolution at mild conditions [10], e.g. with ethylenediaminetetraacetic acid (EDTA), or citric acid - resulting in little osmotic pressure [10]. Importantly, biomacromolecules preserve their biological activities when encapsulated into the vaterite crystals [22, 70, 98].

Biopolymer-based capsules templated on non-porous templates

Advantages of the non-porous templates typically used to from PEMCs are the resulting properties following particle synthesis; including the range of controllable sizes available, starting from as small as tens of nanometres up to a few millimetres, as well as their typical monodispersity and stability as colloidal particles - ideal for PEMC formation and delivery carriers. Despite this, some of such carriers are hindered by their lack of biocompatibility both before and after template dissolution. For instance, non-porous silica templates require hydrofluoric acid to undergo dissolution which is not ideal for biopolymeric materials.

DS/PR-based PEMCs have been templated upon MF cores, and, following treatment of MF with pH 1.7 HCl, MF residues have been retained within the PEMC interior as shown via Raman spectroscopy - likely due to DS-MF complex formation [179]. Although beneficial for the binding of encapsulated conditions. The same was observed for ALG/CHI PEMs in the form of ALG-MF complexes and the binding of positively charged insulin at low pHs [180], as well as within DNA/spermidine (SP) and ALG/PLL microcapsules [181]. The stable PEMC formation is dependent upon the osmotic pressure build-up during core dissolution and the ability of the MF oligomers

to diffuse outwards [178] - which may also be responsible for PEMC swelling during the core dissolution. Moreover, MF resin may become irreversibly adsorbed to the capsule shell and can contribute to up to 20% of the capsule mass.

Further to this, polystyrene latex (PS) templates have also been employed for the formation of biopolymer PEMCs (fucoidan (FC)/CHI, for instance); the templates were treated with tetrahydrofuran (THF) [182] for two hours for removal and the PEMCs shrank by almost 50% of their template size; of note calcination of the coated PS core is also used for template removal [170], both of which are not ideal for many sensitive biogenic capsules. Besides this, as PEMs formed on smooth non-porous templates are typically thinner and well defined [183], the loading and release of bioactives post-template dissolution can be well controlled via alterations in pH, ionic strength and cross-linking of the shell. For instance, silica-templated DS/CHI PEMCs demonstrate a reversible permeability phenomenon; PEMCs were impermeable to dextrans from 4000-250000 Da at pHs < 6.8 but were permeable above pH 8. These permeable capsules were then reduced to pH 5.6, and the dextran was entrapped within the capsule interior (Figure 2.8) [184].
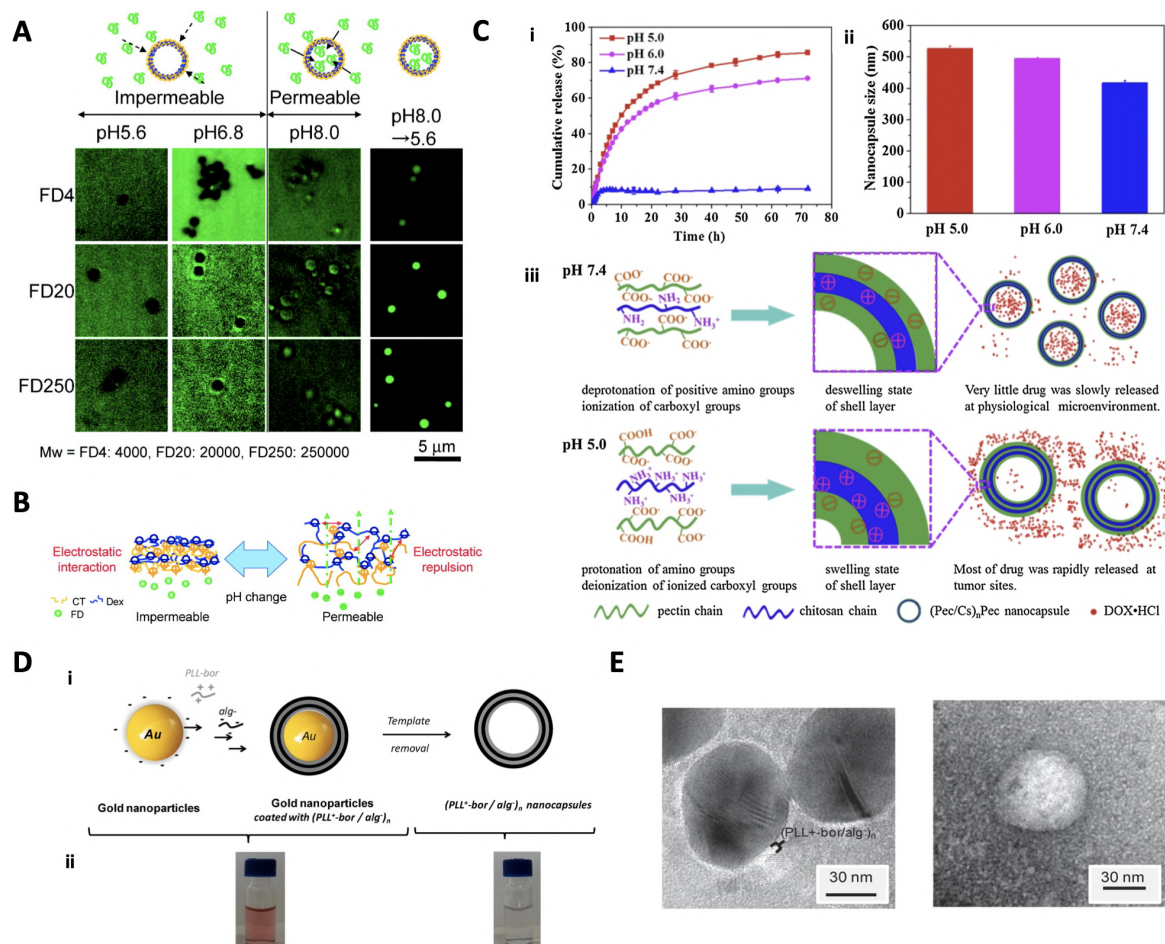
Figure 2.8: (A) Schematic and confocal microscopy images of the relative permeability of dextrans of varying molecular weight; FD4-4000, FD20-20,000, and FD250-250,000 in buffer solutions (pH 5.6, 0.05 M acetic acid buffer; and pH 6.8 and 8.0, 0.05 M Tris buffer) containing dissolved fluorescein isothiocyanate-labelled dextran. (B) A schematic illustrating the change in permeability within the PEM when changing pH. Reprinted with permission from reference [184] Copyright © 2008 American Chemical Society. (C) The cumulative release of DOX from (pectin/CHI)$_3$/pectin nanocapsules (i), the hydrodynamic size of nanocapsules at varying pH (ii), and the schematic illustration of the pH responsive nanocapsules (iii). Reprinted with permission from reference [185] Copyright © 2017 Elsevier. (D) The schematic illustration of the formation of glucose-responsive nanocapsules (i), and the suspensions of coated-gold nanoparticles (left) and nanocapsules following removal of the core (right) (ii). (E) Transmission electron microscopy (TEM) micrographs of (left) (PLL-bor)/ALG)$_4$-coated gold nanoparticles and (right) nanocapsules. Reprinted with permission from reference [186] Copyright © 2019 Elsevier.

This is attributed to the electrostatics of the biopolymers within the PEMs; at higher pHs, there is an increased repulsion between the sulfonate groups upon DS and a reduced cationic charge on CHI, thus causing the polymers to change their conformation and increasing PEM permeability [184], as illustrated in Figure 2.8. Similar behaviour

is observed with HS/PR [187] and pGLU/CHI [188] PEMCs, as well as Pectin/CHI PEMCs with the release of DOX; DOX is not released at pH 7.4 but is rapidly released at pHs 5 and 6. This was attributed to the swelling of the PEMCs upon decrease in pH due to the increased protonation state of CHI below pH 6.5 (pKa value), with a size increase of 418 to 527 nm from pH 7.4 to 5, respectively [185] - a schematic of which is shown in Figure 2.8.

This pH-responsive property is useful as a way to control the release of the bioactive encapsulated, especially in-terms of low intracellular or tumorous pHs in which the PEMCs may be uptaken. Further to this, metal nanoparticles may also be used as PEMC templates. Gold nanoparticles in particular have been utilised as templates for glucose-sensitive ALG/phenylboronic-modified PLL PEMCs; the gold core was removed via the addition of potassium cyanide followed by dialysis for the removal of the gold complex formed (the authors confirmed the lack of gold via inductively coupled plasma (ICP) analysis) [186], as demonstrated in Figure 2.8. The use of such well-established monodisperse metal nanoparticles as templates allows for the formulation of PEMCs on the nanoscale ($\simeq$40 nm in this study). Further examples of non-porous templates utilised for the formation of biopolymer PEMCs can be found in 2.1.

Table 2.1: Summary of successfully fabricated nano- and microcapsules templated on non-porous templates as reported in literature. MF: melamine formaldehyde; NPs: nanoparticles; PS: polystyrene; ALG: alginate; CAR: carrageenan; CHI: chitosan; FC: fucoidan; HS: heparin sulphate; PR: protamine; pGLU: poly-L-glutamic acid; PLL: poly-L-lysine; PLL-pb: phenylboronic modified poly-l-lysine; and SP: spermidine.

Polyanion	Polycation	Template, Size	Layers	Reference
	CHI	MF, 2.1 μm	10	[180]
ALG	PR	MF, 6.5 μm	8 & 16	[189]
	PLL	MF, 5.7 μm	5	[181]
	PLL-pb	Gold NPs, $\sim$40 nm	4 & 8	[186]
CAR	CHI	SiO_2-NH_2, 100 nm	11	[190]
		Silica, 3 μm	14	[184]
DS	CHI	Silica, 330 nm	10	[191]
		Silica, 220 nm	8	[192]
	PR	MF, $\sim$5 μm	8	[172], [179]
HS	PR	Silica, 180 nm	6	[187]
	CHI	Silica, 220 nm	6	[193]
pGLU	CHI	MF, $\sim$1 μm	10	[194]
		Silica, 330 nm	8	[188]
FC	CHI	PS, 90 nm	10	[182]
Pectin	CHI	SiO_2-NH_2, $\sim$100 nm	7	[185]
DNA	SP	MF, 1.8 & 5.7 μm	5	[181]

Biopolymer-based capsules templated on porous templates

The use of porous templates (i.e. $MnCO_3$, $CaCO_3$, and MS) for the formation of PEMCs holds numerous advantages over that of non-porous templates; one most prevalent being the ability to load bioactive material into the template's intrinsic porous structure. Porous vaterite $CaCO_3$ has demonstrated enormous loading capacities, as aforementioned. Moreover, the loading of such bioactives may be enhanced via the pre-encapsulation of a polyelectrolyte of affinity to the material of interest; Shi *et al.* (2018) [24] enhanced the loading of lysozyme by the co-synthesis of heparin sulphate (HS) prior. Of great interest, this can also be applied to the encapsulation of low molecular weight bioactives, of which are difficult to encapsulate due to their small size compared to the large pore sizes of such templates. This has been applied with lentinan [63] with DOX and CMC [195] with daunorubicin. Balabushevich *et al.* (2019) [54] successfully encapsulated DOX via the electrostatic binding to a gel-like mucin

matrix pre-encapsulated within the vaterite crystal, reaching DOX content of up to 1.3 mg/g $CaCO_3$, giving scope for a variety of clinically-relevant drug delivery applications, and the potential use of vaterite as vehicles with mucoadhesive properties [69, 103]. Moreover, due to the variety of loading mechanisms, one is able to tailor the loading technique to the biomaterial of interest; for instance, certain macromolecules or nanoparticles may be sensitive to salt solutions forming the crystal template, and hence, adsorption may be preferred.

Vaterite $CaCO_3$ has also proved itself a diverse material as both a stand-alone drug delivery vehicle [196, 197] as well as a material for surface coatings [85], for functional use as an antimicrobial carrier, for instance [20, 47]. However, there can be an issue with the aggregation of vaterite $CaCO_3$ crystals, making it difficult to form monodisperse templates without the need of additives, such as polypeptides [198]. Due to its low cost production (0.2-0.4 $ per g dried weight), potential ease of scalability [199], and soft dissolution conditions, vaterite $CaCO_3$ presents itself as an attractive template for PEMCs, with example biopolymer PEMCs formed from vaterite $CaCO_3$ are shown in Figure 2.9. Alternate templates, MS, for example, although advantageous regarding pre-loading capability, is typically removed via hydrofluoric acid, much like non-porous silica, which is not suitable for bioapplications, nor ideal for pre-encapsulated bioactives. However, as of recent, PEMCs have been formed via the removal of MS at physiological conditions via dissolution in a buffered salt solution [166], as demonstrated in Figure 2.9. Due to these advantageous properties, many more examples of biopolymer-based PEMCs are emerging, examples of such can be found in Table 2.2.
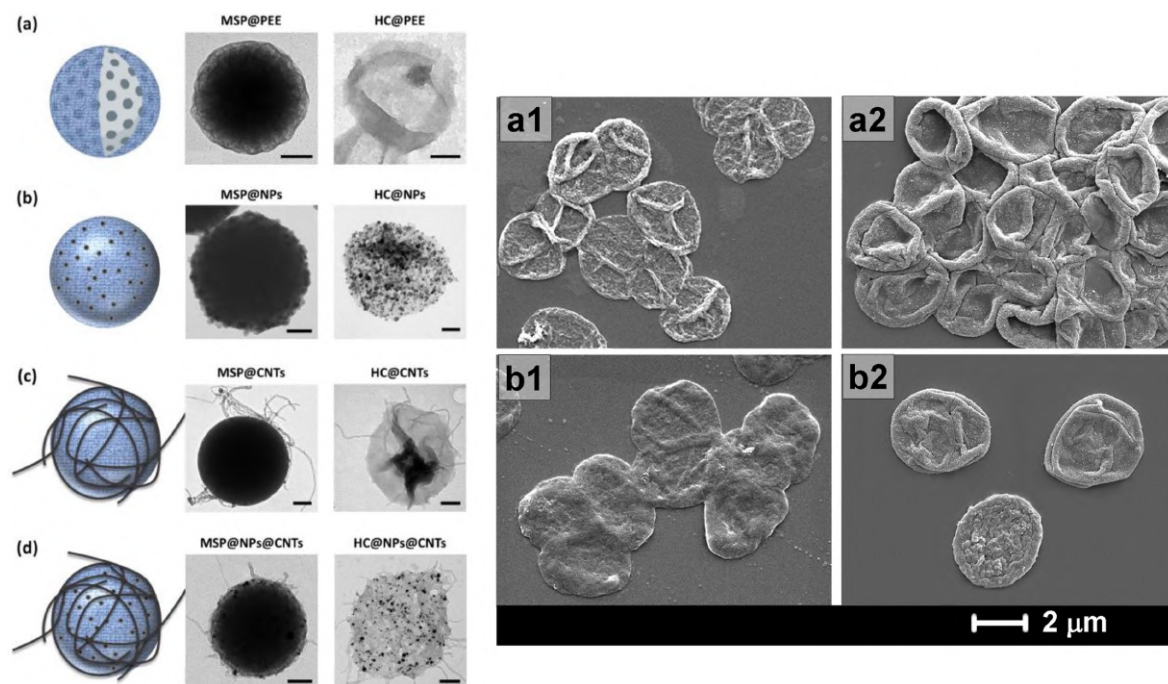
Figure 2.9: Illustrations and transmission electron microscopy images (left) of polyelectrolyte capsules before and after silica core dissolution. Hollow-capsules (a), $CoFe_2O_4$ NP-functionalised capsules (b), carbon nanotube (CNTs)-functionalised capsules (c), and capsules functionalised with both NPs and CNTs (d). Reprinted with permission from reference [166]. SEM images of empty PEMCs (right), $(DS/pARG)_3$-a1 and $(ALG/pARG)_3$-b1, and post-loaded capsules with TRITC-BSA $(DS/pARG)_3$-a2 and $(ALG/pARG)_3$-b2. Reprinted with permission from reference [200] Copyright © 2010 American Chemical Society.

Table 2.2: Summary of successfully fabricated nano- and microcapsules templated upon porous templates reported in literature. V-CaCO$_3$: vaterite CaCO$_3$; ALG: alginate; BSA: bovine serum albumin; CHI: chitosan; CS: chondroitin sulphate; CMC: carboxymethylcellulose; COL: collagen; DOX: doxorubicin; ELR: elastin-like recombinamer; FG2: basic fibroblast growth factor; GA: glutaraldehyde; HA: hyaluronic acid; HS: heparin sulphate; Hgb: hemoglobin; IgY: egg yolk immunoglobulin; LF: lactoferrin; MNP: magnetic nanoparticle; pARG: poly-L-arginine; pASP: poly(L-aspartic acid); pGLU: poly-L-glutamicacid; PLL: poly-L-lysine; pONT: poly-L-ornithine; PAH: poly(allylhydrochloride); PSS: poly(styrene sulfonate); and TA: tannic acid

Polyanion	Polycation	Template, Size	Layers	Reference
		Polysaccharide-based PEMCs		
	pARG	MnCO$_3$, 4 μm	8	[201]
CS	PLL	V-CaCO$_3$ pre-loaded with CS, 3-6 μm	10	[202]
	PR	V-CaCO$_3$ pre-loaded with PSS, 5 μm	4	[203]
		V-CaCO$_3$ pre-loaded with DEX, 3 μm	8	[204]
	pARG	V-CaCO$_3$ pre-loaded with FG2	6-14	[205]
DS		V-CaCO$_3$, 550 nm	6	[26]
	PR	V-CaCO$_3$, 10 μm	7/8	[206]
		V-CaCO$_3$ pre-loaded with PSS, ~4 μm	12	[207]
	CHI	V-CaCO$_3$, pre-loaded with penicillin, ampicillin or ciprofloxacin, 5 μm	1-6	[20]
HA	PLL	V-CaCO$_3$, 5 μm	9	[208]
	COL	V-CaCO$_3$ pre-loaded with BSA, 3-6 μm	12	[209]
	CHI	V-CaCO$_3$ pre-loaded with DOX, 4 μm	10	[210]
HS		V-CaCO$_3$ coated with (PSS/PAH)$_4$, 3-4 μm	9	[211]
	pARG	V-CaCO$_3$ pre-loaded with HS, ~4 μm	4	[212]
		V-CaCO$_3$, 3-5 μm	4	[213]
ALG	CHI	V-CaCO$_3$ pre-loaded with CMC, 3-5 μm	10	[214]
	pARG	V-CaCO$_3$ pre-loaded with PSS, 850 nm	4	[215]
ELR	CHI	V-CaCO$_3$ pre-loaded with ovalbumin, 4 μm	4	[216]
		Protein-based PEMCs		
	Pepsin and BSA	PLL-coated V-CaCO$_3$, 3 μm	8	[217]
TA	BSA	PLL-coated V-CaCO$_3$ pre-loaded with LF, 3 μm	8/16	[218]
		V-CaCO$_3$ pre-loaded with BSA and MNPs, 3 μm	<6	[219]
	GA-cross-linked BSA	MnCO$_3$, 7.4 μm	10	[220]
	GA-crosslinked Hgb	MnCO$_3$, 5 μm	10	[221]
		Polyamino acid-based PEMCs		
pASP	pARG	V-CaCO$_3$ pre-loaded with pronase, 3-6 μm	7	[222]
	pONT	MS pre-loaded with DOX, 2 μm	8	[223]
pGLU		MS bare or pre-loaded with Lys or Cat, 2-4 μm	6	[224]
	PLL	V-CaCO$_3$ pre-loaded with PLL or pGLU, 6 μm	7	[225]
		V-CaCO$_3$ pre-loaded with IgY, 2-10 μm	10	[19]

Apart from typical polysaccharide/amino acid PEMCs, vaterite CaCO$_3$ and MnCO$_3$ have also seen use as a template for DNA-based capsules. Tetramethylrhodamine-modified dextran (TMR-D)-co-synthesised vaterite crystals were coated with a primary layer of positively charged PAH, followed by the LbL-build-up of two hybrid nucleic acids (for full sequences see [226]), of which one sequence contains the anti-adenosine triphosphate (ATP) aptamer. Following addition of EDTA and subsequent dissolution of CaCO$_3$, hollow aptamer-cross-linked capsules were formed (Figure 2.10), and underwent a shrinkage phenomenon ($\simeq$3.2 μm to $\simeq$2.5 μm) [226], which has also been noted in other bio-capsule systems [208, 224]. TMR-D was then subsequently released via the

exposure of the capsules to ATP, of which complexes with its aptamer, disrupting the bridging of DNA within the layers (Figure 2.10). CaCO$_3$-templated DNA-based capsules with size-selective macromolecule permeation have also been produced using the LbL approach; 56 kDa dextran permeated the capsules, whilst 155 kDa dextran was inaccessible to the capsule [227, 228]. Such DNA-based systems may prove useful for the size-selective encapsulation of macromolecules, as well as potentially low molecular weight drugs and genetic material [229, 230].
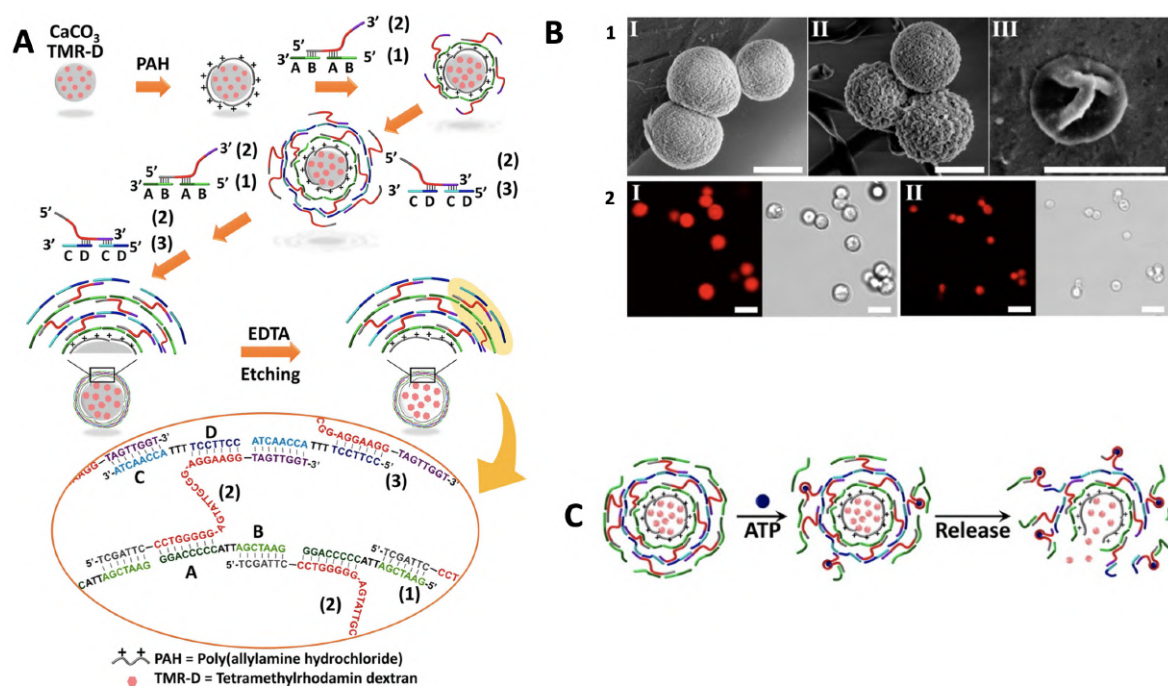
Figure 2.10: (A) Schematic illustration of the preparation of DNA microcapsules via CaCO$_3$ templating. ATP-binding aptamer sequences, labelled in red colour, are embedded into DNA films as stimuli-sensitive switches. (B) SEM images of uncoated (1, I), DNA-coated (1, II) CaCO$_3$ vaterite crystals and DNA PEMCs following EDTA addition (1, III). Below are corresponding confocal and brightfield confocal images of DNA-coated crystals (2, I) and DNA PEMCs (2, II). (C) Representation of ATP-induced PEMC rupture and release of TMR-D. Reprinted with permission from reference [226] Copyright © 2015 American Chemical Society.

The formation of nano-sized PEMCs formed upon porous templates with varying biopolymers can still be challenging; with the typical size of CaCO$_3$ PEMC templates falling within the range of 3-10 μm (Table 2.2). However, as of recent, progress has been made in the formulation of vaterite CaCO$_3$ templates in the sub-micron and nano-regions [44, 66, 85, 231]. Both additive [66] and additive-free [85] approaches

have emerged as facile methods to synthesis sub-micron vectors; for instance, when using a glycerol/gelatin formulation, with ultrasonic treatment of the pre-cursor salt solutions, sizes of 54 ± 9 nm have been achieved, along with a range of other sizes up to $\simeq 800$ nm. Using additive-free methods it is possible to reach sizes of close to 720 nm. Also of note, we are able to reach sizes of up to 55 μm $CaCO_3$ crystals [85], for potential use as porogens for tissue engineering scaffolds (Figure 2.11). Smaller, sub-micron and nano-sized functional delivery vehicles are necessary for the effect treatment of ailments, including cancer, in which the enhanced permeation and retention effect is prevalent. Approaches regarding the shrinkage of PEMCs to reach necessary the sizes for advanced drug delivery are now emerging; recent studies and their applications will be discussed in the next section.
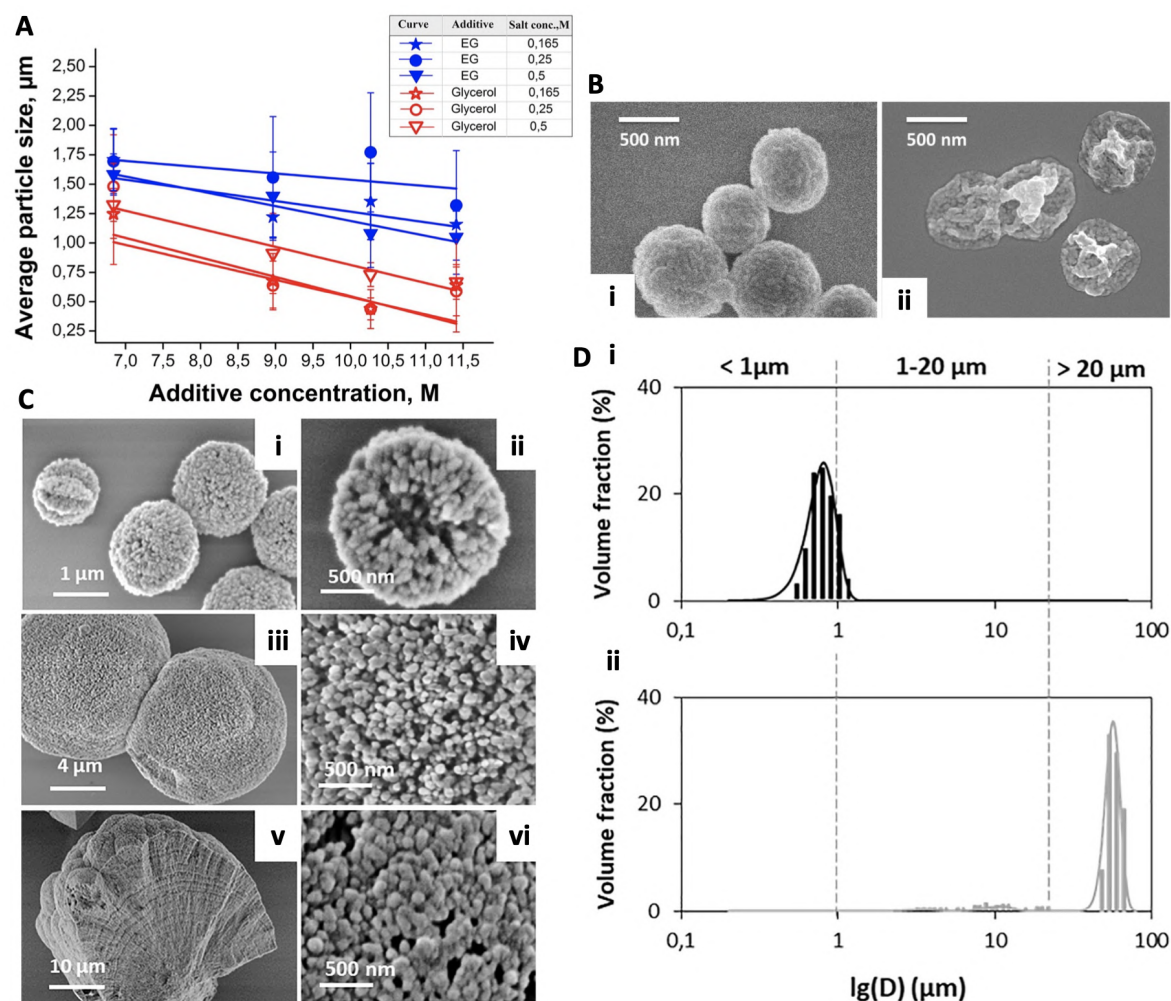
Figure 2.11: (A) Graphical representation of the effect of additive concentration on the size of vaterite CaCO$_3$ crystals at different salt concentrations. (B) SEM images of sub-micron CaCO$_3$ coated with (pARG/DS)$_{4.5}$ layers (i) and hollow PEMCs (ii). Reprinted with permission from reference [44] Copyright © 2016 American Chemical Society. (C) SEM images of vaterite CaCO$_3$ sub-micron crystals (i,ii), middle-sized CaCO$_3$ crystals (iii), and their typical surface (iv). The spall of sub-millimetre vaterite CaCO$_3$ crystal (v), and typical surface (vi). (D) Typical size distribution of sub-micron-CaCO$_3$ (i) and giant CaCO$_3$ (ii) crystals grown by the mixing of CaCl$_2$ and Na$_2$CO$_3$ salts in water. Bars represent experimental data; lines show the fitting with Gaussian function. Reprinted with permission from reference [85] Copyright © 2021 Elsevier.

Shrinkage of biopolymer-based capsules

The shrinkage of PEMCs formed upon vaterite CaCO$_3$ templates has been reported numerously [26, 205, 208], typically via the thermal treatment of capsules [232–234]; The observed shrinkage of PEM films, especially within capsule systems, holds important applications in drug delivery. Controlled shrinkage allows us to readily tune the

size of delivery vehicles depending upon the targeted area, for example, the delivery of nano-capsules to tumorous cells has seen an increase in research as of late due to their biodegradability and their ability to host large amounts of biological cargo. For instance, DS/pARG capsules have seen much recent work in regard to the shrinkage of PEM capsules. Trushina *et al.* [234, 235] subjected DS/pARG capsules to heat treatment at different temperatures (up to 90°C); the heightened temperature results in the shrinkage of nano-capsules by factors of up to 42%. This is due to the temperature-induced annealing of biopolymers forming a more compact capsule shell upon shrinkage; this compaction is demonstrated in Figure 2.12, in which the shell clearly becomes denser upon compaction. Furthermore, it was demonstrated that increasing the ionic strength to that of physiological systems (0.15 M NaCl) and subjecting the capsules to heat treatment causes the capsules to collapse after 30 minutes of incubation, the authors attribute this to the drastic effect of ionic cross-linking upon the increase in ionic strength, inhibiting the shrinking capability of DS/pARG capsules.

These capsules have also been utilised in the encapsulation of chemotherapeutic drugs, including that of gemcitabine, clodronate [12] and doxorubicin [26]. The shrunken capsules held a significantly higher rate of cellular uptake in vitro, and both gemcitabine and clodronate reduced the viability of lung cancer cells and the tumour-promoting function of bone marrow-derived macrophages, respectively. Doxorubicin-loaded capsules showed a sustained release profile as opposed to a burst-release system (Figure 2.12), which is typically observed - this is attributed to the thicker capsule shell, slowing the diffusion of the drug through the polymeric network. Indeed, a thicker capsule shell may be compared to the internal structure of that of matrix-type capsules, which are known alter the release profiles due to the dense polyelectrolyte network within the capsule lumen [25]. Moreover, shrunken doxorubicin-loaded $(DS/pARG)_3$ capsules have been shown to accumulate within human breast adenocarcinoma MCF-7 and MCF-7/ADR (drug resistant) cells and managed to overcome the drug resistance of MCF-7/ADR cells (Figure 2.12). Such sub-micron capsules may prove useful for future chemotherapeutic applications, taking advantage of advanced PEM shrinkage via

highly dynamic biopolymers.
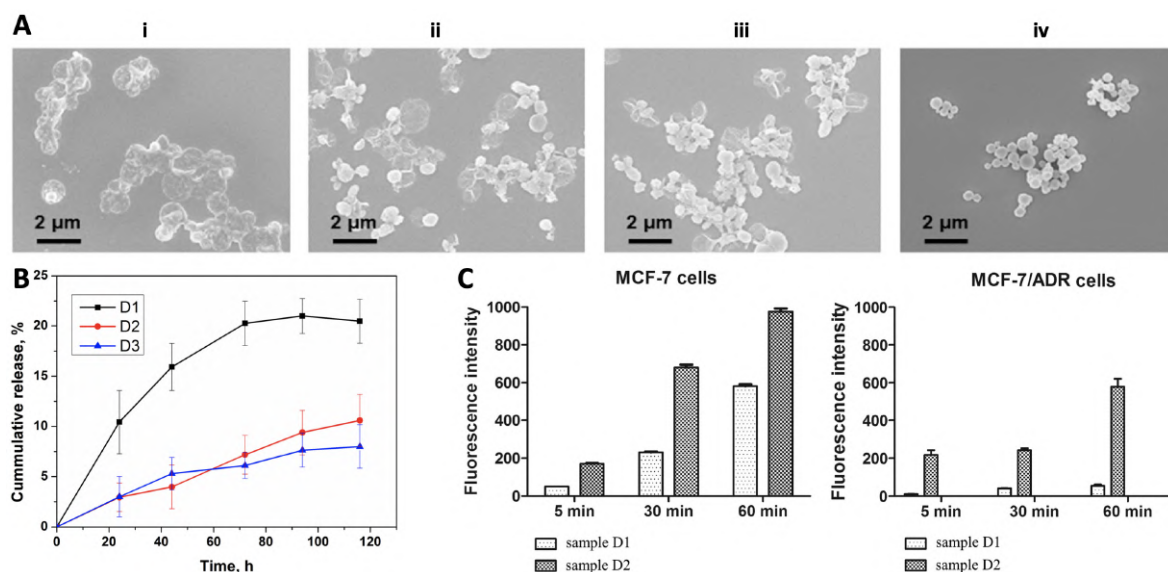
Figure 2.12: (A) SEM images of (pARG/DS)$_{4.5}$ PEMCs: freshly prepared (i) and after the heat treatment at 50°C for 15 min (ii), at 50°C for 120 min (iii), and at 90°C for 60 min (iv). Reprinted with permission from reference [234] Copyright © 2018 Elsevier. (B) DOX release from intact (initial size: 550 nm, final size: 550 nm, D1) and shrunken (initial size: 550 nm, final size: 290 nm, D2; and initial size: 290 nm, final size: 290 nm, D3) PEMCs. (C) Uptake of DOX-loaded PEMCs by human breast adenocarcinoma MCF-7 cells (left) and DOX-resistant MCF-7/ADR cells (right) after 5, 30, and 60 min incubation. Reprinted with permission from reference [26] Copyright © 2019 Elsevier.

Biopolymer PEMCs with the ability to shrink at room temperature have also been reported. Szarpak *et al.* (2010) [208] demonstrated the room temperature shrinkage of HA/PLL capsules upon dissolution of the CaCO$_3$ core by $\simeq$50%, and demonstrated the inhibition of shrinkage upon cross-linking with 1-ethyl-3-(3-dimethylaminopropyl)carbodiimide/N-hydroxysuccinimide (EDC/NHS), as is demonstrated in Figure 2.13. This ambient shrinkage may potentially be used to entrap molecules of interest within the PEMC interior.
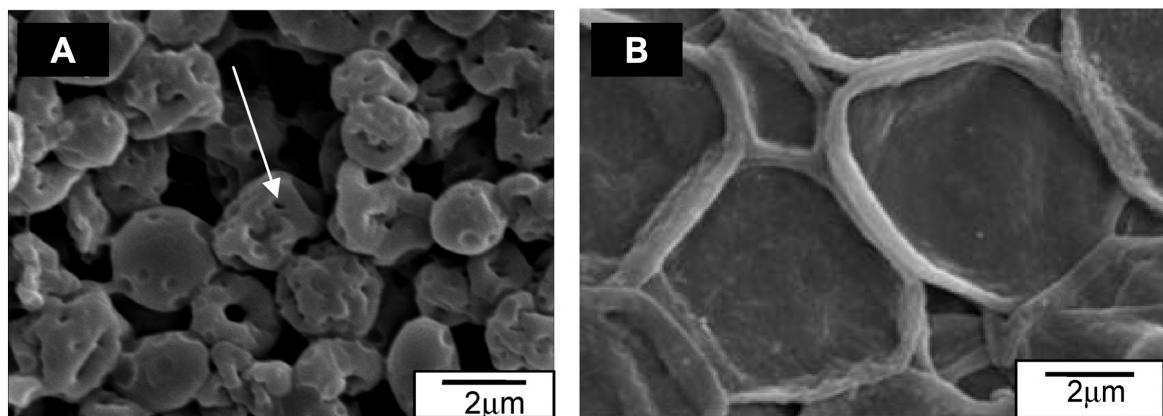
Figure 2.13: SEM images of vaterite $CaCO_3$-templated dried $(HA/PLL)_{4.5}$ PEMCs, the arrow indicates holes in the PEMC shell (A), and cross-linked via means of 200 mM EDC $(HA/PLL)_{4.5}$ PEMCs (B). Reprinted with permission from reference [208] Copyright © 2010 American Chemical Society.

Soft-templated biopolymer-based capsules

Liposomes are spherical micro-/nano-structures that are formed from phospholipid bilayers with an aqueous compartment within. A plethora of lipids can be used to form liposomes, for instance, variations of phosphatidylglycerol (anionic at pH 7) and phosphatidylethanolamine (zwitterionic at pH 7), and phosphatidylcholine (zwitterionic at pH 7) (see [236] and structures therein). Due to this, they possess amphiphilic character and can encapsulate hydrophilic molecules within their core and hydrophobic molecules within their lipid membranes. The lipid character of their structure gives them high biocompatibility and are hence very attractive as drug delivery vehicles due to their versatility. However, liposomes can possess poor stability unless in a buffered environment and can sometimes have poor drug-trapping potential, with some cargo elution [237, 238]; this has led to extensive studies regarding the functionalisation of liposomes with different molecular species (i.e. antibodies, proteins, carbohydrates, poly(ethylene glycol (PEG)) [239–243]. Moreover, multilayer coatings of biopolyelectrolytes to further protect the encapsulated cargo during the delivery phase and functionalise the outer-shell has become attractive [244, 245], for instance, with coatings of PLL/pGLU [246], CHI with DS [247] and ALG [244], as well as protein-based BSA/LF [248]. Besides coatings, few studies report the soft-templating of biopolymer PEMCs upon liposomal

structures. Cuomo *et al.* [249, 250] demonstrated the formation of ALG/CHI PEMCs upon 300 nm phosphatidylcholine/didodecyldimethylammonium bromide (DDAB) liposomes, a schematic of which is shown in Figure 2.14. The removal of the core was performed with a non-ionic surfactant (Triton X-100 in this study) via inducing a liposome-to-micelle transition, of which was monitored with Nile Red dye - sensitive to its microenvironment (whether a micelle or lipid bilayer, example fluorescence maxima in Figure 2.14).

Further to liposomes, microgels may be used as soft templating materials, for instance dextran hydroxyethylmethacrylate (DEX-HEMA) microgels, of which can be synthesised in a broad size range, with so-called giant microgels (150 μm) used for the formation of synthetic capsules [251]. Biopolymer-based PEMCs templated on DEX-HEMA are reported with pARG paired with CS, pASP, pGLU, and DS. The dissolution of the core microgel was performed with 0.1 M NaOH, via hydrolysis of the cross-linking carbonate esters between dextran chains. Upon degradation, only pARG/DS produced stable hollow PEMCs, the rest self-ruptured, attributed to the build-up of osmotic pressure within the polyelectrolyte shell, demonstrated in Figure. 2.15. However, upon increasing the molecular weight of pGLU, a percentage of PEMCs remained intact (Figure 2.15), suggesting a larger polymer chain length may increase PEMC mechanical strength or permeability of the shell. Of note, HA, CHI, PLL, pONT and ALG were tested as LbL components but the authors report instantaneous microgel aggregation upon dispersion into the biopolymer solution, where pARG did not cause this [252]. Disulfide-crosslinked HA gels ($\simeq$16 μm) have also been coated with HA/PLL multilayers followed by the addition of dithiothretinol (at neutral pH) to cleave the sulfide linkages in order to remove the microgel core [253], as shown in Figure 2.15. Using such gels allow us to pre-encapsulate bioactive material pre-LbL deposition, much like that of porous inorganic templates ($CaCO_3$/$MnCO_3$/MS) and produce PEMCs under mild conditions suitable for biopolymers. Other potential soft materials may include that of PNIPAM and alginate gels [89, 254].

Biological templates have also seen use as PEMC templates, erythrocytes in particular
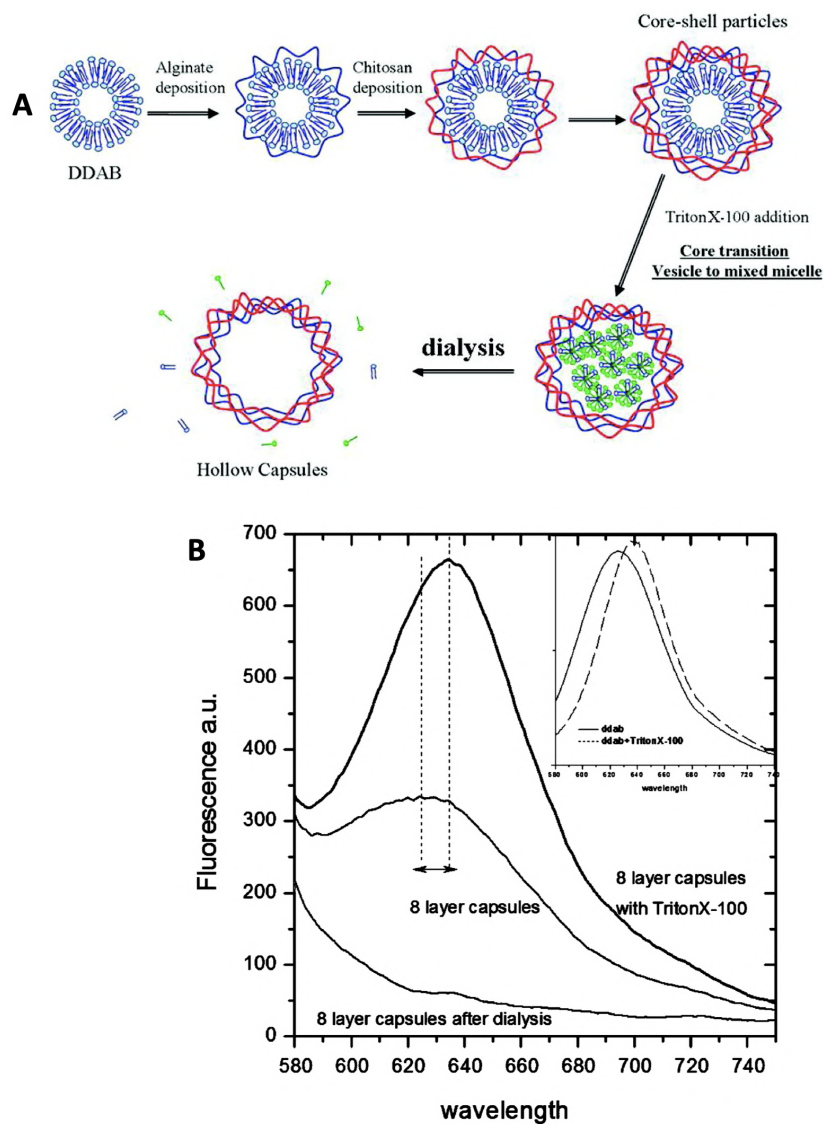
Figure 2.14: (A) Schematic illustration of the formation of liposome templated PEMCs. (B) Nile red fluorescence emission spectra (excitation at 530 nm) in 4 bilayer-coated liposomes (maximum at 625 nm) and following the addition of Triton X (maximum at 635 nm). Following dialysis, the fluorescence disappears. In the inset, a red shift for the bare DDAB vesicles is reported. The solid line refers to the fluorescence of Nile red in DDAB vesicles; the dashed line is the fluorescence spectra in mixed micelles. Reprinted with permission from reference [250] Copyright © 2010 American Chemical Society.
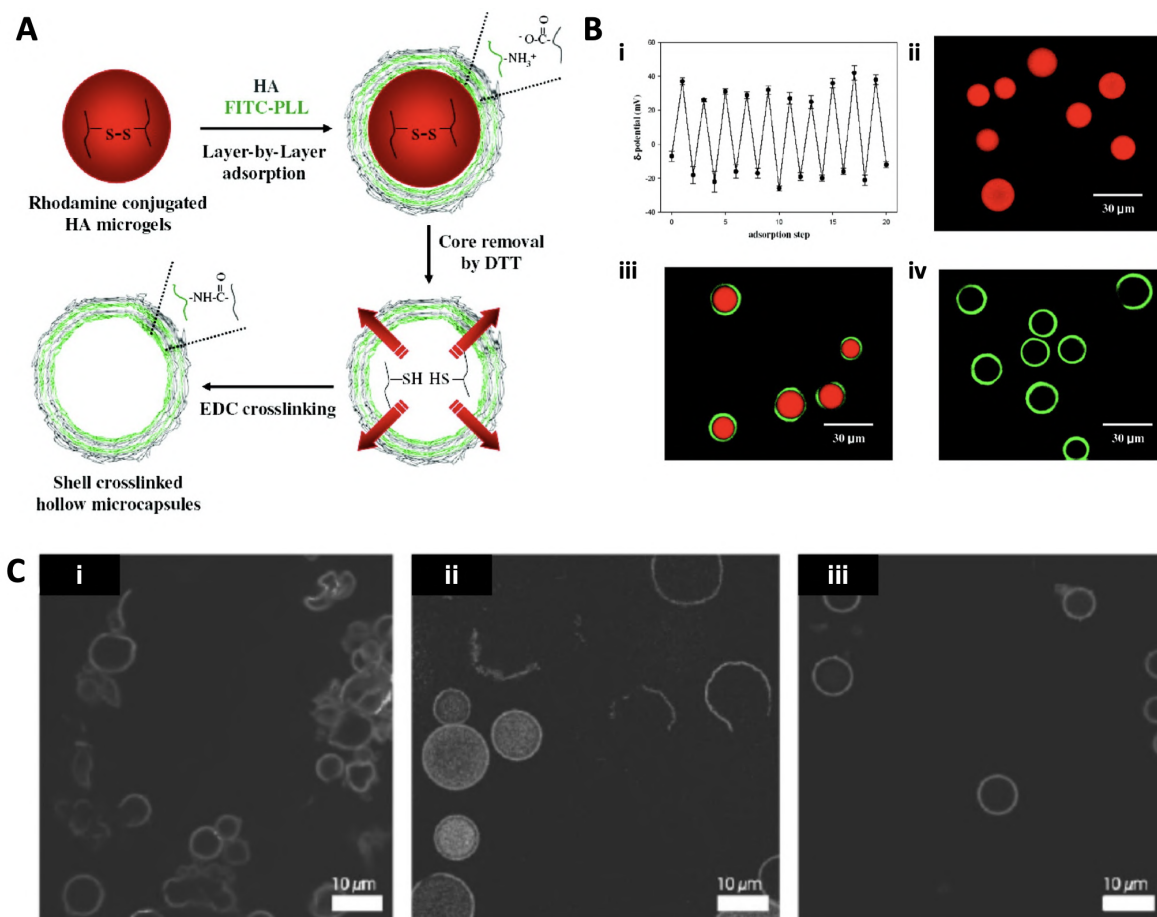
Figure 2.15: (A) Schematic illustration of the formation of cross-linked hollow HA/PLL PEMCs and (B) zeta potential as a function of layer number during LbL deposition upon HA microgels (i), confocal images of rhodamine-conjugated HA microgels (ii), FITC-labelled HA/PLL shell containing rhodamine (iii), and following core removal (iv). Figures taken with permission from reference [253] Copyright © 2007 American Chemical Society. (C) Confocal images of dex-HEMA microgels coated with $(CS/pARG)_4$ (i), $(pGLU(high molecular weight)/pARG)_4$ (ii), and $(DS/pARG)_4$ (iii) after degradation of the microgel core. In (i), all microcapsules were broken and released their contents. In (ii), both broken as well as intact (still filled with 150 kDa FITC-dextran) microcapsules were observed. The capsules in (iii) remained intact, but had released their contents by diffusion through the bio-polyelectrolyte coating. Figure taken with permission from reference [252] Copyright © 2007 John Wiley & Sons.

have been used as templates for synthetic PEMCs [173, 175]. It is reported that the removal of an erythrocyte core via NaOCl can lead to changes in the chemical nature of the polyelectrolytes used - amino groups in PSS/PAH have been oxidised to nitro-, nitroso- and nitrile- groups, causing the subsequent cross-linking of PAH. Although advantageous in terms of mechanical stabilisation, this may not be suitable for such sensitive biopolyelectrolytes [255]. However, as of recent, live *E. coli* has seen use as PEMC template via the coating of ALG/CHI biopolymers, following dissolution via cell lysis (incubation in lysis buffer - (0.1% Triton X-100, 2 mM EDTA in 10 mM Tris-pH 8) with 100 μg/mL lysozyme overnight) [256]. Stable hollow PEMCs were formed with a slight increase in shell thickness, from 10-20 nm to 20-50 nm, attributed to alterations in polymer conformation on *E. coli* degradation - demonstrating the novel formulation of biopolymer PEMCs on bacterial cells formed at soft conditions. This also leaves no harmful polymer residue in the shell, suitable for release of cargo for biotherapeutic applications and perhaps opens up for wider variety of biological PEMC templates.

Drug crystal-templated biopolymer-based capsules

Key properties for the formulation of drug delivery vehicles are bioavailability, biodegradability, and high control over the drug content. A facile method to control drug loading is to use pure drug nano-crystals themselves. A number of approaches have been successfully applied to reduce the size of such pure drug particles from the micro- to the nano-region; these include both top-down [257, 258] and bottom-up [259] approaches. The top-down approach involves the sonication or milling of coarse drug crystals to aid in the production of nano-sized crystals, whereas bottom-up involves the precipitation of nanocrystals from dissolved drug via a solvent-induced supersaturation state, which is then followed by drug nucleation and subsequent growth. Precipitation may also be induced via pH change if the drug of choice holds pH-dependent solubility; as well as via emulsification into organic solvent nanodroplets, in which nanocrystals may grow (for further details see [260]). Many drugs however are typically poorly soluble in aqueous environments, and upon reduction of size, their solubility dramatically

increases; this is due to the increase in the surface area to volume ratio of the crystal, giving increased solvent-crystal contact [261]. Despite this increasing drug bioavailability, such drug nanocrystals may solubilise and release drug molecules instantaneously at the target site or en route. Hence, LbL coatings present themselves as popular methods to control the drug release rate, as well as potentially the biodistribution, if functionalised. Furthermore, one must be sure to deposit the polyelectrolytes at conditions where the solubility of the drug is not increased nor decreased for the polyelectrolytes used, as well as retain their stability.

Nano-crystals of indomethacin, an anti-inflammatory drug, were prepared via the top-down approach via mortar and pestle grinding, followed by sonication. LbL coating of CHI and pectin was performed at pH 4.5 where the drug is almost insoluble, and CHI is fully dissociated, and pectin is dissociated at 80%. Four layers were alternately deposited, and the subsequent release of indomethacin was studied at pH 7; the release was slowed for those drug crystals coated with CHI/pectin [262] (Figure 2.16) to a saturation point within 5 hours, compared to 1 hour for uncoated crystals. This same effect is observed for picloram, a herbicide, coated with lignosulonate (LS)/CHI PEMs [263] (Figure. 2.16) as well as in DS/Gelatin and DS/CHI multilayers with naproxen crystals [264]. Furthermore, following the dissolution of the drug nano-crystal, a PEMC may remain if the shell has not ruptured, following the dissolution of picloram for instance, a hollow PEMC remains [263], as observed in Figure 2.16. Moreover, the coating of such nanocrystals with biopolymer PEMs is of particular interest due to their typically intrinsic biocompatibility and controllable permeability. Further from drug crystals, those particles formed fully from bioactive material, such as the biopolymer beads, enzyme crystals [265] or protein aggregates discussed previously, are of interest to coat in order to control the release of protein or enzyme as well as to protect such fragile cargo [266].
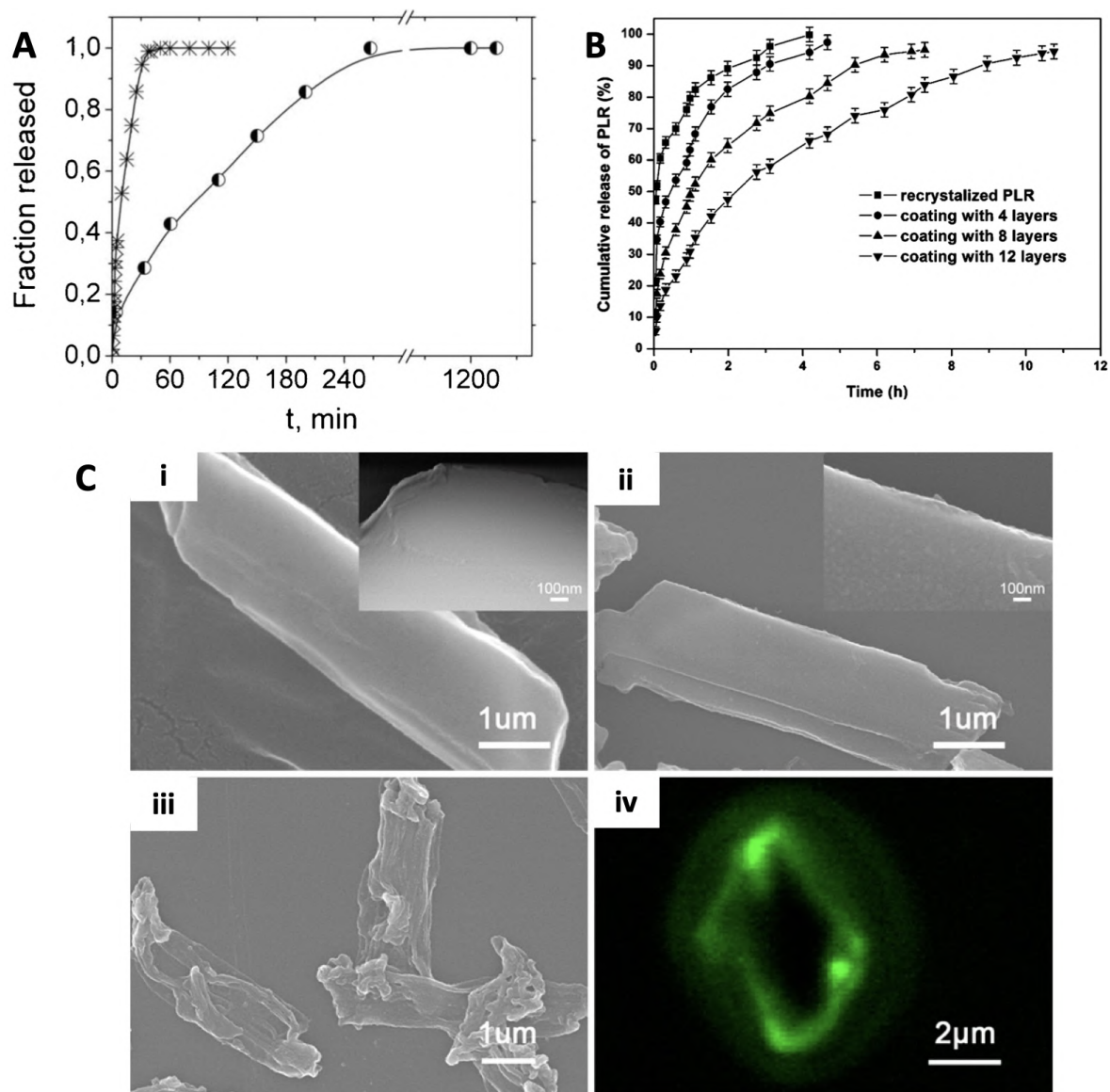
Figure 2.16: (A) Release profile of bare (*) and CHI/pectin coated (◐) indomethacin particles in phosphate buffer pH 7. Figure taken with permission from reference [262] Copyright © 2017 Elsevier. (B) Release profiles of picloram from LS/CHI PEMCs with 0, 4, 8, and 12 polyelectrolyte layers, and (C) SEM images of recrystallised picloram (i), picloram coated with 5 bilayers (ii), and hollow PEMCs after picloram release (iii), with corresponding confocal image (iv). Figures reprinted with permission from reference [263] Copyright © 2013 American Chemical Society.

2.4 *in ovo* feeding

2.4.1 Approaches to *in ovo* feeding

Current, conventional approaches toward IOF involve the mechanical injection of the egg, with this brings many factors of which can affect the production of healthy broilers.

The site of injection for IOF can play a significant role in the production of healthy chicks. Figure 2.17 illustrates six possible injection sites: the chick embryo itself, air sac, albumen, yolk sac, amnion and the allantonic fluid [3]. The site of *in ovo* injection may be highly dependent upon the IOF application. For instance, Wakenell *et al.* (2002) [8] has previously demonstrated the influence of the inoculation site upon the development of Marek's disease vaccine viremia and its efficacy. Inoculation directly to the embryonic body or the amniotic fluid resulted in over 90% protective efficacy, whilst delivery to the allantoic fluid or the air cell resulted in less than 50%, both regardless of day of injection. When injected to the air cell, no virus gains access to the embryo, and there is no vaccinal response.

The precision of the depth of injection is also crucial and may vary due to numerous factors which must be taken into account; for instance, the dehydration occurring during embryonation may increase the size of the air cell [8]. With this, the needle may not penetrate deep enough to reach the target and disperse elsewhere. Whereas penetration too deep may result in trauma to the embryo [8, 9]. Moreover, Ohta *et al.* (2011) [267] has previously demonstrated the inoculation of amino acids utilising a 13 mm needle resulted in the significant increase in body weight post-hatch compared to the control and a 19 mm needle.

The time of injection during the incubation period can also play a crucial role in the development of the embryo and effect on the chick post-hatch. Inoculation during the late stages of incubation is thought to be highly beneficial due to the embryonic consumption of the amniotic fluid pre-hatch. Such amniotic fluid is in contact with the enteric cells [268], of which are distributed within the gastrointestinal tract; this

provides the most effective, guaranteed IOF route.
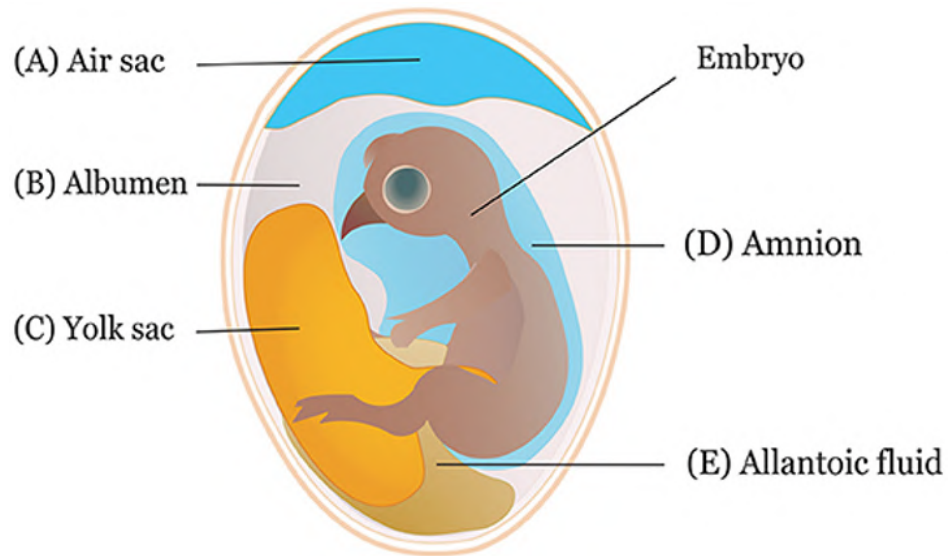
Figure 2.17: Schematic illustrating the possible *in ovo* injection sites. Reprinted with permission from reference [3].

Of note, a newly developed approach toward IOF has been reported by Huang *et al.* (2022) [269], in which a self-developed electromagnetic-driven needle-free IOF injection device was used to inject eggs at day 18 of the incubation period. For this, a 3 mm hole was drilled in the eggshell following sterilisation, the eggs were then injected using various liquid jet pressures and sealed with a sterile acne dressing. This approach allows for the successful direct inoculation to the allantonic and amniotic fluids. A schematic of which is presented in Figure 2.18. Despite this novel approach, this still involves the drilling of the eggshell and potential bacterial infection upon automated production.
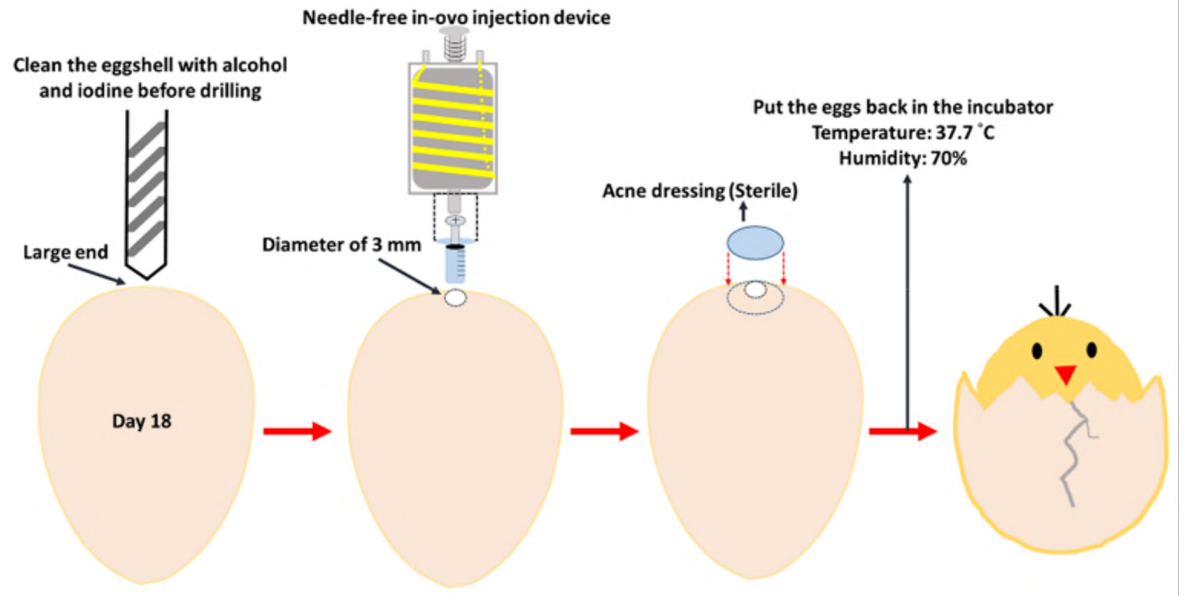
Figure 2.18: Schematic of self-developed electromagnetic-driven needle-free IOF injection device inoculation procedure. Reprinted with permission from reference [269].

2.4.2 Nutrient delivery and their effect post-hatch

Delivery of carbohydrates

The IOF of carbohydrates is a topic highly investigated within the literature owing to its invaluable importance for the developing chick and the hatching process. During the hatching period, a readily available source of carbohydrates is demanded [270]. Glucose, fructose, maltose, sucrose and dextrin are of the most studied carbohydrates with regards to IOF [270, 271], and often as mixtures. Injection of 0.3 mg mL^{-1} of either glucose, fructose, maltose, sucrose or dextrin acted to increase the total body weight of the chick post-hatch, however, all carbohydrates investigated apart from glucose reduced the yolk sac absorption and hence reduced the yolk-free body weight of chicks. The authors attribute these affects to hydration status and osmotic balance within the egg [270]. The delivery of carbohydrates and both antioxidants and carbohydrates resulted in significant increase in post-hatch weight, feed-conversion ratio, as well as feed intake across the rearing period. Here, increased carbohydrate nutrition is associated with increasing glycogen stores and chick weight upon hatch [272]. Despite

these typical beneficial effects, in general, *in ovo* injection of carbohydrate solutions results in reduced hatchability [273].

Delivery of vitamins

Folic acid (vitamin B9) is a water-soluble vitamin, and an essential co-enzyme for both DNA methylation and synthesis [274]. Further, an increase in protein level within the diet of the chick is accompanied by an increase in folic acid requirement; this may be due to the effect folic acid has on downstream protein metabolism [275]. Indeed, *in ovo* injection of folic acid increased the body weight of the chick post-hatch [276]; improvements in hatchability and growth performance has also been observed [274]. Cobalamin, another B-complex vitamin (vitamin B12), plays a vital role in the nervous and immune systems [277], as well as a key role in metabolic functions [278]. When B12 was delivered *in ovo*, positive effects regarding the increase in body weight and the food conversion ratio occurred, as well as increased hatchability. Similar effects were observed upon the *in ovo* injection of thiamine and riboflavin [279].

When supplemented within the poultry diet, ascorbic acid aids in the chick's resistance to disease, oxidation processes and enhances egg hatch performance [280]. Indeed, *in ovo* injection of ascorbic acid through the air cell resulted in increased hatchability and reduced embryo death [281]; similarly, numerically higher body weight percentage and hatchability has also been demonstrated by Zhang *et al.* (2018) [282]. This is in contrast to Mousstaaid *et al.* (2022) [283], where ascorbic acid did not affect the hatchability or the body weight post-hatch, but may reduce embryonic mortality.

Delivery of amino acids

Amino acids are essential for the growth and development of the chick embryo whilst also acting to beneficially augment post-hatch growth. Arginine has been found to have a number of effects when administered *in ovo*. The injection of 1% arginine held no impact on the hatchability, but aided in the improvement of digestive organs via

impacting the release and activity of gastrointenstinal hormones and digestive enzymes leading to improved growth performance of broilers [284–286]. Indeed, IOF at the same initial arginine concentration has also resulted in the increase of glycogen and glucose concentrations, altering the broiler energy metabolism [287]. IOF of methionine has been reported to increase the chick weight by 2.7% compared to control groups, but lead to a decrease in hatchability; the authors attribute this effect on hatchability to the depth of injection [288]. Methionine, when delivered within cysteine, is also known to enhance chick embryonic development following exposure to heat stress [289]. Similar effects upon heat-stress exposure has been seen upon IOF with L-leucine, resulting in increased antioxidative ability and improved recovery rates [290]. Indeed, *in ovo* injection of leucine has been shown to significantly increase levels of reactive oxygen species as well as antioxidative enzymes (including catalase, glutathione peroxidase and superoxide dismutase) [291], as well as enhance the metabolic activity of free amino acids [292]. The delivery of lysine (1%) has acted to significantly improve the bodyweight and intestinal morphology of broilers [293]. Indeed, similar affects of lysine IOF have been demonstrated; where lysine injection acted to increase the hatchability and increase the gastrointestinal weight of the broiler [294, 295], as well as its antioxidant status [296]. The growth performance and digestive organ development has also been reported upon threonine injection; this can be attributed to a higher feed conversion ratio following hatching after threonine inoculation [297]. Indeed, threonine injections of at least 30 mg resulted in no mortality rate increase and improved chick body weight gain [298]. When delivered simultaneously with arginine, the feed intake was also improved across the chick rearing period [299].

Delivery of nanoparticles

Copper is an essential mineral for poultry growth and subsequent health; important for many metalloenzymes, it is indispensable for many biological processes in chickens [300]. Varying sources of copper (sulphate, acetate and CuNPs) have been injected into the amnion on day 10 of incubation. Interestingly, all forms of copper significantly

increased the body weight of the chicks at all ages investigated, with CuNPs recording a higher body weight [300]. This was also the case in [301], where the increase in body weight was attributed to the ability of copper to induce expression of the IGF-II gene, of which is known to control the growth and development of animals [302]. Of note, it has also been reported that the *in ovo* injection of CuNPs also decreased the metabolic rate and organ weight of post-hatch chicks [303]. Similarly, nano-diamonds were able to significantly up-regulate fibroblast growth factor 2, of which is related to the proliferation of muscle cells when the air sac was injected with 0.3 mL of 50 mg L^{-1} nano diamonds on day one of incubation [304]. Similar effects were observed with *in ovo* injection of AgNPs [305]. AgNPs are extensively studied as an antimicrobial and an immunostimulant [306, 307]. Injected at day 18 into the amniotic/yolk sac, AgNPs did not affect the hatchability of the chicks and aids in enhancing the post-hatch immune response without influencing the growth of the chicks. Specifically, concentrations of AgNPs at 12.5 μg per egg resulted in improved cellular immune response whilst concentrations of 25-50 μg per egg improved the humoral and adaptative immunity of chicks. The authors attribute this to the early maturation of the immune system [308].

Beneficial effects were also observed for the *in ovo* injection of selenium nanoparticles (SeNPs). Selenium partakes in a plethora of biological pathways; more than half of known selenoproteins are involved in antioxidant defences and maintaining redox balance [309]. Ibrahim *et al.* (2020) [310] has reported the increased body weight, as well as antioxidant and immunological status of chicks following *in ovo* injection at 10 ppb per egg into the air cell. The authors attribute this gain in body weight to the key role selenium may play as a structural component of 5'-deidinase, of which is a key enzyme in the conversion of thyroxine to triiodothyronine, which may influence protein uptake and hence, chick growth. *in ovo* delivery of SeNPs into the amnion, along with zinc nanoparticles (ZnNPs) and CuNPs did not affect the hatchability of the chicks [311].

Iron, necessary for the synthesis of hemoglobin and myoglobin, has been delivered in nanoparticle form. *in ovo* injection of iron nanoparticles (FeNPs) resulted in in-

creased chick bodyweight upon hatching [312]. Calcium-based supplementation within poultry is mostly needed for bone development [313]. Indeed, $CaCO_3$ nanoparticles were injected into the albumen on the first day of incubation, no negative effects were observed, and meat quality was unaffected; however, it was found that *in ovo* inoculation of $CaCO_3$ increases liver weight and bone osteocalcin within the femur $CaCO_3$ [314]. The nanoparticles discussed here are typically used in chicken feed post-hatch to achieve similar effects; a benefit for IOF here is the reduced mineral content typically needed when compared to the amount needed to supplement the feed. Moreover, IOF with nanoparticles is known to facilitate the uptake of nutrients when delivered in combination [9]. Of note, some of the metals used in feed that may be inoculated *in ovo* also include manganese, chromium and magnesium, as well as other metal oxides [313, 315, 316].

Chapter 3

Methodology

3.1 Introduction

In this Chapter, the materials and methodologies utilised throughout this work are presented. Of note, methods presented in this Chapter have been published as references (5), (8) and (10), as listed in Section 1.3.

3.2 Materials

Calcium chloride dihydrate (Acros Organics, 10158280), sodium carbonate (Acros Organics, 10577182), ethylenediaminetetraacetic acid (Fischer Scientific, 10335460), fluorescein isothiocyanate (FITC) isomer I (Sigma, F7250) fluorescein isothiocyanate-labelled dextran at 4 kDa (Sigma, FD4), 40 kDa (Sigma, FD40S), 70 kDa (Sigma, FD70S), 150 kDa (Sigma, FD150S), 500 kDa (Sigma, 46947) and 2000 kDa (FD2000S), fluorescein isothiocyanate-labelled carboxymethyldextran 150 kDa (Sigma, 74817), fluorescein isothiocyanate-labelled diethylaminoethyldextran 150 kDa (Sigma, 75005), Tris-buffered saline (purchased as 10× Tris) pH 7.4 (Alfa Aesar, J60764) containing 250 mM Tris, 1.37 M sodium chloride and 27 mM potassium chloride, 1 M sodium hydroxide (Fisher, 10528240), 1 M hydrochloric acid (Fisher, 10467640), chondroitin sulfate A 50 kDa (Creative PEGWorks, CS-114), fluorescein isothiocyanate-labelled chondroitin sulfate A 50 kDa (Creative PEGWorks), fluorescein isehtothiocyanate-labelled dextran sulfate sodium salt 40 kDa (Sigma, 51923), hyaluronic acid (Creative PEGWorks, HA-102 (50 kDa), HA-106 (1500 kDa)), fluorescein isothiocyanate-labelled hyaluronic acid 50 kDa (Creative PEGWorks), heparin sodium salt from porcine intestinal mucosa 10-12 kDa (Sigma, H5515), collagen type 1 from rat tail 115-130 and 215-235 kDa (Sigma, 08-115), dextran amine 70 kDa (Creative PEGWorks DE-664), poly-L-lysine hydrobromide (Sigma-Aldrich P7890 (15-30 kDa) and P4832 (150-300 kDa)), protamine from salmon (Grade IV) 5-10 kDa (Sigma, P4005), diiodomethane (Sigma, 158429), ethanol (Fisher Scientific, 10680993), ethylene glycol (Sigma, 107-21-1), glycerol (Sigma, 56-81-5), hydroxypropylmethylcellulose (Sigma, H7509), methylcellulose (Sigma, M0512),

polyethylene glycol (Sigma, 86101), polypropylene glycol (Fisher, Scientific, 10740701), propylene glycol (Sigma, 57-55-8), sodium hypochlorite solution (Sigma, 105614), rhodamine B (Sigma, 81-88-9), cobalt standard for ICP (Sigma, 30329), vitamin B12 (Sigma, V2876).

The water used throughout this thesis was prepared using a Millipore Milli-Q purification system and had a resistivity higher than 18.2 MΩ cm^{-1}.

3.3   Synthesis of vaterite CaCO$_3$ crystals

100 mL of 50 mM CaCl$_2$ in 2× Tris was added to a glass beaker; the solution was then agitated at 650 rpm using a magnetic stirrer, followed by the addition of 100 mL of 50 mM Na$_2$CO$_3$ and further agitation for 60 s. The mixture was transferred from the beaker for crystal growth for 20 min. The crystals were then thoroughly washed twice with water (the crystal suspension was centrifuged at 1100g for 3 min), followed by the removal of the supernatant and the resuspension of the crystals in water. The crystals have been placed in a glass Petri dish and dried for 1-2 h at 70-85°C. For the formation of DEX^{FITC}-loaded crystals, the same protocol was followed adding 1 mL of 50 mg mL^{-1} DEX^{FITC} aqueous solution to the CaCl$_2$ solution before the agitation and addition of Na$_2$CO$_3$.

For the synthesis of CaCO$_3$ crystals of different sizes, the following synthesis parameters were varied: agitation time (10 to 1800 s), agitation speed (150 to 1700 rpm), the molar ratio of CaCl2:Na$_2$CO$_3$ (1:1 to 40:1), initial Na$_2$CO$_3$ concentration (0.05 to 1.00 M), as well as the variation in beaker width.

3.4   Formation of microgels

The prepared crystal templates were alternately incubated (4 mg mL^{-1}) in polymer solutions. For the deposition of the first layer, the crystals were suspended in 0.5 mL of 0.2× Tris buffer solution (5 mM Tris, 27.4 mM NaCl, and 0.54 mM KCl, with

an additional 10 mM CaCl$_2$), followed by the addition of 1.0 mL of 0.5 mg mL^{-1} polymer in 0.2× Tris buffer. The suspension was then incubated on a shaker for 10 min and centrifuged at 900g for 4 min. Then the supernatant was removed, followed by resuspension of the crystals in 1.0 mL of 0.2× Tris buffer solution. A second centrifugal step was performed under the same conditions. The coated crystals were re-suspended in 0.5 mL of 0.2× Tris buffer and the same steps were then applied for the next polyelectrolyte and repeated until the desired number of layers was achieved. The final pH value of 0.2× Tris buffer solution was 7.9. Once the desired number of layers was applied, the multilayer-coated crystals were suspended in 0.5 mL of 0.2× Tris buffer and either analysed the same day or stored in the fridge at 4°C which did not influence the results obtained.

To investigate the encapsulation of DEX^{FITC} within microgels, the same procedure was applied to templates of vaterite/DEX^{FITC} hybrid crystals.

3.4.1 Determination of the microgel shrinkage coefficient

Shrinkage coefficients (SC) were calculated as the ratio between the diameter of coated crystals (d_0) and microgels after complete elimination of the CaCO$_3$ template (d), as shown in equation 3.1:

$$\text{SC} = \frac{d_0}{d} \tag{3.1}$$

The SC of microgels was determined as a function of polymer molecular weight, polyanion charge density, number of deposition steps (2-9), EDTA concentration (20-100 mM), temperature (4-90°C), and polymer composition.

3.4.2 Determination of the relative dextran content

Relative DEX content was estimated as the ratio between the fluorescence signal inside (F_i) and outside (F_o) the microgel, normalised to the microgel diameter (d_m), as shown in equation 3.2:

$$\text{Relative DEX content } = \frac{(F_i/F_o)}{d_m} \tag{3.2}$$

3.4.3 Encapsulation of silver nanoparticles within microgels

Microgels formed of $(HA/PLL)_4$ and $(HA/PLL)_{4.5}$ were formed within gridded ibidi wells (μ-Slide 8 Well Grid-500, 80821-G500) or borosilicate glass coverslips. This was performed using 20 μL of 2 mg mL^{-1} coated $CaCO_3$ crystals in 0.2$\times$ Tris buffer, pH 7.9 followed by the addition of 20 μL of 40 mM EDTA, pH 7.0. The microgels were allowed to form for 30 mins and washed three times with 0.2$\times$ Tris buffer solution, pH 7.9 or Milli-Q water, and were resuspended in 20 μL of the same buffer or Milli-Q water. 20 μL of 0.2 mg mL^{-1} silver nanoparticle suspension was then added and the whole droplet was mixed via gentle pipetting. The system was left to equilibrate for 1 hour, after which, the gels were washed with 0.2$\times$ Tris buffer solution, pH 7.9 or Milli-Q water thrice, followed by resuspension in 40 μL of the same buffer or water for imaging via optical microscopy.

3.4.4 Microgel adhesion studies

The surface the microgels were formed was marked with a needle in order to ensure the same position before and after washing is captured. Microgels were formed as above, followed by light washing with 0.2$\times$ Tris buffer solution, pH 7.9 before imaging. For this, microgels have been formed on surfaces consisting of glass (bare, gold-coated and cold atmospheric plasma-treated (CAP) (CAP treatment performed by Laura Bowker,

NTU)), ibidi hydrophobic and hydrophilic wells, and polystyrene. The microgel adhesion was investigated as a function of ionic strength (0.027-1 M NaCl), temperature (4-80°C), number of deposition steps (2-9), and the polyanion composition (HA doped with HS by mass at 0-100%)

3.4.5 Determination of the microgel adherence

The percentage adherence was calculated using equation 3.3, below. Where, n_0 and n are the number of microgels before and after the washing step, respectively.

$$\text{Adherence (\%)} = \frac{n_0}{n} \times 100\% \tag{3.3}$$

3.5 Turbidimetric titration of polyelectrolyte complexes with NaCl

Polymers have been dissolved in the $0.2\times$ Tris buffer solution pH 7.9. Polyelectrolyte complexes (PECs) have been formed by the rapid addition of 0.4 mL of polycations to 0.4 mL of polyanions under continuous vigorous shaking for 30 s. The mass concentration of polyanions in the PEC has been kept at 0.25 mg mL^{-1} (initial concentration of 0.5 mg mL^{-1}), while concentrations of polycations (except of the COL) have been chosen to keep the 1:1 M ratio between charged and uncharged groups of polyelectrolytes (recalculated per molecular unit). The 1:1 mass ratio has been chosen for COL due to complexity of the COL molecular structure. The 2 M solution of NaCl has been added to PECs by 20 μL drops until the total volume of 1.2 mL has been reached (equivalent of 400 μL of added 2 M NaCl). The absorbance has been recorded using a UV-vis spectrometer at a wavelength of 600 nm.

3.6 Fluorescent labelling of poly-L-lysine

PLL has been conjugated with FITC in a theoretical molar ratio of 1:100 (FITC/monomer unit). The labelling reaction has been performed using 5.0 mg mL^{-1} polymers dissolved in the 0.1 M carbonate buffer solution (pH 9.0). The FITC solution was added dropwise to the polymer solution under constant stirring and left to incubate for 4 h at room temperature, kept out of the light. The resulting mixture was dialyzed with water repeatedly to separate the unreacted FITC; this was done using 3-5 kDa dialysis tubing.

3.7 Eggshell permeability studies

3.7.1 Removal of eggshell cuticle

In order to partially or fully remove the cuticle layer, eggs were incubated within 5% NaOCl solutions for 30 min at 25°C, before washing with Milli-Q water and air drying. Both untreated and NaOCl-treated eggs were used throughout this work.

3.7.2 Screening of carrier gel permeability

The permeation of food-grade carrier gels through the eggshell was investigated utilising Rhodamine B (RhoB) as a fluorescent indicator. For this, eggs were placed (air cell facing upwards) in 6-well plates, in wells occupied with 6 mL of carrier gel with 1 mg mL^{-1} RhoB. The eggs were incubated as such for 24 hours to ensure adequate time for permeation before being removed and broken open to observe their contents. Images were taken of the contents (albumen and yolk), as well as the inner shell. 2 μL aliquots of albumen were taken for fluorescence spectroscopy to confirm the presence of RhoB.

3.7.3 Delivery of bioactive material

Bioactive compounds, including 4, 40, 2000 kDa DEX$^{\text{FITC}}$ (1 mg mL^{-1}), 40 kDa CM- and DEAE-DEX$^{\text{FITC}}$ (1 mg mL^{-1}) and 40 kDa DEX$^{\text{FITC}}$-capped AgNPs (0.1 mg mL^{-1}) were suspended in PPG, and their permeation screened within 6-well plates, as above. Images were taken of the contents (albumen and yolk), as well as the inner shell. 2 μL aliquots of albumen were taken for fluorescence spectroscopy to confirm the presence of FITC. For the permeation of 2000 kDa DEX$^{\text{FITC}}$/vaterite hybrid crystals, 20 μL of 0.1 mg mL^{-1} hybrid crystal suspensions within PPG were deposited upon eggshell fragments and left for 1 h to allow hybrid permeation. After 1 h, aliquots of 2 μL of albumen were taken for fluorescence spectroscopy to confirm the presence of FITC. The eggshell protein membrane was then also removed and placed upon a glass coverslip and taken for optical and fluorescent imaging.

3.8 Characterisation

3.8.1 Confocal laser scanning microscopy

A confocal laser scanning microscope TCS SP5 (Leica, Germany) was used for the imaging of the LbL-coated crystal and microgel structure. It was operated using a 488 nm excitation laser line for the imaging of FITC-labelled structures.

3.8.2 Optical coherence tomography

Optical coherence tomography (OCT) was performed in collaboration with Patrick Atkinson, NTU. Ultra-high resolution 810 nm spectral domain OCT was utilised, using the NKT supercontinuum light source with a 1200 l/mm grating and 4096 pixels linear CCD detector array, as described in [317]. Here, the surface topology and cross-section of eggshell fragments were imaged. The potential permeability of water, PPG and CaCO$_3$-laden PPG through the eggshell was monitored utilising cross-sectional scans

(averaged over 50 scans) of the untreated eggshell and the eggshell following 20 μL droplet deposition.

3.8.3 Optical and Fluorescence microscopy

A Life Technologies EVOS FL microscope equipped with 4x, 20x and 40x lenses (USA) was used for routine analysis of the synthesised $CaCO_3$ crystals, microgels and eggshell samples. Imaging was performed in both transmission and fluorescence modes.

3.8.4 Scanning electron microscopy

Here, samples were imaged using the JSM-7100F field-emission scanning electron microscope (JEOL, USA). All images were processed using ImageJ software (NIH, USA).

$CaCO_3$ crystal samples

$CaCO_3$ crystal samples were prepared via depositing the dried powder onto carbon tape upon the aluminium sample stub to image their internal structure; for this, the crystals were cracked via mechanical force. $CaCO_3$ samples were imaged using a probe current of 1 μA and an accelerating voltage of 2 kV. Images of crystal surface topology at high magnification were again processed using ImageJ in order to determine the nanocrystallite diameter.

Microgel samples

Microgel samples were prepared via depositing 30 μL of coated-crystal suspension onto a circular glass slide, followed by the addition of 30 μL of 50 mM EDTA pH 7.0 for microgel formation. The resulting microgels were then washed with water repeatedly and frozen at -20°C for freeze-drying. The slides with resulting freeze-dried microgels were sputtered with 10 nm of gold and imaged using a probe current of 1 μA and an accelerating voltage of 2 kV.

Eggshell samples

Eggshell samples were prepared via the cutting of 1 cm^2 fragments of eggshell and allowing them to air-dry overnight before fixing to the aluminium stub with carbon tape. The eggshell fragments were sputtered with 10 nm of gold and imaged using a probe current of 1 μA and an accelerating voltage of 2 kV.

3.8.5 Brunauer-Emmett-Teller analysis

Brunauer-Emmett-Teller (BET) N$_2$ adsorption-desorption analysis was performed using a QUADRASORB SI (Quantachrome Instruments, USA) at 77.3 K. Pristine CaCO$_3$ and hybrid DEX/vaterite hybrid crystals have been dried and analysed. 30-100 mg of the powder was used for each measurement. The samples were degassed at 150°C for 20 h prior to measurement. BET theory and Barret-Joyner-Halenda (BJH) model were used for the surface area and pore distribution analysis, respectively.

3.8.6 Contact angle measurements

Measurements were performed using KRÜSS Drop Shape Analyzer DSA100 (KRÜSS GmbH, Germany). A 5 μL drop of water was placed on the surface before taking an average of the left and right angles of the drop via the Young-Laplace fit.

3.8.7 Dynamic light scattering

Dynamic light scattering (DLS) measurements were performed using a ZetasizerNano ZS, Malvern, UK. The values were determined using a scattering angle of 173°. The final values were reported as intensity-, volume-, and number-weighted size distribution over three replicates. Hydrodynamic diameters of polysaccharides and proteins were determined using 1 mg mL^{-1} solutions in the 0.2× Tris buffer solution. Diameters of submicron CaCO$_3$ crystals were determined using 0.1 mg mL^{-1} suspensions taken directly after synthesis.

3.8.8 Energy dispersive X-ray spectroscopy

Samples sputtered with 10 nm of gold were subjected to energy dispersive X-ray (EDX) analysis, operated at a probe current of 10 μA and an accelerating voltage of 10 kV.

3.8.9 Fluorescence spectroscopy

The NanoDrop 3300 Fluorospectrometer (Thermo Scientific, USA) was used for sample analysis. For the FITC and RhoB fluorohores, samples were analysed via blue LED (470 $\pm$ 10 nm) and white LED (460-650 nm) light.

Determination of DEX$^{\text{FITC}}$ mass content within CaCO$_3$ crystals

Following the formation of submicron CaCO$_3$ crystals, they were centrifuged at 10,000g for 10 mins followed by removal of 200 μL of the supernatant. 2 μL of the supernatant was analysed, and the fluorescence maxima measured were in the range of 515-520 nm for DEX$^{\text{FITC}}$, CM-DEX$^{\text{FITC}}$, and DEAE-DEX$^{\text{FITC}}$.

3.8.10 Fourier transform-infrared spectroscopy

Fourier transform-infrared (FT-IR) spectroscopy was performed on a Cary 630 FT-IR Spectrometer (Agilent, USA), 32 scans per sample were performed, with a resolution of 4 cm^{-1}. The attenuated total reflectance (ATR) sampling technique was utilised.

3.8.11 Inductively coupled plasma-mass spectrometry

For the determination of cobalamin content encapsulated within CaCO$_3$ crystals, cobalt content was determined via ICP-MS. Following the co-synthesis of cobalamin into CaCO$_3$ crystals, the samples were centrifuged at 10,000g for 10 min, and 50 μL of the supernatant was taken and added to 200 μL of 70% HNO$_3$ for digestion for over 1 h in the absence of light. After digestion, samples were diluted with 1% HNO$_3$ before

analysis. The concentration of the ^{59}Co isotope was determined, using ^{69}Ga as an internal standard.

3.8.12 Surface free energy determination

To determine the surface energy of solids, the Owens-Wendt-Rabel-Kälble (OWRK) model was utilised. Through use of the linear equation 3.4, the polar and dispersive components of the surface free energy were determined via use of contact angle measurements with liquids of known surface tensions.

$$\frac{\gamma_l(1 + \cos(\theta))}{2\sqrt{\gamma_l{}^d}} = \sqrt{\gamma_s{}^p}\frac{\sqrt{\gamma_l{}^p}}{\sqrt{\gamma_l{}^d}} + \sqrt{\gamma_s{}^d} \tag{3.4}$$

Where, γ_l and γ_s are the total surface tension of the liquid and solid, respectively. Superscripts d and p correspond to the dispersive and polar components, respectively.

3.8.13 Thermogravimetric analysis

Here, a TGA 4000 thermogravimetric analyzer (PerkinElmer, USA) was used. All samples were heated within a helium atmosphere. Samples were heated from 30 to 800°C at a heating rate of 5°C min^{-1}.

3.8.14 UV-vis spectroscopy

UV-Vis spectroscopy was performed using the NanoDrop One spectrophotometer (Thermo Scientific, USA), within the range of 190 to 850 nm. Here, the stability of AgNPs was investigated via the measurement of UV-Vis extinction spectra of diluted suspensions of AgNPs in the presence of 0.2× Tris buffer solution, pH 7.9 or Milli-Q water. For the stability of AgNPs adsorbed to HA/PLL microgels, (HA/PLL)$_4$ and (HA/PLL)$_{4.5}$ were formed upon glass coverslips cut to size with a diamond knife (7

x 50 mm) and incubated in AgNPs as described previously. Following optical imaging, the microgel-laden slide was placed within a quartz cuvette, ensuring the slide was flat against the cuvette wall with the adsorbed AgNPs facing the bulk solution, and the spectrum was taken. Of note, the NanoDrop beam is 2 mm in diameter and 8.5 mm above the bottom of the cuvette - it was ensured the AgNP-laden microgels were positioned so the beam passed through the sample.

Chapter 4

Development of vectors for *in ovo* delivery

4.1 Introduction

In this chapter, the potential vectors for IOF were developed, and their properties were investigated; these include both porous vaterite $CaCO_3$ crystals as well as biopolymer-based $CaCO_3$-templated microgels. Of note, part of the work presented in this Chapter has been published as reference (5), as listed in Section 1.3.

4.2 Vaterite $CaCO_3$ crystals

4.2.1 $CaCO_3$ synthesis optimisation

For the preparation of vaterite $CaCO_3$ crystals, the popular method of the intermixing of two supersaturated salt solutions was performed [44, 45]: namely aqueous solutions of calcium chloride and sodium carbonate. Here, low initial salt concentrations were used (50 mM - 70 mM) as to allow for the retention of the structure and activity of potential co-synthesised bioactive compounds, whether low-molecular-weight or macro-molecular. However, low salt concentrations may hinder the range of crystal sizes that can be obtained using standard equimolar intermixing. According to classical nucleation theory [44], increasing the supersaturation, causes an increase in the nucleation rate. As the nucleation rate increases, the number of crystals generated is increased per unit time, and hence smaller crystal sizes are produced (equations 4.1 and 4.2). This, however, is much easier achieved using higher initial salt concentrations to synthesise such crystals, as the activity of Ca^{2+} and CO_3^{2-} will be much larger.

$$S = \sqrt{\frac{\alpha_{Ca^{2+}} + \alpha_{CO_3^{2-}}}{K_{sp}}} \tag{4.1}$$

$$J = A \exp\left(\frac{-16\pi\gamma^3\nu^2}{3k_B{}^3T^3(v\ln S)^2}\right) \tag{4.2}$$

Where S - supersaturation, α - ionic activity (of either CO$_3$$^{2-}$ or Ca^{2+}), K_{sp} - thermodynamic solubility constant of vaterite CaCO$_3$, γ - interfacial tension, ν - volume of a molecule inside the nucleus, k_B - Boltzmann constant, T - temperature.

Smaller crystal sizes have been previously achieved through the use of various polymer additives whilst retaining low supersaturation, such as glycerol, ethylene glycol and gelatin [44, 66]. Here, there was a need to retain low salt concentrations, as well as an additive-free approach in order to produce a universal one-step synthesis of vaterite CaCO$_3$ crystals of various sizes, ranging from submicron to tens of micrometres. This was achieved via the variation of multiple synthesis parameters.

Firstly, the molar ratio of CaCl$_2$:Na$_2$CO$_3$ was varied, ranging from 1:1 to 40:1; this resulted in the reduction of crystal sizes from 7.9 $\pm$ 1.7 μm to 2.0 $\pm$ 0.3 μm (Figure 4.1). This can be explained via the increase in $\alpha_{Ca^{2+}}$ whilst $\alpha_{CO_3^{2-}}$ remains constant, resulting in higher supersaturation at higher molar ratios, hence smaller crystal diameters [44, 85]. Of note, when increasing the initial Na$_2$CO$_3$ concentration from 0.05 M to 1.00 M, whilst maintaining the same final Ca^{2+}:CO$_3$$^{2-}$ molar ratio (4:1), this had no significant effect on the final vaterite crystal size (Figure 4.2), suggesting the intermixing here was enough to homogeneously distribute Na$_2$CO$_3$ throughout the reaction mixture despite the increased carbonate local concentration.
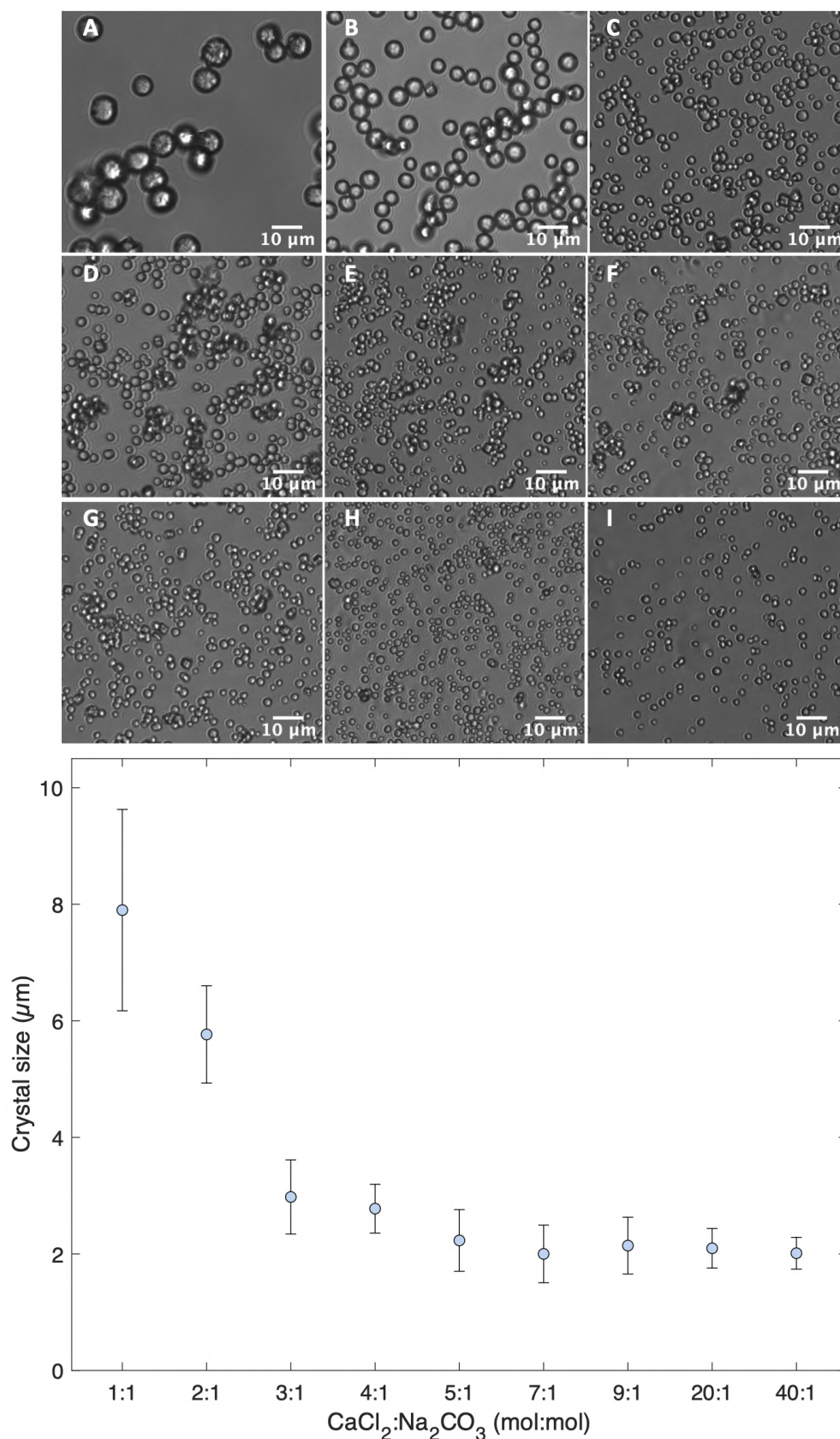
Figure 4.1: Transmittance images of vaterite crystals formed at various CaCl$_2$:Na$_2$CO$_3$ molar ratios: (A) 1:1, (B) 2:1, (C) 3:1, (D) 4:1, (E) 5:1, (F) 7:1, (G) 9:1, (H) 20:1 and (I) 40:1. Scalebars are 10 μm. Graph demonstrating the average vaterite crystal size as a function of the CaCl$_2$:Na$_2$CO$_3$ molar ratio. Error bars are SD, n=100.
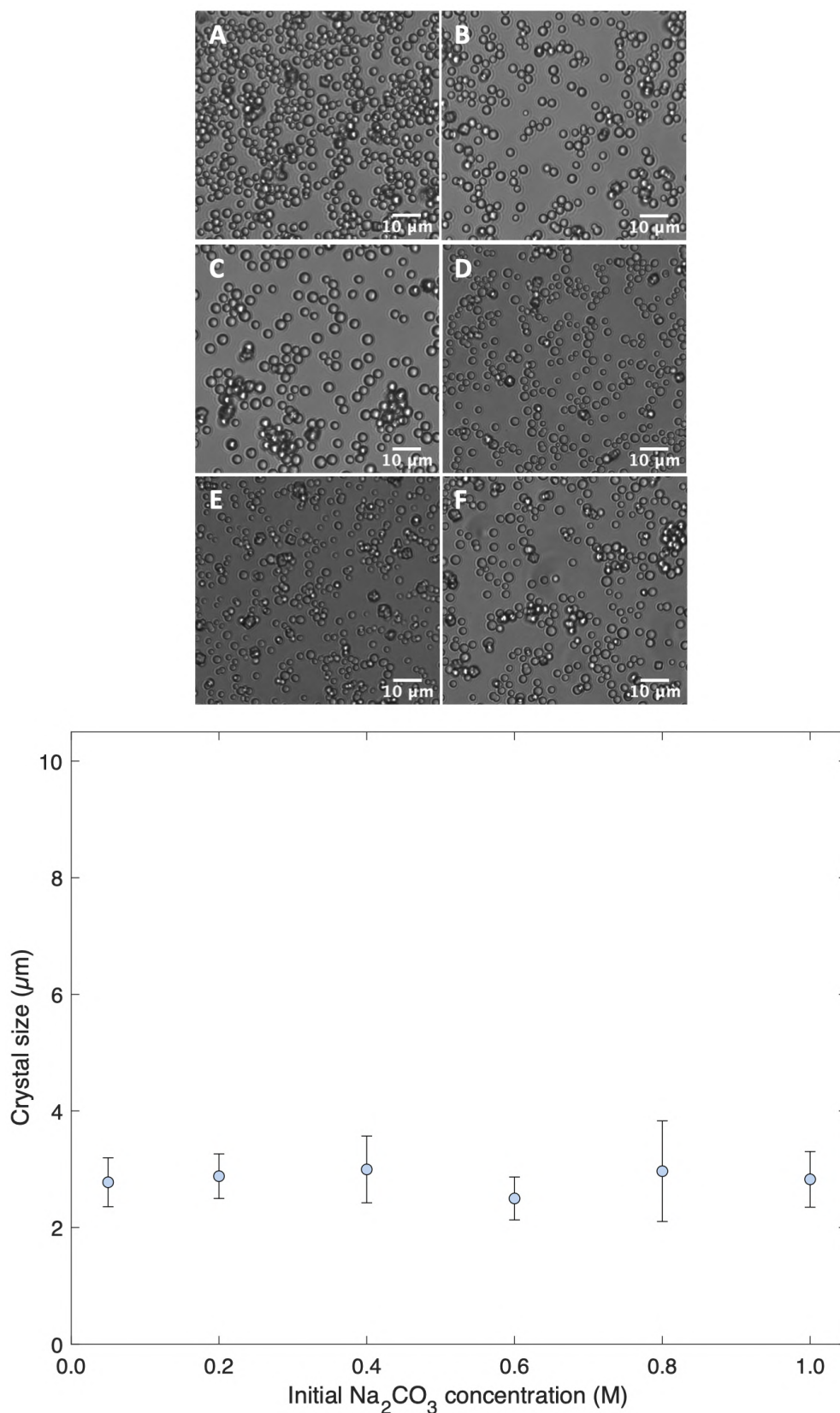
Figure 4.2: Transmittance images of vaterite crystals formed using various Na$_2$CO$_3$ initial concentrations: (A) 0.05 M, (B) 0.2 M, (C) 0.4 M, (D) 0.6 M, (E) 0.8 M and (F) 1.0 M. Scalebars are 10 μm. A graph demonstrating the average vaterite crystal size as a function of the Na$_2$CO$_3$ initial concentration. Error bars are SD, n=100.

It is well known that increasing the agitation speed of the synthesis mixture reduces the vaterite crystal size [10]. This may be due to the superior intermixing of ions at higher shear rates, resulting in the formation of a higher number of nuclei. Interestingly, this phenomenon was observed independent of the molar ratio of the salt solutions (i.e. for 1:1, 4:1 and 9:1), with this size reduction factor decreasing with increasing molar ratio. This effect can be seen in Figure 4.3. A similar trend was observed for the increase in agitation time (Figure 4.4), again, likely due to the increased extent of intermixing of salt solutions, prior to the same crystal growth period, as is typical of such systems [85].
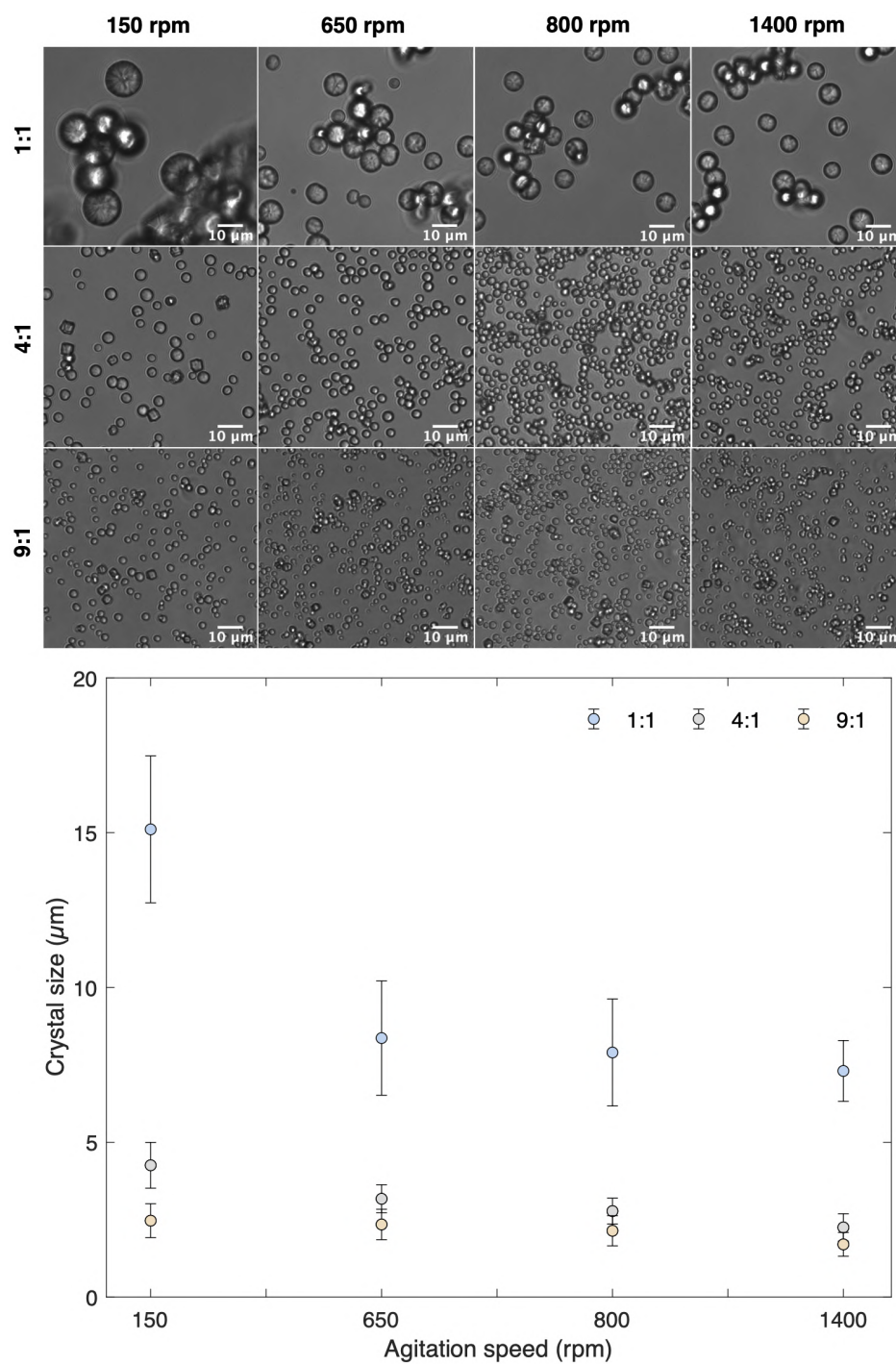
Figure 4.3: Transmittance images of the vaterite crystals formed at CaCl$_2$:Na$_2$CO$_3$ molar ratios of 1:1, 4:1 and 9:1, with agitation speeds of 150, 650, 800 and 1400 rpm. Scalebars are 10 μm. A graph demonstrating the average vaterite crystal size as a function of the agitation speed. Error bars are SD, n=100.
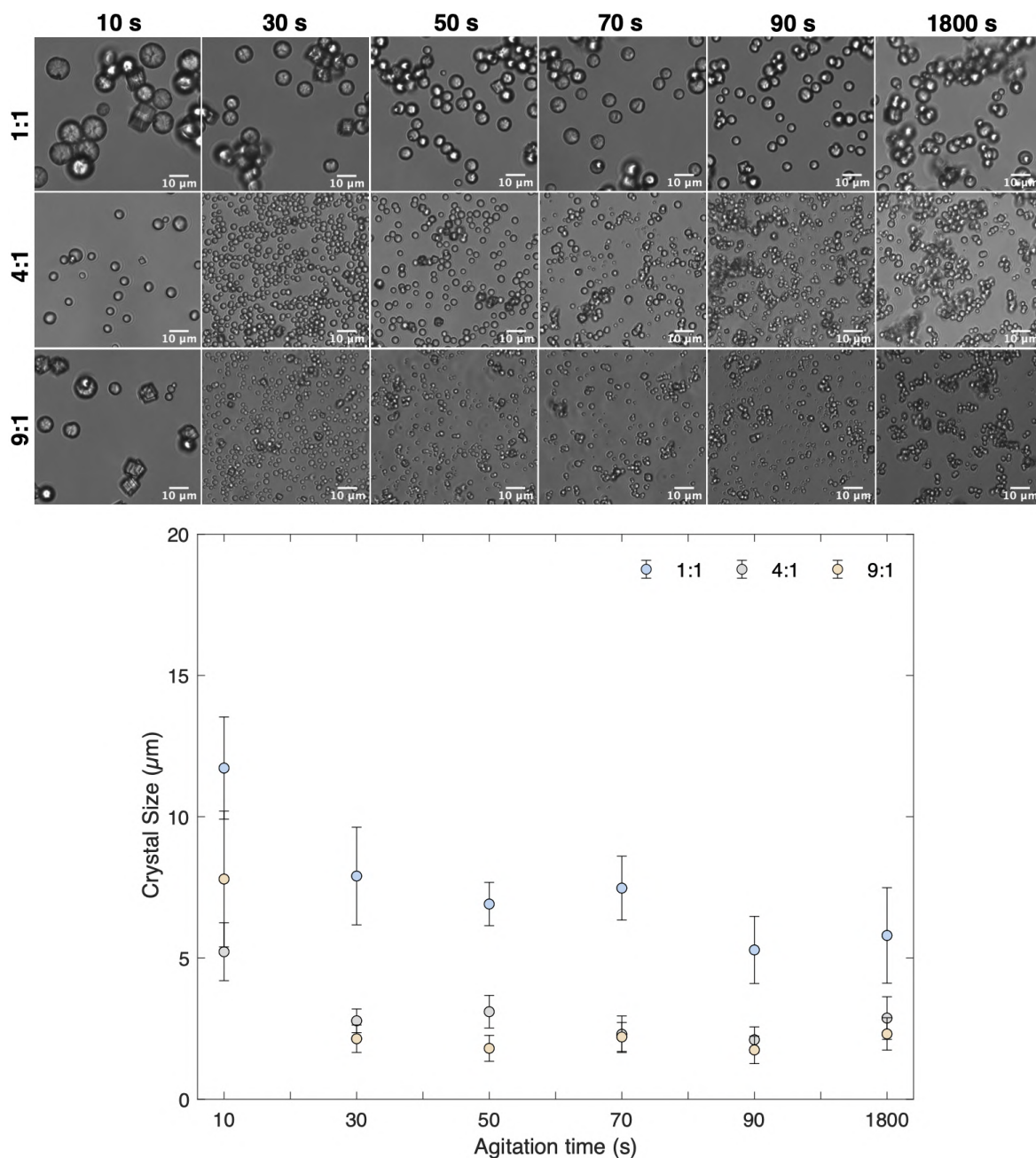
Figure 4.4: Transmittance images of the vaterite crystals formed at CaCl$_2$:Na$_2$CO$_3$ molar ratios of 1:1, 4:1 and 9:1, with agitation times of 10, 30, 50, 70, 90 and 1800 s. Scalebars are 10 μm. A graph demonstrating the average vaterite crystal size as a function of the agitation time. Error bars are SD, n=100.

The effect of the extent of intermixing upon the vaterite crystal size became further evident upon varying the reaction vessel geometry. For instance, the circular base of a glass beaker was increased from just $\sim$7 cm to $\sim$8 cm whilst retaining the same reaction conditions. This small change resulted in the significant reduction of crystal sizes at longer agitation times (20 s and 40 s) due to increased contact between the

two salt solutions as a consequence of increased beaker volume, and hence greater stirring. Of note, during a 3 s reaction time there was no observed effect as not enough time had elapsed for such intermixing to occur (Figure 4.5). This observation may have important implications with regards to the upscaling of vaterite crystals; larger reaction vessels may be used to decrease the crystal size, however, increasing the quantity of salt solution will result in less intermixing and produce larger crystals. Suitable up-scaled reaction conditions should be investigated to produce the crystal sizes desired in large quantities.
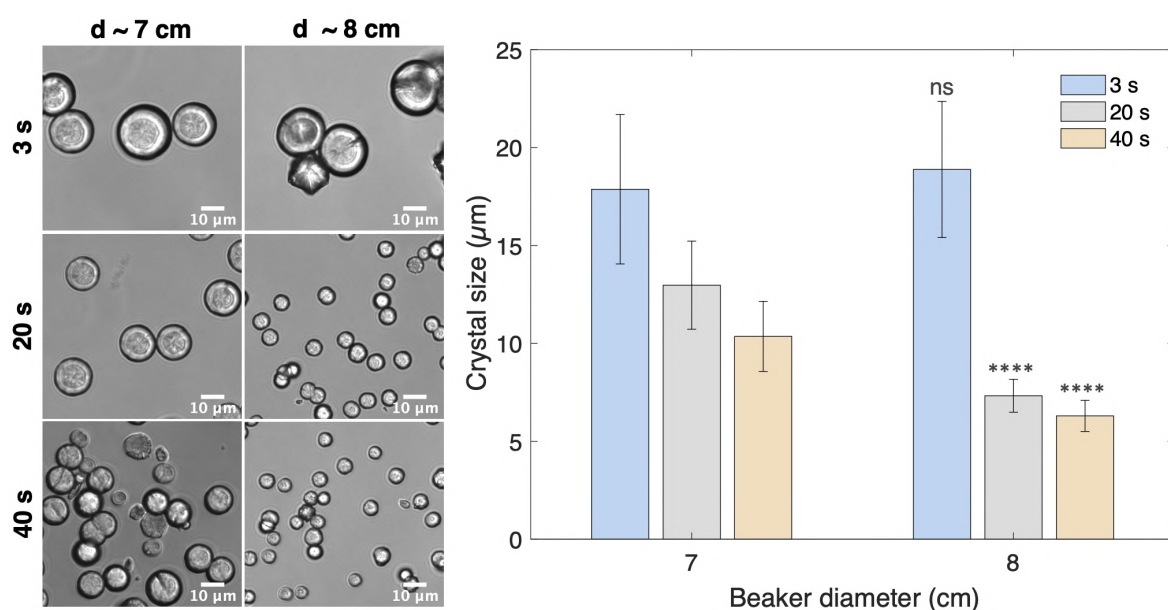
Figure 4.5: Transmittances images of vaterite crystals formed in two different beakers with varying base diameters (7 or 8 cm) at agitation times of 3, 20 or 40 s. Scalebars are 10 μm. A graph demonstrating the average vaterite crystal size as a function of beaker geometry. Error bars are SD, n=100. Statistical analysis was made using the t-test (normal distribution); ns: non-significant difference and $****p<0.0001$. Comparison was performed between the same agitation times using different beaker diameters.

From these data, additive-free submicron vaterite CaCO₃ crystals were also successfully synthesised in water via the reduction of working volume, increase in agitation speed and time, as well as the molar ratio. Such crystals hold an average hydrodynamic diameter of 500 ± 210 nm, as determined by DLS. Moreover, these crystals do not grow further over a 60 min period and retain their initial size from immediate post-synthesis - this indicates these submicron crystals grow during the mixing period during the synthesis (Figure 4.6). Alternatively, via increasing the working volume and reducing

agitation time, sizes of up to 15-20 μm vaterite crystals were also synthesised; these various crystals are used as standards throughout this work, and were characterised accordingly, as demonstrated within the next section.
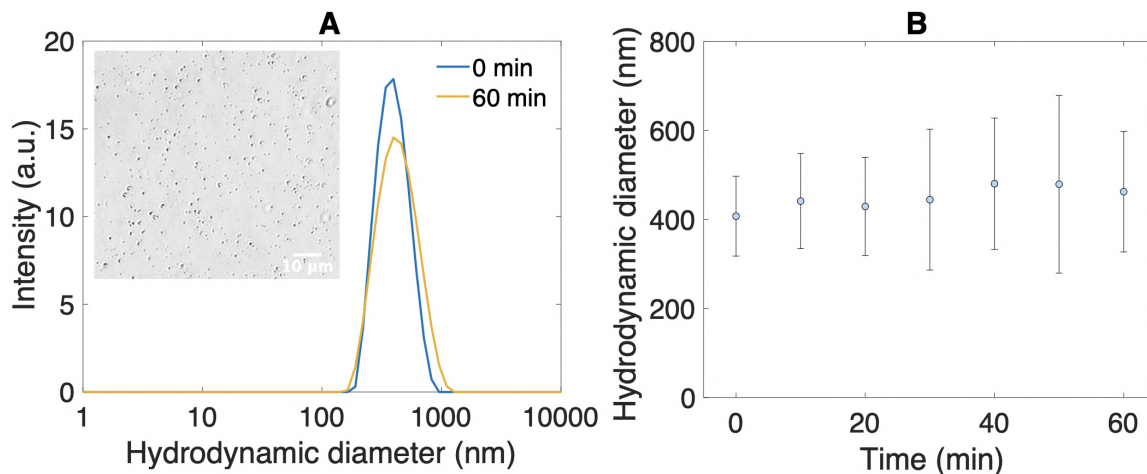
Figure 4.6: DLS size distribution by intensity (A) of submicron vaterite crystals immediately after synthesis (0 min) and after 60 mins of growth; the inset (i) is transmittance image of the submicron vaterite crystals after 60 mins of growth. Scalebar is 10 μm. Hydrodynamic diameter as a function of time (B).

4.2.2 CaCO$_3$ characterisation

Various vaterite crystals were produced ranging from $\sim$500 nm to 20 μm. Figure 4.7 displays the SEM images of the micron-sized crystals. As can be seen, despite their size, the crystals are all spherical in their shape and possess similar morphologies. The surface of these crystals is formed of interconnected nanocrystallites, the size of which was determined via ImageJ, and varied insignificantly with the increase in total crystal diameter (Figure 4.7). In-between these nanocrystallites are pores which can be observed within Figure 4.7, in which a mechanically cracked crystal can be observed, baring cylindrical radial pores - this is typical for vaterite crystals and is reported throughout the literature [24, 100]. This porous, spherical morphology is indicative of the vaterite polymorph and has been confirmed via FT-IR analysis (typical vaterite peak at 745 cm^{-1} [318]) and is independent on the crystal size here (Figure 4.8).
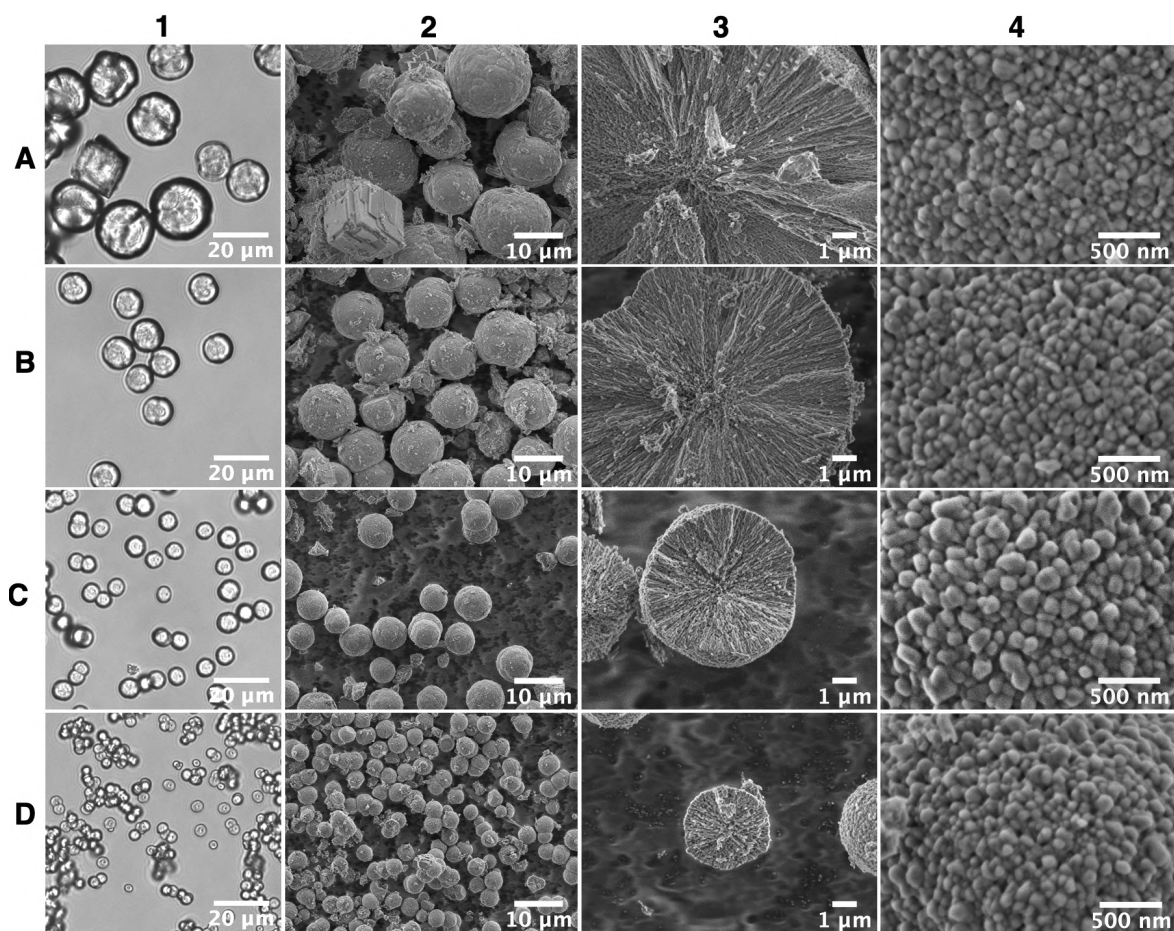
Figure 4.7: Typical images of vaterite crystals of various sizes: (A) 17 $\pm$ 2, (B) 11 $\pm$ 1, (C) 7 $\pm$ 1 and (D) 4 $\pm$ 1 μm. (1) Transmittance images of the vaterite crystals and SEM images of a (2) sample overview, (3) cross-section of a single crystal and (4) the crystal surface morphology. Scalebars are (1) 20 μm, (2) 10 μm, (3) 1 μm and (4) 500 nm.
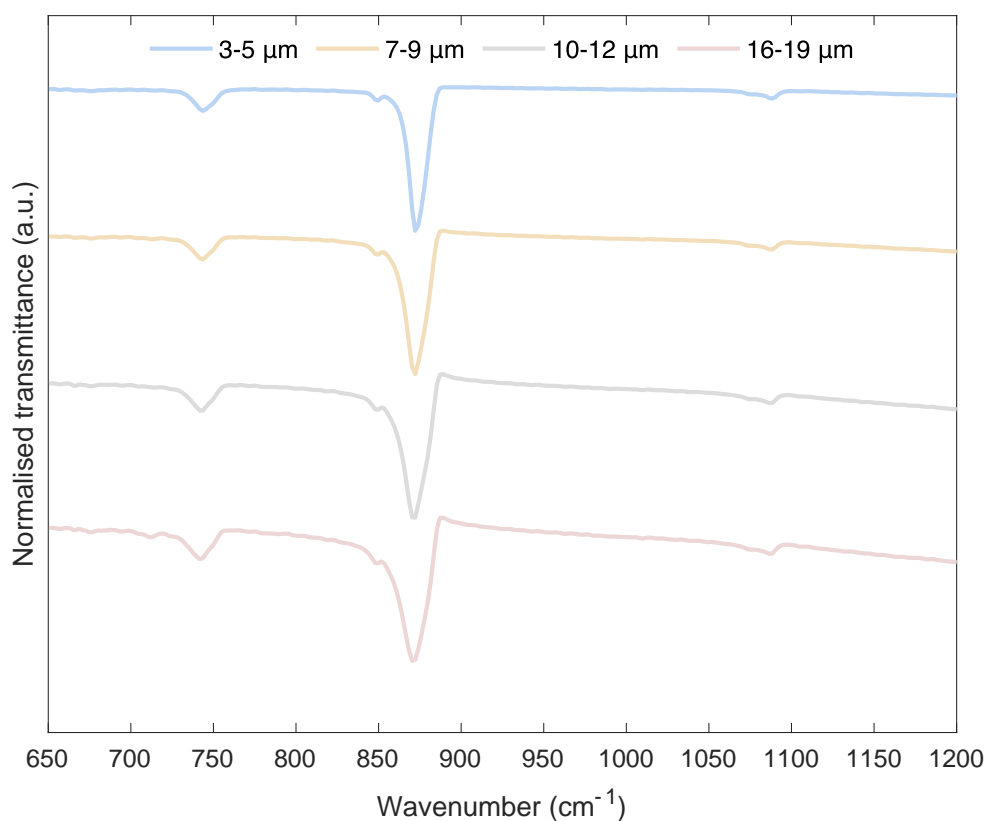
Figure 4.8: FT-IR spectra of the vaterite crystals of various crystal sizes.

Typical N$_2$ adsorption-desorption isotherms are shown in Figure 4.9. The hysteresis presented here is indicative of H1 type hysteresis, and represents uniform cylindrical-shaped pores [319], of which is evident from the internal crystal structure depicted in Figure 4.7, and is typical of vaterite CaCO$_3$. The surface area decreased with increasing crystal size, from ∼8 to ∼4 m^2 g^{-1} for 3-5 and 15-17 μm crystals, respectively, whilst retaining the typical pore distribution of 5-30 nm.
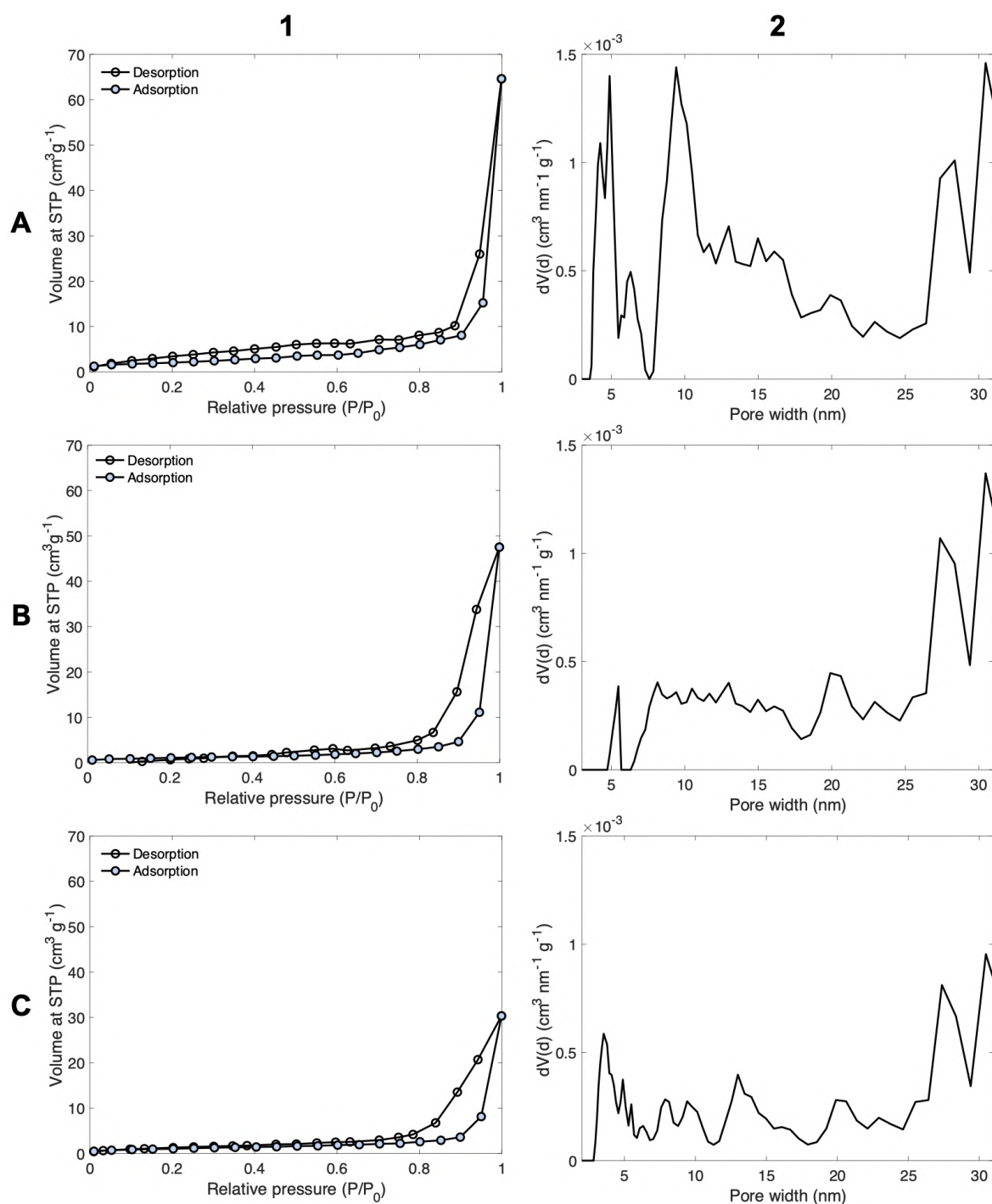
Figure 4.9: (1) Nitrogen adsorption-desorption isotherms and (2) pore distributions of (A) 4 ± 1 μm, (B) 11 ± 1 and (C) 17 ± 2 vaterite crystals.

SEM and FT-IR analysis of these additive-free submicron vaterite crystals revealed their spherical shape and typical vaterite morphology (Figure 4.10). Moreover, these submicron crystals were also synthesised in Tris buffer pH 7.4, in order to control the pH of the system and aid in preserving the activity and stability of any sensitive

bioactives to be encapsulated in these crystals. Interestingly, these submicron crystals were not able to form in 1× or 0.5× but were able to form in 0.1× Tris pH 7.4; where crystals were formed in 1× Tris pH 7.4 with equimolar concentrations of CaCl$_2$ and Na$_2$CO$_3$. This implies that a component within the Tris buffer may interact with or scavenge Na$_2$CO$_3$/CO$_3^{2-}$, as the only difference is the use of a 40:1 CaCl$_2$:Na$_2$CO$_3$ reaction mixture, as opposed to equimolar. This is also evident from a reduction in the final reaction yield of CaCO$_3$ when Tris is used (from >90% to 60-70% for water- and Tris-based syntheses, respectively). Nevertheless, Figure 4.11 illustrates the Tris-based submicron crystals' typical vaterite morphology; from these SEM images the typical size of water- and Tris-based submicron crystals were 457 ± 94 and 404 ± 69 nm, respectively, with nanocrystallite sizes of 60 ± 11 and 77 ± 16 nm, respectively. Further, both crystals held positive Zeta-potentials of 30 ± 2 and 31 ± 2 mV for water- and Tris-based submicron crystals, respectively. Such positive Zeta-potentials are typical of vaterite and are common within the literature [70].
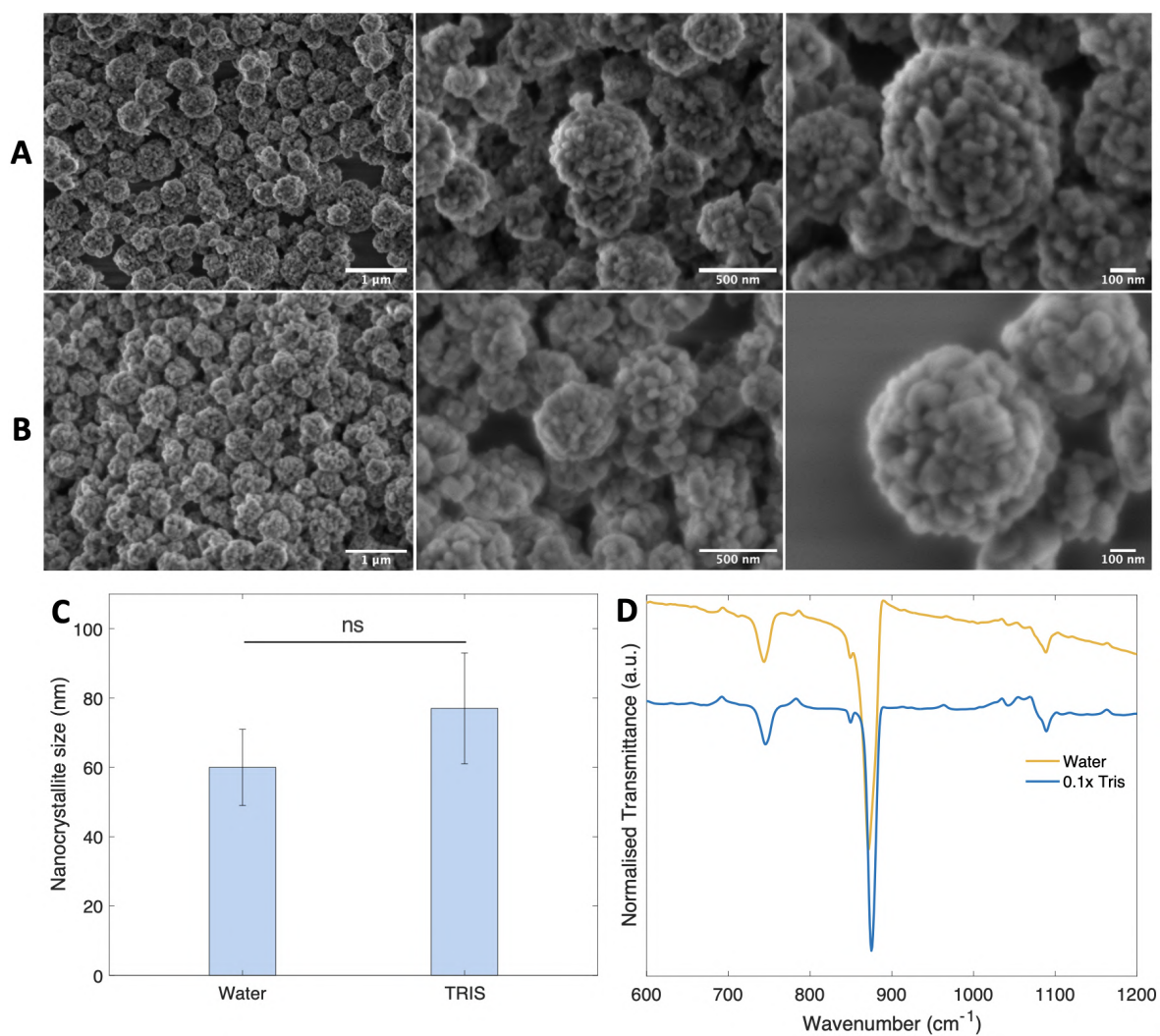
Figure 4.10: Typical SEM images of submicron vaterite crystals formed in (A) water and (B) 0.1× Tris pH 7.4. Scalebars are 1 μm, 500 nm and 100 nm. (C) a graph illustrating the nanocrystallite sizes and (D) FT-IR spectra of submicron crystals formed in both water and 0.1× Tris pH 7.4. Error bars are SD, n=100. Statistical analysis made using the t-test (normal distribution); ns: non-significant difference.
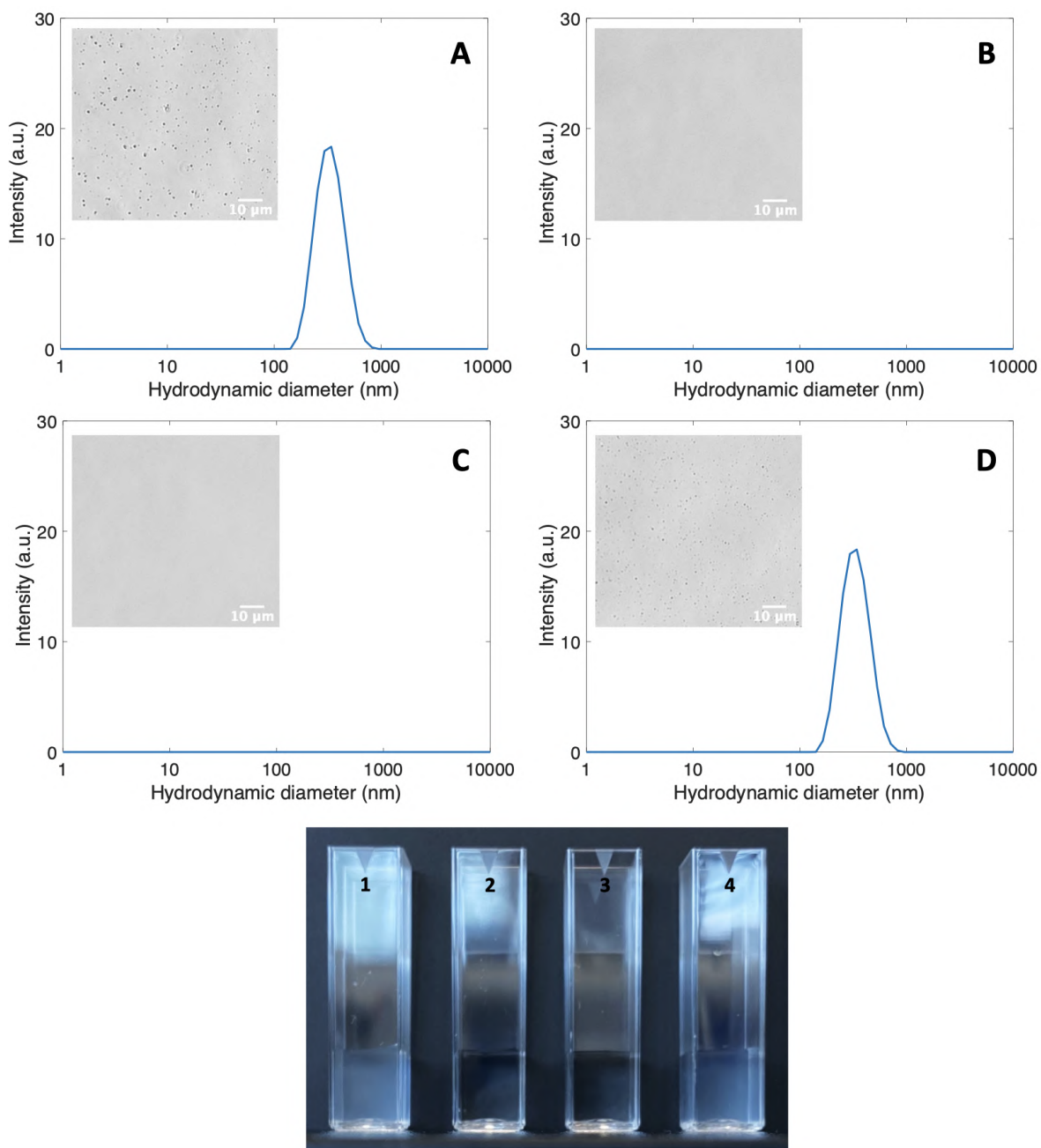
Figure 4.11: DLS size distributions by intensity of submicron vaterite crystals formed in (A) water, (B) 1×, (C) 0.5× and (D) 0.1× Tris, pH 7.4 with corresponding transmittance images. Sample images of vaterite suspensions formed within (1) water, (2) 1×, (3) 0.5× and (4) 0.1× Tris, pH 7.4. Scalebars are 10 μm.

Of note, in terms of the potential storage of these submicron vaterite crystals - these crystals can be stored directly after synthesis at -20°C for periods of up to at least 4 weeks (only up to 4 weeks was investigated). Indeed, DLS analysis revealed these crystals display almost identical hydrodynamic diameters before and after 4 weeks at -20°C, with no detection of aggregation or calcite formation, as displayed in Figure

4.12.
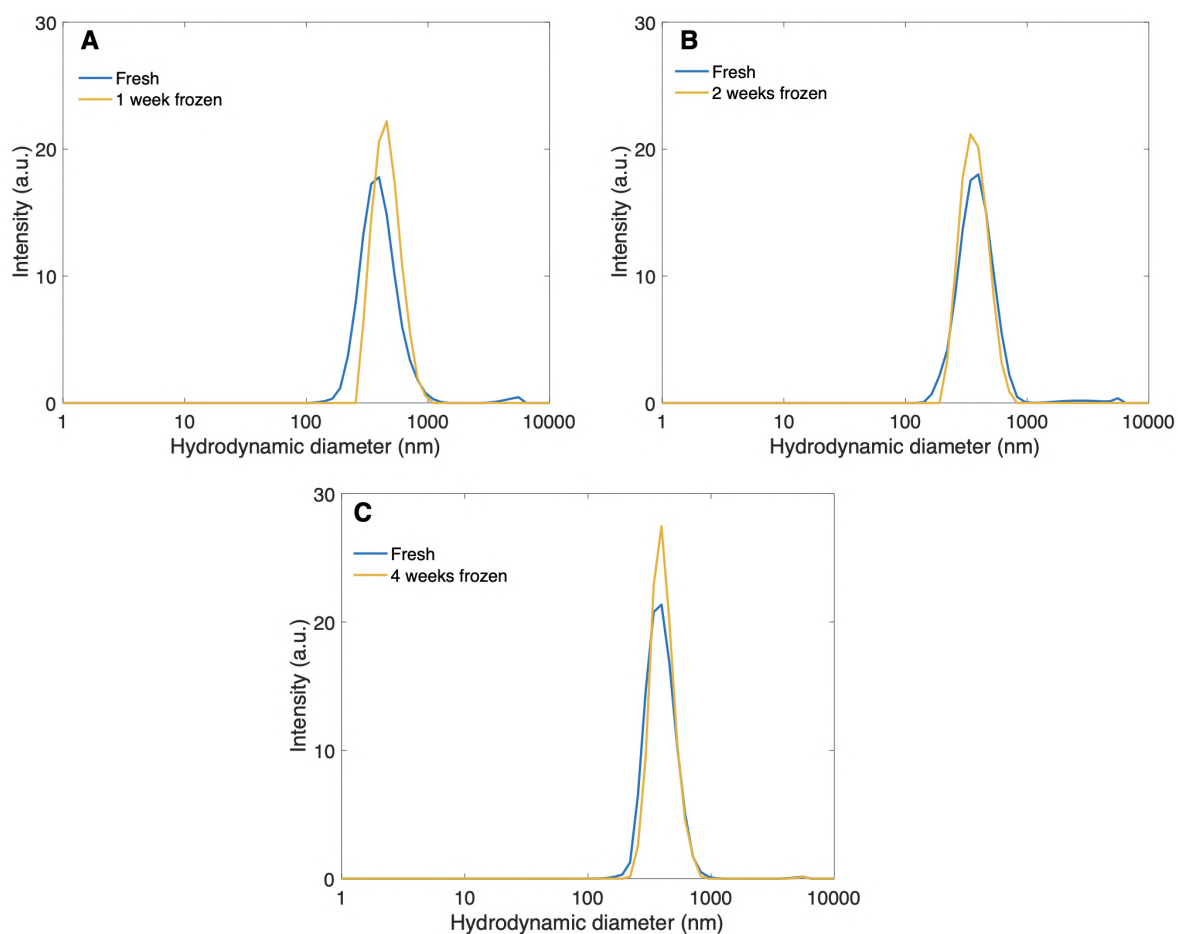
Figure 4.12: DLS size distributions by intensity of submicron vaterite crystals both fresh and frozen at −20°C for (A) 1, (B) 2 and (C) 4 weeks.

4.3 Biopolymer-based microgels

4.3.1 Vaterite templates

The ∼7 μm vaterite microcrystals were used here as a standard (if not stated otherwise). Recent reports revealed that the substitution of conventionally used water with buffered solutions is important for the preservation of bioactivity of some biomolecules while having no pronounced effect on the crystal structure [70]; when $CaCO_3$ is present in water, pHs of ∼10 are reached due to hydrolysis. For instance, there is the problem of potential irreversible conformational changes at pHs above 9, as shown during the loading of catalase into such vaterite templates [70], while pHs below 7 are not suitable

for the LbL coating of $CaCO_3$ crystals due to their dissolution. Baring the protection of such macromolecular drugs in mind, the pH was maintained at 7.9 throughout.

4.3.2 Biopolyelectrolytes in solution

The bio-polyelectrolytes chosen for this study included four polycations and four polyanions (Figure 4.13). The polyelectrolytes that generated anions were of either purely carboxylic (HA) and purely sulfuric (DS) nature or contained both COO^- and sulfate groups in ratios 1:1 and 1:3 (for CS and HS, respectively). The four polycations used generated amino groups and had different conformations and structures, that is, two proteins - fibrous COL and globular PR and two linear polymers - highly charged PLL and DA, which carries a lower net charge.
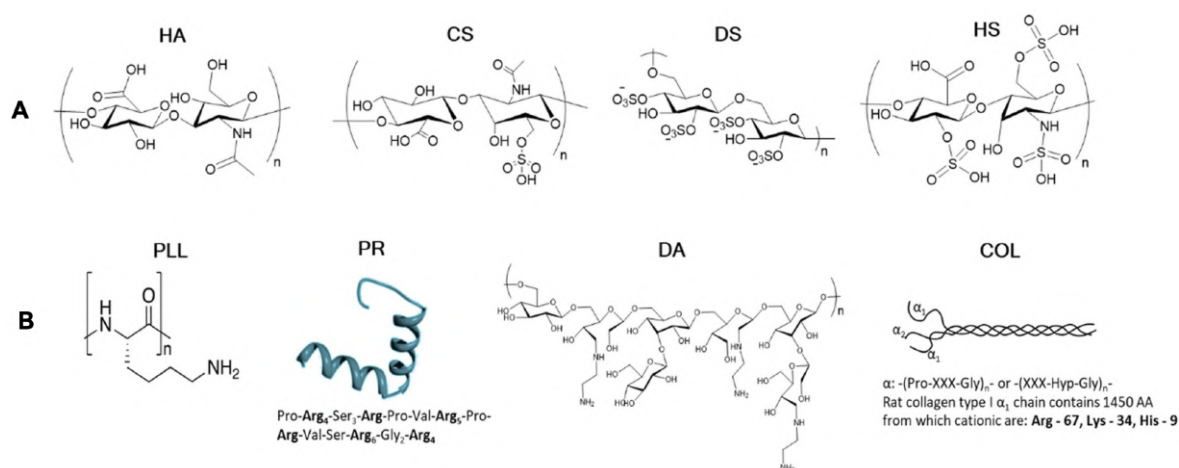
Figure 4.13: Structure of polymers utilised to form microgels separated into two categories: (A) polyanionic and (B) polycationic. For the proteins, the amino acid sequence (for PR) or the number of positively charged amino acids (Arg, Lys, and His) per α_1-helix (for COL) is given. Structure of PR reprinted with permission from reference [320].

Table 4.1 displays the pK_a and isoelectric points of polymers and proteins used here, respectively. The hydrodynamic radii (r_h) of these polymers in the Tris buffer solution were determined by DLS. Figure 4.14 presents their DLS size distributions; such data suggest that polyanions were of a similar size, that is, r_h in the range of 3-4 nm for CS, DS, and HS and slightly more (7.2 $\pm$ 3.4 nm) for HA. In contrast, r_h of polycations significantly increased in the series PR $\simeq$ PLL < COL < DA ranging from a

few nanometers for PR and PLL, 107 ± 14 nm for COL, and up to a few micrometers for DA. Intensity- and number-weighted size distributions were also obtained for the polymers used in this study [321]. From the intensity spectra, much broader distributions are observed, with all polysaccharides (besides that of HA) displaying two separate peaks (r_h of $\simeq 5$ nm and $\simeq 50$ nm). This may imply the samples are forming small aggregates within the buffer solution or are polydisperse in nature; indeed, the polysaccharides purchased here display polydispersity indices of 1.5-2.0, implying heterogeneous chain lengths within the same sample. Those r_h reported and seen in Figure 4.14 are a result of the volume-weighted distribution, comparable values are also observed within both the intensity- and number-weight distributions. Notably, only DA was prone to aggregation and predominantly formed micro-sized clusters in the Tris buffer solution. The other polymers were present in a non-aggregated state.

Table 4.1: pK$_a$ and isoelectric point values for biopolymers and proteins used throughout this work.

Polymer	Isoelectric point (protein)/pKa (polymers)	Ref
HA	3-4	[322]
CS	2-4	[323, 324]
DS	2	[192]
HS	1-4	[325, 326]
PLL	9-10	[243, 327]
PR	12-13	[328]
DA	Unknown	-
COL	7-9	[329, 330]
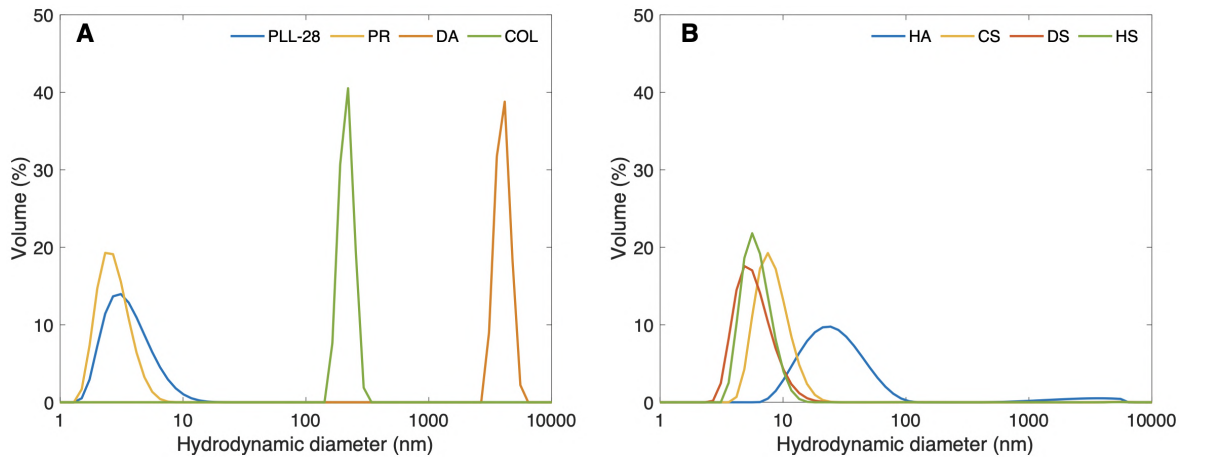
Figure 4.14: DLS size distribution of the polycations (A) and polyanions (B) utilised to form microgels in the $0.2\times$ Tris buffer solution, pH 7.9.

4.3.3 Formation of biopolymer-based microgels

$CaCO_3$ crystals have been coated with (polyanion/polycation)$_{2.5}$ multilayers made of 16 combinations of these polymers. Within the literature, the number of layers to produce $CaCO_3$-templated capsules/microgels ranges from 1 to 12 layers (Table 2.2), from this, a suitable middle-ground of 2.5 bilayers (i.e. 5 layers) was selected as a standard throughout this work, unless stated otherwise. During the coating and microgel formation processes, the temperature remained standard; it is reasonable to assume that the increase of temperature, for example, to a physiological value of 37°C, may promote enhanced polyelectrolyte adsorption and the formation of a thicker multilayer shell, in accordance with modern LbL concepts. This, in turn, may significantly affect the structure and functionality of the final microgels.

Elimination of the template was induced by the addition of EDTA, which caused the dissolution of $CaCO_3$ crystals and either the formation of the microgels or disaggregation of their final structure (Figures 4.15 and 4.16). Under these conditions, none of the DA- and COL-based microgels coupled with HA, CS, DS, nor HS; all DA- and COL-based coatings underwent complete dissolution upon the elimination of the template. However, 8 out of 16 investigated biopolymer pairs, that is, PLL-based (HA/PLL, CS/PLL, DS/PLL, and HS/PLL) and PR-based (HA/PR, CS/PR, DS/PR, and HS/PR), formed stable microgels.

While some of the pairs have been reported here for the first time (HA/PR; HS/PR; HS/PLL; and DS/PLL), other biogenic polyelectrolyte pairs were used for the fabrication of $CaCO_3$-templated microgels/capsules in recent reports. Thus, multilayer CS/PLL [202] and CS/PR [203] capsules were templated on vaterite microcrystals. In contrast to this work, the microcrystals were pre-loaded with polyanionic CS [202] or PSS [203] via co-synthesis. The CS/PLL capsules were not stable, and this instability was solved via capsule cross-linking [202]. Besides this, the capsules formed by CS and pARG, were reported [201]. Similarly, $CaCO_3$-templated HS/pARG and DS/pARG capsules were also investigated [26, 204, 213]; successful fabrication of CS/pARG and

DS/pARG capsules from soft microtemplates is also reported [252]. Fabrication of DS/PR capsules has also been attempted but faced either the problem of capsule aggregation when DS was a capping layer [206] or significant (up to 40%) retention of $CaCO_3$ after core dissolution when $CaCO_3$ was doped with PSS [207].
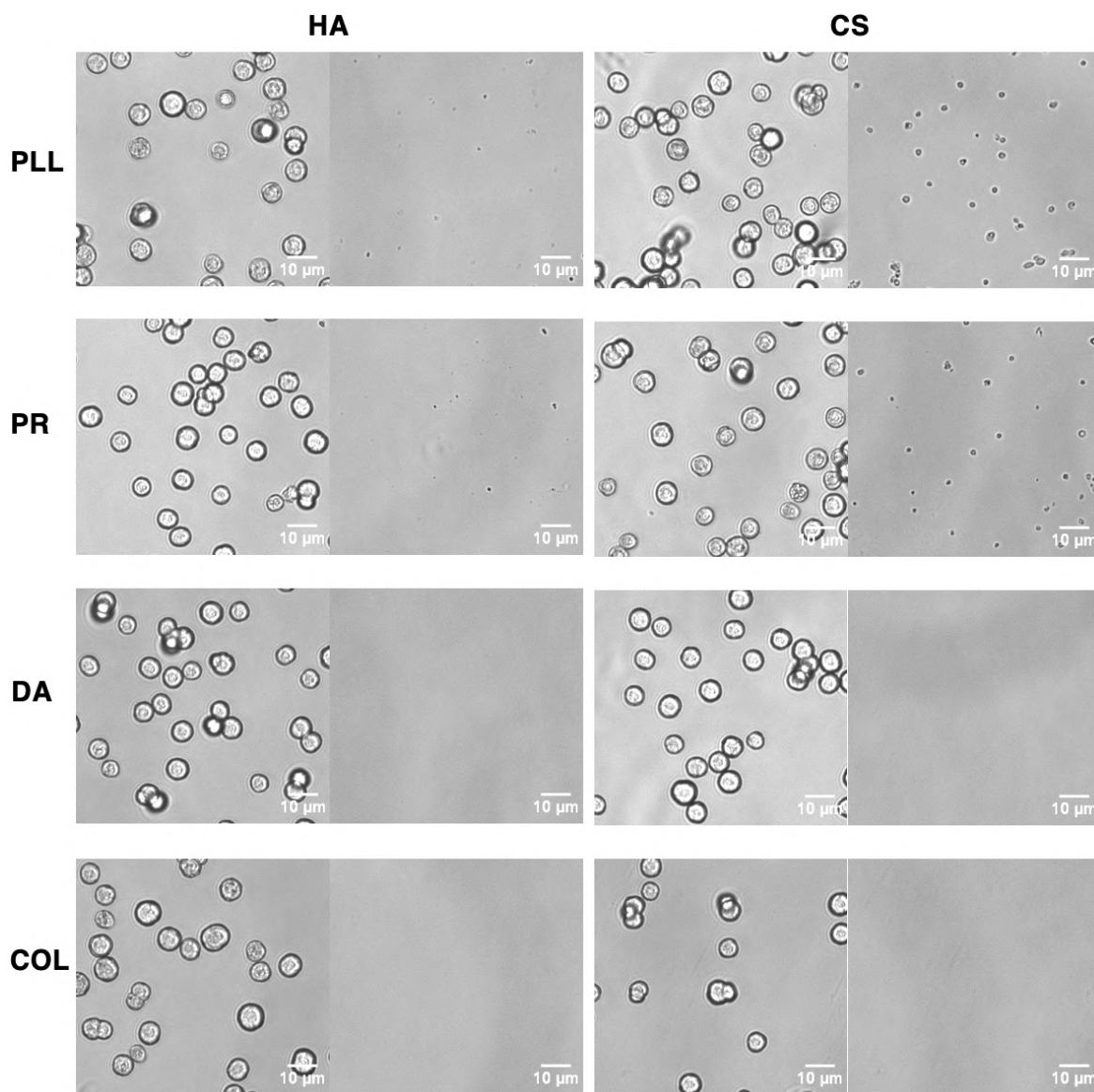
Figure 4.15: Transmittance images of (polyanion/polycation)$_{2.5}$ coated $CaCO_3$ crystals (left) and microgels (right) for the 16 biopolymer combinations investigated (HA and CS paired with PLL, PR, DA and COL). Scalebars are 10 μm.
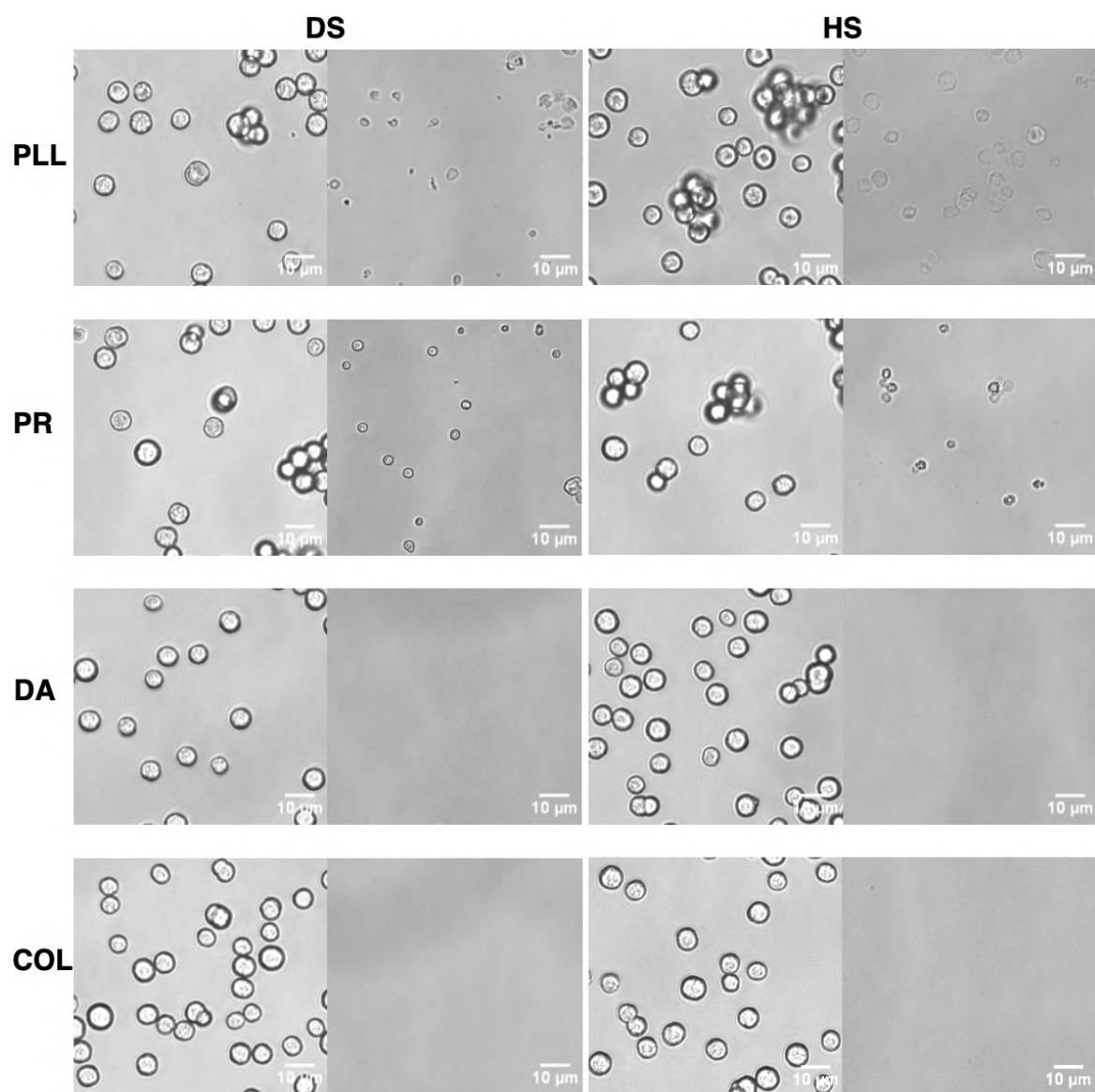
Figure 4.16: Transmittance images of (polyanion/polycation)$_{2.5}$ coated CaCO$_3$ crystals (left) and microgels (right) for the 16 biopolymer combinations investigated (DS and HS paired with PLL, PR, DA and COL). Scalebars are 10 μm.

Interestingly, although HA/PLL capsules were reported, they did not receive proper attention due to a high degree of capsule shrinkage during their preparation [208]. However, it may be that such a behaviour is beneficial for drug delivery purposes as a way to intrinsically reduce the microgel size and entrap molecules of interest. Notably, fabrication of HA/COL capsules utilising cross-linked COL was also reported [209]. It seems that the fabrication of COL-based microgels without chemical modifications cannot be achieved. This suggests that the integrity and stability of the microgels that underwent dissolution in this work can be improved via chemical modifications of the

polymers and their cross-linking.

Probability of microgel formation versus PEC stability

For this purpose, interactions of oppositely charged polymers in an aqueous environment have been probed by means of turbidimetric titration of equimolar complexes. Such experiments have been performed in collaboration with Georgia Kastania and Jordan Abnett, NTU.

PECs were formed in the Tris buffer solution, pH 7.9, which had the same composition as the solution used for the fabrication of microgels themselves. Then, PECs were titrated with salt (NaCl) until their dissolution. Figure 4.17(A) shows the turbidimetric curves obtained for the titration of PECs composed from HA and different polycations as an example. The ionic strength was increased stepwise until the critical concentration of NaCl (C_{crit}) was reached, at which point the PECs underwent dissolution due to the extensive screening of polyelectrolyte permanent charges by salt. It is expected that the higher the value of this C_{crit}, the more the ion pairs are formed between the polymer chains in the initial PECs. Since the conditions used for the formation of PECs and corresponding microgels are the same, in its turn, the higher C_{crit} should correspond to stronger microgel integrity. Indeed, the results of the turbidimetric titration of PECs correlate with the probability of microgel formation upon template dissolution. As follows from turbidimetric titrations, HA is not prone to forming strong PECs with COL and DA in solution. Of note, slight turbidity of HA/DA is most likely associated with the formation of DA aggregates in the buffer solution (Figure 4.14). Weak complexation with COL is likely due to its low pI value (Table 4.1). In contrast, PR and PLL form complexes that dissolve due to extrinsic charge compensation at $C_{crit} \sim 300$ mM. This correlates with their high pI/pK$_a$ value. Other PECs behaved similarly (Figure 4.17(B) for CS/polycation PECs); this allows the correlation of the formation of the microgels with the formation of PECs in solution.
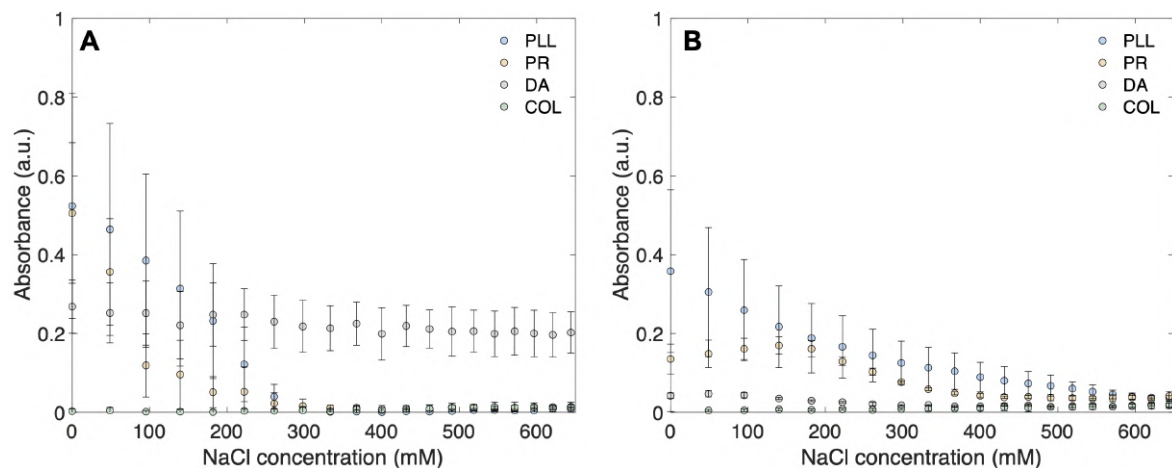
Figure 4.17: Turbidimetric titration of PECs of (A) HA and (B) CS with PLL, PR, COL, or DA, formed in 0.2× Tris buffer solution pH 7.9. The initial concentration of NaCl is subtracted; the x-axis represents the added amount of NaCl. Error bars are SD, n=3.

4.3.4 Internal structure of microgels

Successfully fabricated microgels were lyophilised and visualised by SEM (Figure 4.18). The complete elimination of the $CaCO_3$ template was confirmed via EDX analysis (Figure 4.18). Indeed, the characteristic X-ray energy bands of calcium were not found in the spectra of the microgels (red lines). Similarly, the complete elimination of vaterite has been proven for all other microgels. Of note, the Si peak observed within the EDX spectra arises from the glass coverslip upon which the microgels were deposited. The final microgels are of different sizes, but they all maintain a clear spherical structure and are filled with a polymer matrix, resulting in the formation of microgels rather than classical hollow structures (Figures 4.18). This may be important for microgel stabilisation during template dissolution and for their further performance of drug encapsulation and release. A deeper investigation is necessary to further probe the microgel internal structure via use of advanced approaches including small-angle X-ray scattering analysis [331] and confirm the presence of such a polymer matrix within the microgels.
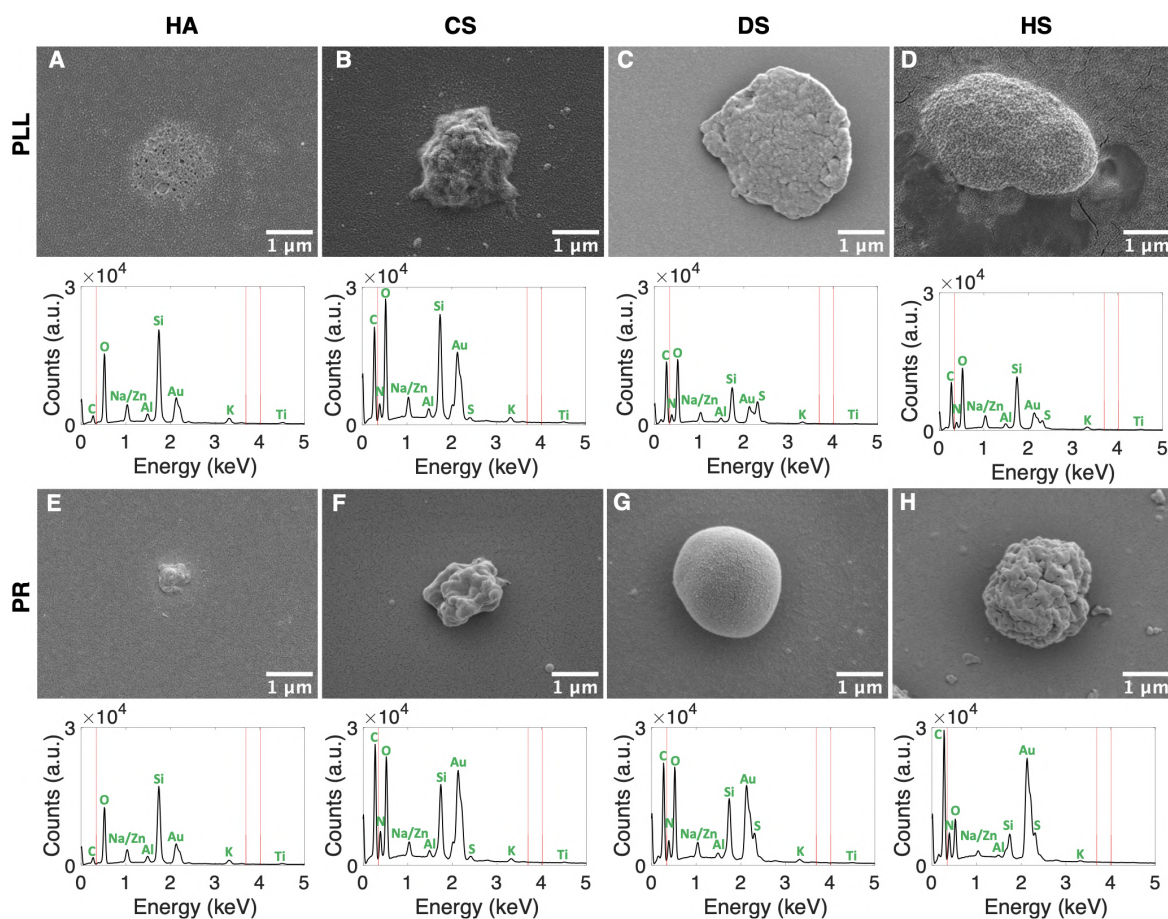
Figure 4.18: Typical SEM images of 10 nm gold-sputtered microgels consisting of 2.5 bilayers. PLL-based (top) microgels consisting of HA, CS, DS, and HS are shown in images (A), (B), (C), and (D), respectively. PR-based (bottom) microgels, consisting of HA, CS, DS, and HS, are shown in images (E), (F), (G), and (H), respectively. Scale bars are 1 μm. Corresponding typical EDX spectra are shown beneath the respective SEM image - the red lines correspond to the characteristic energies of X-ray emission for calcium.

Polyelectrolyte distribution within the microgels has been investigated by means of fluorescence imaging of the crystals coated with (polyanion/polycation$^{\text{FITC}}$)$_{2.5}$ before the elimination of CaCO$_3$ and the imaging of corresponding microgels. Figure 4.19 shows the uniform and homogeneous distribution of polycation$^{\text{FITC}}$ within the entire internal volume of mesoporous vaterite crystals.
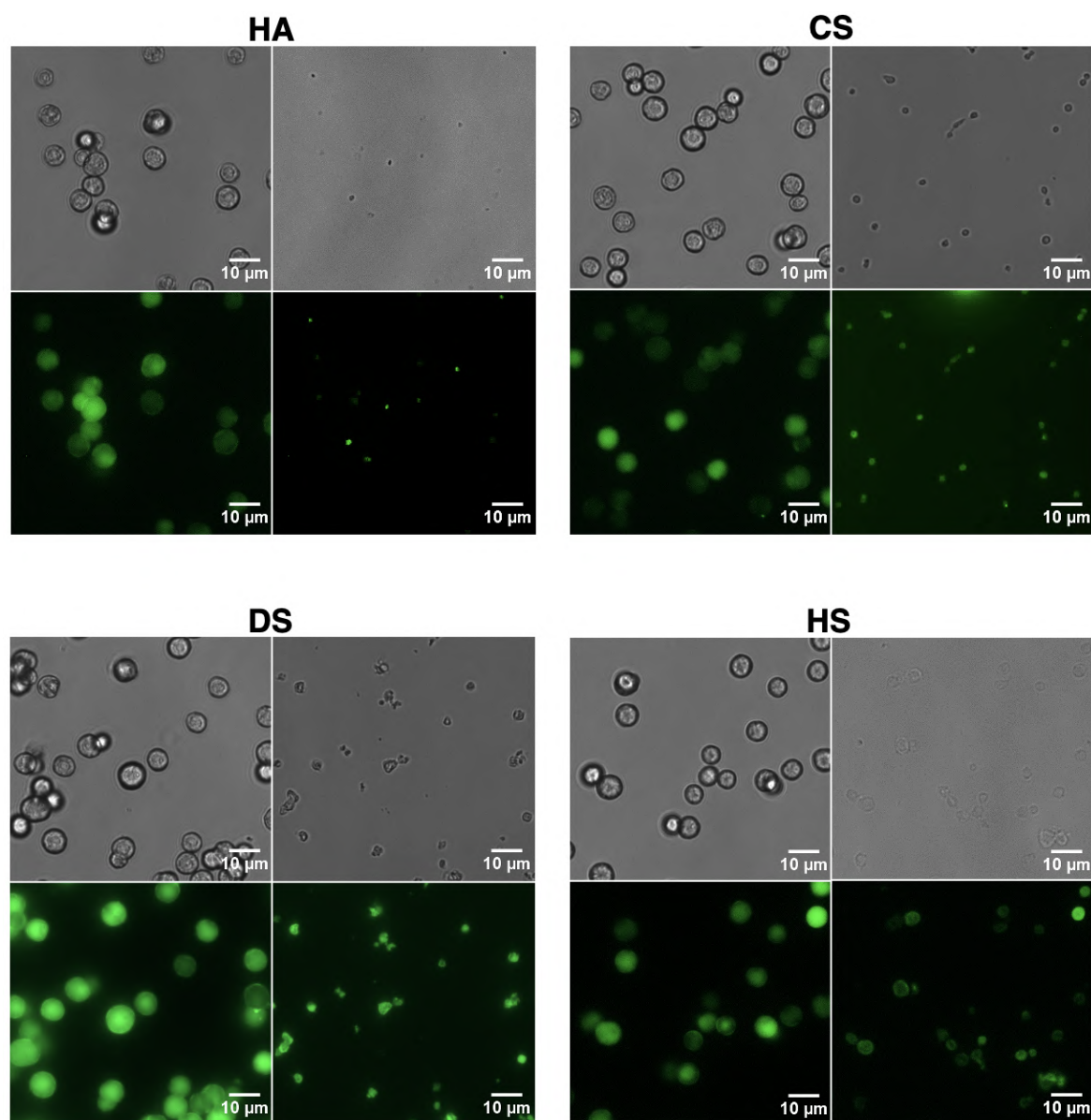
Figure 4.19: Typical optical transmittance (above) and fluorescence (below) images of (polyanion/PLL$^{\text{FITC}}$)$_{2.5}$ coated crystals (right) and resultant microgels (left). Images shown are for polyanions HA, CS, DS and HS. Scalebars are 10 μm.

To probe further, CLSM imaging of the microgels (Figure 4.20) revealed that the polymers remain within the lumen after the dissolution of the template and therefore occupy the interior instead of forming a thin shell. Such a matrix-type structure was common for all of the microgels probed here; however, the degree of the microgel "filling" with polyelectrolyte differed for the microgels of different compositions. Namely, it seems to decrease in a series of HA > CS > DS > HS. However, this may be an artificial trend that cannot be reliably attributed to the nature of biopolymers used. The possible

reason for the observed difference in the microgel "filling" is the insufficient resolution for smaller HA/PLL and CS/PLL microgels, which does not allow for the probing of their internal structure accurately. These possible optical effects restrict us from the deeper analysis of "filling" dependencies on the polymer composition. In the literature, biopolymer-based microgels prepared under similar conditions were more often denoted as hollow-type capsules [201, 209, 213]. Perhaps, to a large extent, this is a question of terminology and should be considered with care. For example, Figures 4.20 and 4.18 show that DS-based microgels maintain their core-shell structure; however, they still have a polymer matrix within the interior. In this particular case, the presence of the polymer matrix is obvious and cannot be neglected, and therefore, the microgels cannot be denoted as hollow. However, if the microgels contain less polymer inside, the presence of the polymer matrix is often ignored due to its insignificance [213]. The question of establishing a proper threshold of the degree of polymer "filling" between matrix- and hollow-type structures has been addressed in other studies [25]. Here, they are better defined as microgels.
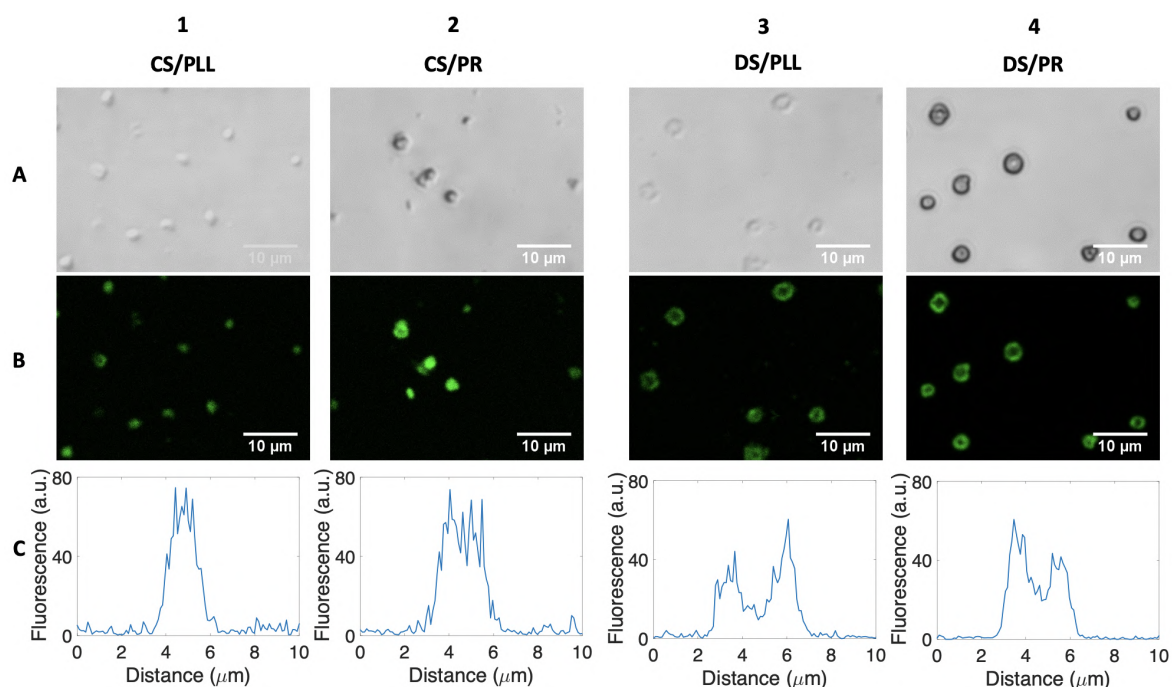
Figure 4.20: Typical CLSM images of (1) $(CS^{FITC}/PLL)_{2.5}$, (2) $(CS^{FITC}/PR)_{2.5}$, (3) $(DS^{FITC}/PLL)_{2.5}$, and (4) $(DS^{FITC}/PR)_{2.5}$ microgels. (A) Bright field, (B) fluorescence (excitation at 488 nm) images of microgels, and (C) corresponding linear fluorescence profiles taken across the centre of the microgels. Scalebars are 10 μm.

Effect of polymer molecular weight

Bearing in mind that the filling of the microgels with polymer matrices is important for their loading/release performance, next, it was attempted to find a way to control the internal structure of these microgels and investigate the effect of the polymer length on the microgel internal structure. For this, microgels have been fabricated using PLL with two different median molecular weights of 28 and 280 kDa (denoted as PLL_{28} and PLL_{280}, respectively), as previously determined by the HPLC system in a previous study [242]. Hydrodynamic diameters of PLL_{28} and PLL_{280} in the Tris buffer solution have been measured by DLS and found to be 3.9 ± 1.9 and 15.6 ± 7.6 nm, respectively. Both polymers have been conjugated with FITC for the probing of their distribution inside the microgels by means of CLSM imaging. Figure 4.21 shows confocal images of HS/PLL_{28} and HS/PLL_{280} microgels as a representative example. Despite the larger molecular size of PLL_{280}, its penetration into the large pores of vaterite crystals during polymer deposition leads to the formation of a polymer matrix, similar to that of smaller PLL_{28}, that is, both PLLs are evenly distributed throughout the entire volume of the microgels. Figure 4.22 also displays SEM images of PLL_{280}-based microgels; much akin to those microgels formed from PLL_{28}, there is an evident internal polymer matrix. This suggests that only altering the PLL length makes little difference to the internal structure of microgels when the polyanion remains constant.
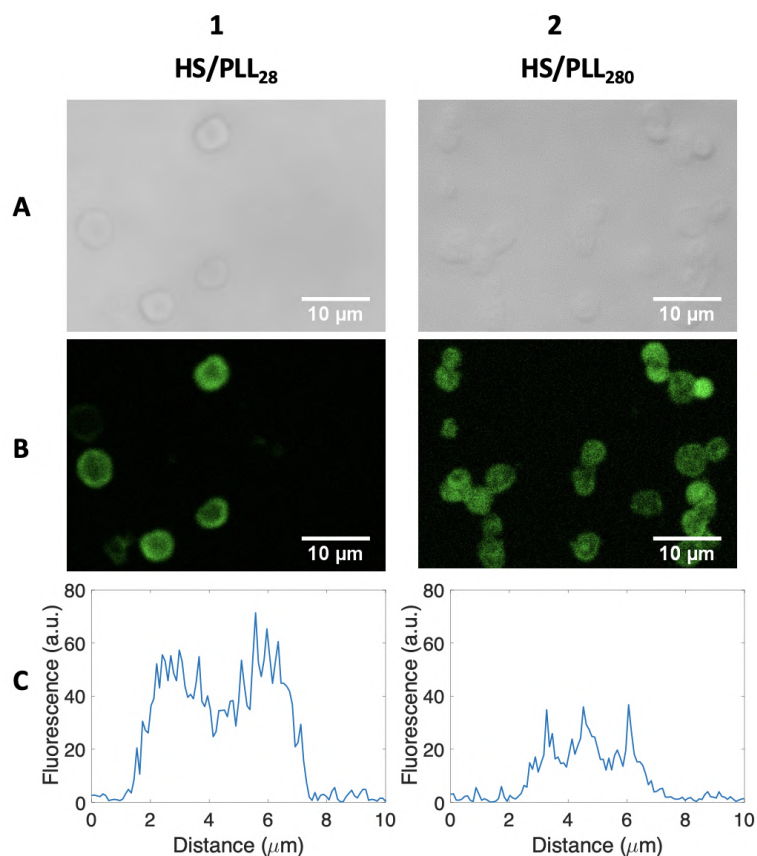
Figure 4.21: Typical CLSM images of HS/PLL$_{28}$$^{\mathrm{FITC}}$ and HS/PLL$_{280}$$^{\mathrm{FITC}}$ microgels: (A) bright field, (B) fluorescence (excitation at 488 nm) images of microgels, and (C) corresponding linear fluorescence profiles taken across the centre of the microgels. Scalebars are 10 μm.
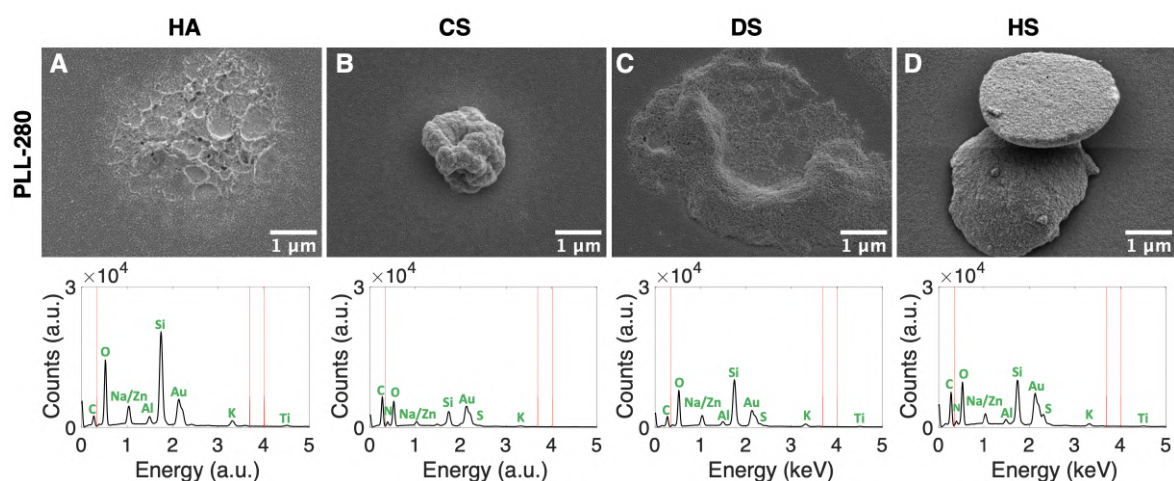
Figure 4.22: Typical SEM images of 10 nm gold-sputtered microgels consisting of 2.5 bilayers. PLL$_{280}$-based microgels consisting of HA, CS, DS, and HS are shown in images (A), (B), (C), and (D), respectively. Scale bars are 1 μm. Corresponding typical EDX spectra are shown beneath the respective SEM image - the red lines correspond to the characteristic energies of X-ray emission for calcium

Moreover, despite this little change in PLL distribution, following the formation of $(HS/PLL)_{2.5}$ microgels of the two PLL molecular weights they have been agitated at 800 rpm. $(HS/PLL_{28})_{2.5}$ were fragmented and disaggregated upon shaking, where $(HS/PLL_{280})_{2.5}$ remain stable and keep their spherical shape, according to optical microscopy (Figure 4.23). Indeed, reducing this agitation speed to 400 rpm resulted in more stable $(HS/PLL_{28})_{2.5}$ microgels. This resistance is likely due to the longer chain length of PLL_{280}, which acts to provide more integrity to microgel structure. Such sensitivity to agitation may be of great interest in terms of ultrasound-mediated release from such short-chained microgels.
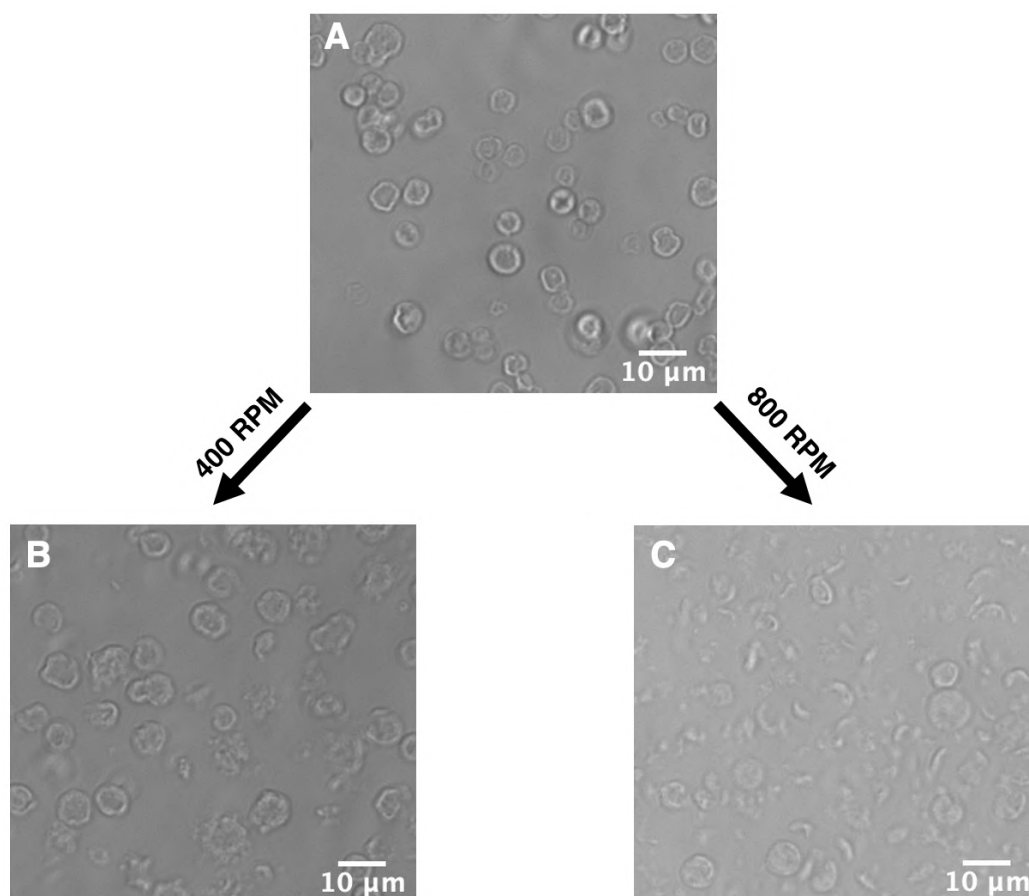
Figure 4.23: Transmittance images of $(HS/PLL_{28})_{2.5}$ microgels freshly formed (A), followed by agitation at (B) 400 and (C) 800 rpm. Scalebars are 10 μm.

4.3.5 Shrinkage of microgels

The elimination of the vaterite template resulted in the reorganisation of the polymer matrices, resulting in the reduction of final microgel sizes; the factors of which affect this phenomenon will be discussed below.

Effect of polyelectrolyte charge density

The degree of shrinkage was dependent on the type of the polymer used; a clear trend of increasing degrees of shrinkage was observed following a series of DS $\simeq$ HS < CS < HA. Interestingly, it can be correlated with the increasing number of charged groups per polyanion monomer (Figure 4.24). At the same time, despite the lower charge density, PR-based microgels are prone to a higher degree of shrinkage than PLL-based microgels. This may be associated with lower diffusivity and the larger number of polyion contacts of highly charged PLL with the polyanions, which leads to the reduced and slower PLL molecular and chain dynamics during the elimination of the core and consequently results in a lower degree of shrinkage.
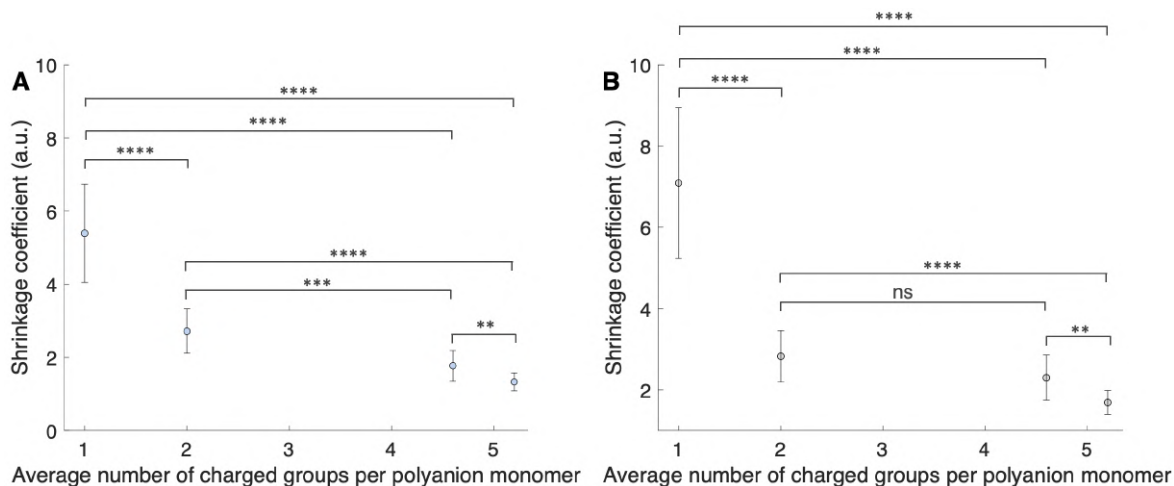
Figure 4.24: Effect of the number of charged groups within the polyanion monomer unit upon the shrinkage coefficient of (A) PLL$_{28}$- and (B) PR-based microgels following CaCO$_3$ dissolution at 50 mM EDTA. Error bars are SD, n=100. Statistical analysis made using one-way ANOVA test; ns: non-significant difference, $**p<0.001$, $***p<0.0005$, and $****p<0.0001$.

Effect of polyelectrolyte molecular weight

The shrinkage behaviour of PLL_{28}- and PLL_{280}-based microgels has been compared. It was found that, similarly to PLL_{28}, the degree of the shrinkage of PLL_{280}-based microgels decreases with the increase of the number of charged groups on the polyanion. Simultaneously, increasing the PLL length significantly decreases the shrinkage coefficients of such systems (Figure 4.25). This effect is more pronounced for HA/PLL microgels, creating twice the difference in the shrinkage of these microgels. The lower degree of the shrinkage in PLL_{280}-based microgels may be attributed to lower diffusivity and dynamics of PLL_{280} molecules, which results in reduced polymer reorganisation during the dissolution of the vaterite template. This provides a simple approach to control the degree of microgel shrinkage, which is important for their utilisation as vectors for drug delivery.
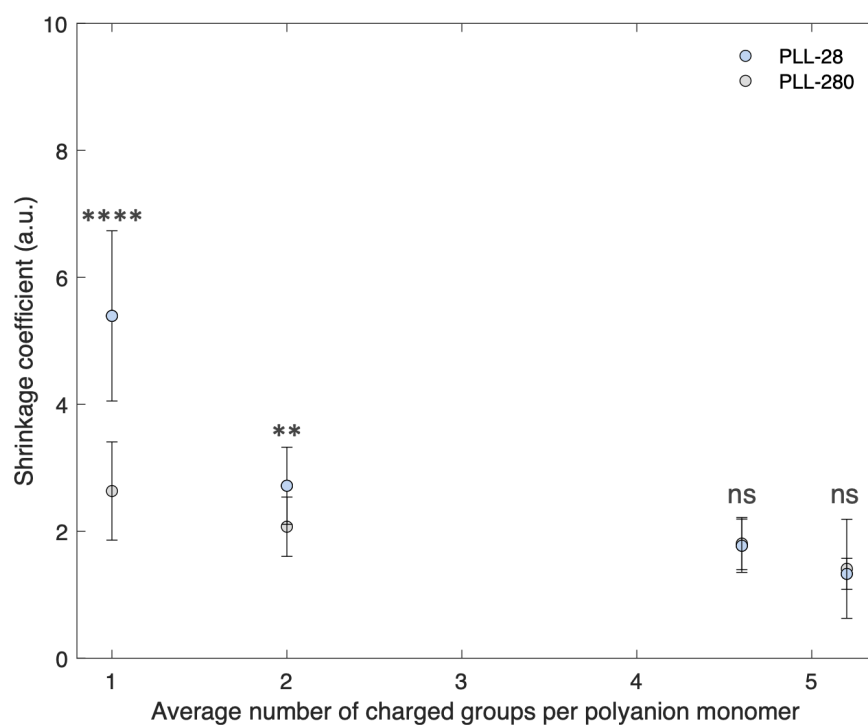
Figure 4.25: Effect of the number of charged groups within the polyanion monomer unit upon the shrinkage coefficient of PLL_{28}- and PLL_{280}-based microgels following $CaCO_3$ dissolution at 50 mM EDTA. Error bars are SD, n=100. Statistical analysis made using one-way ANOVA test; ns: non-significant difference, $**p<0.001$, and $****p<0.0001$. Comparison was made using the same polyanion and the two PLL molecular weights.

Interestingly, when both the molecular weight of the polyanion and polycation are in-

creased, there is a pronounced effect on the shrinkage of such microgels. Here, two microgel systems are compared: $(HA_{50}/PLL_{28})_{2.5}$ and $(HA_{1500}/PLL_{280})_{2.5}$, denoted as short-chained (S-S) and long-chained (L-L) throughout this thesis. The shrinkage dynamics of both L-L and S-S microgel systems were investigated as a function of EDTA concentration, as shown in Figure 4.26. Both the kinetics of microgel shrinkage and $CaCO_3$ dissolution were evaluated during a 60 second time period, and both occur simultaneously and on a similar time scale. Moreover, the extent of shrinkage increases with increasing EDTA concentration for S-S microgels (Figure 4.27). This can be explained via the increase in local ionic strength upon the addition EDTA; the counter ions brought into the system via EDTA (i.e. Ca^{2+} and CO_3^{2-}) screen the charges along the polyelectrolyte backbone (extrinsic compensation), which provides higher segment mobility within the polymer network. This allows for annealing of the network, the closure of voids and the release of water, resulting in the shrinkage observed. Increasing the EDTA concentration gives in a higher local flux of ions resulting from the faster dissolution of the vaterite matrix, which may play a role in the higher extent of shrinkage at higher EDTA concentrations. Indeed, the shrinkage of capsules has been previously related to increase in the ionic strength of the system [332].
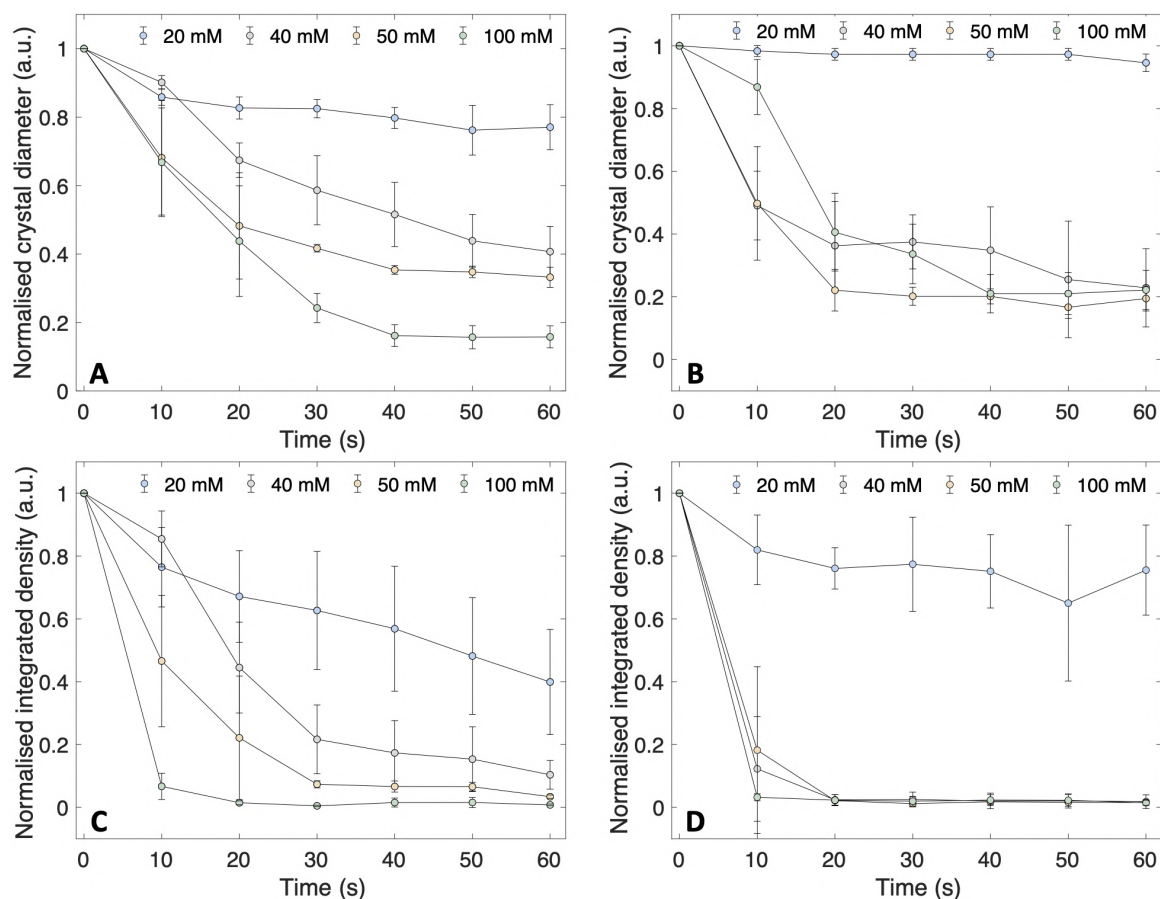
Figure 4.26: Normalised CaCO$_3$ crystal diameter (A and B) and integrated density (i.e. CaCO$_3$ dissolution) (C and D) for S-S (A and C) and L-L multilayers (B and D).
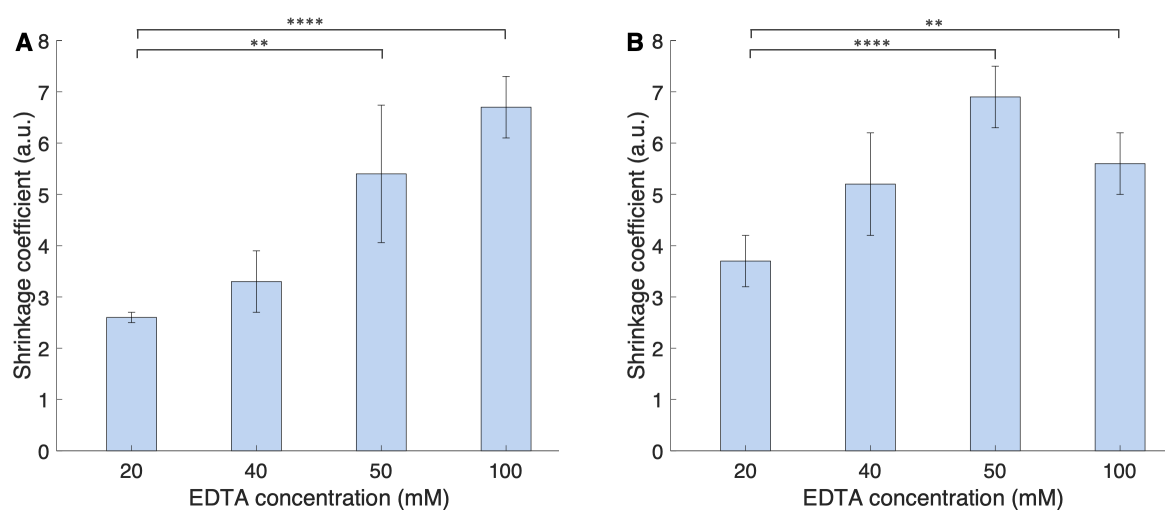
Figure 4.27: Shrinkage coefficient of (A) S-S and (B) L-L microgels as a function of EDTA concentration. Error bars are SD, n=5. Statistical analysis made using one-way ANOVA test; $**p<0.001$ and $****p<0.0001$.

When utilising L-L polyelectrolytes, the shrinkage of the resultant microgels is greater

than that of S-S microgels (SCs of 5.2 ± 2.0 and 3.2 ± 0.6 for L-L and S-S microgels, respectively). This difference in shrinkage can be explained via the extent of polyelectrolyte matrix formation within the pores of the vaterite crystal. Long-chained polymers (i.e. L-L) are not able to permeate the vaterite porous matrix, and hence, form more of a core-shell structure, where short-chained polymers (i.e. S-S) are, and can form a gel-like internal matrix of polyelectrolyte complex. CLSM has confirmed this, via probing of the internal structure of such L-L and S-S coated $CaCO_3$ crystals, as shown in Figure 4.28. This internal polyelectrolyte matrix acts to supress the complete collapse of the microgel structure and gives rise to the gel-like interpolylectrolyte structures observed. Typical SEM images of the lyophilised L-L and S-S microgels are shown in Figure 4.28, where no calcium was detected within the microgel structures, indicating all $CaCO_3$ has undergone dissolution from both structures and plays no role in their final shrunken state.
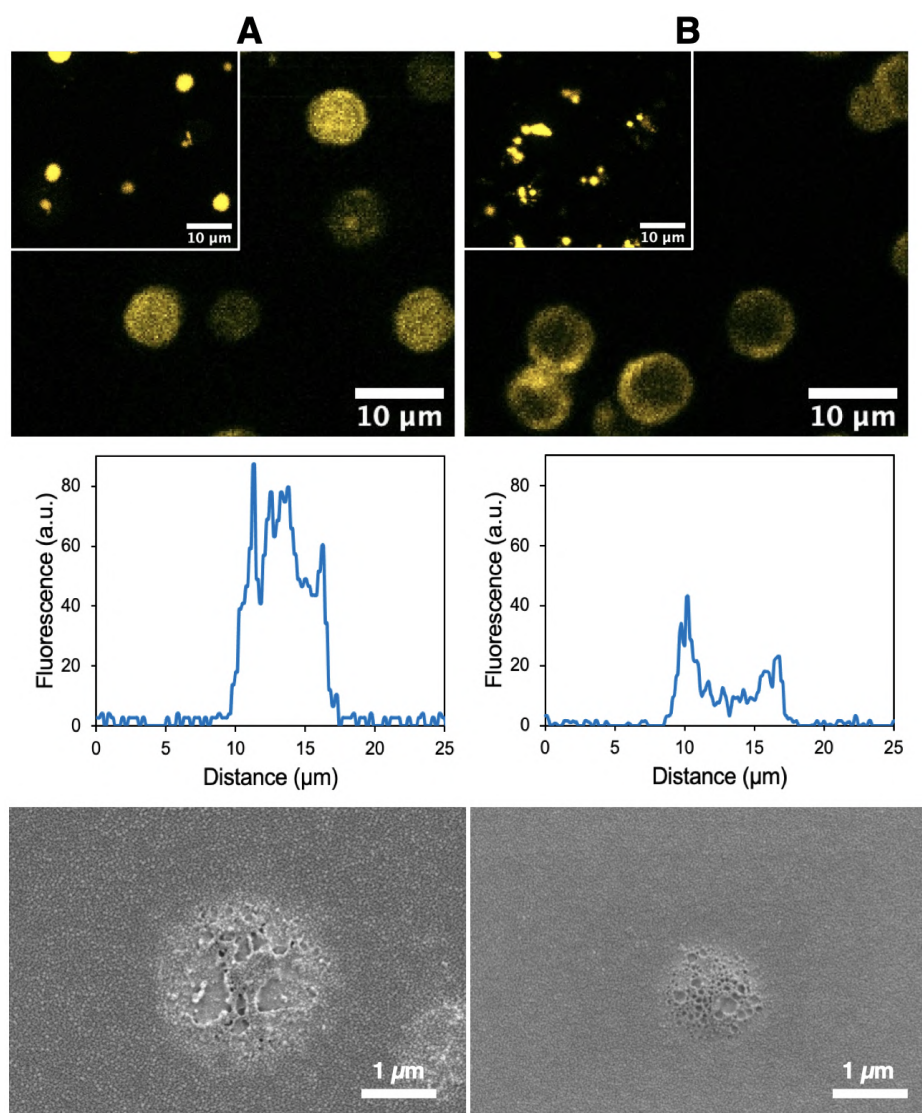
Figure 4.28: Typical CLSM images of $(HA/PLL)_{2.5}$-coated $CaCO_3$ crystals (microgels following $CaCO_3$ dissolution in the insets), typical fluorescence profile of a $(HA/PLL)_{2.5}$-coated $CaCO_3$ crystal, and SEM image of a microgel following $CaCO_3$ crystal dissolution. (A) S-S and (B) L-L microgels. Scalebars are 10 μm for CLSM images and 1 μm for SEM images.

Effect of the number of polyelectrolyte layers

Another way to control the shrinkage of such HA/PLL S-S microgels is to vary the number of layers applied during the LbL deposition process. Here, whilst keeping the size of the vaterite crystals consistent ($\sim$7 μm), the number of layers was varied from 2 to 9 layers before washing and dissolution of the vaterite matrix with EDTA as previously. It was found the shrinkage of S-S microgels decreases with increasing number of

deposition steps, until a plateau is reached at 7 layers i.e. at $(HA/PLL)_{3.5}$ (Figure 4.29). This also supports the aforementioned hypothesis of the shrinkage being predominately controlled by vaterite pore occupation in the case of the HA/PLL system, as, with the increasing number of deposition steps, there is increased filling of the vaterite crystal pores with polymer, and hence a more well-defined polyelectrolyte matrix to suppress the shrinkage. Indeed, this is an effective way to control the microgel shrinkage, as this can range from SCs of 6.5 ± 1.0 to 2.0 ± 0.3 for $(HA/PLL)_1$ and $(HA/PLL)_{4.5}$, respectively.
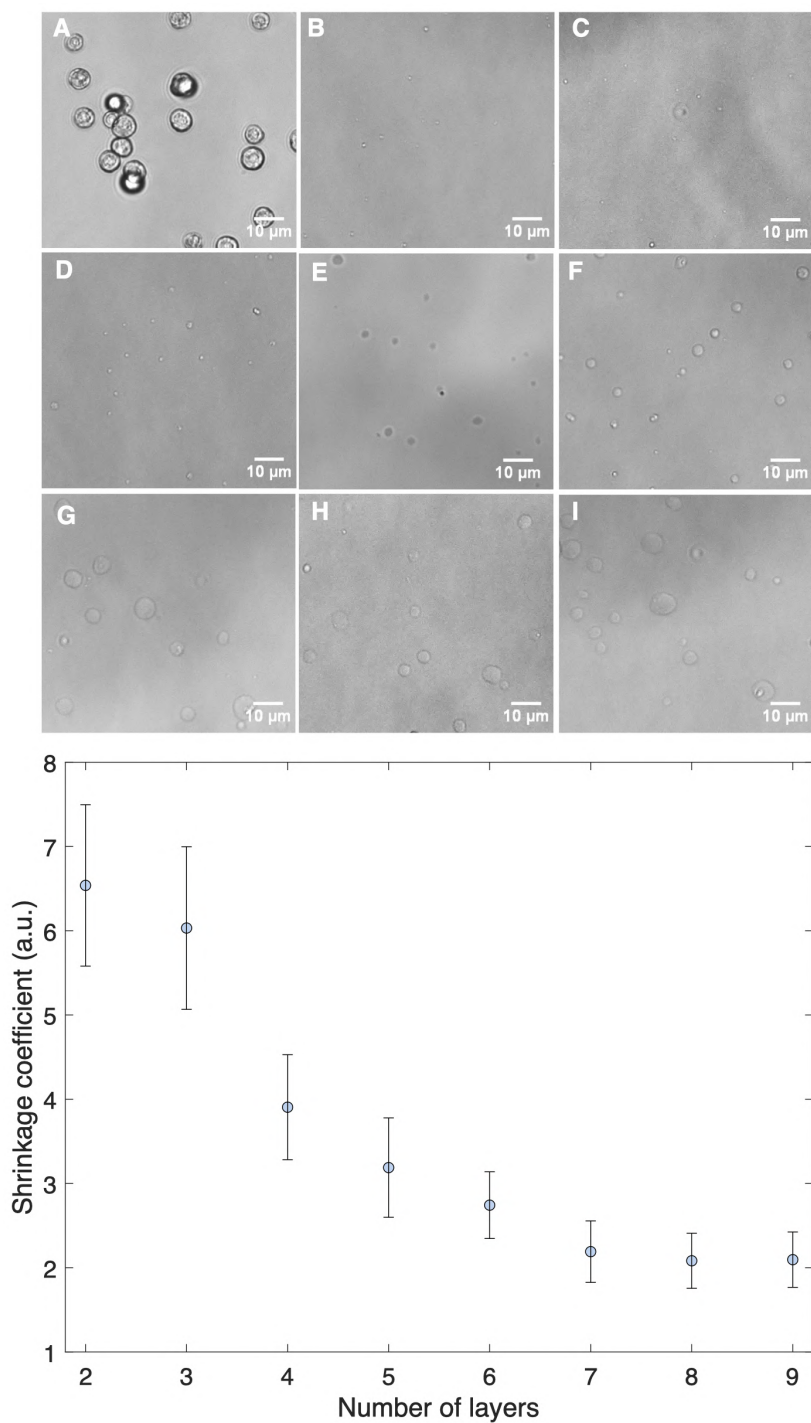
Figure 4.29: A graph depicting the shrinkage coefficient of HA/PLL$_{28}$ microgels as a function of the number of layers. Error bars are SD, n=100. Transmittance images of (A) typical (HA/PLL$_{28}$)-coated CaCO$_3$ crystals and microgels formed formed from (B) 2, (C) 3, (D) 4, (E) 5, (F) 6, (G) 7, (H) 8 and (I) 9 layers. Scalebars are 10 μm.

Effect of CaCO₃ crystal size

The ability to change the size of the vaterite crystal template whilst retaining the same established shrinkage properties is important with regards to the ability to produce microgels of a plethora of sizes, ranging from the sub-micron region to tens of microns. Indeed, $(HA/PLL_{28})_{2.5}$, $(HA/PLL_{280})_{2.5}$ and $(HS/PLL_{280})_{2.5}$ microgels have successfully formed from crystal sizes of ca. 4, 8 and 15 μm vaterite crystals; the SCs of which did not vary significantly with the crystal size, as illustrated in Figure 4.30. Typical fluorescence profiles are illustrated in Figure 4.31, as shown, PLL^{FITC} is able to permeate the entire crystal volume in all cases.
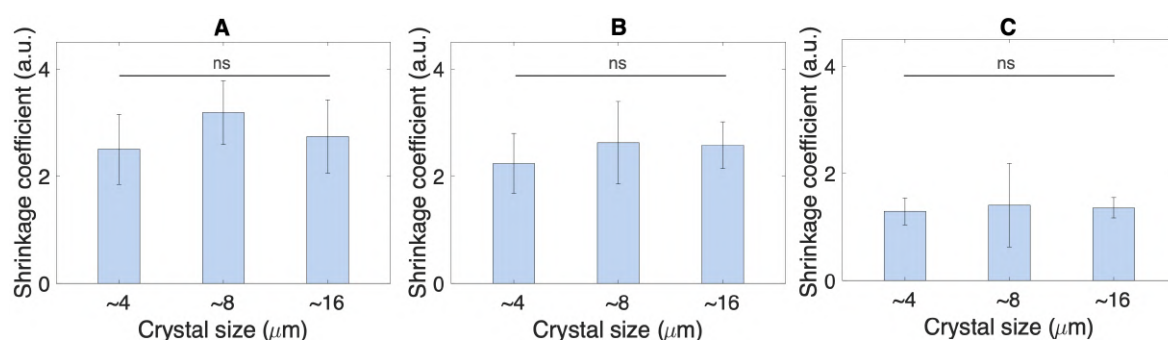
Figure 4.30: Graphs demonstrating the shrinkage coefficient of (A) $(HA/PLL_{28})_{2.5}$, (B) $(HA/PLL_{280})_{2.5}$ and (C) $(HS/PLL_{280})_{2.5}$ microgels as a function of CaCO₃ crystal size. Error bars are SD, n=50. Statistical analysis made using one-way ANOVA test; ns: non-significant difference.
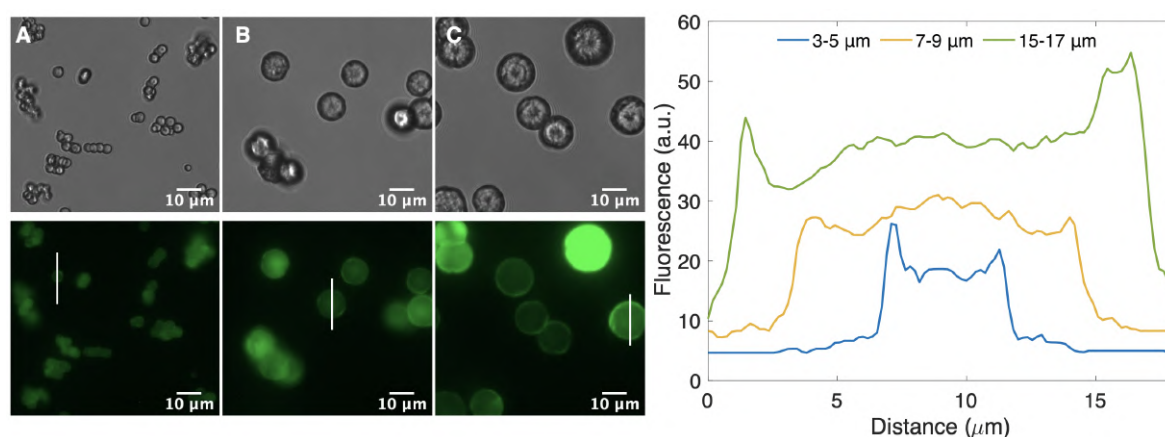
Figure 4.31: Transmittance and fluorescence images (left) of $(HA/PLL_{28})_{2.5}$-coated (A) 3-5, (B) 7-9 and (C) 15-17 μm CaCO₃ crystals. Scalebars are 10 μm. Typical fluorescence profiles of these coated crystals (right).

Effect of temperature

Heat-induced shrinkage is something well-established within the literature, namely with the DS/pARG capsule pair [235]. This process is performed via the heating of the capsule/microgel suspension, resulting in improved polymer mobility, and hence the annealing of the multilayers and subsequent shrinkage of the structure. HA/PLL-based microgels were cooled/heated to temperatures of 4, 25, 37 or 80°C for 60 mins. There was no observable change in the microgel size at any of these temperatures. Here, HA and PLL_{28} are likely already in their preferred polymer conformation following increases in polyelectrolyte fluidity following increase in ionic strength upon $CaCO_3$ dissolution, resulting in no shrinkage. This indicates the high extent of polymer annealing already performed at room temperature. Moreover, this inherent stability at a range of temperatures bodes well for the storage of potential encapsulated bioactives.

Interestingly both HS/PLL_{28}- and HS/PLL_{280}-based microgels display a shrinkage behaviour with increasing temperature. This is reported for the first time here, but such thermoshrinkage has been reported previously for DS/pARG capsules [234, 235]. Both microgel sets were heated from 25°C to 90°C in increments of 10°C from 30°C onward; images were taken at 20, 40 and 60 mins. There was no significant difference between PLL_{28}- or PLL_{280}-based microgels (Figure 4.32), with $59 \pm 10\%$ and $51 \pm 10\%$ reduction in diameter at 60 mins at 90°C from the initial coated vaterite crystal size, respectively. Furthermore, there was no observable difference in % shrinkage for microgels formed from ca. 4, 8 or 15 μm vaterite crystals, with percentages of $48 \pm 13\%$, $51 \pm 10\%$ and $54 \pm 9\%$, respectively (90°C for 60 mins), as depicted in Figure 4.33. Of note, shrunken microgels can retain their size for up to at least 6 months, regardless of the initial crystal size. Figure 4.34 depicts the microgels after 6 months incubation at 4°C. Again, these results imply the tight control over this shrinkage phenomenon possible; with HS/PLL microgels presenting themselves as a novel standard for microgel/capsule research work, as well as malleable drug delivery vehicles for a variety of applications.
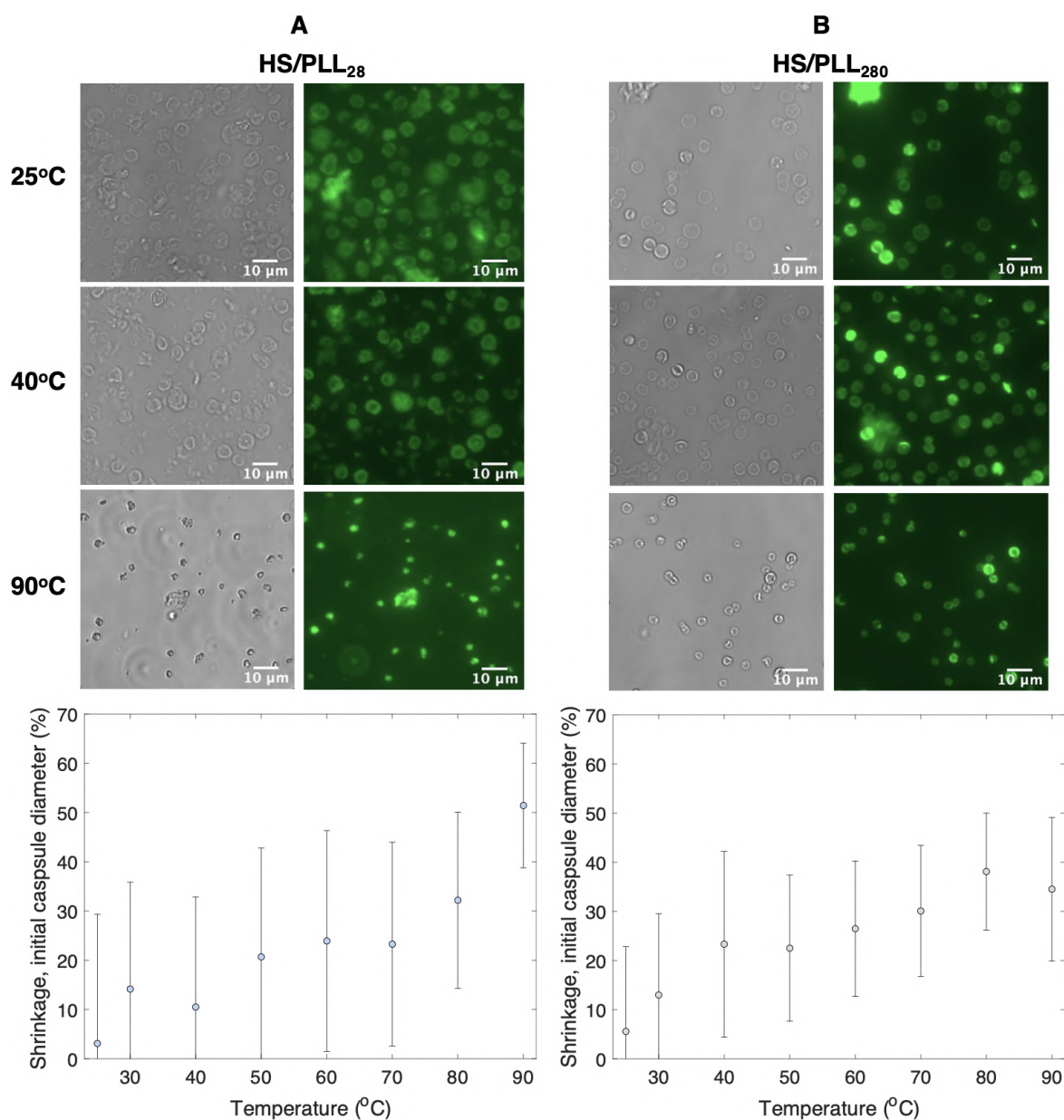
Figure 4.32: Transmittance and fluorescence images of (A) $(HS/PLL_{28})_{2.5}$ and (B) $(HS/PLL_{280})_{2.5}$ microgels after incubation at 25, 40 and 90°C for 60 mins. Scalebars are 10 μm. The % shrinkage of HS/PLL_{28} and HS/PLL_{280} microgels as a function of temperature. Error bars are SD, n=100.
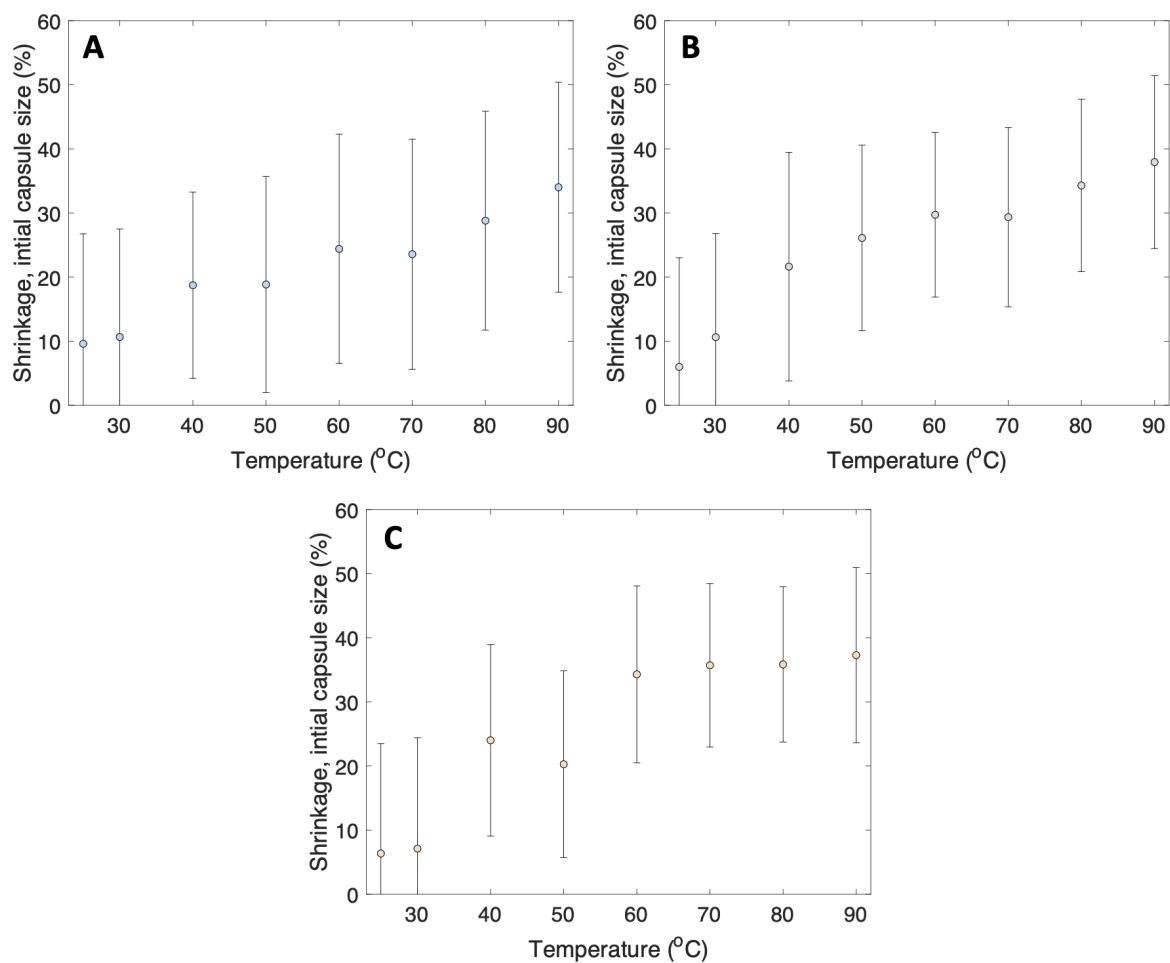
Figure 4.33: The % shrinkage of HS/PLL$_{280}$ microgels as a function of temperature for crystal sizes of $\sim$ (A) 4, (B) 8 and (C) 16 μm. Error bars are SD, n=100.
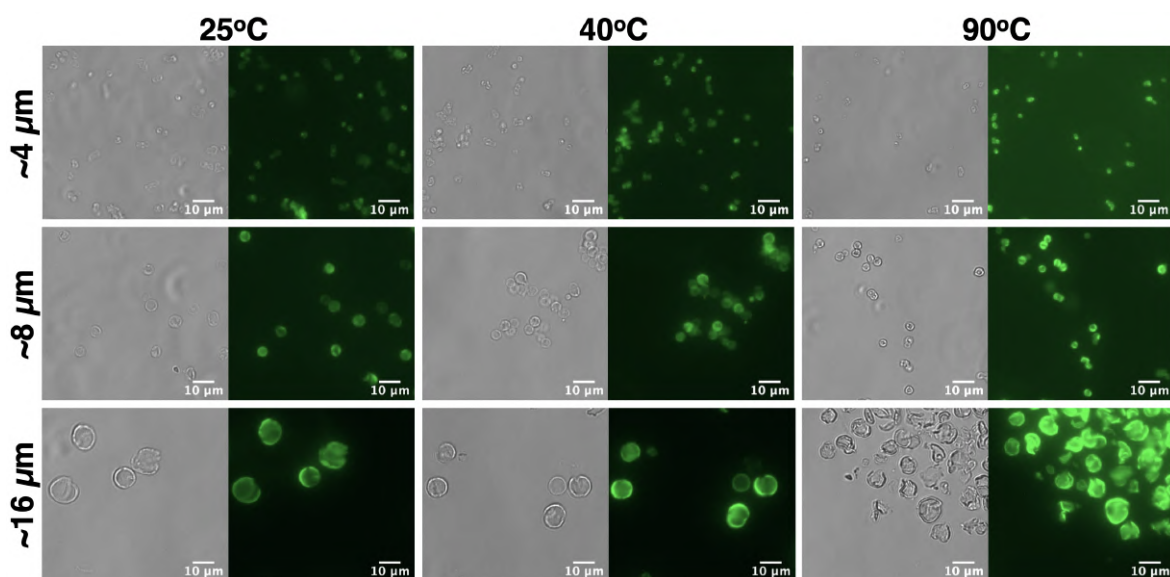
Figure 4.34: Transmittance and fluorescence images of (HS/PLL$_{280}$)$_{2.5}$ microgels formed from crystal sizes of $\sim$4, 8 and 16 μm after 60 min incubation at 25, 40 and 90°C. Images shown are following 6 months storage 4°C. Scalebars are 10 μm.

4.3.6 Microgel adhesion

Upon the shrinkage of these microgels, they adhere to the surface upon which they are formed. PLL-based microgels display a trend in adhesion of HA > CS > DS > HS, where HS possesses an adherence of 0%. Simultaneously, however, PR-based microgels display no trend in adherence, with all microgels being ∼100% adherent. In order to better understand this phenomenon, PLL- and PR-based microgels have also been prepared on the surfaces of other types: polystyrene-, ibidi-hydrophobic- and ibidi-hydrophilic-coated wells (Figure 4.35). The type of the surface coating did not affect the adherence of both PLL- and PR-based microgels; this may indicate the pivotal role of the hydrophobicity of the microgels on their adhesion. This is also supported by the decrease of the adhesion of PLL-based microgels with the decrease of their shrinkage coefficient and, consequently, increase of their water content. However, no similar trend was observed for PR-based microgels: their adherence was close to 100% even for the PR/HS biopolyelectrolyte pair, and no correlation between microgel adhesion and degree of microgel shrinkage was observed (Figure 4.35). This may be associated with the globular structure, compact size, and protein nature of PR that may undergo conformational changes upon interaction with polyanions and upon microgel adsorption to the respective surface, which introduces new interactions into the system. In addition, the microgels formed by DS displayed significantly lower adherence to the polystyrene surface when compared to other substrates as well as other polyelectrolytes. Further, HA/PLL$_{28}$ microgels have also shown ∼100% adhesion to gold-coated and cold atmospheric plasma-treated surfaces, which are highly hydrophilic surfaces (water contact angles of ∼10°), as shown in Figure 4.36 These findings may be important for alternate applications such as micropatterning of surfaces and the decoration of implants with functional microgels. To better understand the mechanism of adhesion and, perhaps produce these microgels as free-standing structures suitable for *in ovo* drug delivery, HA/PLL-based microgels will become the focus and their adhesive properties will be discussed further in the next section.
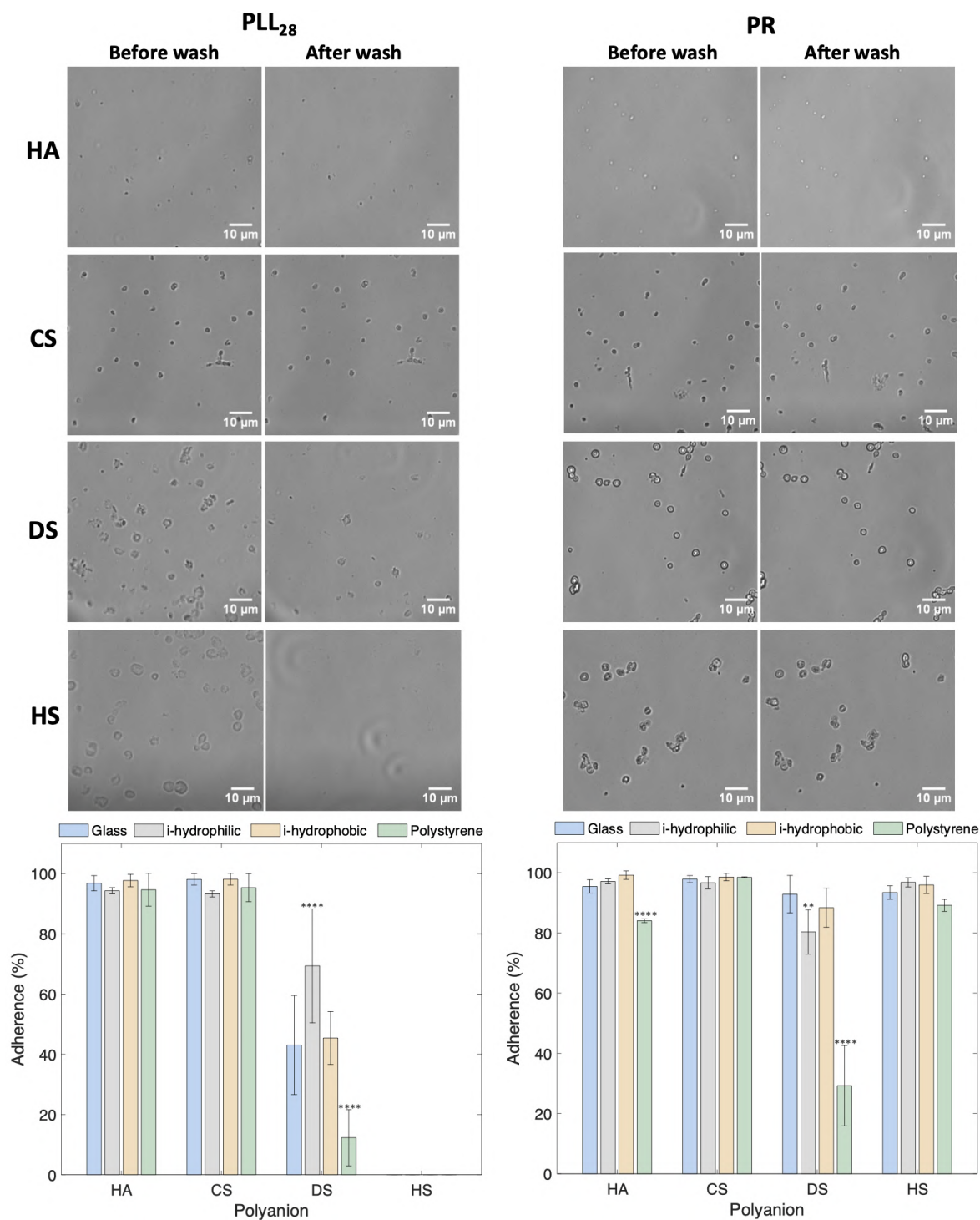
Figure 4.35: Transmittance images of PLL$_{28}$- and PR-based microgels formed on a glass coverslip before (left) and after (right) washing. Scalebars are 10 μm. Below are graphs displaying the % adherence of PLL$_{28}$- and PR-based microgels as a function of the polyanion upon various surfaces (glass, ibidi- hydrophobic and hydrophilic coatings and polystyrene). Error bars are SD, n = at least 30. Statistical analysis made using one-way ANOVA test; $**p<0.001$ and $****p<0.0001$. Comparison was made to the adherence of the microgels upon glass for the respective polyanion.
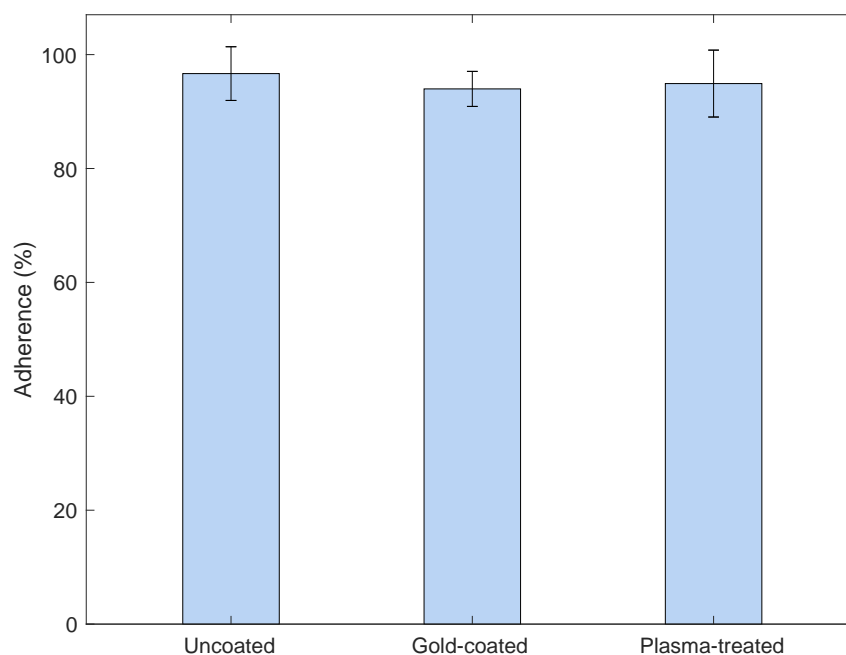
Figure 4.36: Adherence of $(HA/PLL_{28})_{2.5}$ upon functionalised surfaces (uncoated, gold-coated and cold atmospheric plasma-treated surfaces). Error bars are SD, n=3.

Effect of microgel polyelectrolyte composition

As aforementioned, HA/PLL microgels display a superior adhesion phenomenon post-shrinkage on varying surfaces, including glass, standard polystyrene cell culture plates and both hydrophobic and hydrophilic ibidi wells. To investigate how the polymer composition of the microgels plays a role in the microgel adhesion and final properties HS was selected as a microgel doping and capping agent, of which has been previously used in the build-up of polymer multilayers and LbL structures [138, 211]. As aforementioned, HS/PLL microgels are non-adhesive and display significantly less shrinkage when compared to HA/PLL microgels, which are more gel-like. This provides us with the opportunity to compare two oppositely behaving systems by just alternating one polymer. During the LbL deposition process, the HA solution has been doped with HS at varying concentrations, followed by the formation of microgels via addition of EDTA. From just 0.5% HS content in the HA solution, the shrinkage of the microgels is significantly affected (Figure 4.37), with a SC similar to that of 100% HS (SCs of 1.75

± 0.36 and 1.33 ± 0.24, respectively). Despite this, they adhere to the surface after washing and remain intact, as confirmed via optical microscopy. Upon increasing the HS content to 1% the microgels remain adherent, however, upon washing with TRIS buffer the remaining microgels are damaged and are abnormal in their structure. This suggests pure HA/PLL microgels are of a higher integrity compared to HS/PLL microgels, likely explained via the larger extent of polymer annealing and complexation they undergo upon template removal, forming a more-tightly knit interpolyelectrolyte internal matrix. Replacement of the HA layer with HS during the deposition sequence results in HS/PLL-like microgels regardless of when the HS layer was deposited, as shown in Figure 4.38. This may be due to the preferential binding of HS-PLL complex compared to the HA-PLL complex [333], hence the majority of HA in the $CaCO_3$ pores has been displaced with HS. Adhesion is not even observed for $(HS/PLL)_1(HA/PLL)_{1.5}$ microgels where HS was the first deposited layer, as the resultant microgels behave as HS/PLL-like. This suggests the polymers are not deposited in a linear fashion, but instead deposit in the crystal pores and on the surface in a non-linear regime, as is typical for multilayers formed of biopolymers due to their liable structure. If deposited in a linear fashion, HS would be present as a single "layer", and not diffuse through the entire structure. Such capping approaches have been previously seen for the capping of dextran sulphate and protamine capsules with bovine serum albumin [206] or chitosan-folic acid [334] in order to prevent aggregation or increase mucoadhesive properties, respectively. Despite this, PLL remains distributed throughout the volume of the microgels, however this is may be explained through the excess of PLL in such systems regardless of the polyanion [333].
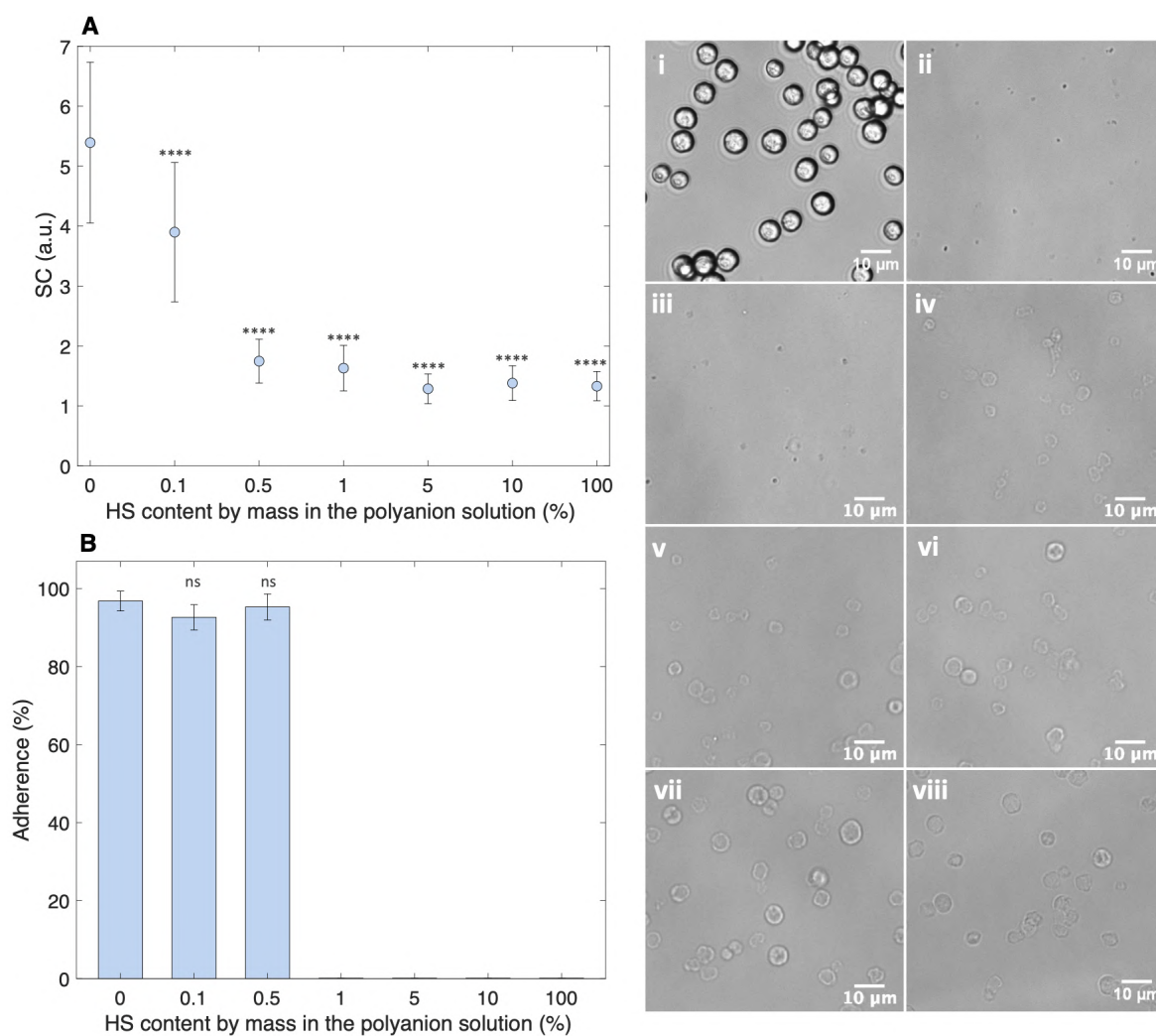
Figure 4.37: Transmittance images of $CaCO_3$ crystals (i) used here, and $(HA/PLL)_{2.5}$ microgels formed from HA doped with varying mass percentages of HS: 0% (ii), 0.1% (iii), 0.5% (iv), 1% (v), 5% (vi), 10% (vii), and 100% (viii). Scalebars are 10 μm. (A) The effect of HS doping percentage upon the microgel shrinkage coefficient and (B) microgel adhesion is shown. Error bars are SD, (A) n=100 and (B) n=3. Statistical analysis made using one-way ANOVA test; ns: non-significant difference and ∗∗∗∗p<0.0001. Comparison was made to the control sample (first experimental point on each graph).
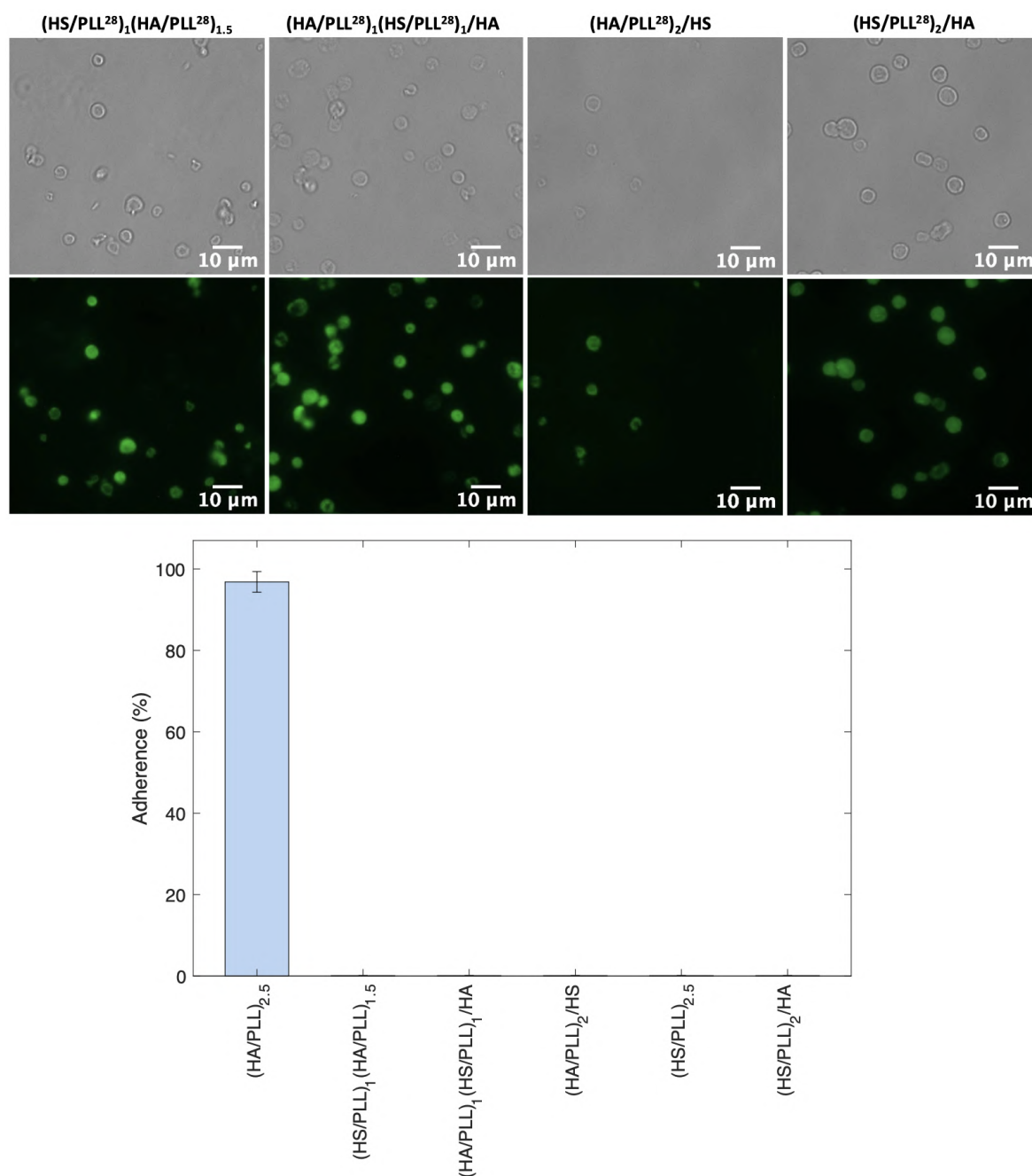
Figure 4.38: Transmittance images and their respective fluorescent images (below) of the displacement of HA layers with HS in $(\text{HA/PLL}^{\text{FITC}})_{2.5}$ microgels, and the displacement of the final layer of $(\text{HS/PLL}^{\text{FITC}})_{2.5}$ with HA. Scalebars are 10 μm. A graph illustrating the adhesion of microgels after the displacement of HA with HS at different stages of the LbL deposition. Error bars are SD, n=3.

Effect of microgel size

The effect of the number of polyelectrolyte deposition steps was investigated (from 2 to 9 steps). It is worth noting here that the terminating layer of multilayer microgel or

capsule systems can influence their final properties, such as their charge or shrinkage [233, 335], for instance. However, here, varying deposition steps had no effect on the adhesive properties (Figure 4.39) of resultant microgels, implying the HA/PLL microgel polymer content and size have little role in this phenomenon. Of note, HA/PLL microgels formed from 3-5 μm (SC = 2.50 $\pm$ 0.65) and 15-17 μm (SC = 2.74 $\pm$ 0.69) $CaCO_3$ crystals remain adhesive regardless of their size (Figure 4.39).
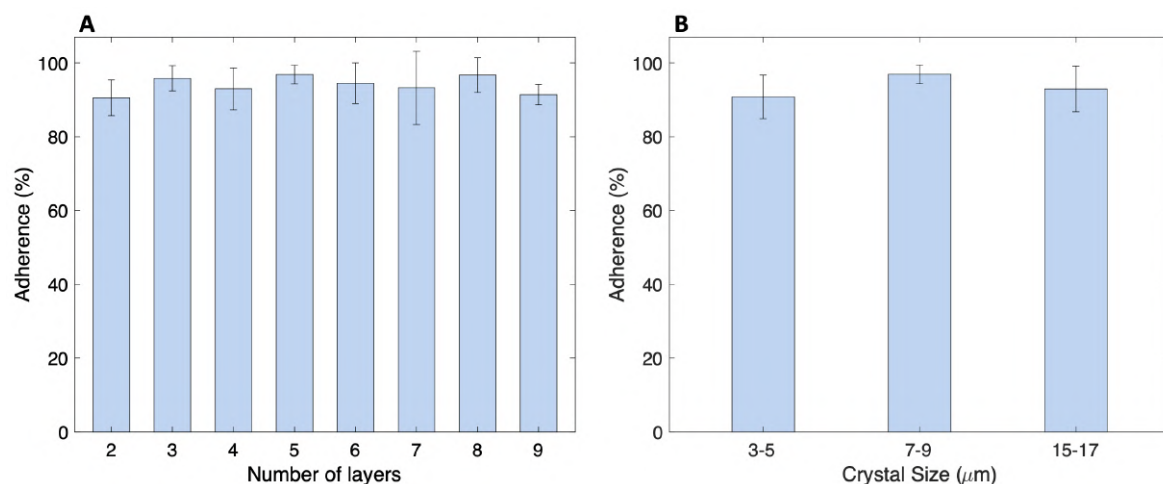
Figure 4.39: Adhesion of $(HA/PLL_{28})_{2.5}$ as a function of (A) number of layers and (B) $CaCO_3$ crystal size. Error bars are SD, n=3.

Effect of ionic strength

Increasing the ionic strength of the surrounding medium also had little effect on the microgel adhesion, as observed in Figure 4.40. The increase in the number of counter ions should effectively screen the charges on the polyelectrolyte backbones at the surface, which did not occur here, suggesting charge does not play a significant role in the adhesive properties of such gels. Furthermore, the size of microgels remained unaffected during the increase in ionic strength as was demonstrated with HA/PLL microgels as well as CS/PLL and CS/PR microgels, even after 72 hours in 1 M NaCl (Figure 4.41); this is contrary to literature findings in which salt concentration greatly influences the swellability, shrinkage and stability of such multilayer structures [99, 336]. It is likely here that, due to the large extent of shrinkage and polymer annealing, the local counter ion concentration within the microgels is exceedingly high and they remain unaffected

by changes in environmental ionic strength within the range investigated (0.027 M to 1 M NaCl).
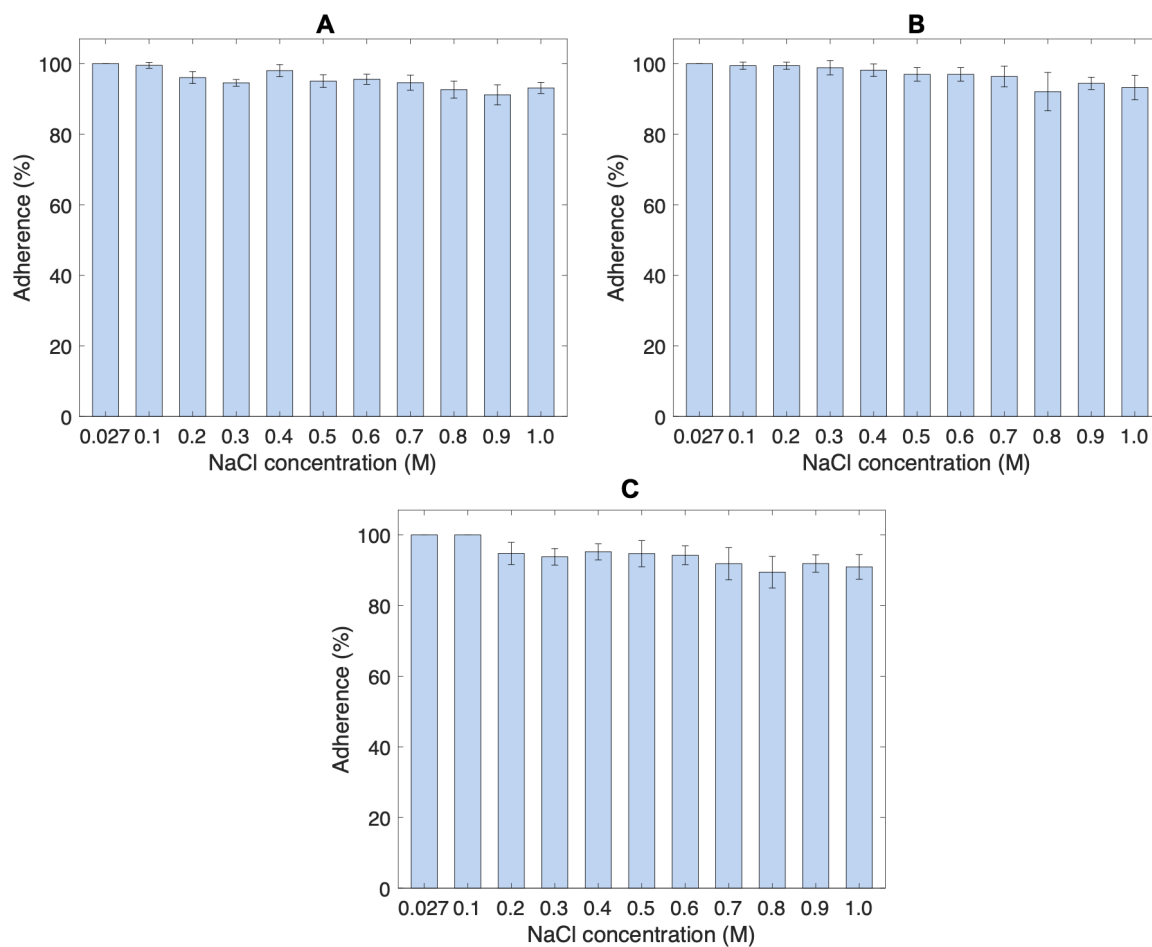
Figure 4.40: The adhesion of (A) $(HA/PLL_{28})_{2.5}$, (B) $(CS/PLL_{28})_{2.5}$, and (C) $(CS/PR_{28})_{2.5}$ microgels after each stepwise increase in NaCl concentration. A wash was performed after a 30-minute incubation period at each NaCl concentration. Error bars are SD, n=3.
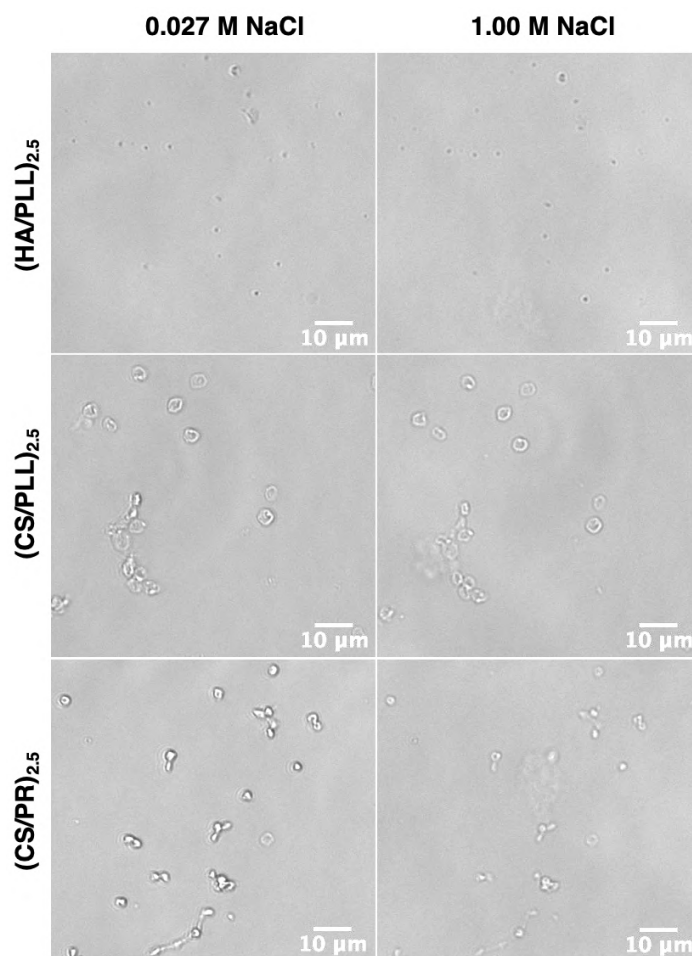
Figure 4.41: Transmittance images of $(HA/PLL_{28})_{2.5}$, $(CS/PLL_{28})_{2.5}$, and $(CS/PR_{28})_{2.5}$ microgels at 0.027 M NaCl (left) and 1.00 M NaCl (right), following 72 hours in 1.00 M NaCl and a washing step. Scalebars are 10 μm.

Effect of temperature

Alterations in temperature also had no effect on HA/PLL microgel adhesion within the range of 4°C to 80°C (Figure 4.42). Of note, HA/PLL microgels subjected to freezing at -20°C also remained adhered (85% adherence) following thawing to room temperature and washing with Tris buffer solution, similar was observed following their drying and re-hydration at room temperature (97% adherence). Autoclaving (15 mins at 120°C, 1.37 bar) of HA/PLL microgels when in the wet state also had no effect on their adhesion, this however, despite the lack of detachment, is beneficial for the sterilisation of such structures (Figure 4.42).
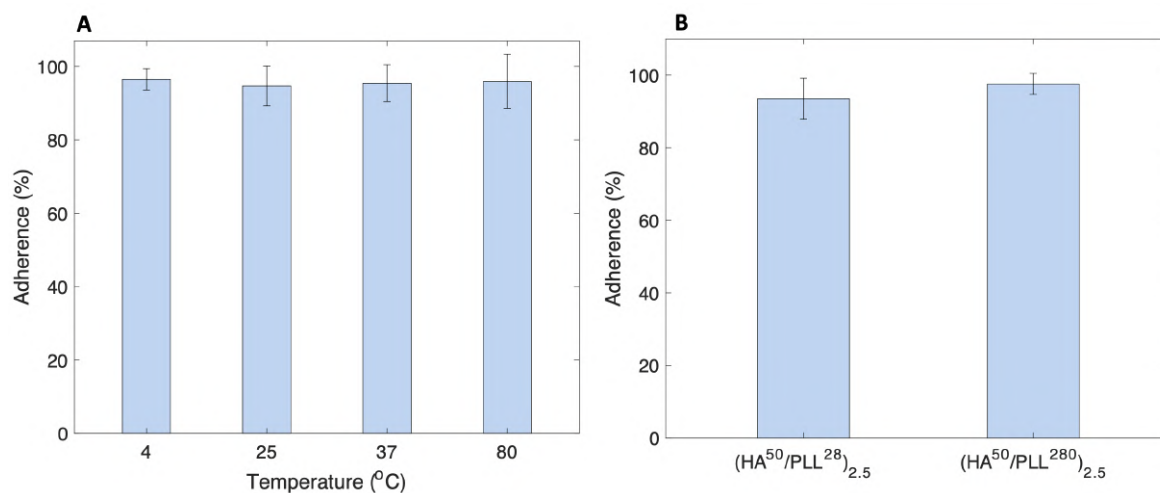
Figure 4.42: (A) The effect of temperature on the adhesion of $(HA/PLL_{28})_{2.5}$ microgels; microgels were formed at 25°C and washed after 1 hour incubation at varying temperatures. (B) The effect of autoclaving glass-adhered $(HA/PLL_{28})_{2.5}$ and $(HA/PLL_{280})_{2.5}$ microgels upon the adhesion. Error bars are SD, n=3.

Mechanism of adhesion

The adhesion mechanism may be related to the water content within the "voids" of the polymer network and hydration of these biopolymer complexes (step iii in Figure 4.43). HA/PLL multilayers are more hydrated due to the presence of water affinitive carboxyl groups, and hence are more viscous and hydrogel-like compared to the HS/PLL films, of which the sulphate groups possess a low affinity to water [333, 337]; this directly relates to the viscoelastic and elastic behaviour of HA/PLL and HS/PLL films, respectively [337]. Moreover, it was previously demonstrated that microgel shrinkage directly correlates to the charge density of the polyanion and hence the extent of ionic pairs between the polyanion and PLL. The excessive shrinkage of HA/PLL microgels upon $CaCO_3$ template dissolution comes with the extrusion of much more water from the system during polymer annealing compared to HS/PLL microgels - this process is due to the increase in extrinsic charge compensation within the network (Ca^{2+} and CO_3^{2-}). In turn, this increases the hydrophobicity of the system via the minimization of microgel contact with surrounding water, which is more energetically favourable for the system, and results in the observed adhesive properties through surface-microgel hydrophobic interactions. HS/PLL films are not very hydrated, and so the microgels are

not able to shrink to the same extent at these conditions - giving little-to-no surface-microgel hydrophobic interaction, and no microgel adhesion as observed. Notably, due to the heavily sulphated nature of DS/PLL films, it is likely that the lack of adhesion displayed by these microgels may be explained by the same phenomenon.
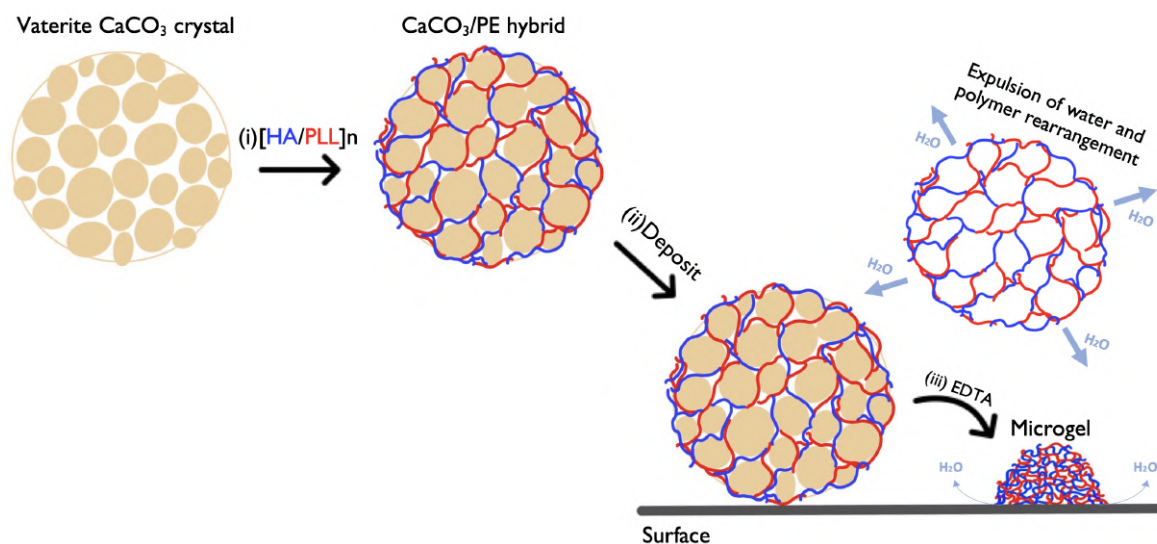
Figure 4.43: Schematic for the formation of HA/PLL$_{28}$ microgels and their adhesion to the surface. i: LbL of HA/PLL$_{28}$ to form a CaCO$_3$/polyelectrolyte hybrid, ii: depositing the hybrid suspension on the surface. iii: The addition of EDTA to form a surface-adhered microgel. An intermediate is shown during the addition of EDTA in which water is extruded from the voids in the polymer network of the microgel.

4.4   Conclusion

This Chapter of the thesis sought to develop CaCO$_3$-based vectors to be utilised as vectors for *in ovo* delivery. Vaterite CaCO$_3$ crystals of varying sizes (ranging from 500 nm to 20 μm) have been synthesised in an additive-free, aqueous environment. The crystals were shown to form in physiologically-relevant conditions. These crystals have been characterised accordingly and display typical vaterite morphologies and characteristics; including typical porosity, surface topology, internal structure and shape, according to BET and FT-IR analyses, as well as optical microscopy and SEM. In terms of the storage of such crystals, it was shown that pristine vaterite can be stored frozen at -20°C for up to at least 4 months and indefinitely in the dry state at room temperature, as shown via microscopy and DLS studies.

A comparative study of 16 types of biopolymer-based microgels formed of biopolyelectrolytes templated upon vaterite $CaCO_3$ microcrystals was performed. PLL and PR form stable microgels with all tested polyanions and are prone to shrinkage upon the template dissolution. The degree of shrinkage increased in a series of HS < DS < CS < HA, which correlates with the decrease in polyanion charge density. All tested COL- and DA-based microgels underwent dissolution during template elimination. The internal structure of the microgels was investigated by means of CLSM and SEM, revealing the presence of an internal polymer matrix. The effect of the polymer molecular weight on the shrinkage and internal structure of microgels was verified using PLL of increased molecular weight, which exhibit no influence on polymer distribution within the microgel and a decrease of the shrinkage coefficients. Upon increase of the molecular weight of both the polycation and polyanion (HA and PLL here), the shrinkage is increased, and is explained through vaterite pore filling. The shrinkage and $CaCO_3$ dissolution was also found to occur simultaneously and on a similar timescale, and is independent of the crystal size. Microgel adherence to the surface upon which they are formed appeared to increase in a series of HS < DS < CS $\sim$ HA for PLL-based microgels; where PR-based microgels displayed 100% adherence for all microgels regardless of the polyanion. For both sets of microgels, this adhesion was independent of the crystal size, temperature and ionic strength. A mechanism of microgel adhesion is also proposed, correlating the adhesion of the microgels to their water content, and hence their shrinkage.

Chapter 5

Encapsulation into vectors

5.1 Introduction

In this Chapter of the thesis, model compounds are encapsulated into those vectors formulated in Chapter 4. The encapsulation processes, as well as the effect on the properties of the vectors are explored and discussed. Of note, part of the work presented in this Chapter has been published as references (8) and (10), as listed in Section 1.3.

5.2 Encapsulation within CaCO$_3$ crystals

5.2.1 Dextran encapsulation

Non-ionic DEX encapsulation

Pristine vaterite CaCO$_3$ crystals (diameter within the range of $\simeq$7-11 μm) were utilised as a control, with their vaterite polymorphism confirmed via and FT-IR (Figure 5.1). SEM images of representative vaterite CaCO$_3$ crystals are provided in Figure 5.2(A). For co-synthesis of DEX, non-ionic DEXs (average molecular weights from 4 to 2000 kDa) were added to the CaCl$_2$ solution, of which was then mixed with Na$_2$CO$_3$, at an initial ratio (DEX:CaCO$_3$) of 1:10 w/w. Under these conditions, DEXs of different molecular weights were entrapped within the pores of the vaterite during its growth, resulting in the formation of hybrid DEX^{FITC}/vaterite CaCO$_3$ crystals containing less than 10% w/w of DEX^{FITC}, as was estimated by TGA from the weight loss at 550°C, as shown in Figure 5.1. The homogeneous distribution of DEX^{FITC} molecules throughout the entire volume of the crystals was confirmed by fluorescence microscopy of the hybrid crystals (Figure 5.2) and did not depend on DEX molecular weight.
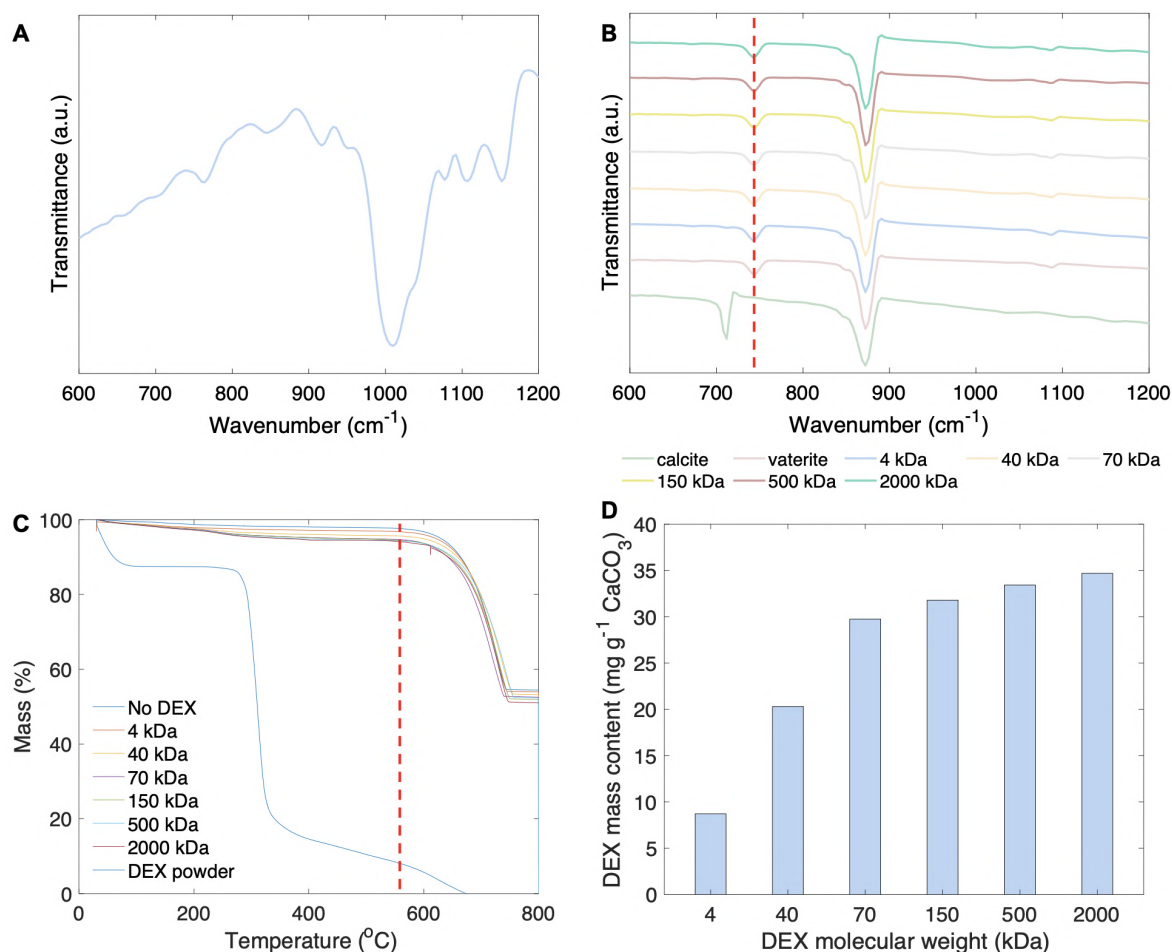
Figure 5.1: (A) FT-IR spectrum of 150 kDa DEX, (B) FT-IR spectra of DEX/vaterite hybrids (the dashed red line corresponds to the characteristic vaterite FT-IR wavenumber), (C) representative TGA curves (the dashed red line at 550 °C corresponds to the temperature where the mass of DEX$^{\text{FITC}}$ within the crystals was taken). (D) DEX mass content within CaCO$_3$ as determined via TGA.

Co-synthesis of vaterite and non-ionic DEXs of different molecular weights did not influence the polymorphism of the crystals, preserving the predominant formation of vaterite, and had negligible effect on the secondary crystal size, as confirmed by FT-IR spectroscopy (Figure 5.1) and SEM (Figure 5.2), respectively. Of note, there is a slight shift of the ν_4 band (in-plane O-C-O bending [198, 338]) of vaterite to lower wavenumbers, from 745 cm^{-1} to 741 cm^{-1} in vaterite/DEX hybrids; this is likely due to the interaction of the carbonate ions with DEX molecules during the crystal growth phase, such as the hydrogen bonding to amorphous calcium carbonate [339]. Moreover, mechanically cracked crystals of vaterite and vaterite/DEX$^{\text{FITC}}$ hybrids bare a similar structure of interconnected cylindrical radial pores, as typically seen throughout the

literature [18, 25].

Calculation of the size of the nanocrystallites visible at the external surface of the crystals suggests a $\simeq$ 2 times reduction of their size in the presence of non-ionic DEXs, wherein the molecular weight of DEX had no significant influence on this effect (Figure 5.3). Interestingly, the effects of non-ionic DEX addition on the crystallisation of calcium carbonate established in this study for the mixing method at constant pH, drastically differ from those found for the mixing of H$_2$CO$_3$ and Ca(OH)$_2$. In this case, the addition of DEX significantly affected the pH values during the crystallisation process, of which resulted in the inhibition of vaterite nucleation and the predominant formation of the calcite [340]. Of note, typically, the co-precipitation of both small drugs and macromolecules does not affect the crystallinity of the CaCO$_3$ crystals [23, 42], even with loading capacities of up to 588 mg g^{-1} mucin [54]. This is evidenced by the typical vaterite morphologies observed via microscopy and typical FT-IR wavenumbers we obtain for such DEX/vaterite hybrids. The suppression of the nanocrystallite growth by non-ionic DEXs can be attributed to the adsorption of DEX molecules on the nanocrystallite surface, and consequent suppression of CaCO$_3$ dissolution, which is a known step in crystal ripening [341].

Crystal porosity

Figure 5.4 illustrates typical N$_2$ adsorption-desorption isotherms obtained for bare vaterite crystals and non-ionic DEX$^{\text{FITC}}$/vaterite hybrids. Analysis of the surface area and typical pore distributions (Table 5.1), estimated in accordance with the BJH model, indicates the elevation of the total surface area of the hybrid crystals compared to pristine vaterite, whilst preserving the pore size distribution; this correlates with the reduced nanocrystallite size, schematically shown in Figure 5.3. Typical pore distributions for pristine vaterite and non-ionic DEX$^{\text{FITC}}$/vaterite hybrids are shown in Figure 5.4. The molecular weight of DEX held no influence on these effects, despite the range in hydrodynamic diameter of DEXs investigated in this study (13.2-53.8 nm). Of note, the surface area of pure vaterite correlated with that of the literature reported [177],
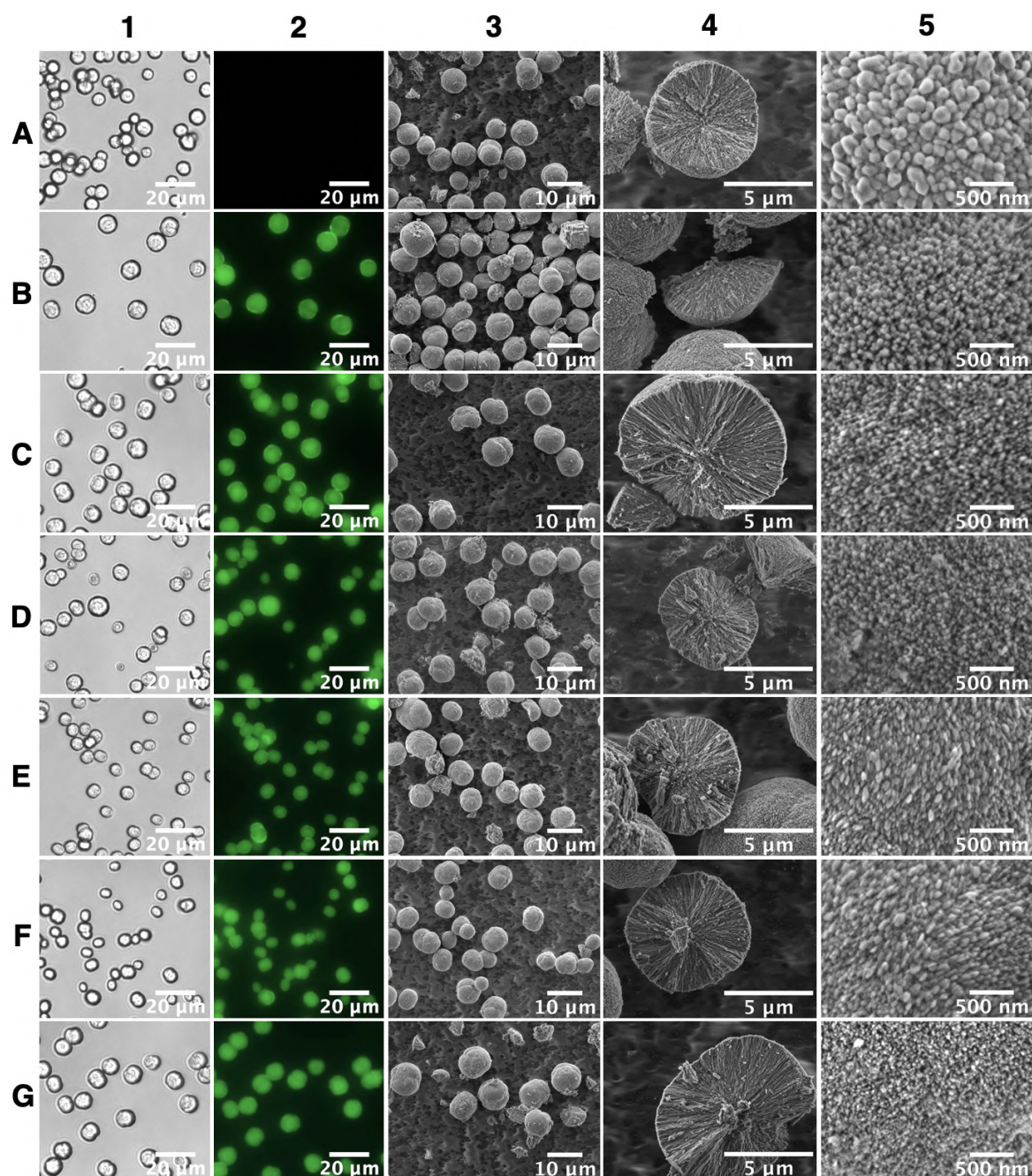
Figure 5.2: Imaging of non-ionic DEX$^{\text{FITC}}$/vaterite hybrid crystals. Crystals loaded with different molecular weights of DEX$^{\text{FITC}}$ are shown: (A) No DEX$^{\text{FITC}}$; (B) 4 kDa, (C) 40 kDa, (D) 70 kDa, (E) 150 kDa, (F) 500 kDa, and (G) 2000 kDa. (1) Transmittance and (2) fluorescent images of crystals, (3) SEM overview of spherical vaterite crystals, (4) cross-section of a single crystal, and (5) the typical surface morphology is shown. Scalebar is 20 μm for (1) and (2), 10 μm for (3), 5 μm for (4), and 500 nm for (5).
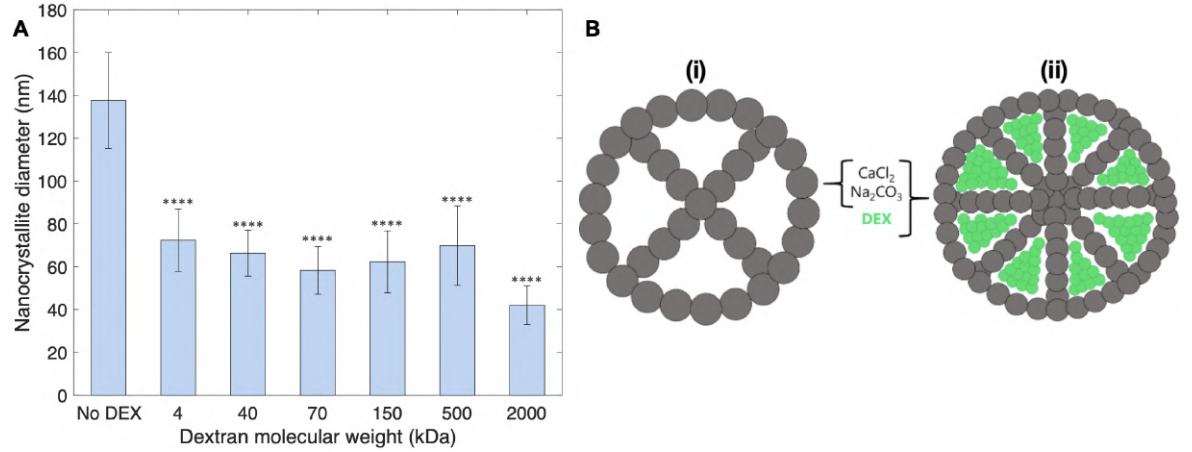
Figure 5.3: (A) The effect of DEX^{FITC} molecular weight upon the average size of DEX^{FITC}/vaterite hybrid crystal nanocrystallites. Error bars are SD, n=100. Statistical analysis made using the one-way ANOVA test; $****p<0.0001$. Comparison was performed between No DEX and DEX-loaded samples. (B) A schematic of the effect the presence of DEX^{FITC} upon the crystal properties of vaterite CaCO$_3$ (i.e., nanocrystallite size and pore occupation).

hence the control crystals synthesised in this study have typical total surface area.

Table 5.1: The effect of neutral DEX^{FITC} molecular weight upon the average crystal size, specific surface area, and the pore distribution of the DEX^{FITC}/vaterite hybrids.

DEX molecular weight (kDa)	DEX r_h [342, 343] (nm)	Crystal size (μm)	Surface area (m^{2}g^{-1})	Pore distribution (nm)
No DEX	-	11.4 $\pm$ 1.0	3.95	5-30
40	6.6	8.6 $\pm$ 1.1	19.0	3-28
150	9.0	8.2 $\pm$ 1.3	19.6	2-30
500	15.9	7.3 $\pm$ 0.8	28.7	3-28
2000	26.9	9.3 $\pm$ 0.8	20.1	5-30
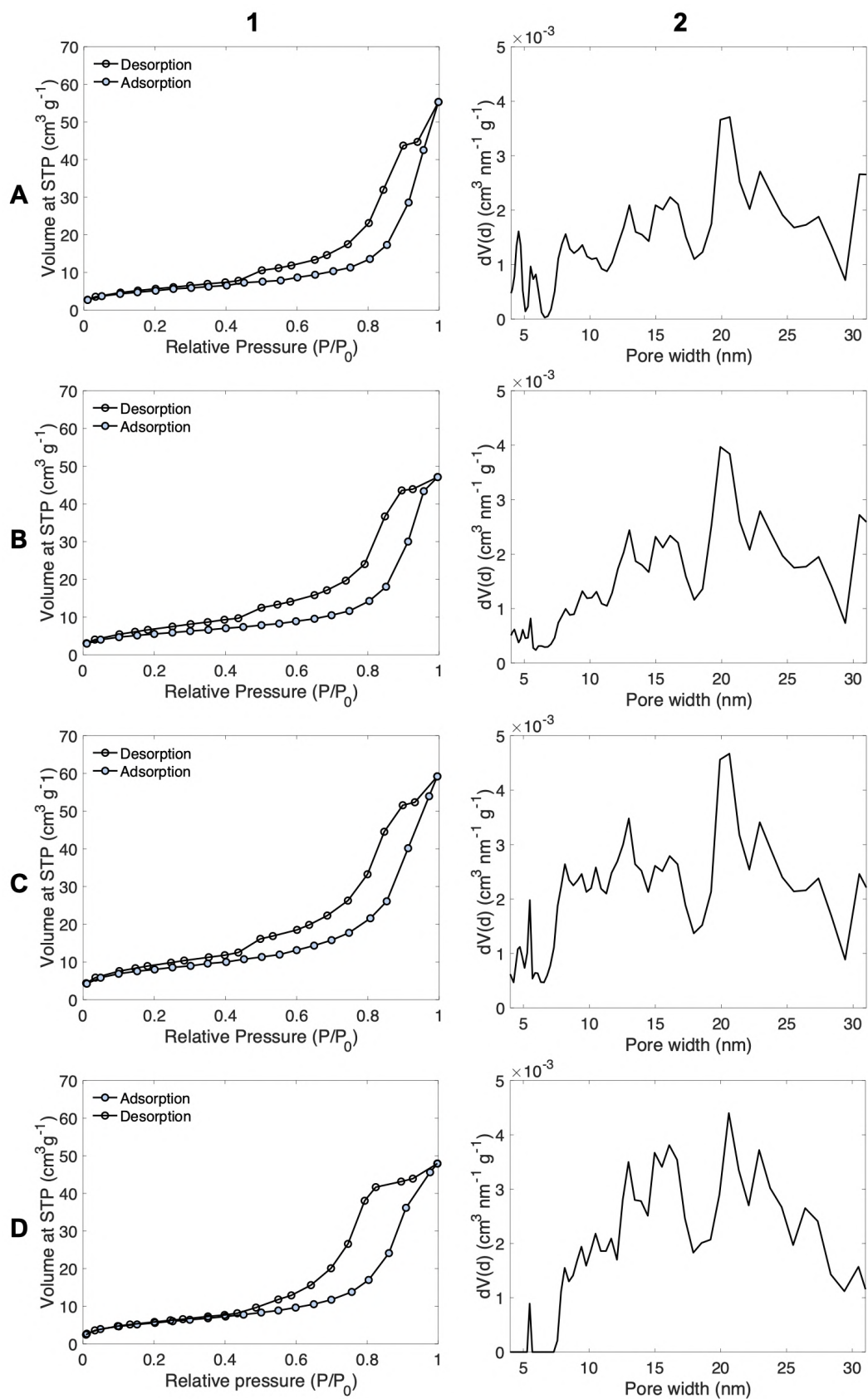
Figure 5.4: (1) Nitrogen adsorption-desorption isotherms and (2) pore distributions for (A) 40, (B) 150, (C) 500, and (D) 2000 kDa DEX$^{\text{FITC}}$/vaterite hybrids.

A significant adsorption-desorption hysteresis loop, denoted type H2a, was observed for DEX$^{\text{FITC}}$/vaterite hybrids (Figure 5.4). Its width was estimated as the numerically integrated area enclosed within the adsorption-desorption isotherms (Figure 5.5). The widening of the hysteresis loop for DEX$^{\text{FITC}}$/vaterite hybrids indicates that a significant volume fraction of the pores remains filled until a lower vapor pressure - which is typical if the narrowing of the pore openings takes place, i.e., cylindrical pores are converted into ink-bottle-like pores [344]. In other words, the incorporation of DEX leads to the partial blocking of the vaterite crystal pores. This is in contrast to pristine vaterite crystals in which a type H1 isotherm is observed, suggesting uniform cylindrical pores with minimal pore blocking [319]. The filling of crystal pores with DEX occurs regardless of DEX size, however, there is an increase in hysteresis loop area when DEX molecular weight increases above 40 kDa; this may be due to the larger hydrodynamic radii of higher molecular weight DEXs, and perhaps a greater interaction with the vaterite crystal surface, and hence increased DEX uptake and pore blockage. This may have important consequences for future drug release kinetics.
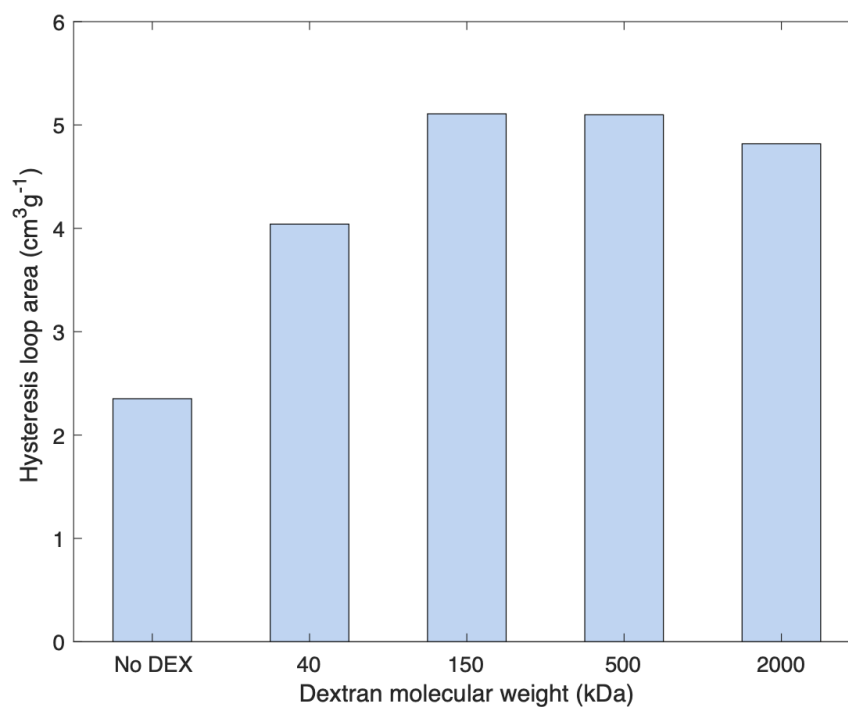
Figure 5.5: The effect of DEX$^{\text{FITC}}$ molecular weight upon the hysteresis loop area (as determined by numerical integration) of DEX$^{\text{FITC}}$/vaterite hybrid crystals.

Ionic DEX encapsulation

Crystal size and morphology

Ionic DEXs, namely anionic CM-DEX and cationic DEAE-DEX, were incorporated into the vaterite crystals identically to that of non-ionic DEX. The higher adsorption capacity for CM-DEX^{FITC} and lower capacity for DEAE-DEX^{FITC} (Figure 5.6) correlate with their charges and can be explained in view of the electrostatic attraction or repulsion between positively charged surface of the vaterite template (zeta-potential in the range from +11 to +15 mV in water) [70] and CM-DEX^{FITC} or DEAE-DEX^{FITC}, respectively. Despite clear dependence of loading capacity on the net charge of the DEX^{FITC} molecules, all fabricated hybrid particles contained less than 10% of DEX^{FITC} by weight. Similarly, to non-ionic DEX, the presence of ionic DEX had no effect on the polymorphism of the CaCO$_3$ (Figure 5.6), of which they had the tendency to form typical spherical vaterite crystals regardless of DEX charge, as observed via SEM (Figure 5.7). The null effect of DEAE-DEX on the polymorphism differs to that reported in the literature, with the addition of DEAE-DEX resulting in a mixture of CaCO$_3$ polymorphs, including aragonite, calcite and vaterite [340, 345]. Instead, the polymorphism is akin to the co-precipitation of other negatively charged bioactives, such as heparin [73] and catalase [84] in similar conditions. Here, we note distinct similarities to pristine vaterite CaCO$_3$; upon mechanical cracking, the internal structure appears to resemble that of the pristine vaterite, with exposed cylindrical channels forming the interior of the hybrids, as observed via SEM. The average nanocrystallite size of CM-DEX^{FITC}/vaterite hybrids is reduced compared to both pristine vaterite and non-ionic DEX^{FITC}/vaterite hybrids of the same DEX molecular weight. Wherein DEAE-DEX^{FITC}/vaterite hybrid nanocrystallites are enlarged when compared to non-ionic hybrids of the same molecular weight, as observed in Figure 5.7 and 5.8. This was also observed with vaterite grown in the presence of poly(aspartic acid), poly(glutamic acid), and poly(lysine); where the decrease in nanocrystallite size is related to the adsorption of negatively charge poly(amino acids) to the crystalline surface, and sub-

sequent growth of smaller nanocrystallites [346]. It is likely here that CM-DEX preferentially adsorbs to the CaCO$_3$ surface, compared to DEAE-DEX. This is due to their relative charge at these synthetic conditions [18] (pKa of CM-DEX is 4 [347] where pKas of DEAE-DEX are 9.2 for the DEAE substituent, 5.5 for tertiary group, and $\simeq$14 for the quaternary group [348]). These electrostatics, coinciding with the typical positive zeta potentials of vaterite formed in similar conditions, as well as the exposed Ca^{2+} plane on the crystal surface [59, 69, 349], results in the hybrid crystal morphologies observed. Despite these morphological effects, both CM- and DEAE-DEX are distributed throughout the CaCO$_3$ crystals as evidenced via fluorescence microscopy. CM-DEX holds an apparent slight accumulation within the centre of the vaterite crystals, which may be due to the formation of CM aggregates during co-synthesis, as reported with certain proteins in the presence of the same ions [72, 84]. DEAE-DEX has a higher fluorescent signal on the crystal surface; in either case it is unclear why, but this is likely due to the difference in encapsulation capacities between the two DEXs, of which is related to the electrostatics of the DEX molecule and CaCO$_3$ crystal.
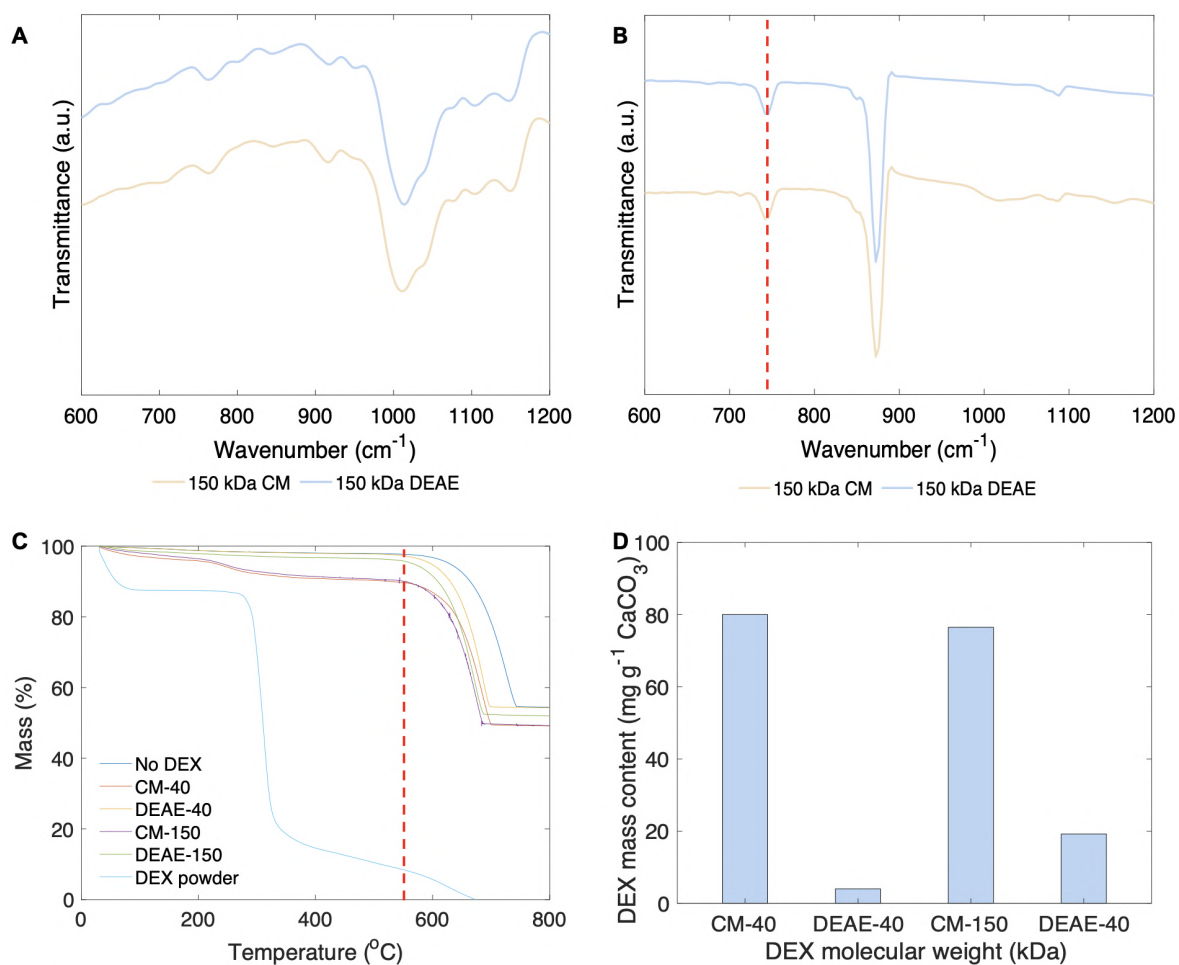
Figure 5.6: (A) FT-IR spectrum of 150 kDa CM- and DEAE-DEX, (B) FT-IR spectra of DEX/vaterite hybrids (the dashed red line corresponds to the characteristic vaterite FT-IR wavenumber), (C) representative TGA curves (the dashed red line at 550 °C corresponds to the temperature where the mass of DEX^{FITC} within the crystals was taken). (D) DEX mass content within CaCO$_3$ as determined via TGA.
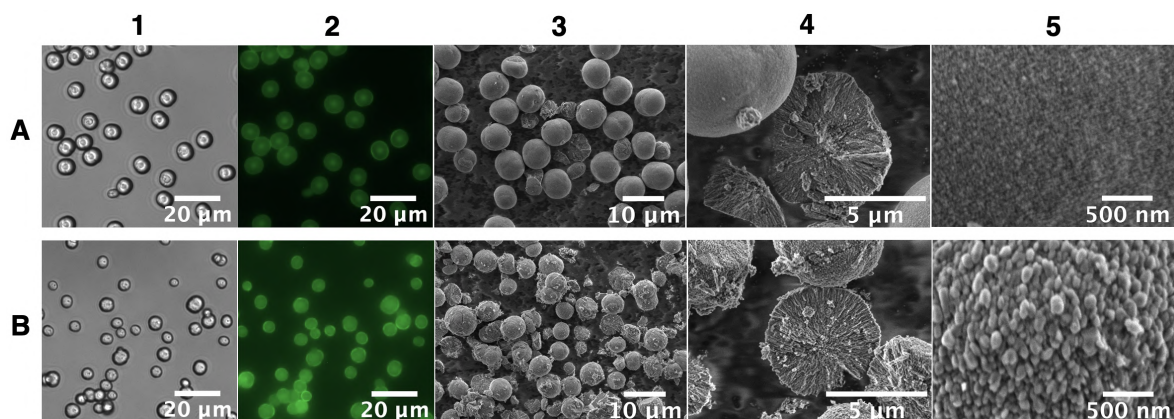
Figure 5.7: Imaging of ionic DEX^{FITC}/vaterite hybrid crystals. (A) CM-DEX^{FITC}/vaterite hybrids and (B) DEAE-DEX^{FITC}/vaterite hybrids are shown, with (1) transmittance and (2) fluorescent images of crystals, (3) SEM overview of spherical vaterite crystals, (4) cross-section of a single crystal, and (5) the typical surface morphology is shown. Scalebar is 20 μm for (1) and (2), 10 μm for (3), 5 μm for (4), and 500 nm for (5). The DEX molecular weight used was 150 kDa.
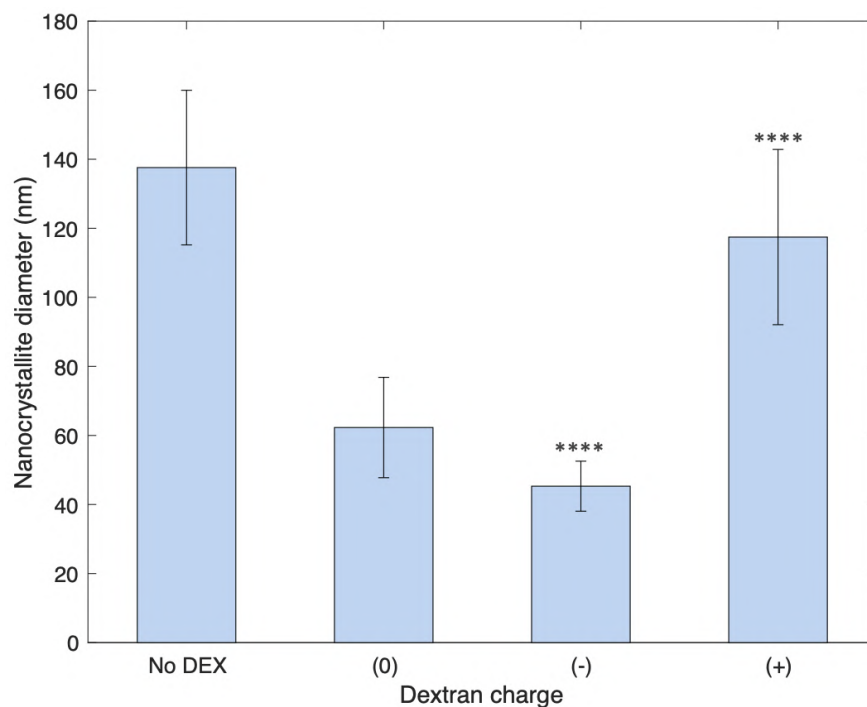
Figure 5.8: The effect of DEX^{FITC} charge upon the average size of charged 150 kDa DEX^{FITC}/vaterite hybrid crystal nanocrystallites. Error bars are SD, n=100. Statistical analysis made using the one-way ANOVA test; $****p<0.0001$. Comparison was performed between (0) and both (-) and (+).

Crystal porosity

From the analysis of N$_2$ adsorption-desorption isotherms (Figure 5.9), notably, the surface area of CM-DEX$^{\text{FITC}}$/vaterite hybrids is dramatically increased to $\simeq$41 m^2 g^{-1}, despite no significant alteration in the crystal size. This can be explained by the reduction of the nanocrystallite size upon CM-DEX co-synthesis with vaterite as well as the possible effect from the presence of precipitated DEX itself; such effect of nanocrystallite size on the surface area is also reported [100]. The large extent of vaterite crystal filling with CM-DEX is evident from the sizeable increase in hysteresis loop width compared to pristine vaterite and non-ionic DEX$^{\text{FITC}}$/vaterite hybrids, indicating partial blocking of internal pores. Comparatively, DEAE-DEX slightly increases the surface area of these hybrids to $\simeq$6 m^2 g^{-1} compared to the bare crystals, of which correlates to the small decrease in average nanocrystallite size (Figure 5.8) and the little uptake of DEX as evidenced by the small change in mass during TGA curve analysis (Figure 5.6). Despite these differences in the extent of pore filling, both CM- and DEAE-DEX$^{\text{FITC}}$/vaterite hybrids hold similar pore distributions (Figure 5.9), of which are akin to that of pristine vaterite and non-ionic DEX$^{\text{FITC}}$/vaterite hybrids as determined via BET analysis; such parameters are summarised in Table 5.2. The ability to produce DEX$^{\text{FITC}}$/vaterite hybrids of varying charge with negligible effect on the crystal size and pore distribution may be invaluable for future drug delivery applications; especially for the selective encapsulation of charged low molecular weight species, of which the large pore sizes of pristine vaterite are typically a hindrance.

Table 5.2: The effect of charged 150 kDa DEX$^{\text{FITC}}$ upon the average crystal size, specific surface area, and the pore distribution of the DEX$^{\text{FITC}}$/vaterite hybrids.

DEX charge	Crystal size (μm)	Surface area (m^2 g^{-1})	Pore distribution (nm)
No DEX	11.4 $\pm$ 1.0	3.95	5-30
(-)	7.8 $\pm$ 0.6	40.5	3-28
(+)	6.2 $\pm$ 1.0	5.89	3-30
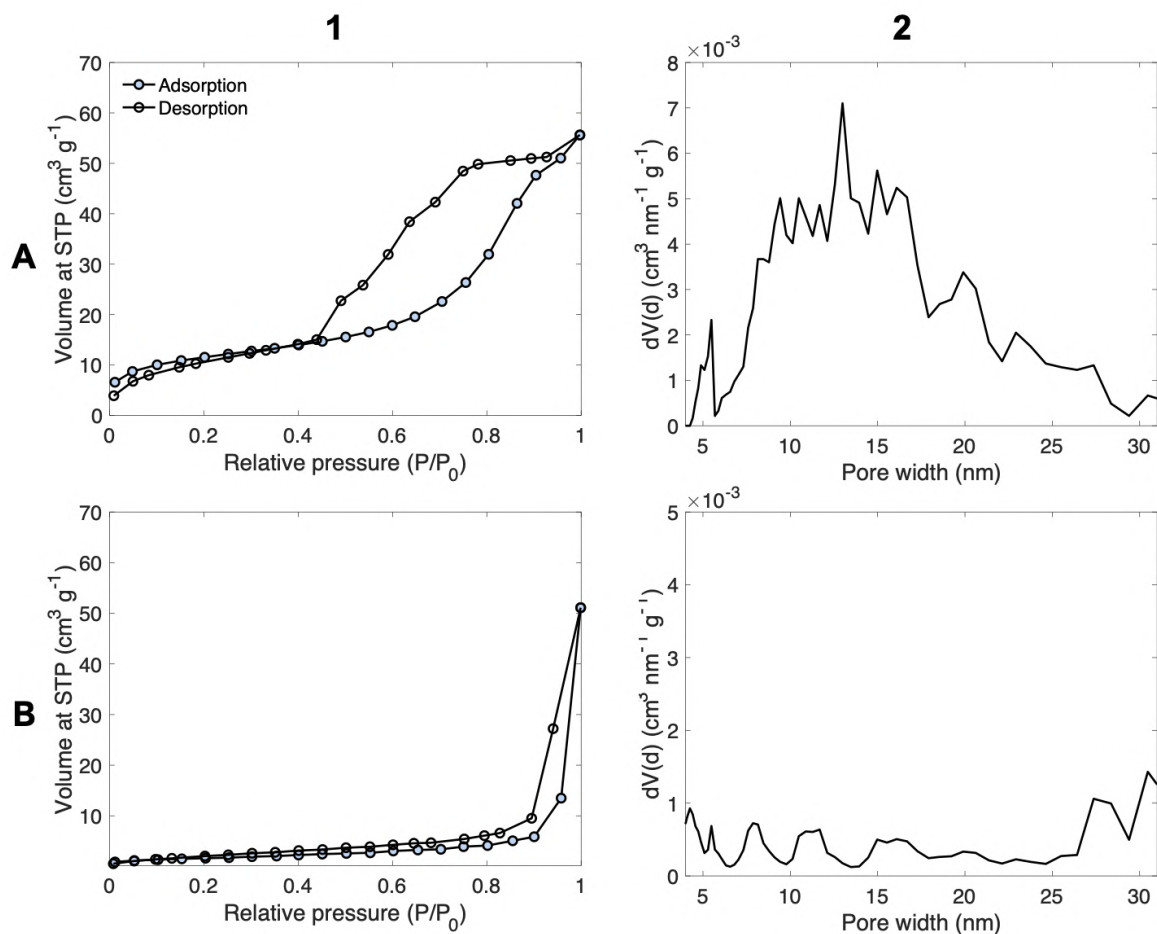
Figure 5.9: (1) Nitrogen adsorption-desorption isotherms and (2) pore distributions for (A) CM-DEX and (B) DEAE-DEX/vaterite hybrid crystals.

Effect of DEX loading ratio

The control of DEX content may be crucial for the control of the DEX/vaterite hybrid morphology and porosity. The effect of the initial DEX concentration during co-synthesis upon the final DEX/vaterite hybrid morphology was investigated. Indeed, no significant effect was observed for the co-synthesis of 5, 20 or 50 mg mL^{-1} 40 kDa DEX (DEX mass content of 0.4, 10.9 and 20.3 mg DEX/g CaCO$_3$, respectively, as determined by TGA), with each hybrid batch displaying the crystalline internal structure of cylindrical radial pores, similar nanocrystallite size, as well as overall crystal size. This suggests the content of DEX matrix within the crystals can be controlled without significant effects on the crystal morphology, and from the established relationship between nanocrystallite size and the internal porosity, the crystal pore distribution -

of which is important regarding the encapsulation of a range of bioactives.

Variation of crystal size

Of note, larger 15-20 μm DEX/vaterite hybrid crystals were also synthesised. Figure 5.10 illustrates the hybrids formed from non-ionic 40 kDa and 2000 kDa DEX as well as 40 kDa DEAE- and CM-DEX; the crystals display highly similar morphological properties to that of $\simeq$ 7 μm sized hybrids for both ionic and non-ionic DEXs. The presence of CM-DEX at these conditions however, results in a mixture of DEX/vaterite and calcite hybrids. It is unclear as to why, however it may be due to the decrease in the extent of mixing between both pre-cursor salt solutions in the presence of this highly negatively charged DEX, resulting in differences in nucleation, as was observed when co-precipitating ionic DEXs previously [340, 345]. Despite this, the CM-DEX/vaterite hybrids hold similar morphologies to those formed at 7 μm in size. This indicates the potential use of these DEX/vaterite hybrids as potential *in ovo* vectors of varying size, or use in further bioapplications, as porogens for bio-scaffolds for instance.
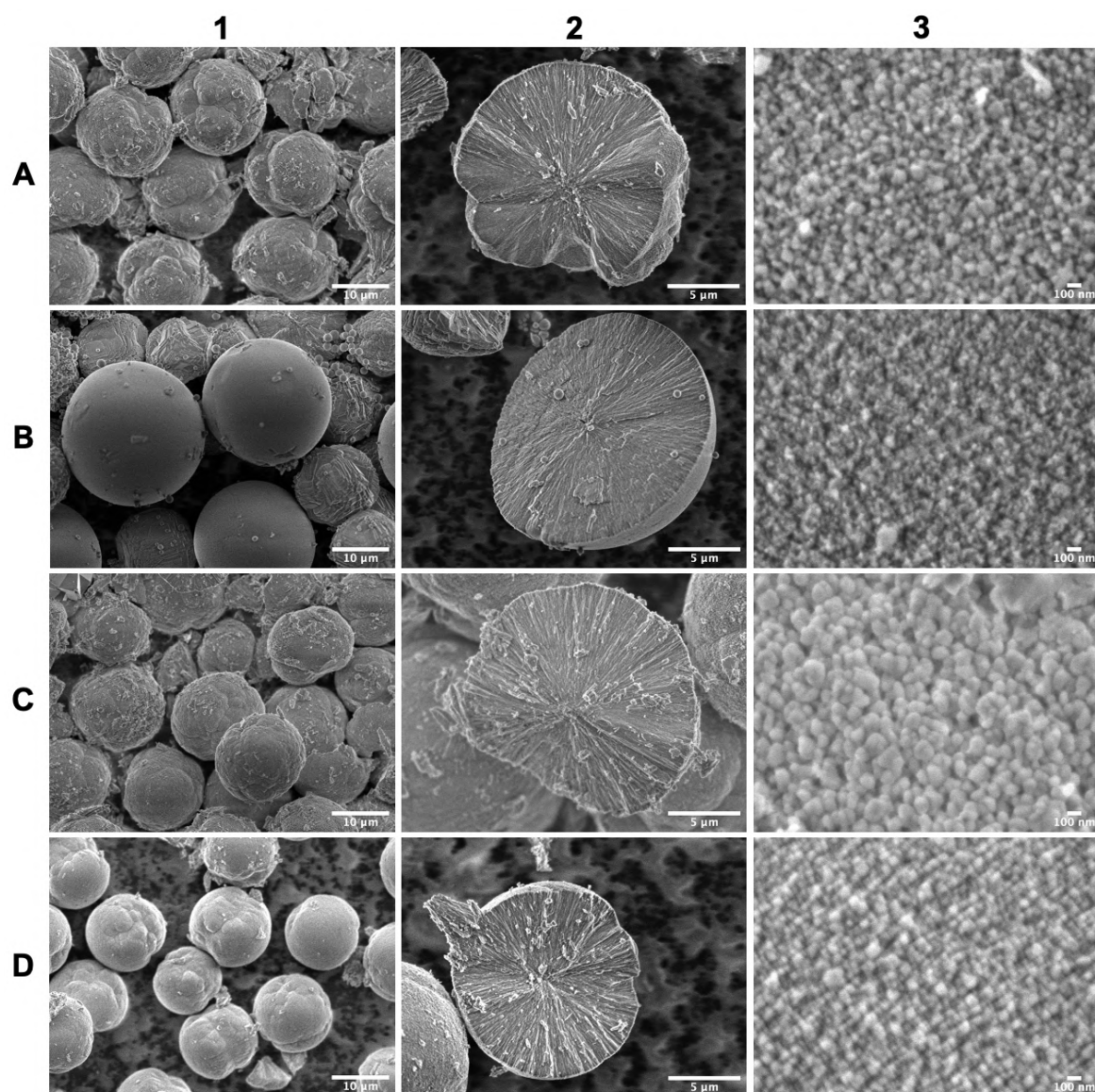
Figure 5.10: SEM images of 15-17 μm (A) 40 kDa, (B) 40 kDa CM-, (C) 40 kDa DEAE- and (D) 2000 kDa DEX/vaterite hybrid crystals. (1) Overview of the crystal sample, (2) mechanically cracked crystal cross-section and (3) surface morphology of the crystals. Scalebar is 10 μm for (1), 5 μm for (2) and 100 nm for (3).

Further, additive-free submicron DEX/vaterite hybrids have also been successfully synthesised, typical images are displayed in Figure 5.11, along with the typical DLS intensity size distributions. Both the DLS distributions and the transmittance and fluorescence images shown in Figure 5.12 indicate little crystal aggregation occurs upon DEX co-synthesis. Indeed, the average hydrodynamic diameters of submicron DEX/vaterite hybrids were 687 $\pm$ 174, 756 $\pm$ 173, 426 $\pm$ 81, 585 $\pm$ 269 nm for non-ionic 40 kDa DEX, non-ionic 2000 kDa DEX, as well as ionic CM-DEX and DEAE-DEX, respec-

tively. Compared to the hydrodynamic diameter of pristine submicron vaterite crystals (500 ± 210 nm), both non-ionic and ionic DEXs do not significantly affect this size. The SEM images of these hybrids support this, however, the average size of CM-DEX determined from the SEM images is significantly larger (617 ± 77 nm), this can be explained by the continued growth of these hybrids past the typical analysis time. Figure 5.13 illustrates the DEX/vaterite hybrid size as a function of time allowed for crystallisation. Pristine submicron vaterite crystals do not grow further from their initial crystallisation and for over a period of 60 mins. This was not observed for both 40 kDa DEX and CM-DEX/vaterite hybrids; the continued growth of up to ≃1 μm for these hybrids may be related to the negative zeta potentials of these DEXs (−10 ± 8 mV and −20 ± 6 mV for 40 kDa DEX and CM-DEX, respectively) and the excess of Ca^{2+} necessary for the formation of these submicron crystals (CaCl$_2$:Na$_2$CO$_3$ of 40:1), resulting in the larger crystal sizes observed after 30 min of continued growth. This effect was not observed for 2000 kDa DEX despite the negative zeta potential, nor DEAE-DEX (16 ± 5 mV). Regarding 2000 kDa DEX, this may be due to the large molecular weight of the DEX in question, which may impair crystal growth at these conditions.
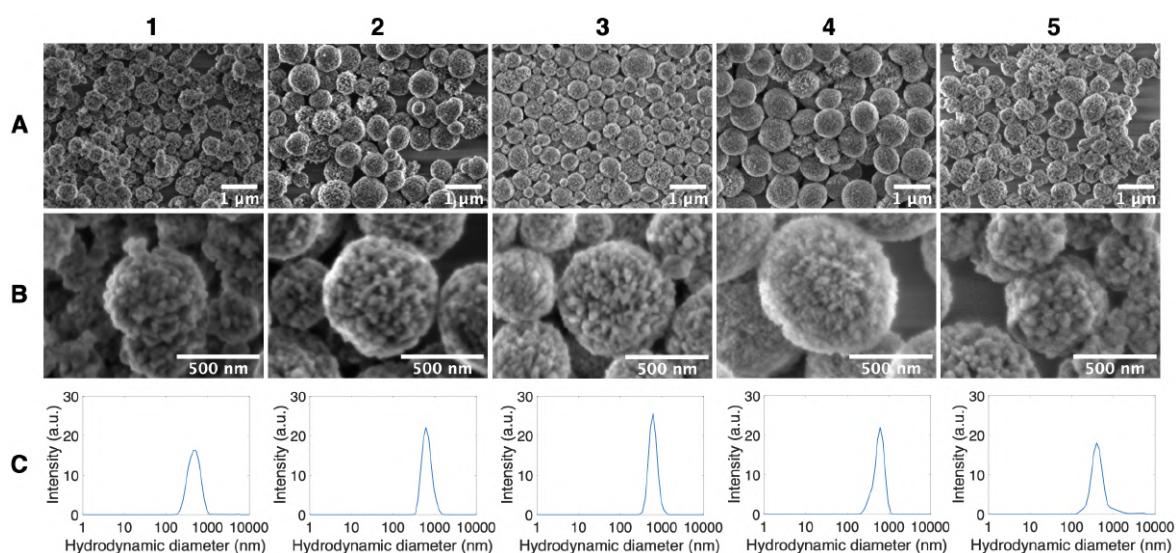
Figure 5.11: (A, B) typical SEM images of submicron vaterite crystals formed in the presence of (1) No DEX, (2) 40 kDa DEX, (3) 2000 kDa DEX, (4) 40 kDa DEX-CM and (5) 40 kDa DEX-DEAE. (A) overview of crystal sample and (B) single crystals are shown. (C) Corresponding DLS size distributions by intensity are shown beneath the respective vaterite sample. Scalebars are (A) 1 μm and (B) 100 nm.
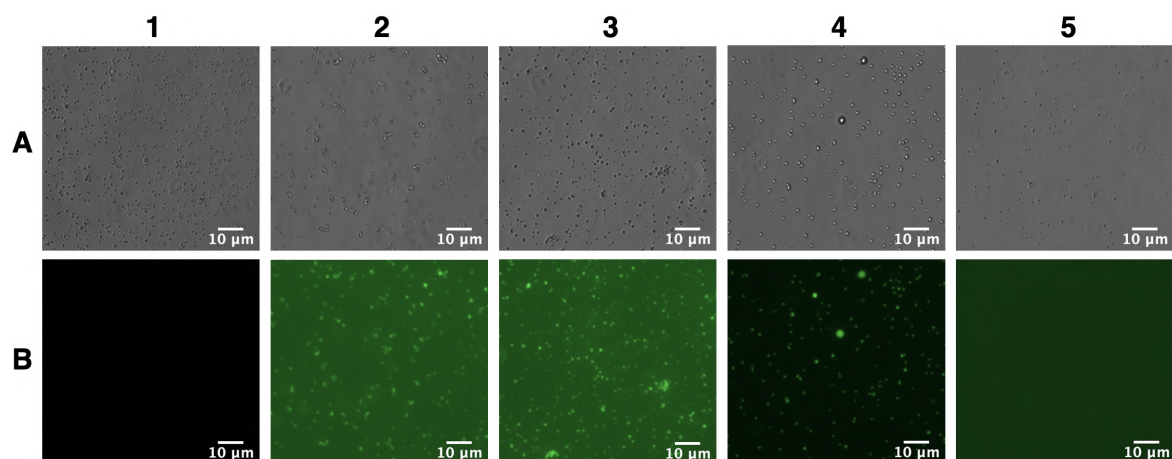
Figure 5.12: (A) typical transmittance and (B) fluorescence images of submicron vaterite crystals formed in the presence of (1) No DEX, (2) 40 kDa DEX, (3) 2000 kDa DEX, (4) 40 kDa DEX-CM and (5) 40 kDa DEX-DEAE. Scalebars are (A) 10 μm.

Despite these differences in growth period, all submicron DEX/vaterite hybrids hold similar morphologies to that of the micron-sized crystals discussed earlier as well as a similar trend in regard to the nanocrystallite size for both ionic DEXs. The DEX content (mg DEX per g CaCO$_3$) within the hybrids was also determined via fluorescence spectroscopy and a similar trend was observed to that of $\simeq$7 μm hybrids as determined by TGA, as summarised in Figure 5.14 below. Submicron hybrids displayed a higher non-ionic DEX content than that of $\simeq$7 μm hybrids, however this is to be expected due to the greatly increased surface area of such submicron crystals. Indeed, this is similar to that previously reported in the literature regarding the increased lysozyme uptake in smaller CaCO$_3$ crystals [85].
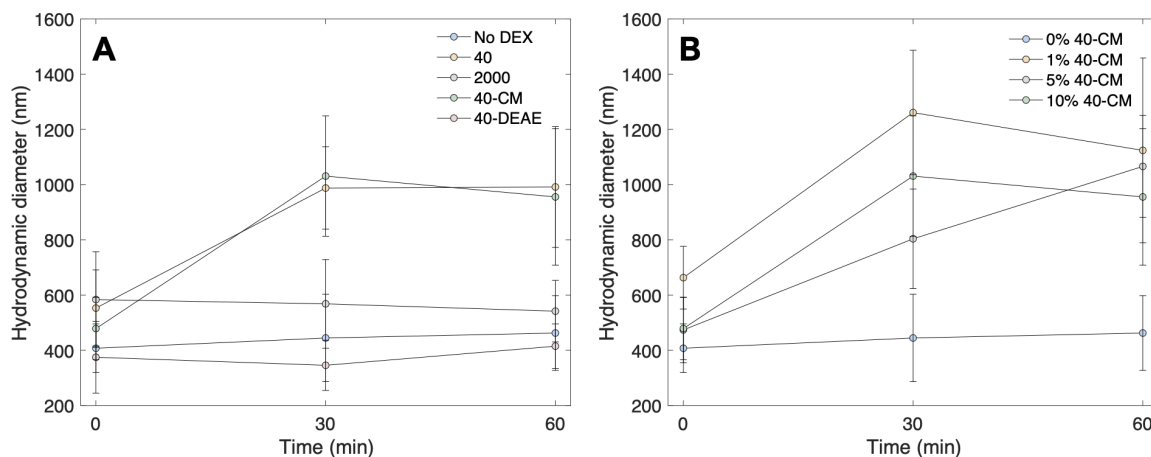
Figure 5.13: (A) Hydrodynamic diameters of submicron DEX$^{\text{FITC}}$/hybrids as a function of time and (B) hydrodynamic diameters of 40 kDa CM-DEX$^{\text{FITC}}$/vaterite hybrids as a function of time and theoretical % mass content. Error bars are SD, n=3.
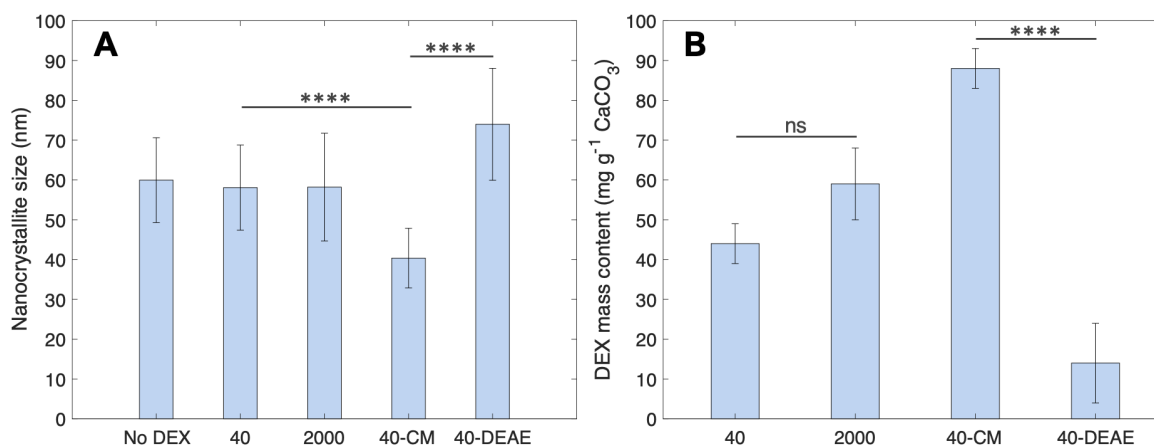
Figure 5.14: (A) nanocrystallite sizes and (B) DEX mass content of the submicron DEX$^{\text{FITC}}$/vaterite hybrids as a function of the DEX co-synthesised. Error bars are SD, (A) n=100, (B) n=3. Statistical analysis made using the one-way ANOVA test; ns: non-significant difference and $****p<0.0001$.

Vaterite recrystallisation in the presence of DEX

The controlled recrystallisation of vaterite to calcite at varying pH is of great importance regarding their use as drug delivery vehicles, as the encapsulated drug should not be released before reaching its target site. The pH-dependent recrystallisation of pristine vaterite to calcite is shown, with enhanced recrystallisation at lower pHs. This is likely due to the enhanced solubility of CaCO$_3$ at these conditions [53], wherein the dissolution and subsequent re-precipitation of CaCO$_3$ is the main mechanism respon-

sible for calcite formation [52]. Here, demonstrated, is the enhanced stabilisation of CM-DEX$^{\text{FITC}}$/vaterite hybrids, with no vaterite-to-calcite transformation within the range of pH 5.7-9.0 across a 54-day period. Whereas DEAE-DEX$^{\text{FITC}}$/vaterite hybrids appear to transform independent of DEAE-DEX presence, similarly to the pristine vaterite CaCO$_3$ within a range of 5 to 8 hours for pHs 6 and 7.6, and $\simeq$ 20 to 30 hours for pH 9. The higher uptake of anionic CM-DEX likely inhibits the recrystallisation of vaterite via the binding of Ca^{2+} to carboxyl groups along the DEX backbone, and hence limits the ion transport rate in solution [59]. Further to the presence of an internal polymeric matrix, the vaterite crystals may be coated with the layer-by-layer (LbL) coating of polyelectrolytes to suppress the recrystallisation, however, such coatings typical only suppress the vaterite-to-calcite transformation for a few days [350], as opposed to pre-encapsulated matrices as shown here, for instance. Notably, neutral 2000 kDa DEX also acted to suppress the recrystallisation of submicron 2000 kDa DEX$^{\text{FITC}}$/vaterite hybrids across a 48 hour period, as confirmed via SEM and FT-IR (Figure 5.15). Experiments regarding the recrystallisation of ionic DEX/vaterite hybrids have been performed in collaboration with Ana Ferreira, NTU, and published in reference (8), as listed in Section 1.3.
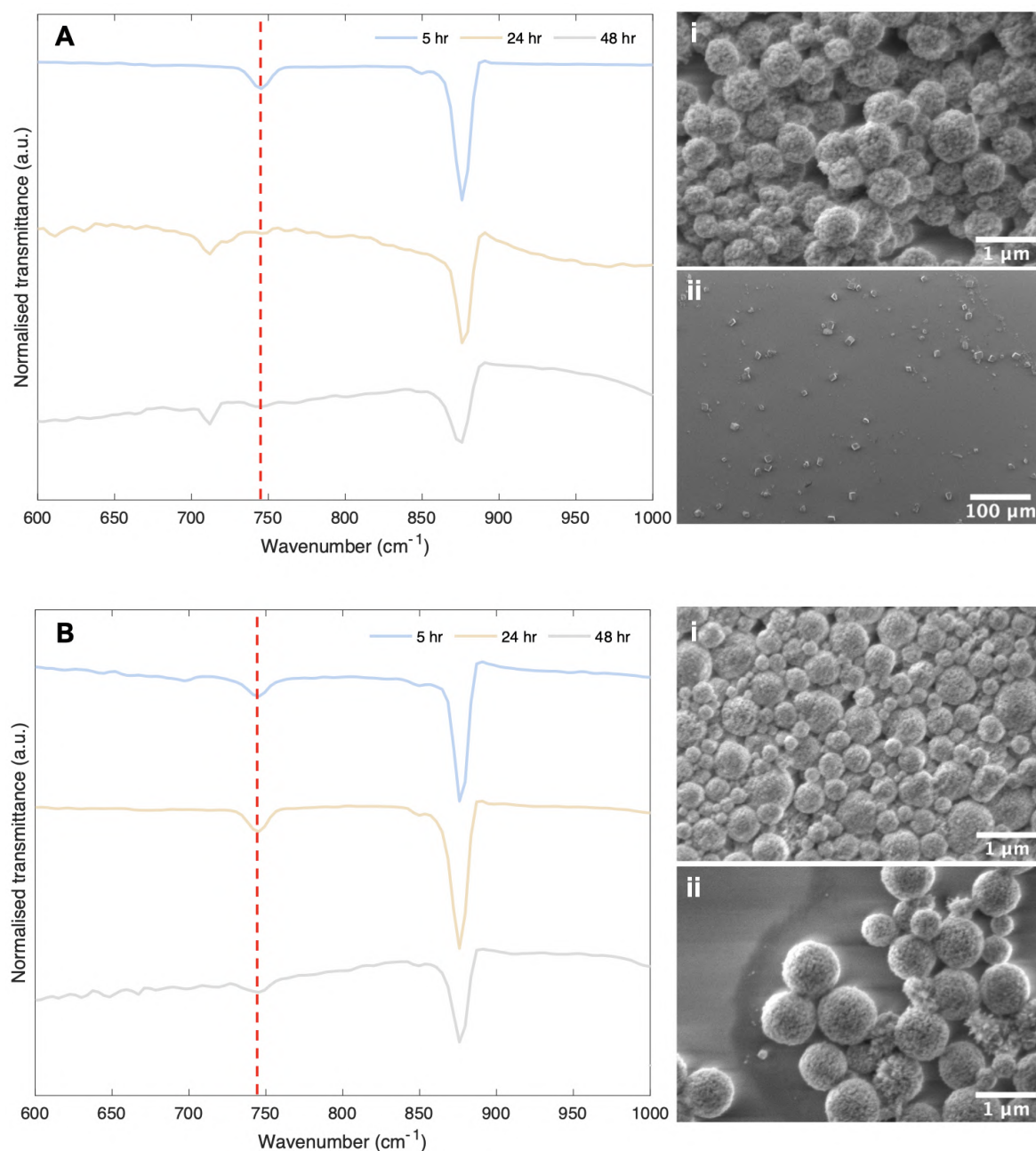
Figure 5.15: FT-IR spectra of (A) pristine and (B) 2000 kDa DEX^{FITC}/vaterite hybrids at 5, 24 and 48 hours in water; the dashed red line corresponds to the characteristic vaterite FT-IR wavenumber. SEM images of crystals at (i) 5 and (ii) 48 hours. Scalebars are (Ai, Bi, Bii) 1 μm and (Aii) 100 μm.

5.2.2   Cobalamin encapsulation

Cobalamin (B12) was chosen as an example model vitamin due to its lack of formal charge as well as its beneficial effects when implemented as an *in ovo* feeding supplement. Preliminary studies were carried out to determine whether such vaterite crystals

are suitable as a host for such small non-ionic species. B12 was successfully encapsulated into submicron vaterite crystals via co-synthesis, as determined via ICP-MS analysis. The maximum B12 uptake was 10 $\pm$ 5 mg B12 per g CaCO$_3$, indeed B12 held no significant effect on the final crystal size over a period of 60 mins and remained a similar size to that of pristine vaterite crystals (500 $\pm$ 210 and 470 $\pm$ 137 nm, respectively), whilst also retaining the same vaterite polymorph and morphology, as evidenced from FT-IR and SEM imaging, as summarised in Figure 5.16. Notably, the nanocrystallite sizes for both pristine vaterite and B12-loaded vaterite are 60 $\pm$ 11 and 58 $\pm$ 10 nm, respectively. The size of the B12-loaded vaterite crystal is not affected by the initial concentration of B12 used during the co-synthesis of such crystals (Figure 5.16). The lack of effect B12 has upon the crystal properties is perhaps expected due to a lower extent of interaction between B12 and the CaCO$_3$ surface, unlike the interaction between DEX and CaCO$_3$, which results in the greater effect upon the nanocrystallite size. Indeed, electrostatics and the larger size of the co-synthesised cargo appears to impact the final crystal properties (i.e. size, morphology, porosity); the lack of a formal charge and the small size of the B12 molecule results in the similar properties of pristine vaterite. The successful encapsulation of B12 implies such additive-free vaterite crystals may be utilised as universal carriers for both low-molecular-weight and macromolecular species, of which may be enhanced via charged matrices pre-encapsulated within the vaterite crystal (e.g. CM- and DEAE-DEX/vaterite hybrids). The ability of these carriers to be utilised as *in ovo* delivery vectors will be discussed in Chapter 6.
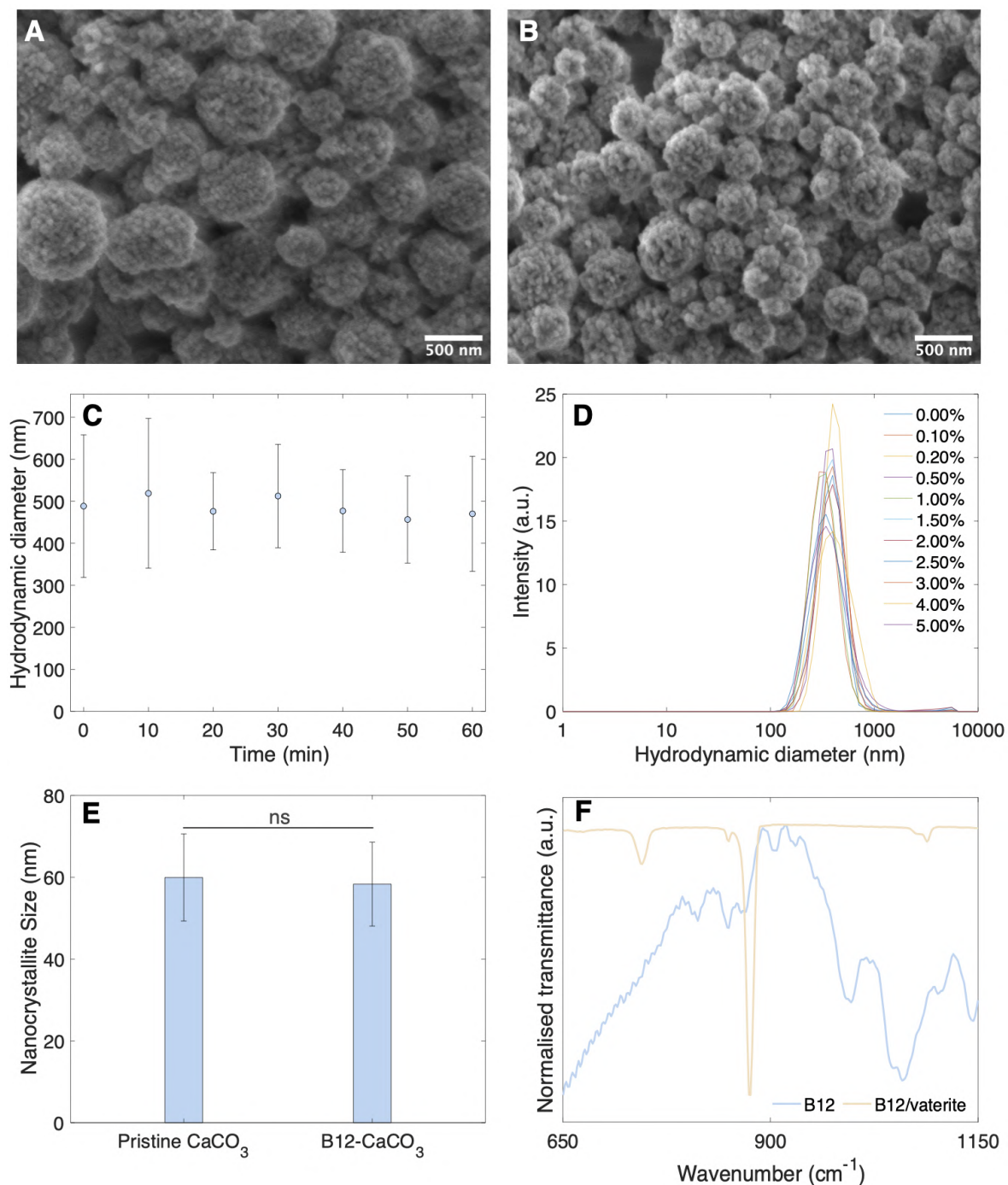
Figure 5.16: SEM images of (A) pristine and (B) B12-loaded CaCO$_3$ crystals. (C) hydrodynamic diameter of B12-loaded CaCO$_3$ crystals overtime, (D) DLS size distributions by intensity of B12-loaded CaCO$_3$ crystals as a function of varying initial B12 concentrations during co-synthesis. (E) Nanocrystallite sizes and (F) FT-IR spectra of both B12 and B12-loaded CaCO$_3$ crystals. Error bars are SD, (C) n=3 and (E) n=100. Statistical analysis made using the one-way ANOVA test; ns: non-significant difference.

5.3 Encapsulation within CaCO$_3$-templated microgels

5.3.1 Dextran encapsulation

Mechanism of encapsulation

The encapsulation capability within S-S (HA/PLL)$_{2.5}$ multilayers using three different methods was evaluated in order to determine a suitable encapsulation approach; these include incubation of DEX$^{\text{FITC}}$ with coated crystals (INC), capture of DEX$^{\text{FITC}}$ via the annealing of multilayers (CAP) and adsorption of DEX onto (HA/PLL)$_{2.5}$ microgels (ADS). This experiment was performed such that there was a final concentration of 1 mg mL^{-1} DEX within each system. Typical radial fluorescence profiles were taken for microgels of similar sizes and fitted with a Gaussian function (Figure 5.17), and their area taken. The average area under the curves for INC, CAP and ADS were 61 $\pm$ 9, 28 $\pm$ 2, and 22 $\pm$ 5 a.u., respectively. Such a drastic difference in the apparent accumulated fluorescence within the INC system compared to that of CAP is to be expected; the coated crystals are able to achieve equilibrium saturation with the DEX prior to CaCO$_3$ dissolution, whereas the CAP system is not allowed to reach such a saturation, hence less DEX is present initially. There is little difference between CAP and ADS system; this is due to the similar kinetics of CaCO$_3$ dissolution and microgel shrinkage, as shown in Figure 5.17. One can infer that the high flux of ions and water leaving the system upon dissolution will reduce the amount of DEX captured upon dissolution, and the resulting fluorescence signal is mostly due to adsorption of DEX onto the microgel (CAP). Therefore, a mechanical trap mechanism leads to greater DEX encapsulation when compared to CAP and ADS, thus encapsulation is much more efficient via the use of co-synthesised CaCO$_3$ crystals.
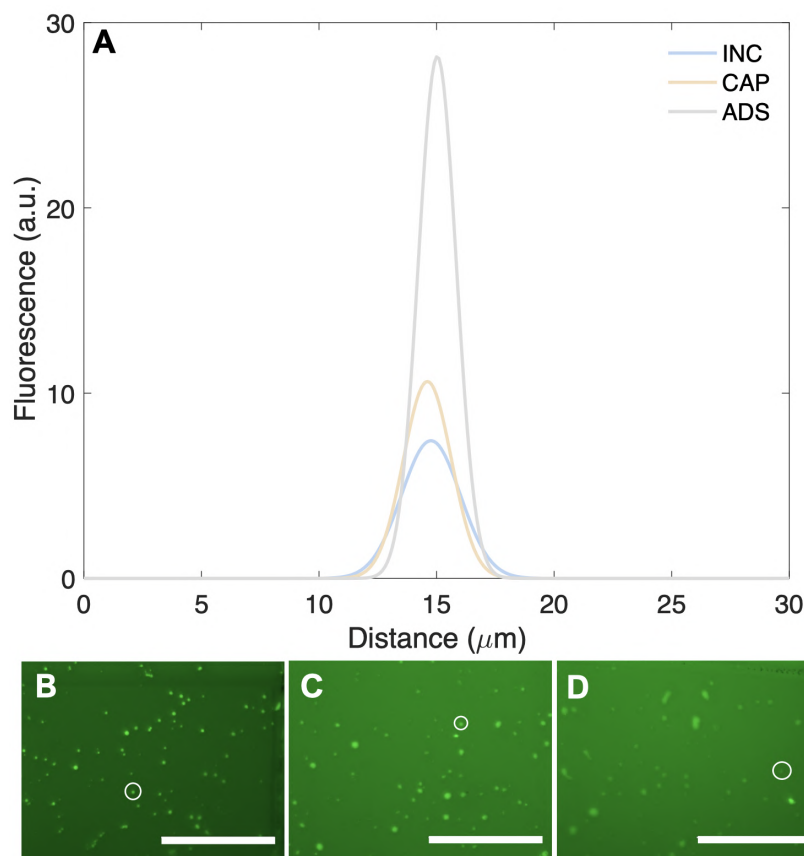
Figure 5.17: (A) Gaussian-fitted fluorescence profiles of (HA/PLL$_{28}$)$_{2.5}$ incubated with 1 mg mL^{-1} 10 kDa DEX^{FITC} under different encapsulation mechanisms: (B) INC, (C) CAP and (D) ADS. Scalebars are 100 μm.

The ability to encapsulate both neutral and charged DEX derivatives has important implications for the prospect of these types of microgels to be utilised as delivery vectors for *in ovo* applications; as aforementioned, the use of an encapsulated DEX matrix may be vital for the encapsulation of small ionic molecules useful *in ovo* feeding applications. Moreover, it will increase the scope of these microgels for use within the wider medical field, including macromolecular therapeutic applications. In recent decades, there is an apparent trend towards the broader use of the pharmaceutics of macromolecular nature, such as antimicrobial peptides, therapeutic proteins and nucleic acids, in medical practice. In this context, the encapsulation of high molecular weight cargo represents an especially important task. The charge of the cargo holds great influence over the targeting of specific macromolecules and drugs. For example, positive charges are useful for cell transduction, and, at the sub-cellular level, for the targeting of the

mitochondria and nuclei, for instance [351–353]. In this respect, one should highlight the prospects of the use of cationic peptides as positively charged macromolecular therapeutics. The ability to encapsulate negatively charged biomacromolecules may be useful for the delivery of nucleic acid therapeutics for potential cancer treatments [354]; neutral therapeutics are helpful to avoid off-target effects that charged therapeutics may possess [353]. The schematic presented in Figure 5.18 illustrates the possible fates of HA/PLL microgels upon dissolution of the CaCO$_3$ template: (step ii-iii) no-to-minimal influence of the payload on the shrinkage, (step ii-iv) hindrance of shrinkage by the encapsulated molecules and (step ii-v) the rupture of the microgels upon template dissolution. Accordingly, crystal cargo can be partially or completely released during the formation of the final microgel structures. These possible fates will be discussed in detail throughout this section.
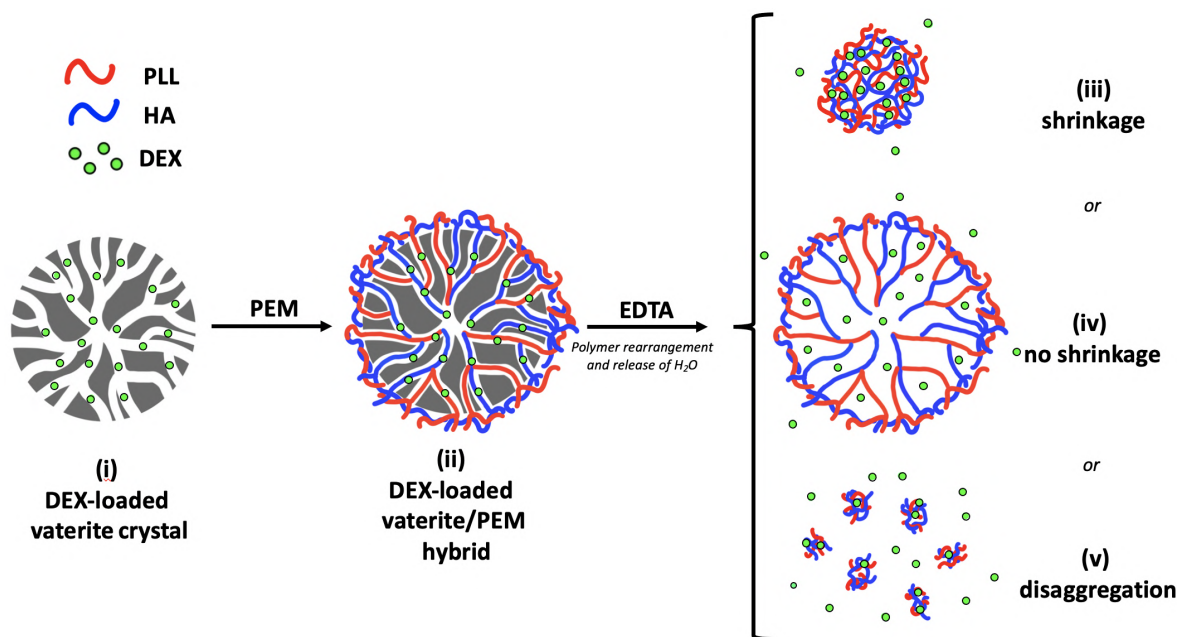
Figure 5.18: Schematic illustration of the fabrication of DEX^{FITC}-loaded HA/PLL multilayer microgels. Formation (i, ii) and possible fates (iii-v) are shown. (i-ii): coating of the hybrid crystals with polyelectrolyte multilayers; (iii-v): shrinkage, no shrinkage, or disaggregation upon the dissolution of the CaCO$_3$, respectively. The possible partial loss of DEX^{FITC} upon template dissolution is also sketched.

Non-ionic DEX encapsulation

The shrinkage of HA/PLL multilayers and the entrapment or release of neutral DEX$^{\text{FITC}}$, driven by the dissolution of the CaCO$_3$, have been monitored via fluorescence microscopy. Notably, There was no detectable desorption of DEX from the surface of the crystals during the washing stages as confirmed via fluorescence profiling (Figure 5.19).
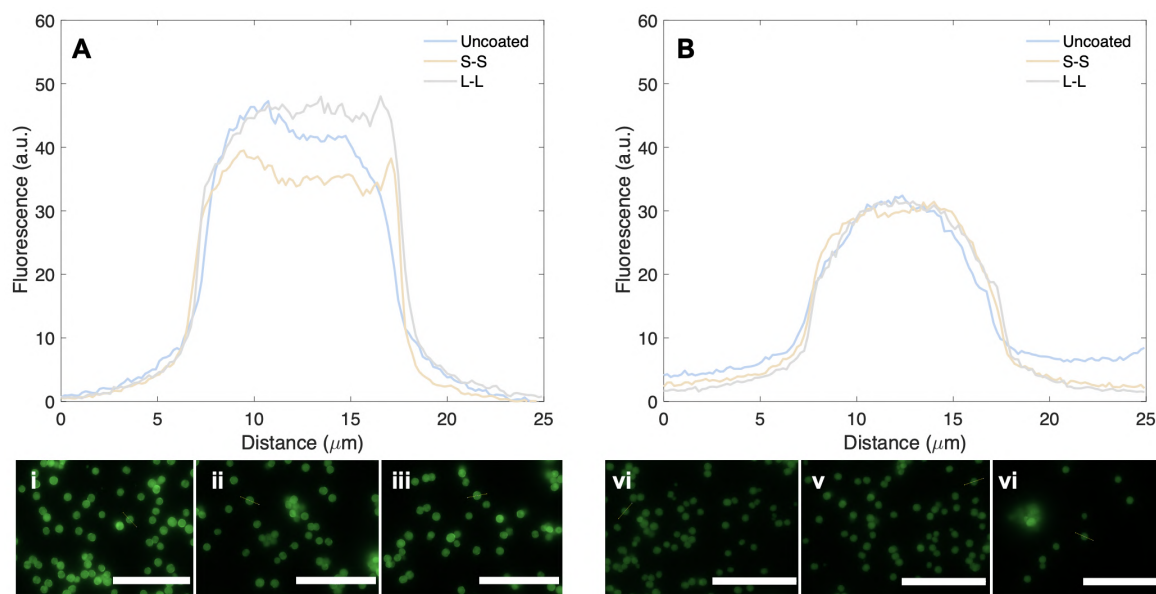
Figure 5.19: Fluorescence images of 4 kDa DEX$^{\text{FITC}}$/vaterite hybrid crystals (i) uncoated, and (ii) S-S, (iii) L-L coated hybrids. Fluorescence images of 2000 kDa DEX$^{\text{FITC}}$/vaterite hybrid crystals (iv) uncoated, and (v) S-S, (vi) L-L coated hybrids. Scalebars are 100 μm. Overlaid fluorescence profiles are displayed above: (A) - 4 kDa DEX$^{\text{FITC}}$ and (B) - 2000 kDa DEX$^{\text{FITC}}$.

Figure 5.20 shows typical images of S-S (HA/PLL)$_{2.5}$-coated DEX$^{\text{FITC}}$/vaterite hybrid crystals and the final polymer structures obtained after the complete dissolution of vaterite via the addition of 40 mM EDTA. Interestingly, S-S HA/PLL multilayers (Figure 5.20) formed using 40 kDa and 70 kDa DEX$^{\text{FITC}}$/CaCO$_3$ hybrids were not stable, and ruptured upon dissolution of the template, releasing DEX$^{\text{FITC}}$ to surrounding medium. When utilising 4 kDa DEX$^{\text{FITC}}$, the microgels remained stable upon dissolution of the vaterite template. This may be attributed to the low amount of DEX co-synthesised into the crystals prior to coating, as confirmed from TGA (0.9 w/w% compared to 2 w/w% for 4 kDa and 40 kDa DEX$^{\text{FITC}}$/vaterite hybrids, respectively). With the

increase of DEX$^{\text{FITC}}$ molecular weight stable S-S microgels have been formed. The dependence of the SC on the molecular weight of DEX$^{\text{FITC}}$ pre-loaded into the porous crystal matrix for both S S and L-L polyelectrolyte pairs is shown in Figure 5.22. Those S-S microgels which were formed (starting from 150 kDa DEX$^{\text{FITC}}$) underwent significantly lower shrinkage compared to HA/PLL microgels produced in the absence of DEX, with no distinct dependence on DEX$^{\text{FITC}}$ molecular weight.
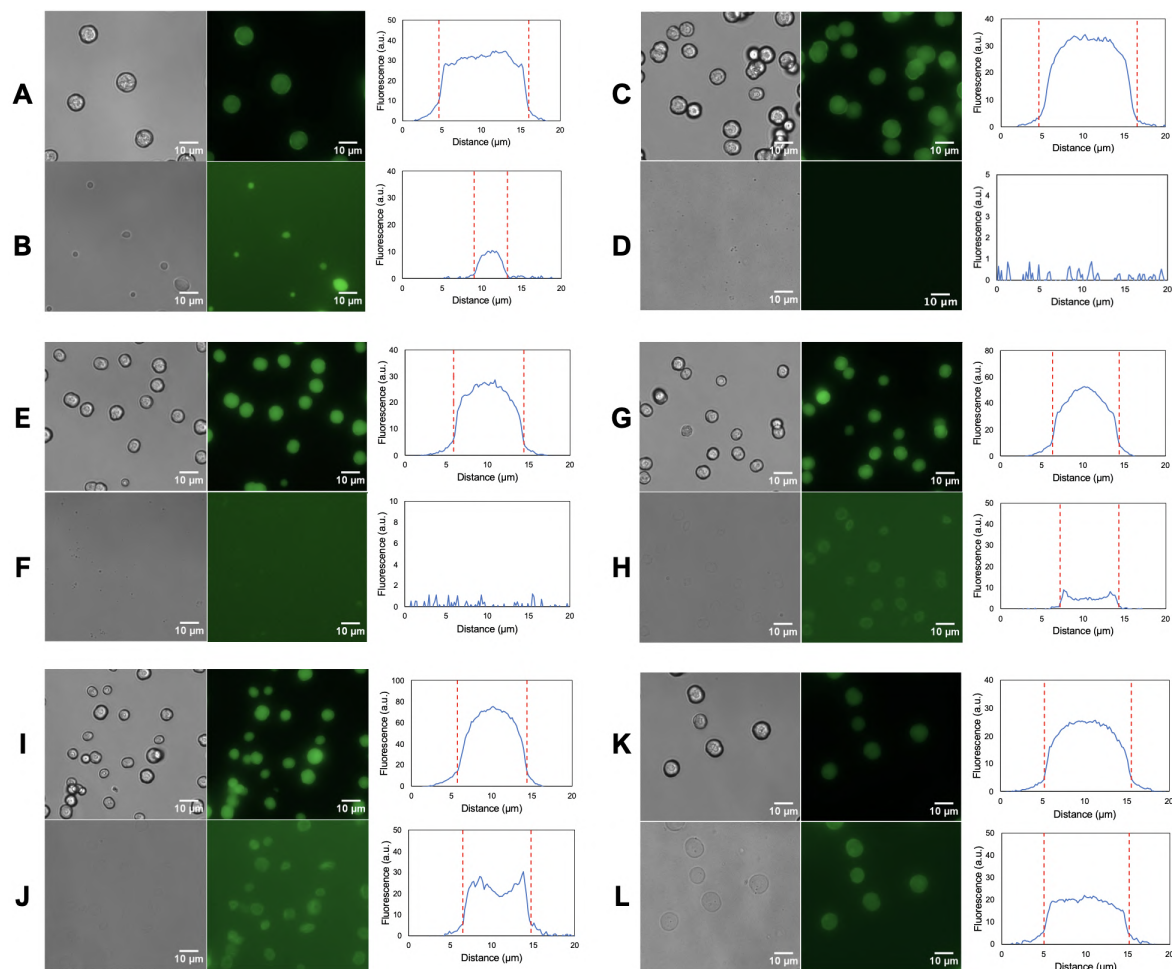
Figure 5.20: Typical transmittance (left) and fluorescence (right) images of S-S-coated DEX$^{\text{FITC}}$/vaterite hybrids (A, C, E, G, I, K) and microgels (B, D, F, H, J, L) following hybrid dissolution with EDTA. Corresponding typical background-subtracted fluorescent profiles are displayed beside the respective fluorescence image. (A, B) 4 kDa, (C, D) 40 kDa, (E, F) 70 kDa, (G, H) 150 kDa, (I, J) 500 kDa and (K, L) 2000 kDa DEX$^{\text{FITC}}$. Scalebars are 10 μm. The dashed-red lines represent the diameters before and after template dissolution.

Similar trends have been observed for the L-L polyelectrolyte pair (Figure 5.21), however, in this case the microgels have been formed even on 40 kDa DEX$^{\text{FITC}}$/CaCO$_3$

hybrids, although the degree of 40 kDa DEX$^{\text{FITC}}$ retention in the microgel was rather low (Figure 5.22). Moreover, microgels formed upon 4 kDa DEX$^{\text{FITC}}$/vaterite hybrids undergo disaggregation. This may be attributed to the small amount of DEX$^{\text{FITC}}$ pre-loaded into the vaterite template, resulting in the lack of shrinkage repression and the rupture of the polyelectrolyte network.
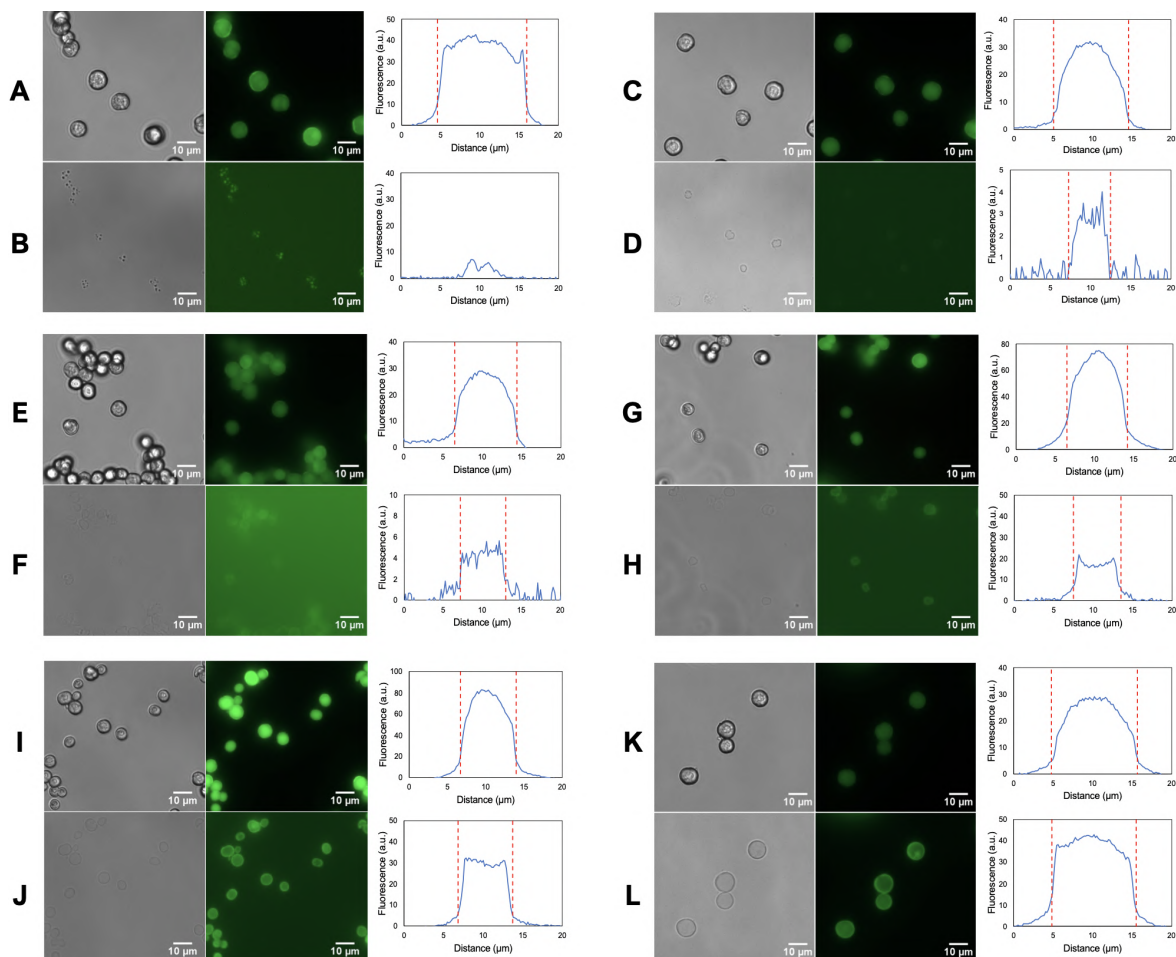
Figure 5.21: Typical transmittance (left) and fluorescence (right) images of L-L-coated DEX$^{\text{FITC}}$/vaterite hybrids (A, C, E, G, I, K) and microgels (B, D, F, H, J, L) following hybrid dissolution with EDTA. Corresponding typical background-subtracted fluorescent profiles are displayed beside the respective fluorescence image. (A, B) 4 kDa, (C, D) 40 kDa, (E, F) 70 kDa, (G, H) 150 kDa, (I, J) 500 kDa and (K, L) 2000 kDa DEX$^{\text{FITC}}$. Scalebars are 10 μm. The dashed-red lines represent the diameters before and after template dissolution.

In order to compare the relative entrapment of DEX$^{\text{FITC}}$ inside the microgels, the relative DEX content has been calculated as the ratio between the fluorescence signal inside and outside the microgel, normalized to the microgel diameter (Figure 5.22). This value reflects the relative dextran content within the microgels, as release of the

DEX$^{\text{FITC}}$ will reduce the fluorescence signal from the microgel interior and increase the signal outside the microgels. This cannot be considered as quantitative analysis but serves as an indicator of the DEX content. Of note, there was no influence of HA and PLL on DEX$^{\text{FITC}}$ fluorescence, as determined by fluorescence spectroscopy (Figure 5.22). The DEX content appeared to increase with increasing DEX molecular weight; this can be attributed to the size of the DEX molecule relative to the pores of the microgels (40 and 2000 kDa DEX have hydrodynamic radii of 6.6 [343] and 26.9 nm [342], respectively). Hence, 2000 kDa may have higher retention due to limited diffusion outwards through the polymer network. Futher, the decrease in the degree of the SC reciprocally correlates with the initial mass amount of DEX$^{\text{FITC}}$ in DEX$^{\text{FITC}}$/CaCO$_3$ crystals (Figure 5.22).
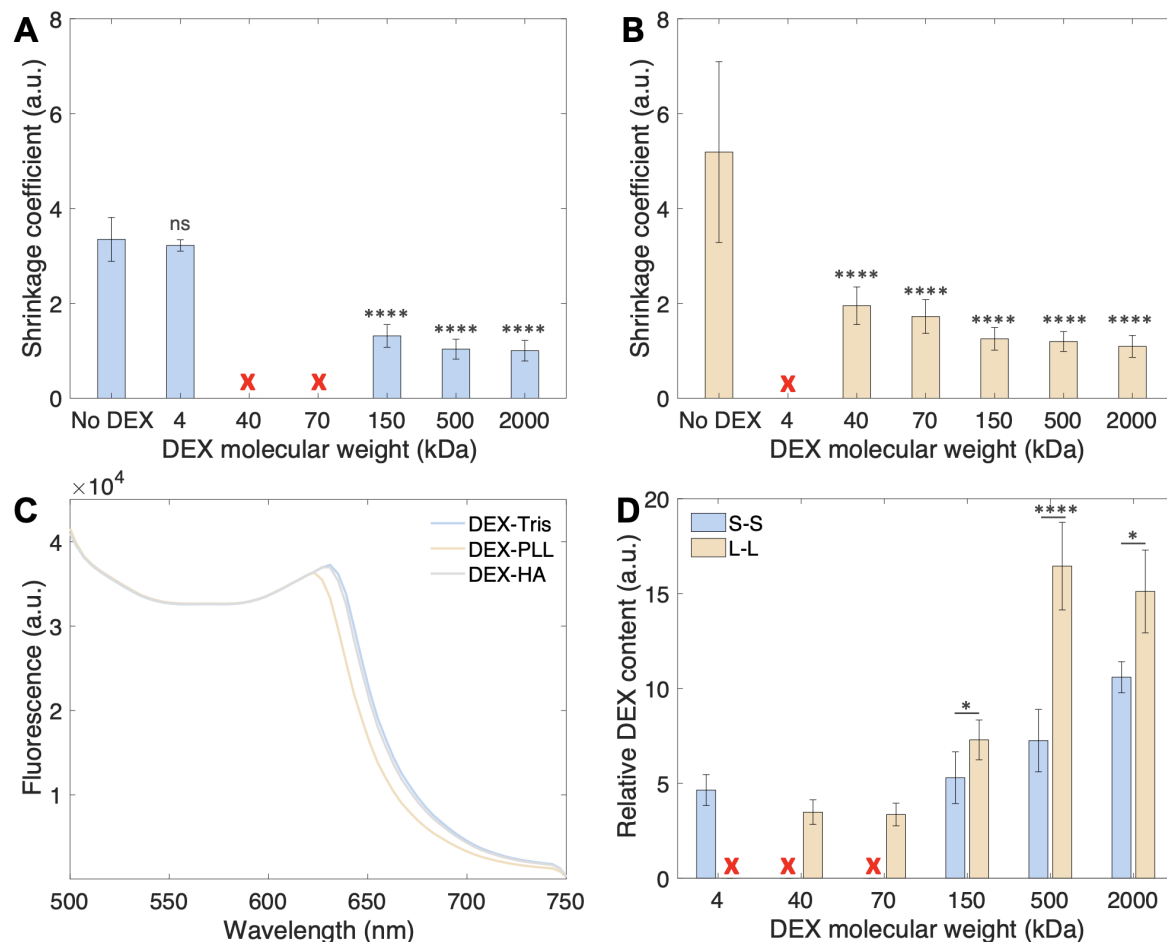
Figure 5.22: The effect of DEX^{FITC} molecular weight on the shrinkage coefficient of (A) S-S and (B) L-L microgels, (C) Fluorescence spectra (excitation wavelength 470 nm $\pm$ 10 nm) of pure DEX^{FITC} and DEX^{FITC} in the presence of HA and PLL (5 mg mL^{-1} DEX^{FITC}, 5 mg mL^{-1} HA and PLL) and the (D) relative DEX^{FITC} content of both S-S and L-L microgels. The red cross represents microgel rupture. Error bars are SD, (A, B) n=50 and (D) n=5. Statistical analysis made using the one-way ANOVA test; ns: non-significant difference, $*p<0.05$, and $****p<0.0001$.

The rupture of HA/PLL multilayers in the case of 40 and 70 kDa DEX may be explained by too high osmotic pressure and the flux of rather small DEX^{FITC} molecules within the microgels upon template dissolution, which led to the disaggregation of microgels into polyelectrolyte complexes. The osmotic pressure of Ca^{2+} ions and coprecipitated 70 and 500 kDa DEXs has been previously estimated upon the dissolution of $\sim$ 9 μm CaCO$_3$ templates. Assuming gel impermeability and instantaneous template dissolution (at 0 s), the osmotic pressure for 70 kDa DEX-loaded CaCO$_3$ was higher than that of 500 kDa DEX by a factor of 7 [89]. Indeed, decreasing the mass content of 40 kDa DEX^{FITC} allowed for the stabilisation of S-S HA/PLL microgels

and the entrapment of DEX^{FITC} (Figure 5.23). This may be due to the lower osmotic pressure generated upon dissolution. Moreover, due to the decreased amount of DEX present within these crystals, there is not enough of a matrix to retain the stability of L-L microgels, resulting in their disaggregation; this highlights the importance of polyelectrolyte molecular weight in regard to the content of vaterite payload and the microgel stability (Figure 5.23).
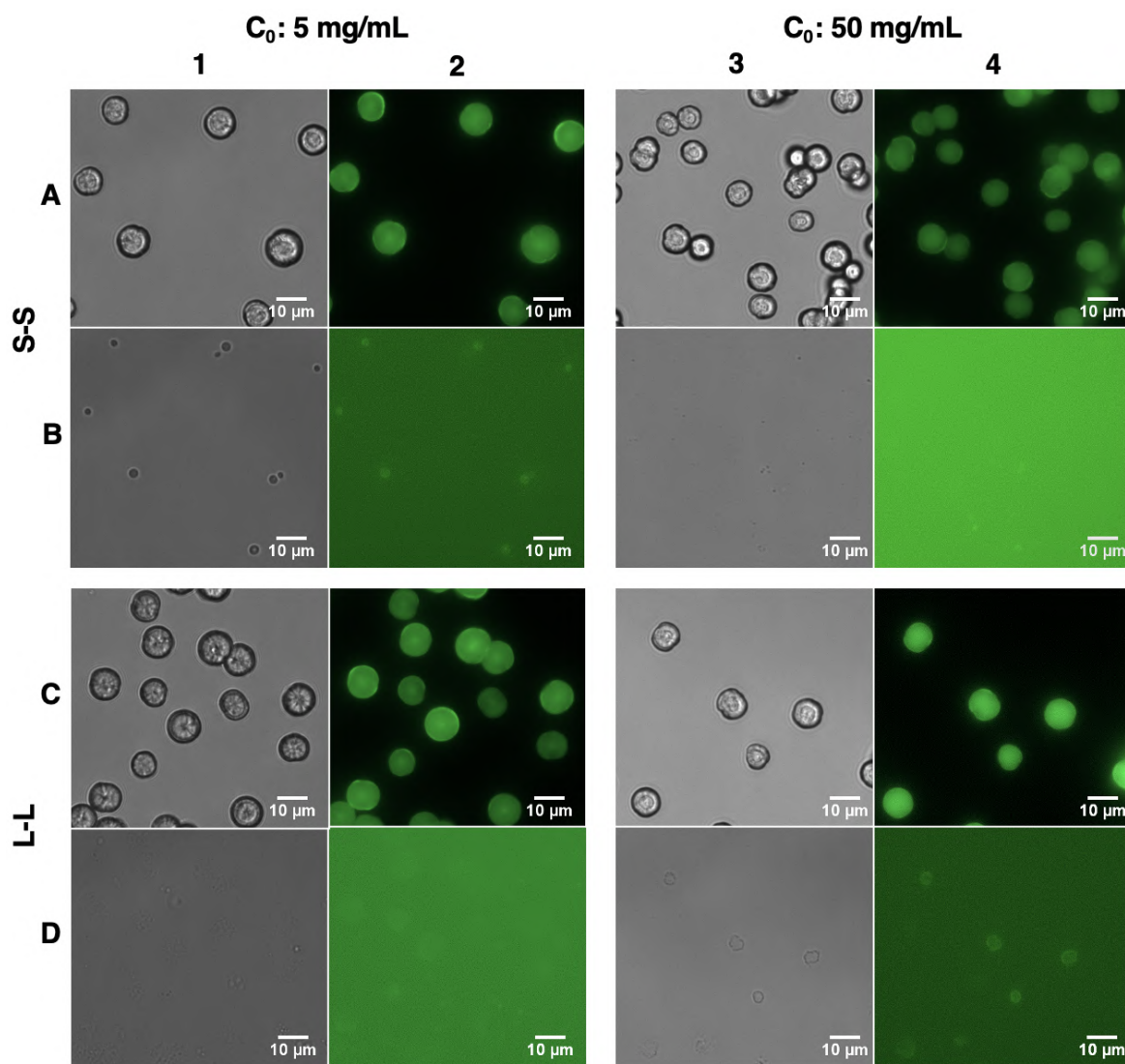
Figure 5.23: The effect of DEX^{FITC} mass content within hybrid crystals on the stability of 40 kDa DEX^{FITC}-loaded (A, B) S-S and (C, D) L-L microgels. Transmittance (1, 3) and fluorescence (2, 4) images of coated crystals (A, C) and microgels (B, D) are shown. CaCO$_3$ crystals have been pre-loaded with DEX^{FITC} via co-synthesis. Scalebars are 10 μm.

.

Increasing the number of polyelectrolyte layers from 5 to 9 had no effect on the forma-

tion of S-S 40 kDa DEX$^{\text{FITC}}$-loaded microgels, implying the osmotic pressure produced upon template dissolution is still too great for (HA/PLL$_{28}$)$_{4.5}$ to withstand. Indeed, there was also no effect upon the shrinkage of the S-S 150 kDa DEX$^{\text{FITC}}$-loaded microgels, but slightly improved the retention of DEX$^{\text{FITC}}$ within the microgels, as indicated by the relative DEX content elevation from 11.1 $\pm$ 0.5 to 14.6 $\pm$ 1.9 a.u. (Figure 5.24). It is likely here that the shrinkage of these microgels at these layer numbers remains unaffected due to the presence of DEX within the vaterite crystal pores. DEX acts to partially block the crystal pores, and it may be that 5 layers is already enough to saturate the remaining free volume of the crystal with polyelectrolyte, resulting in the little difference in shrinkage observed.
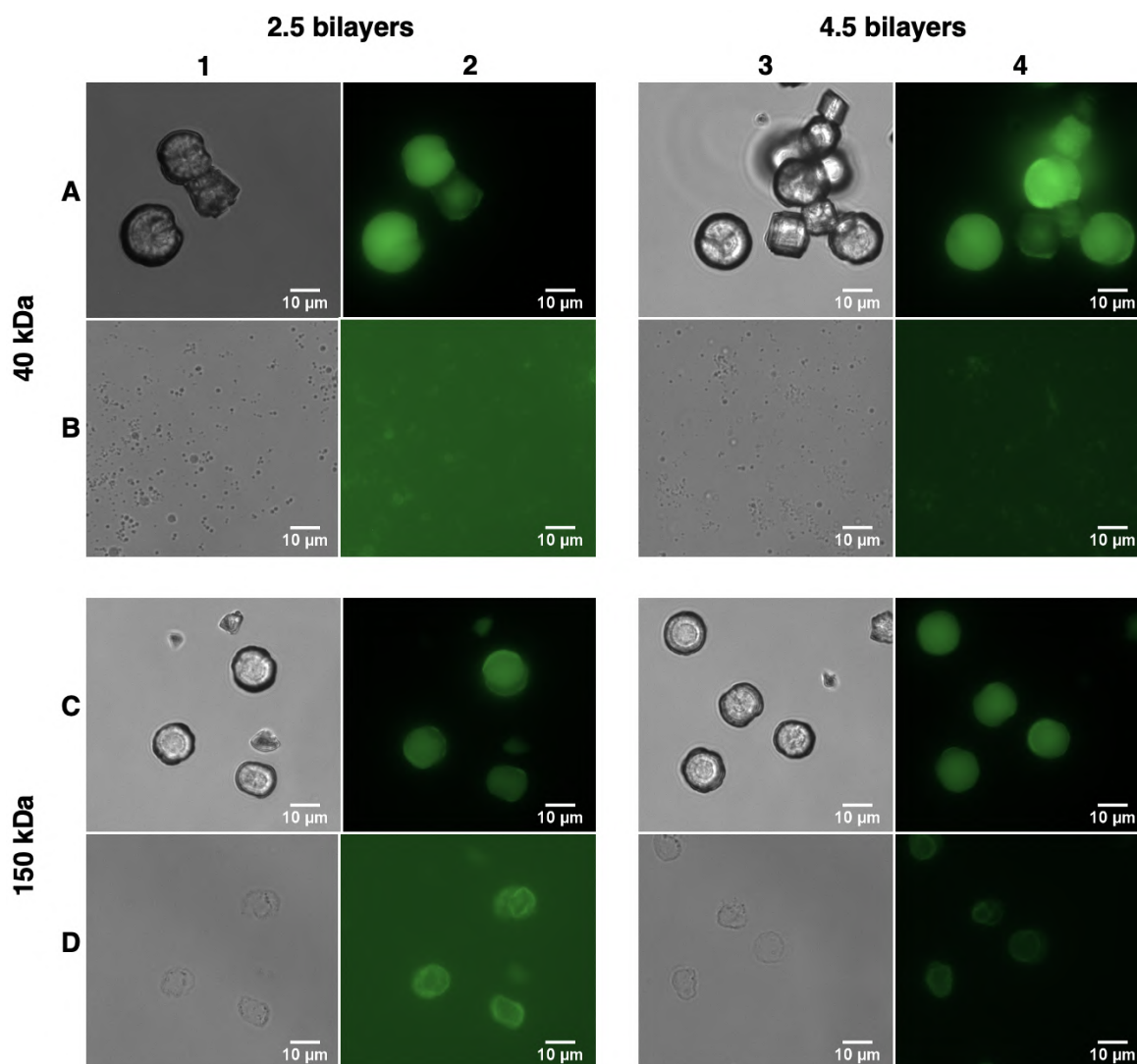
Figure 5.24: The stability of both (A, B) 40 kDa and (C, D) 150 kDa DEX^{FITC}-loaded S-S microgels formed of (1, 2) 2.5 and (3, 4) 4.5 bilayers. Transmittance (1, 3) and fluorescence (2, 4) images of coated crystals (A, C) and microgels (B, D) are shown. CaCO$_3$ crystals have been pre-loaded with DEX^{FITC} via co-synthesis (C$_0$: 50 mg mL^{-1}). Scalebars are 10 μm.

Ionic DEX encapsulation

For the investigation of the effect of negative and positive net charge of the cargo on the shrinkage and cargo entrapment efficiency, S-S microgels were fabricated using 40 kDa CM-DEX^{FITC}/vaterite and DEAE-DEX^{FITC}/vaterite crystals. Whilst neutral 40 kDa DEX^{FITC} causes increased osmotic pressure leading to the rupture of the microgels, both negatively and positively charged derivatives of DEX^{FITC} did not significantly affect the SC of the microgels (SCs of 4.0 $\pm$ 1.1 and 2.5 $\pm$ 0.6 for CM- and DEAE-

158

DEX, respectively) and remain encapsulated within the microgels (Figure 5.25).
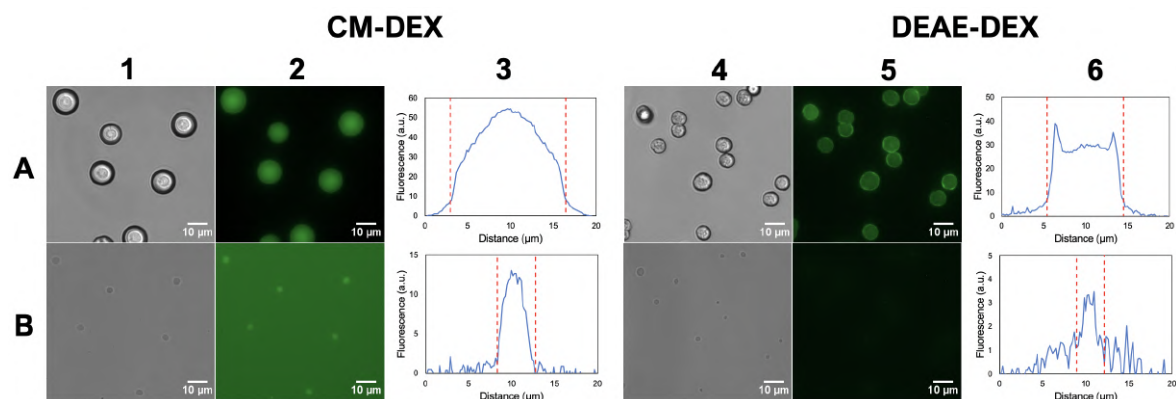
Figure 5.25: Transmittance (1, 4) and fluorescence (2, 5) images of S-S coated DEX^{FITC}-loaded (A) CaCO$_3$ crystals and (B) microgels. 40 kDa CM- (left) and DEAE- (right) DEX^{FITC} systems are shown. (3, 6) Corresponding typical background-subtracted fluorescent profiles are also shown for both microgels and coated crystals besides the respective fluorescence image. The dashed-red lines represent the diameters before and after template dissolution. Scalebars are 10 μm.

Mechanism of macromolecular entrapment

In contrast to uncharged DEX^{FITC}, charged DEX^{FITC} interacts with the polymer chains of opposite charge (Figure 5.26). Inter-polymer interactions in the microgels depicted in Figure 5.26, demonstrate how the interaction of DEXs of different charges affects the annealing of these multilayers. As soon as the solid CaCO$_3$ matrix is dissolved by EDTA, voids left after the carbonate core removal can close due to the collapsing of the polymer multilayers. This is caused by an annealing process when polymer chains with significant dynamics can find each other to compensate their charges. Another factor promoting the annealing is an increase in the ionic strength during the dissolution of the CaCO$_3$ matrix. The ionic strength increases the polymer dynamics due to the significant extrinsic compensation (by counter-ions, in this case Ca^{2+} and CO$_3$$^{2-}$) of permanent polymer charges. However, in the case of a very high ionic strength, the extrinsic compensation can dominate over intrinsic compensation, resulting in the partial or full decomposition of the multilayers (Figure 5.26). This is what is presumably occurring upon microgel decomposition into small pieces (Figure 5.18 (1, step ii-v)). Below, the effect of DEXs of different charges upon multilayer annealing will be

described in further detail.
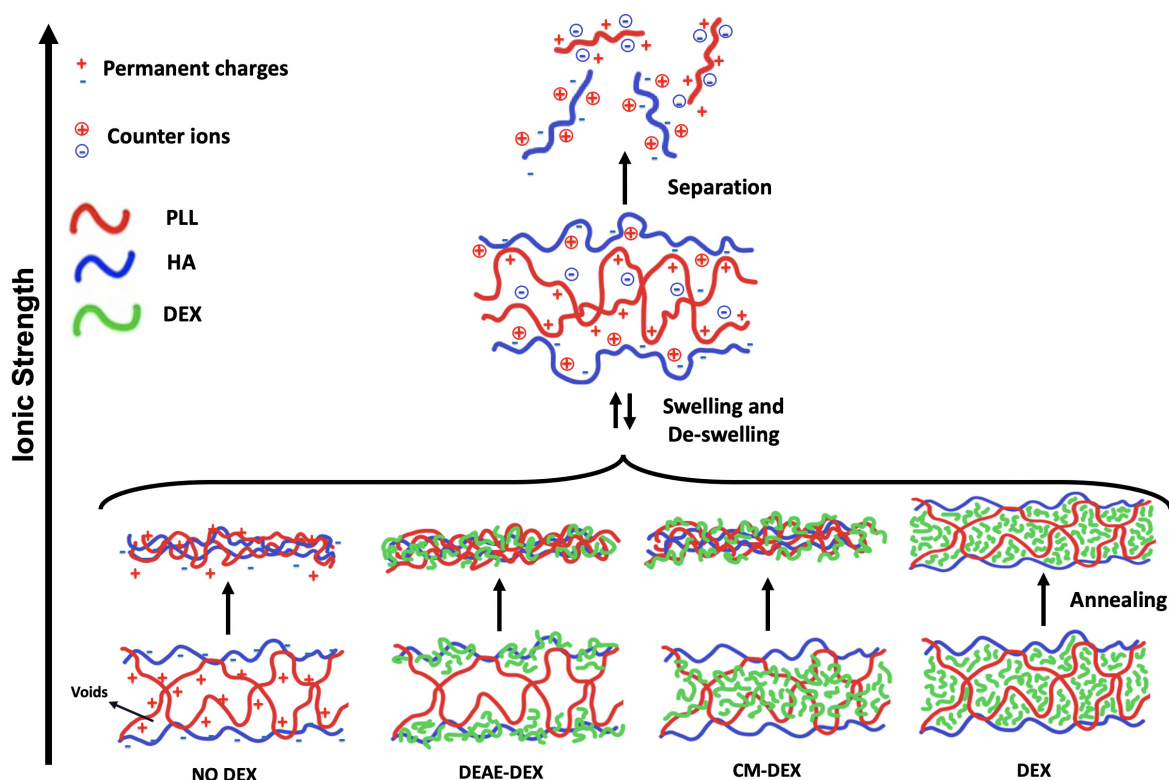
Figure 5.26: Schematic displaying the effect of different charge modifications of DEX upon the annealing of HA/PLL multilayers in the formed microgels, as well as the effect of increasing ionic strength on multilayer stability.

CM-DEX$^{\text{FITC}}$ and DEAE-DEX$^{\text{FITC}}$ better adopt to the oppositely charged polyelectrolyte backbones, which allows for intrinsic charge compensation (via permanent charges on the DEX backbone) and annealing of the multilayers, of which results in microgel shrinkage comparable with that of the microgels templated on pristine vaterite crystals. The retention of negatively charged CM-DEX$^{\text{FITC}}$ appeared to be significantly higher than that for DEAE-DEX$^{\text{FITC}}$ (Relative DEX content of 9.0 ± 0.7 and 4.6 ± 0.9 a.u. for CM- and DEAE-DEX, respectively). A plausible reason for this is the electrostatic binding of CM-DEX$^{\text{FITC}}$ to the amino groups of PLL within the crystal pores, whilst DEAE-DEX$^{\text{FITC}}$ does not interact with PLL and enters interaction with the oppositely charged HA backbone only during the dissolution of the core and rearrangement of the multilayers. There is typically an excess of PLL (about two times per mole of charged groups) present in HA/PLL multilayers when the system is left to equilibrate [333]; this may impact the extent of retention of charged species.

5.3.2   Silver nanoparticle encapsulation

AgNPs were synthesised and provided by Ana Ferreira, NTU. AgNPs have been encapsulated into (HA/PLL$_{28}$)$_{4 \text{ and } 4.5}$ microgels. Such nanoparticles, although highly useful for *in ovo* feeding, also act as a model for further NPs to be encapsulated into such biopolymer microgels (e.g. mineral-based NPs including selenium, zinc etc.). AgNPs were produced with capping agents of the same molecular weight (40 kDa) and various electrostatic charge, including polyvinylpyrrolidone, DEX, CM-DEX and DEAE-DEX. The use of capping agents aids in the colloidal stabilisation of these particles by either electrostatic repulsion or steric hindrance. Figure 5.27 shows TEM images of the AgNPs used in this study. The observed particles were spherical in shape with an average size of 13 ± 3.2, 7 ± 2.3, 7 ± 2.8 and 10 ± 2.5 nm for PVP-, DEX-, CM-DEX-, DEAE-DEX-capped AgNPs, respectively. These AgNPs have been characterised fully in [21].
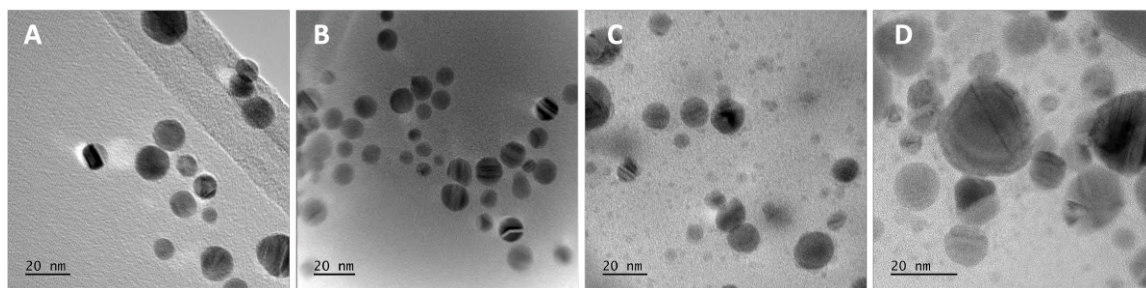
Figure 5.27: TEM images of (A) PVP- (B) 40 kDa DEX- (C) 40 kDa DEAE-DEX- and (D) 40 kDa CM-DEX-capped AgNPs. Scalebars are 20 nm. TEM was performed by Ana Ferreira, NTU.

The stability of these nanoparticles is crucial regarding their antimicrobial properties and dictates their future use in bioapplications [47, 355, 356]. AgNP stability was determined in either ultrapure water or 0.2× Tris buffer solution (the same working buffer used throughout this work) via UV-vis. All AgNPs present in water are stable and hold a maximum absorbance (λ_{max}), or surface plasmon resonance peak, of approximately 400 nm (Figure 5.28), which is typical for such AgNPs [357, 358]. However, when replaced into 0.2× Tris, DEX and CM-DEX capped AgNPs exhibit broadened peaks, which is typical if destabilisation and aggregation of the particles occurs [355]

(Figure 5.28 (B,D)). This is likely due to the screening or displacement of the capping layer with the ions present in the Tris buffer solution. Indeed, it has been shown that CaCl$_2$ induces this peak shift and broadening, of which 10 mM is present within the buffer solution. PVP and DEAE-DEX remain stable and display a similar λ_{max} in both water and Tris buffer solutions (Figure 5.28 (A,C)). These observations were also accompanied by a distinct change in the colour of the suspensions. Stable AgNP suspensions (i.e. PVP and DEAE-DEX) remain a yellow/light brown colour, where more unstable suspensions (DEX and CM-DEX) turn a darker brown or grey in colour [21].
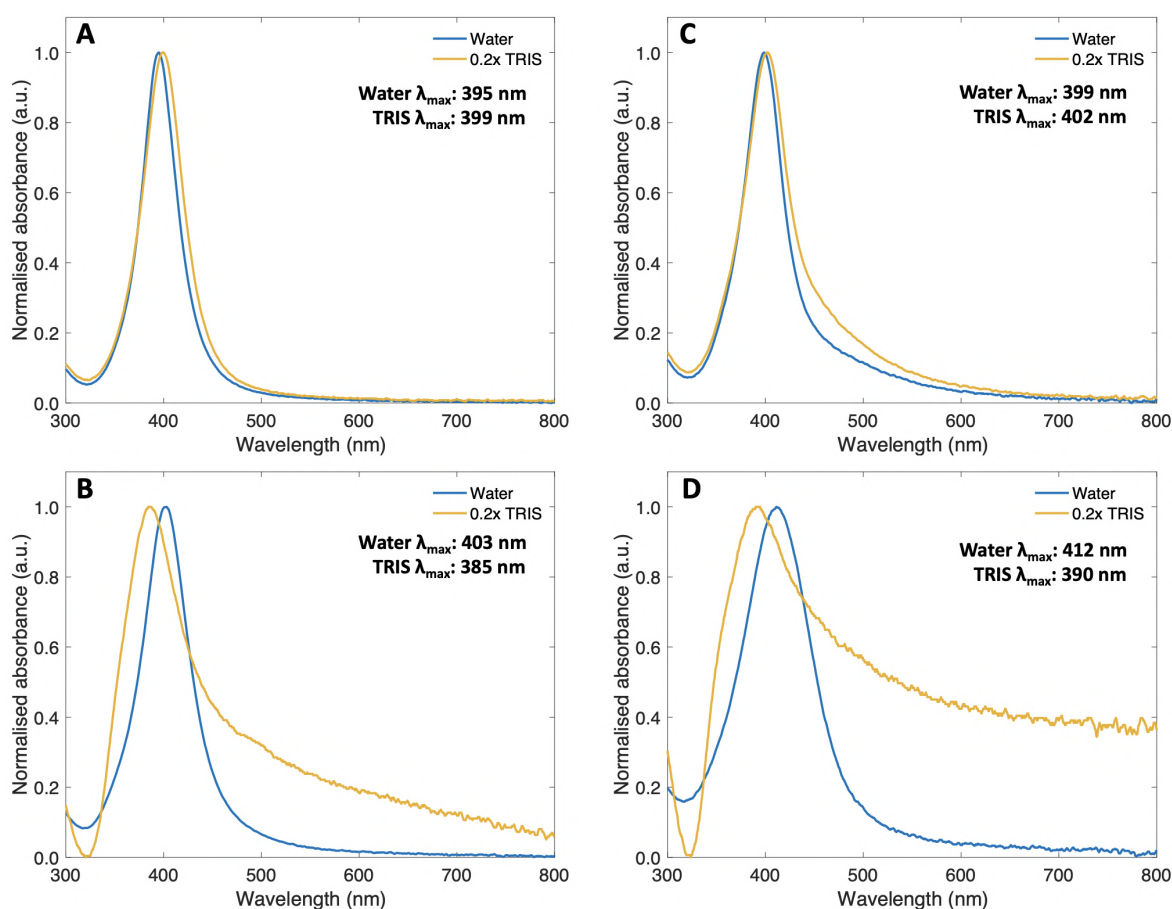
Figure 5.28: Normalised UV-Vis spectra of coated silver nanoparticles suspended in water or 0.2× Tris, pH 7.9. PVP-capped (A), DEX-capped (B), DEAE-DEX-capped (C), and CM-DEX-coated (D) AgNPs.

A schematic is displayed in Figure 5.29, illustrating the fabrication of AgNP-laden microgels. The AgNPs were encapsulated via an adsorption approach, in which AgNP suspensions were incubated with (HA/PLL$_{28}$)$_{\mathrm{n}}$ coated CaCO$_3$ crystals (either 4 or 4.5 bilayers) following EDTA treatment. This was performed in both water and 0.2× Tris

buffer solution, pH 7.9. 4 and 4.5 bilayers were used for AgNP adsorption due to the larger microgel sizes produced. This ensured for the facile visualisation of AgNP-laden microgels and greater microgel surface coverage for subsequent UV-Vis stability studies.
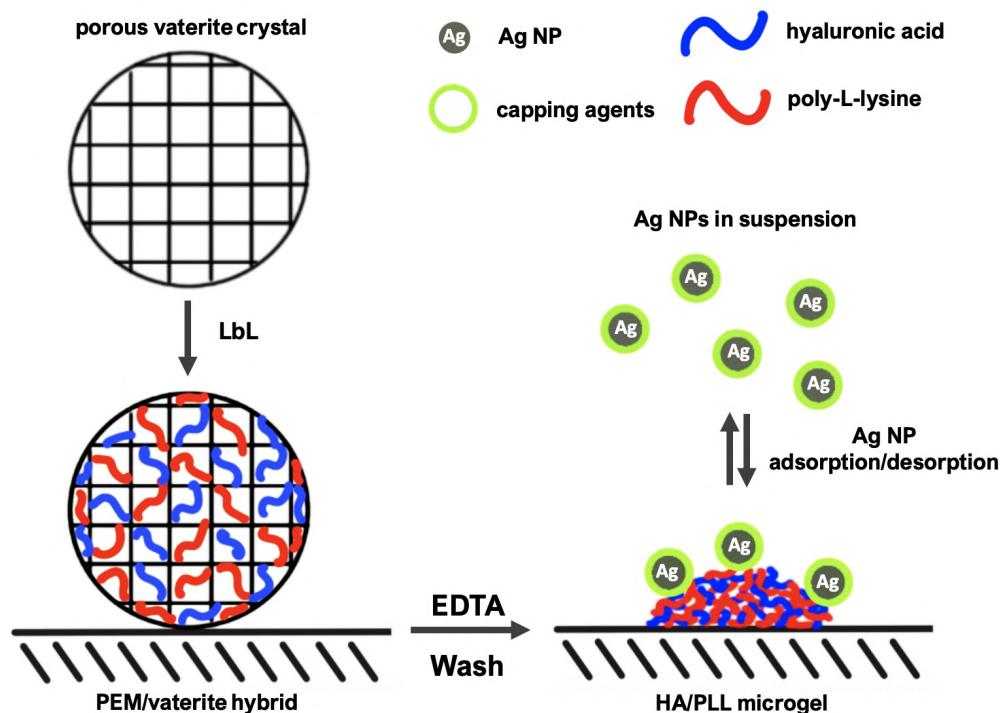
Figure 5.29: Schematic illustrating the formation of AgNP-laden HA/PLL microgels.

Regarding (HA/PLL)$_4$ microgels (Figure 5.30), in water (pH 6.1), the only notable difference in respect to the transmittance images was the interaction between DEX/CM-DEX- capped AgNPs and the microgels. DEX-capped AgNPs appear to saturate the microgel, resulting in the reduced light transmittance when compared to the pristine microgels (no AgNPs). Further, DEX-capped AgNPs appear to settle and bind to the area surrounding the microgel (up to $\simeq 3$ μm from the microgel exterior), suggesting the microgels possess a surrounding polyelectrolyte matrix which is also adhered to the surface immediately surrounding them - perhaps any excess polyelectrolyte released upon microgel annealing. However, this excess polymer would likely be observed during the fluorescence imaging of the pristine microgels, which was not observed. Therefore, this may be result of the polymer dynamics within the system; indeed, it has been demonstrated that polymers within microgel and multilayer systems are able, to an

extent, freely diffuse throughout their structures [130]. It may be here that excess PLL is released into the microenvironment of the microgel and interacts and binds with the AgNPs of negative surface charge, resulting in their binding and adherence in the immediate vicinity of the microgels. As observed with CM-DEX-capped AgNPs, this also occurs, however, much less homogenously opposed to DEX-capped AgNPs. The various AgNPs also behave similarly when incubated with (HA/PLL)$_{4.5}$ microgels (Figure 5.31) within water, CM-DEX however, to a lesser extent, likely due to the electrostatic repulsion of the CM-DEX capping layer and the HA exterior of the microgel. PVP-capped AgNPs appear to interact stronger with (HA/PLL)$_{4.5}$ microgels, however, it is unclear as to why due to the slight negative zeta potential of PVP AgNPs, as reported in [21], suggesting this is the result of a non-electrostatic interaction between PVP and the HA terminating layer of the microgel (e.g. hydrogen bonding). Moreover, despite this negatively charged terminating microgel layer, DEAE-DEX-capped AgNPs displays no obvious visual interaction according to these transmittance images.

When incubated in 0.2× Tris buffer solution, all AgNPs appear to adsorb to the microgels besides that of CM-DEX-capped AgNPs which displays aggregation, as was expected from the peak broadening in Figure 5.28. Interestingly, the presence of the Tris buffer solution results in the partial adherence of AgNPs to the glass or ibidi-polymer surface. This may indicate the potential role of these salts in the adhesion process of such biopolymers to the surface, as such adhesive aggregates were not observed in the presence of ultra-pure water. In both 4 and 4.5 bilayer systems, there is a significant difference between DEAE-DEX-capped AgNPs in Tris compared to that in ultrapure water in terms of the transmittance through the microgels, with dark grey or almost black microgels produced when in the presence of Tris, suggesting a large uptake/adsorption of AgNPs. When in the presence of 4.5 bilayer microgels, DEAE-DEX-capped AgNPs induces a swelling phenomenon within the microgel as evidenced by the increase in size between Figure 5.31 (C,D); indeed, this implies the AgNPs are uptaken into the microgel network at these conditions, likely aided by the increase in ionic strength and electrostatic attraction between positively charged DEAE-DEX and

negatively charged HA.
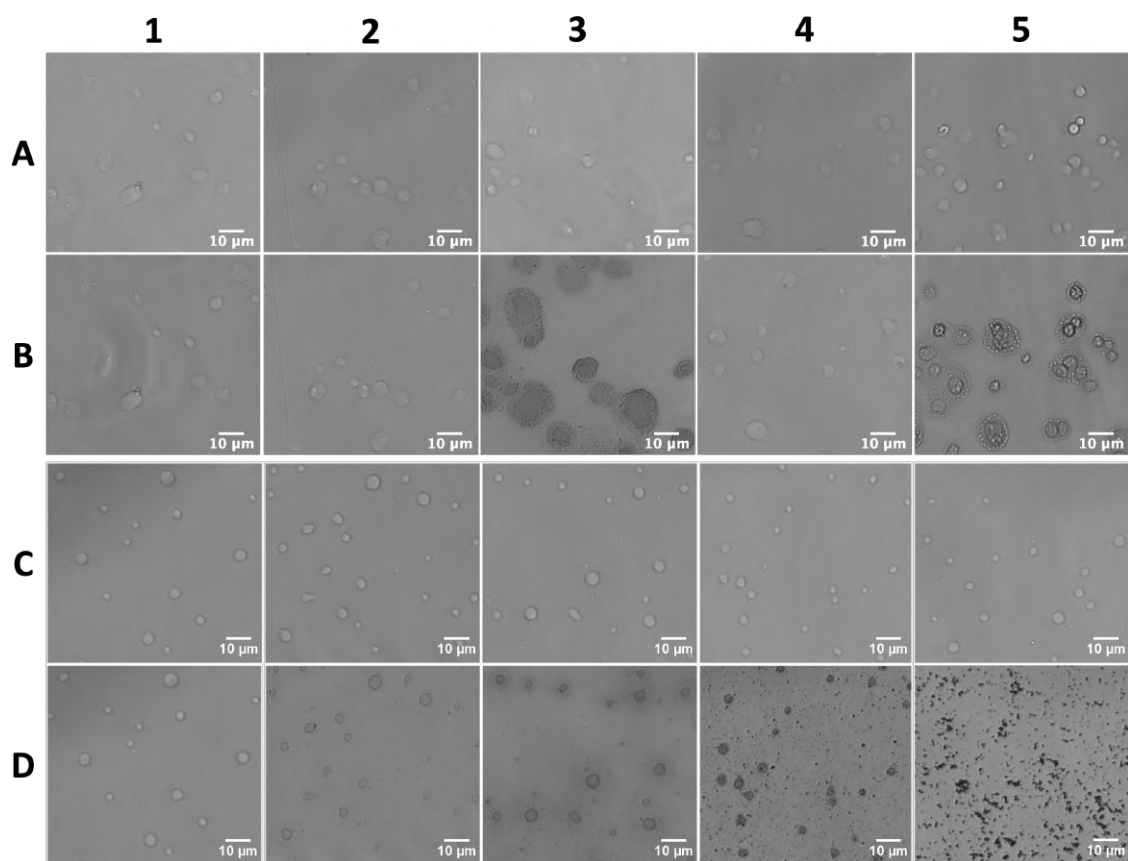
Figure 5.30: Transmittance images of (HA/PLL$_{28}$)$_4$ microgels before (A, C) and after (B, D) incubation with the various coated silver nanoparticles within water (A, B) and 0.2× Tris buffer 7.9 (C, D). No Ag (1), PVP-capped (2), DEX-capped (3), DEAE-DEX-capped (4), and CM-DEX-capped (5) AgNPs. Scalebars are 10 μm.
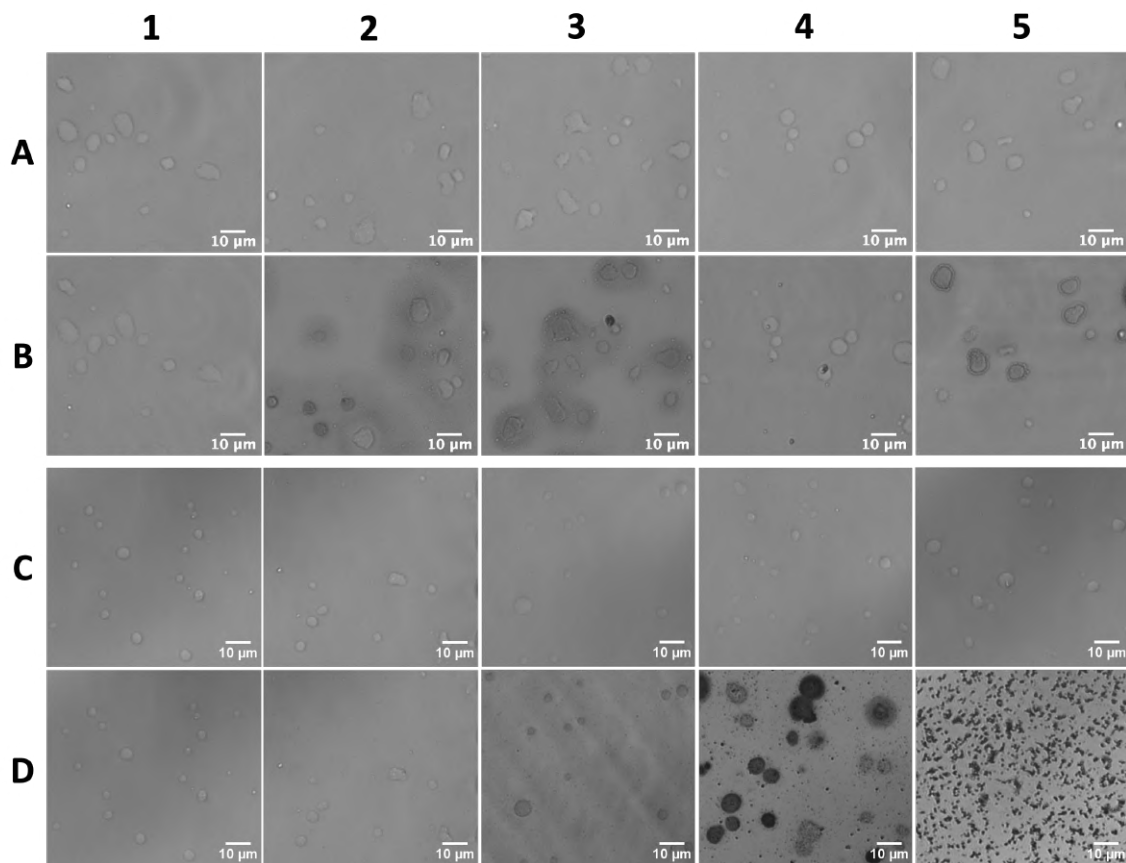
Figure 5.31: Transmittance images of (HA/PLL$_{28}$)$_{4.5}$ microgels before (A, C) and after (B, D) incubation with the various coated silver nanoparticles within water (A, B) and 0.2× Tris buffer, pH 7.9 (C, D). No Ag (1), PVP-capped (2), DEX-capped (3), DEAE-DEX-capped (4), and CM-DEX-capped (5) AgNPs. Scalebars are 10 μm.

Figure 5.32 illustrates the typical UV-Vis spectra of the various AgNPs following incubation and washing with both 4 and 4.5 bilayer HA/PLL microgels in ultrapure water and in the Tris buffer solution. These spectra were performed on glass coverslips within quartz cuvettes; of note, the behaviour of these AgNP-laden microgels was similar to that upon the ibidi surface used for transmittance screening. From these spectra, peak widening is evident in DEX- and CM-DEX-capped AgNPs, suggesting these NPs aggregate in the presence of these polyelectrolytes. Bathochromic shifts to higher wavelengths are noted for all AgNPs when incubated with the microgels in both water and the Tris buffer solution when compared to their respective bulk absorbance. This shift, also denoted red shift, is typically due to the presence of larger nanoparticles or growth in their size; this implies the potential aggregation of the AgNPs [355], perhaps due to the presence and adsorption of polyelectrolytes to the NP surface - such

166

wavelength shifts are summarised in Tables 5.3 and 5.4.

Table 5.3: The shift of λ_{max} of various capped AgNPs within 4 and 4.5 BL from λ_{max} of the AgNPs in the bulk in water.

System	Difference in λ_{max} from Ag in the bulk			
	PVP	DEX	DEAE-DEX	CM-DEX
Ag, no microgels	-	-	-	-
Ag, 4 BL microgels	+6	+11	+8	+15
Ag, 4.5 BL microgels	+4	+2	+8	+10

Table 5.4: The shift of λ_{max} of various capped AgNPs within 4 and 4.5 BL from λ_{max} of the AgNPs in the bulk in 0.2× Tris buffer solution, pH 7.9.

System	Difference in λ_{max} from Ag in the bulk			
	PVP	DEX	DEAE-DEX	CM-DEX
Ag, no microgels	-3	+1	+4	+8
Ag, 4 BL microgels	+1	+7	+5	+11
Ag, 4.5 BL microgels	+3	+5	+7	+6
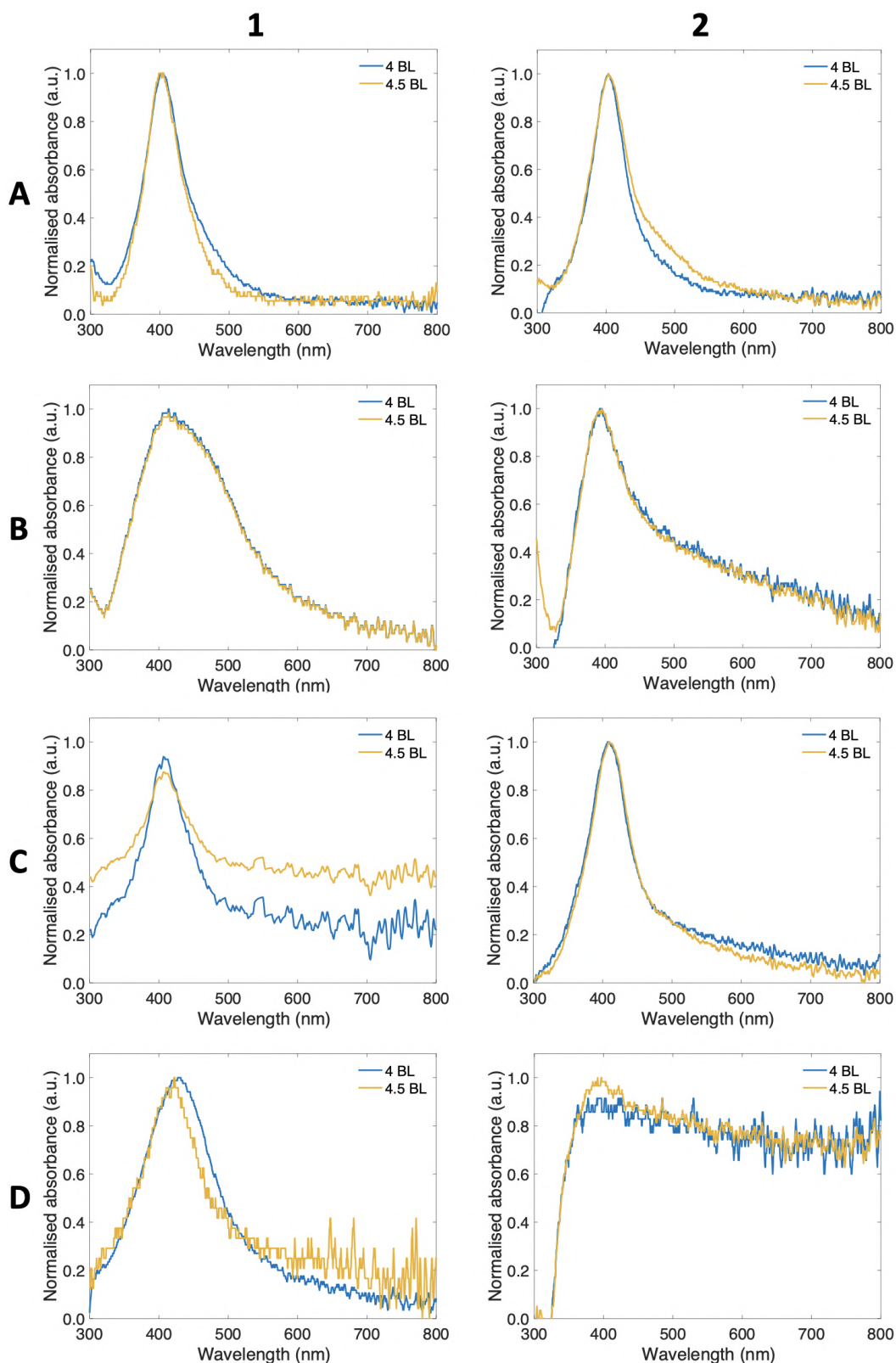
Figure 5.32: Normalised UV-Vis spectra of the various silver nanoparticles adsorbed to (HA/PLL$_{28}$)$_4$ and (HA/PLL$_{280}$)$_{4.5}$ (4 BL and 4.5 BL, respectively) within water (1) and 0.2× Tris buffer pH 7.9 (2). PVP-capped (A), DEX-capped (B), DEAE-DEX-capped (C), and CM-DEX-capped (D) AgNPs.

5.4 Conclusion

The influence of DEX and its charged derivatives on the crystallisation and stability of the vaterite was investigated. DEX was incorporated into the vaterite crystals via co-synthesis at physiologically relevant pH 7.4. The presence of DEX, DEAE-DEX, or CM-DEX did not influence the polymorphism of the crystals and had negligible effect on the crystal size, as shown by FT-IR, optical and fluorescence microscopy, as well as SEM. The incorporation of non-ionic DEX decreased the nanocrystallite size, and lead to the partial blocking the crystal pores. Variation of the molecular weight of DEX had no significant influence on these effects. CM- and DEAE-DEX increased the overall crystal porosity without influencing the crystal size. In addition, the inclusion of CM-DEX significantly retarded the vaterite-to-calcite recrystallisation within the pH range of 5.7-9, whereas DEAE-DEX did not affect the kinetics of recrystallisation. From these data, vaterite $CaCO_3$/DEX hybrids of sizes 500 nm to ~16 μm were successfully synthesised; it was found that the effects of DEX are independent upon the crystal sizes formed throughout this thesis. Increasing the molecular weight of DEX resulted in increased DEX mass content in the crystals, as shown via TGA; this content was also directly dependent upon the charge of the DEX, wherein CM-DEX mass content within the crystals was significantly increased when compared to DEAE-DEX, which was reduced - this effect was observed independent of the crystal size and remained less than 10% w/w.

The effects of this co-synthesised DEX on the shrinkage of HA/PLL microgels has been investigated. The inclusion of neutral DEX decreases the shrinkage coefficient several times, of which is dependent upon the mass content of DEX pre-loaded into the crystals. Osmotic pressure due to the ions produced during microgel formation accompanied by the $CaCO_3$ dissolution and the presence of DEX leads to the rupture of HA/PLL multilayers and disaggregation of the microgels. By decreasing DEX mass content, the stabilisation of the microgels is achieved. Interestingly, no dependence on the number of polyelectrolyte layers (5 and 9 deposited layers have been tested) on

the shrinkage of DEX microgels was found. In contrast to neutral DEX, charged DEX interacts with the polymer chains of opposite charge and results in microgel shrinkage comparable with that for microgels templated on pristine vaterite $CaCO_3$ crystals. Interestingly, the retention of negatively charged CM-DEX appeared to be higher than that of positively charged DEAE-DEX.

HA/PLL microgels have also been utilised to encapsulate AgNPs via adsorption. Indeed, it was found the extent of AgNP adsorption was dependent upon the capping layer of both the NP and the microgel, owing to the electrostatic attraction and repulsion between the two polymer layers. The ionic strength of the medium also held a pronounced affect on the extent of AgNP encapsulation, as was demonstrated via optical microscopies.

Chapter 6

in ovo delivery of vectors

6.1 Introduction

In this Chapter, the microstructure of the eggshell is presented, paying particular interest to eggshell porosity and permeability. Preliminary results regarding a novel injection-free method of *in ovo* delivery are also presented, as well as a discussion of the suitability of $CaCO_3$ vaterite crystals and newly developed biopolymer-based microgels as potential vectors for IOF.

6.2 Eggshell characterisation

6.2.1 Eggshell structure

Class A free-range chicken eggs (average weight of $\sim$60 g) were purchased from British supermarkets and characterised accordingly. Upon the surface of the egg lies the cuticle (Figure 6.1) of the eggshell acts as a protective waxy, water-insoluble layer mainly constituting of glycoproteins. The cuticle itself is uneven and ranges in thickness over the surface of the eggshell (0.5 - 12.8 μm in thickness) [359]. The layer itself is host to micrometre-thin cracks as well as funnel-like pores [360] (diameters of $\sim$10 μm [361, 362]), as shown in Figure 6.1; such cracks and pores allow for gaseous exchange.
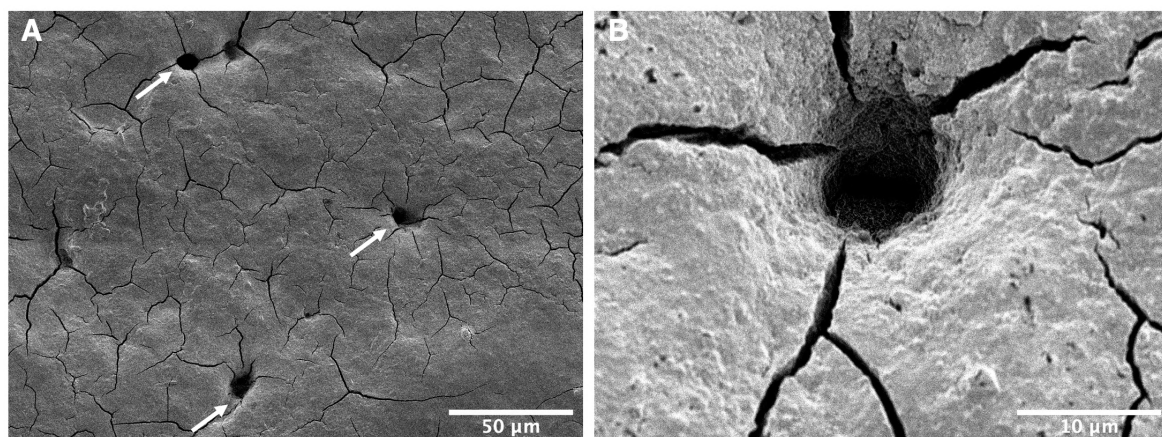
Figure 6.1: (A) top-down view of the cuticle, with the white arrows indicating surface pores, and (B) zoomed in image of a typical pore. Scalebars are (A) 50 μm and (B) 10 μm.

Figure 6.2 displays a typical SEM image of a cross-section of the eggshell. Beneath the cuticle lies the palisade layer, of which is accountable for the majority of the shell thickness (approximately two thirds of the thickness of the eggshell) [363]. The palisade is predominantly formed of calcite crystals, of which are vertical and aligned perpendicular to the shell surface, with an embedded organic matrix [363, 364]. This organic matrix is host to an array of proteins, examples of such proteins include ovalbumin, lysozyme and ovotransferrin [365, 366] of which are major constituents of the egg white. These egg white proteins may play a role in the calcification of the eggshell but are also inherently antibacterial in nature and may aid in the microbial protection of the embryo [367]. Other proteins are also present within the calcified matrix, e.g. ovocleidin-17 and ovocalyxin-32 [363], of which may play roles in regard to the different phases of the mineralisation. Proteoglycans (e.g. ovoglycan), of which are highly sulphated polyanionic macromolecules, also play key roles in the nucleation and growth of the $CaCO_3$ crystalline phase [363, 368, 369]. The spongy, vertical arrangement of the palisade layer aids increased mechanical strength of the eggshell against its breakage. Protruding from the palisade layer are rounded knobs or columns that are known as the mammillary layer, of which are composed of a similar $CaCO_3$-protein matrix and intercalate with the outer protein membrane (Figure 6.2). The outer protein membrane is one of two protein membranes (inner and outer); as aforementioned the outer membrane is intercalated with the mammillary knobs, where the inner protein membrane is tightly fused to its outer counterpart. Indeed, both protein membranes are very similar in composition, including proteins (e.g. collagen, lysozyme, ovotrasnferrin, ovocalixin), a polysaccharide component: including glycosaminoglycans and their components (e.g. glucosamine and chondroitin sulphate), as well as hyaluronic acid [367, 370]. Any non-invasively applied vector will need to be able to permeate these complex layers to reach the egg contents.
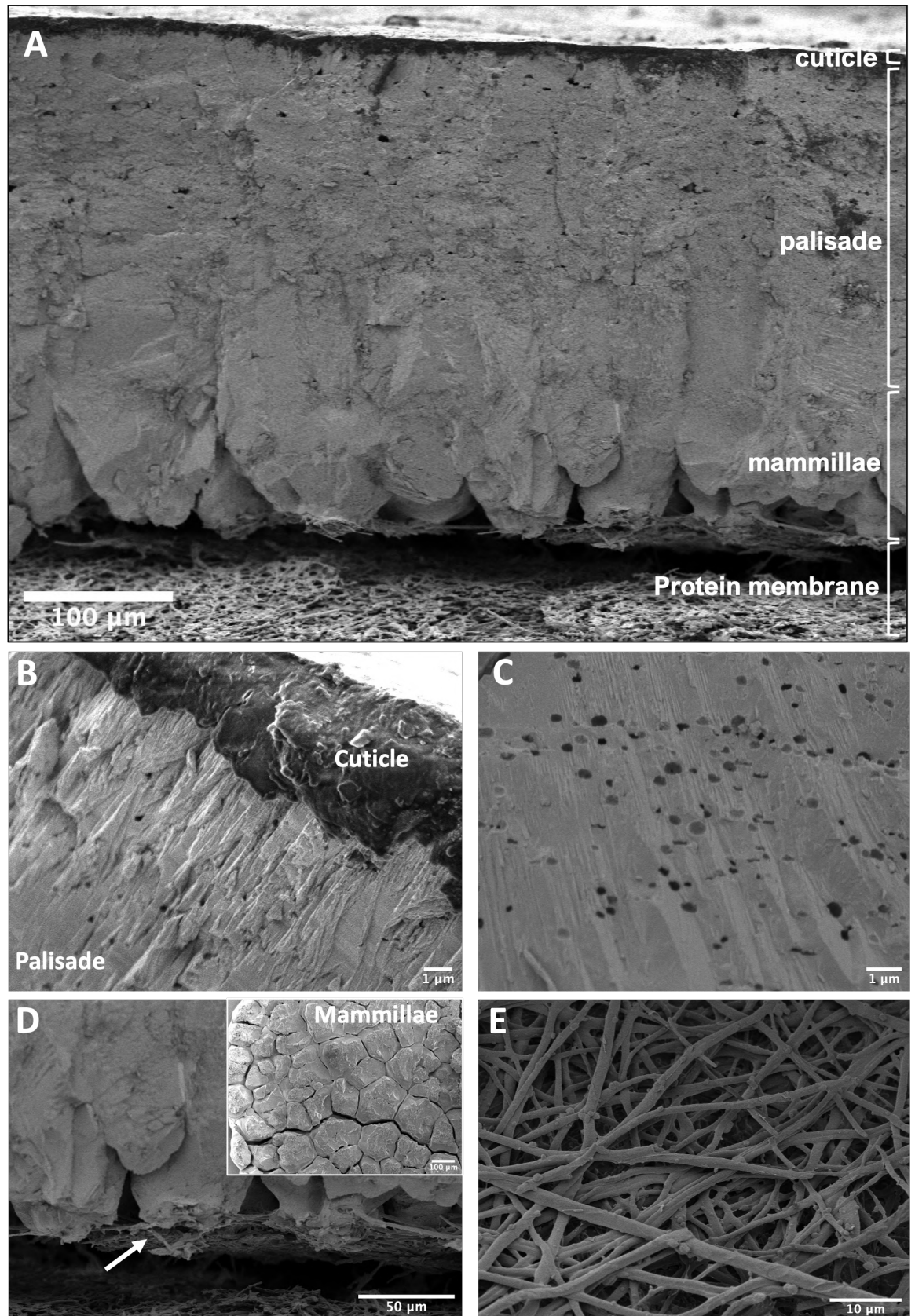
Figure 6.2: SEM imaging of eggshell components. (A) cross-section of the eggshell displaying each component of the eggshell: cuticle, palisade, mammillae and the protein membranes. Zoomed sections of each component (B) cuticle and palisade, (C) palisade, (D) mamillae and (E) protein membranes. Scalebars are (A) 100 μm, (B, C) 1 μm, (D) 50 μm, and (E) 10 μm. The white arrow indicates the intercalation of the mamillae and protein membranes.

6.2.2 Eggshell surface properties

In order to develop an injection-free *in ovo* delivery method, the permeability and porosity of the eggshell should first be evaluated. The permeation of eggshells regarding their water conductance and bacterial permeation in relation to food safety and hatchability rates, have been explored previously [371–375].

An approach to increase the porosity of the egg is to treat the shell with sodium hypochlorite (NaOCl). This acts to remove the protective cuticle layer and expose the surface of the palisade, allowing us direct access to more surface pores. Here, the eggs were incubated in 5% NaOCl for 30 mins at 25°C, before washing with ultrapure water and air drying. Figure 6.3 shows typical SEM images of the eggshell surface before and after NaOCl treatment. At these conditions, the cuticle was not stripped completely, but many more pores were exposed; indeed, across an average of 10 eggs for both untreated and NaOCl-treated eggs, 6 ± 6 and 78 ± 46 pores per mm^2 were exposed to the surface, respectively.
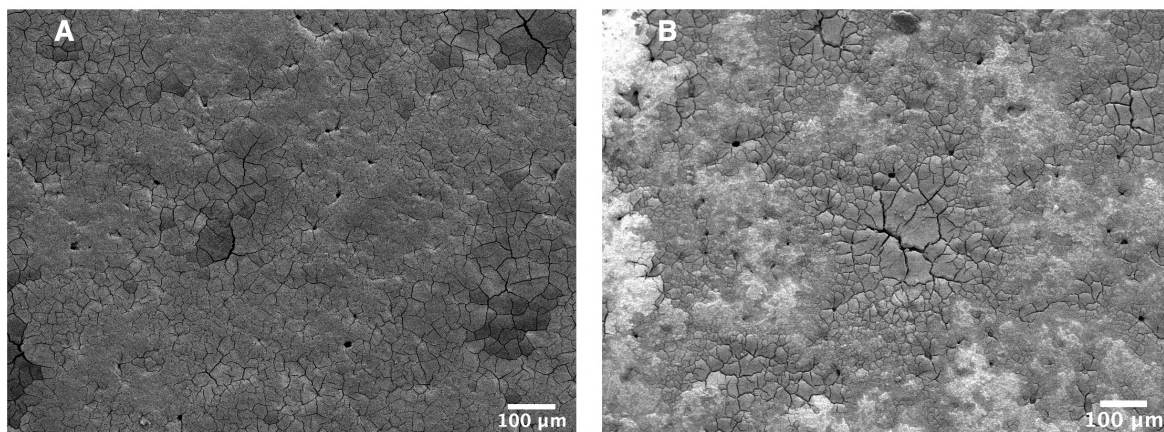
Figure 6.3: SEM images of an (A) untreated and (B) NaOCl-treated eggshell surface. Scalebars are 100 μm.

An assessment of cuticle quality is to determine its water contact angle [360]. Typically, the more hydrophobic this surface, the higher the quality. This can be explained by waxy protein content of this layer; if this is depleted in anyway, the layer will become more hydrophilic and reduce this water contact angle. For this, the contact angle of water was determined on both untreated and NaOCl-treated eggshell fragments, in-

deed, the angles determined were $90 \pm 8°$ and $45 \pm 8°$, for untreated and NaOCl-treated shells, respectively. By definition, a surface is hydrophobic if the water contact angle is $>90°$, where it is hydrophilic if the contact angle is $<90°$; hence, the untreated egg can be said to be hydrophobic in nature, where the NaOCl-treated egg is hydrophilic. Moreover, an estimation of the eggshell surface polarity was performed via the OWRK method (Figure 6.4). The untreated eggshell holds a major dispersive component and a minor polar component, as is to be expected due to its hydrophobic nature. Upon treatment with NaOCl, this polar component increases; this is attributed to the damaging of the cuticle of which gives rise to the contribution of the polar palisade layer beneath. Moreover, the overall surface free energy of the shell increases upon NaOCl treatment, implying the surface itself has become more wetting; a summary of surface energy values is presented in Table 6.1. Below, the permeation of model carrier gels through the eggshell and its membranes is discussed.
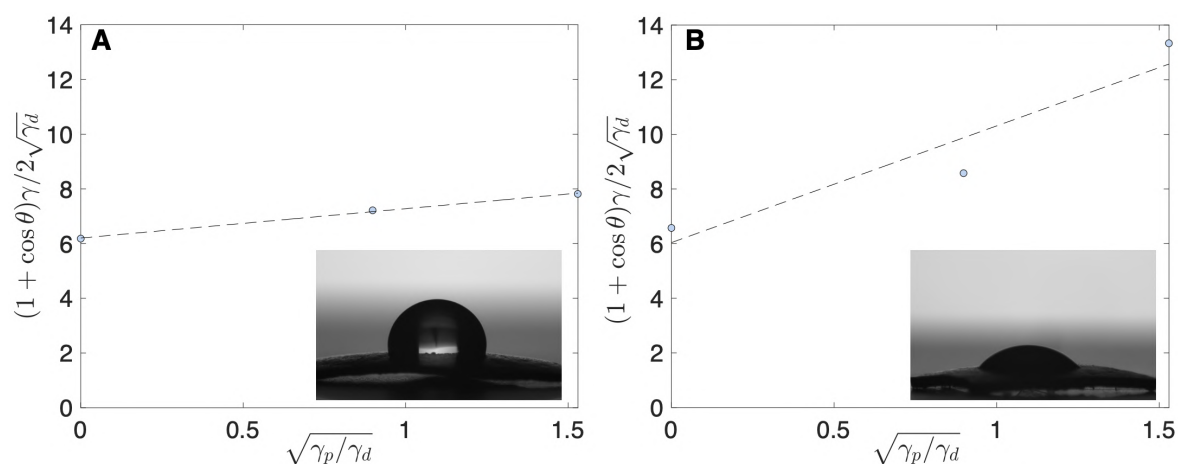
Figure 6.4: Determination of the surface free energy of the eggshell surface for both (A) untreated and (B) NaOCl-treated surfaces. Insets depict water droplets on the respective surface.

Table 6.1: The total surface free energy and respective dispersive and polar components for both untreated and NaOCl-treated eggshells.

Treatment	Surface free energy mJ m^{-2}	Dispersive component mJ m^{-2}	Polar component mJ m^{-2}
Untreated	39.6 ± 0.7	38.5 ± 0.7	1.1 ± 0.1
NaOCl	54.7 ± 22.1	36.5 ± 18.2	18.2 ± 12.5

6.3 Eggshell permeation

6.3.1 Permeation of carrier gels

Here, the permeation of carrier gels through the eggshell is now explored as a potential method for the delivery of the vectors described through this work. The permeation of carrier gels through chicken eggshells is novel, and, as far as the literature searches conducted, has not been previously reported, besides that of water. The key criteria for these carrier gels is that they are already food-grade approved and widely available. For this, glycerol, methylcellulose (MC), hydroxypropylmethylcellulose (HPMC), PEG, polypropylene glycol (PPG), and propylene glycol (PG) were of those selected for permeation screening, with water as a control. In order to observe the permeation of these carrier gels through the eggshell, each carrier gel was doped with RhoB, a fluorescent dye which is bright pink in colour. For this, RhoB was added to to the carrier gel and agitated - this ensured the dye was dispersed throughout the carrier gel. For this screening, eggs were left incubating in this RhoB-laden carrier gel for 24 hours before observing their contents (images in Figure 6.5). As these chosen carrier gels possess an array of dielectric constants, ranging from 5.59 to 78.5 for PPG and water, respectively (Figure 6.5), when the RhoB suspension was added to PPG, a water-PPG emulsion was formed due to the little-to-no miscibility of PPG with water. However, despite this formation of an emulsion, the RhoB-laden PPG was able to cross the eggshell and deposit within the albumen of the egg, where this was not possible with the remainder of the carrier gels, as well as water. This can be explained by the relative polarities of both the eggshell surface and the carrier gel itself; due to the aforementioned hydrophobicity and largely dispersive component of the cuticle, polar gels are not able to transverse this layer and remain at the surface of the eggshell, where non-polar gels are able to. Indeed, upon partial removal of this cuticle layer and increased hydrophilicity and polarity of the eggshell surface, all carrier gels, including water, were able to permeate the shell. This is evident via the visual deposition of the pink dye within the albumen and the inner-protein membrane within the egg itself, as

well as the raw fluorescence spectra illustrated below in Figure 6.5. Furthermore, as all carrier gels were able to cross the eggshell upon removal of the cuticle, this suggests that the formation of an emulsion played no role in this permeation; moreover, the ability of this emulsion to permeate the eggshell implies these emulsion droplets were of a diameter of <1 μm, in order to transverse the web-like protein membranes (Figure 6.2). These results imply any bioactive may be dispersed within the PPG gel, despite its polarity, and be delivered *in ovo*. A potential alternative to PPG that is in frequent use may be polydimethylsiloxane (PDMS), of which is a hydrophobic (dielectric constant of ~ 2.7 [376]) viscous liquid. It is a biologically inert compound, and used in food (additive E900), pharmaceutical, as well as medical products [377]. PDMS, however, is likely less cost effective compared to PPG due to its higher cost.
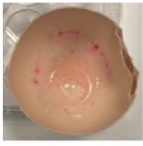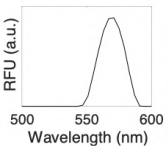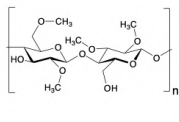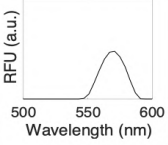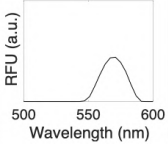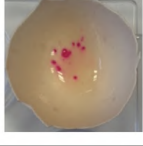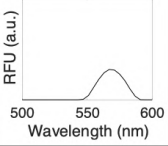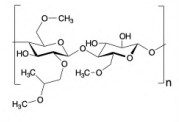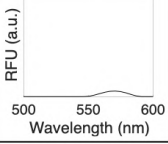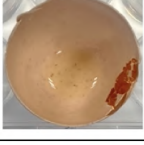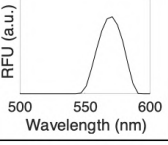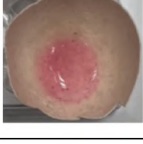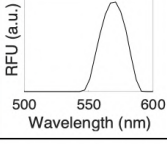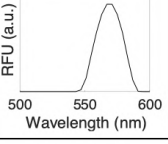
Carrier	Structure	ε	Untreated	NaOCl-treated	Raw fluorescence spectra (untreated)	Raw fluorescence spectra (NaOCl-treated)
Water		78.5				
MC		56.8				
Glycerol		42.5				
PG		27.5				
HPMC		~22				
PEG		11.6				
PPG		5.59				

Figure 6.5: Structures and dielectric constants of the polymers used as potential carrier gels for *in ovo* delivery, as well as images and raw fluorescence spectra (white LED with a virtual filter was used to excite the fluorophore: wavelength of 460-650 nm) of the permeation of rhodamine-laden carrier gel through the untreated or NaOCl-treated eggshell following incubation in the gel for 24 hours. If no spectra is present, no fluorescence was detected. References for dielectric constants: Water [378], MC [379], Glycerol [380], PG [381], HPMC [382], PEG [383], and PPG [384].

To determine the length of time necessary for the permeation of the PPG gel to cross the eggshell into the albumen, half of an eggshell, filled with albumen and the yolk removed, was placed into the well of a 6-well plate pre-filled with RhoB-laden PPG.

179

This set-up allowed for the visual observation of the dye crossing the eggshell as a function of time. It was found the PPG begins to permeate the eggshell within <1 min of incubation, as seen by the pink flecks from the dye within the inner protein membrane, as shown in Figure 6.6; the colour of which became more intense over the 24-hour period. OCT was performed to assess the permeation of the PPG carrier gel through the eggshell; for this, fragments of untreated eggshell were cut and used for the analysis. A small volume of the PPG or water was deposited on this fragment; after 30 mins to ensure permeation the fragments were scanned. Upon interpretation of these results, there is no explicit evidence for the permeation of PPG through the eggshell via OCT. Figure 6.7 shows typical OCT average cross-sections; Figure 6.7 (3) shows the eggshell before and after the application of the $CaCO_3$-laden PPG emulsion, here there are clear regions in which the refractive index changes (white arrow in Figure 6.7 (3)), which may indicate the permeation of these emulsion droplets through the shell itself. However, this may also be due to the reflection of light away from the probe, causing shadows within the scan. Indeed, there are no obvious changes in refractive index in the presence of solely water or PPG (Figure 6.7(1) & (2), respectively). Of note, the dip (in Figure 6.7 (1)) in the surface upon the addition of the droplet is due to the time delay from light having to travel through the droplet to the detector.
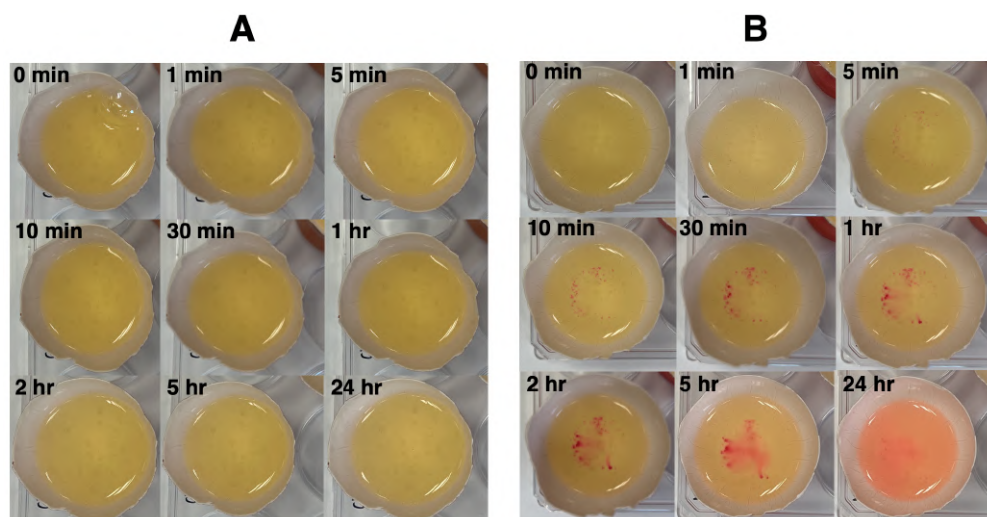
Figure 6.6: Images of eggshells half-filled with albumen incubated with (A) PPG and (B) RhoB-laden PPG overtime.
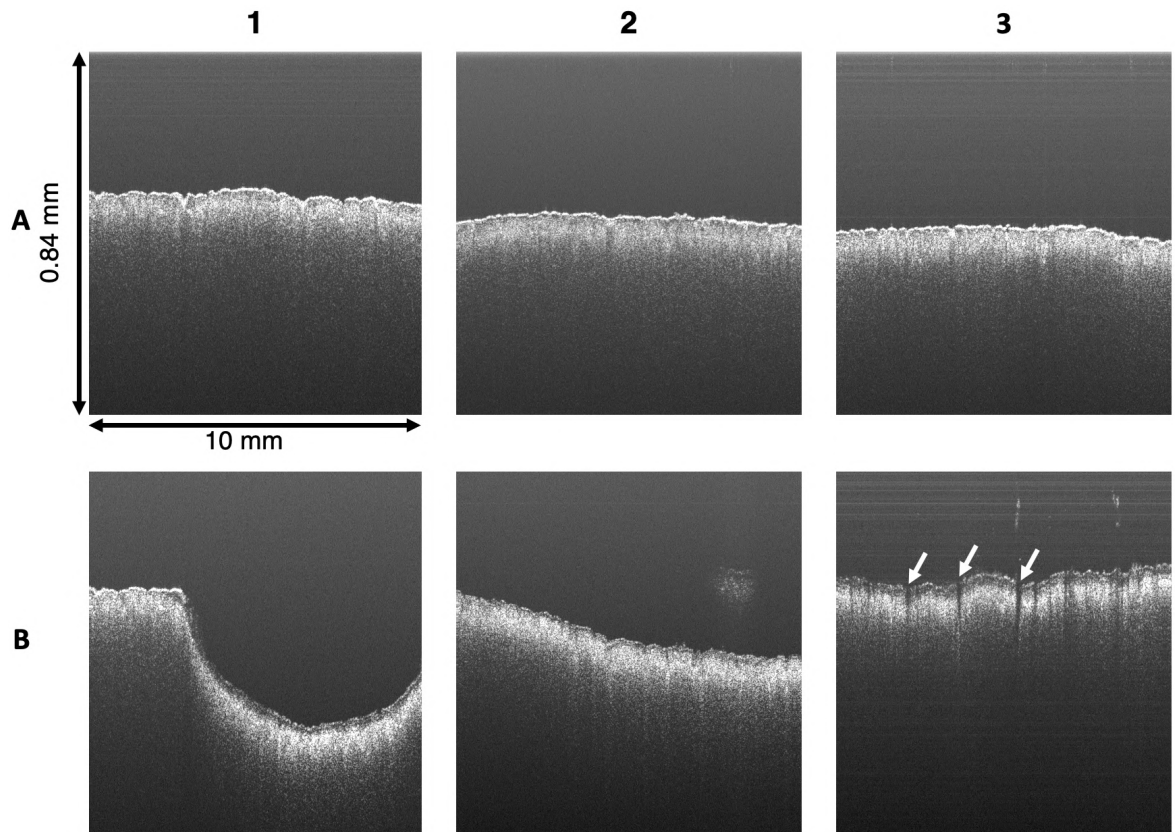
Figure 6.7: Cross-sectional OCT scans of the eggshell with a droplet of (1) water, (2) PPG and (3) $CaCO_3$-laden PPG. Bare eggshell (A) and eggshell with deposited droplet (B). White arrows depict significant changes in refractive index.

Following the application of the PPG to the egg and its permeation, both the surface of the eggshell and inner-protein membrane were imaged via SEM, as shown in Figure 6.8. There were no significant structural differences between untreated (Figure 6.2) and PPG-treated (Figure 6.8) layers. Importantly, it appears there is no observable blocking of the cuticle pores nor the web-like protein matrix; of note the brighter regions outlining the protein web are likely related to the charging effect of the SEM arising from the electron beam due to a layer of PPG on the membrane surface.
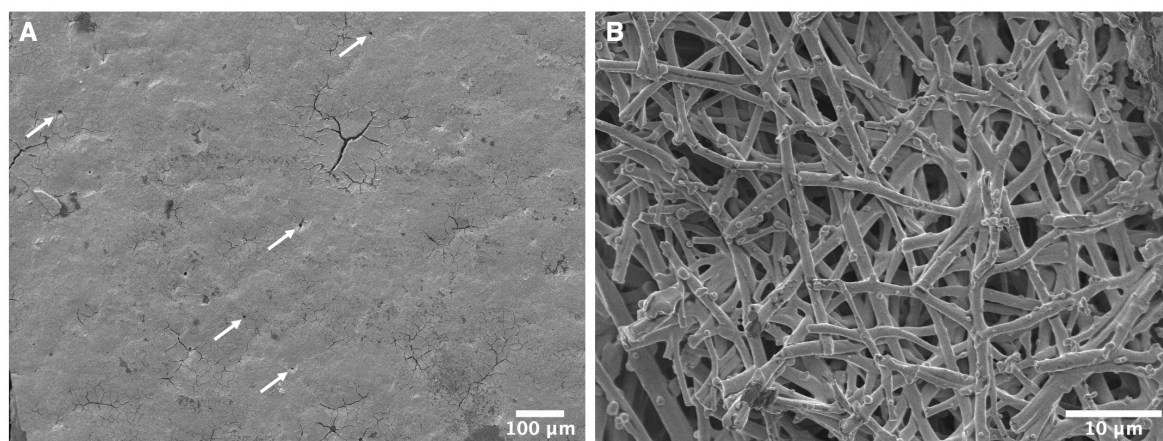
Figure 6.8: SEM images of (A) cuticle surface and (B) protein membranes following egg incubation with PPG after 24 hours. The white arrows indicate surface pores. Scalebars are (A) 100 μm and (B) 10 μm

6.3.2 Delivery of bioactives and developed vectors

Here, the model permeation of bioactives and delivery vectors distributed within the PPG carrier gel was explored. Firstly, DEX$^{\text{FITC}}$ was delivered *in ovo*; 1 mg mL^{-1} suspensions of DEX$^{\text{FITC}}$ of average molecular weights of 4, 40 and 2000 kDa were successfully delivered through the eggshell and into the albumen of the egg. Further, both CM- and DEAE-DEX$^{\text{FITC}}$ (40 kDa) were successfully delivered, implying the formal charge of the deliverable plays little role in its permeation. Notably, 0.1 mg mL^{-1} suspensions of $\sim$10 nm DEX$^{\text{FITC}}$-capped AgNPs were also able to cross the eggshell when dispersed in PPG. The presence of these bioactives in the albumen was detected via fluorescence spectroscopy (FITC detection), spectra of which can be seen in Figure 6.9. This examination of bioactive permeation is strictly qualitative; the maxima of each bioactive cannot be directly compared to one another due to the difference in FITC:monomer labelling ratio, of which will significantly impact the fluorescence intensity. However, these data imply any bioactive material, regardless of molecular size and charge, may permeate the eggshell when suspended within a dispersive carrier gel.
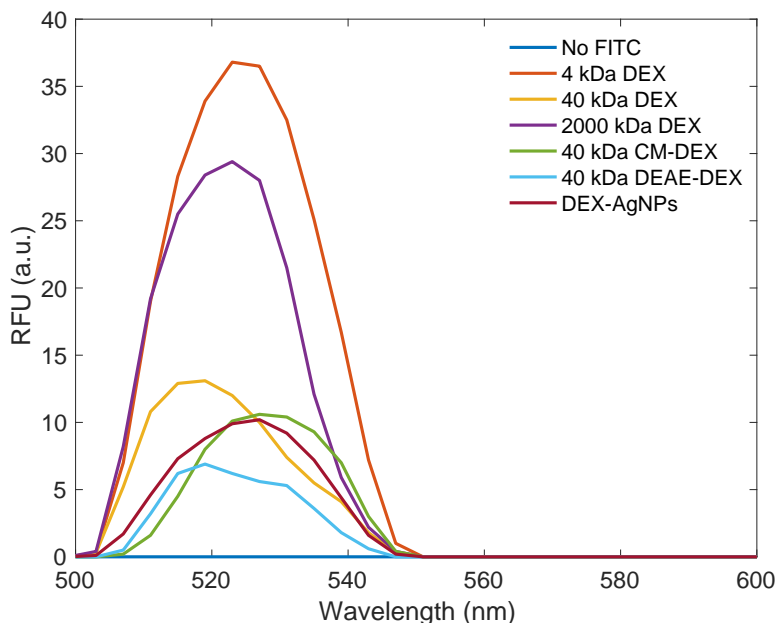
Figure 6.9: Raw fluorescence spectra (excitation wavelength of 470 ± 10 nm) of FITC-labelled bioactives detected within the albumen, spectra shown here are post-incubation in FITC-labelled bioactive-laden PPG for 24 hours.

Following this, in order to confirm the permeation of $CaCO_3$ crystals across the eggshell, 2000 kDa DEX^{FITC} was encapsulated into the $CaCO_3$ vaterite crystals of varying sizes via co-synthesis, including $\sim$500 nm, $\sim$1 μm, $\sim$4 μm, $\sim$8 μm and 15 μm sized crystals. The fluorescence signals of all $CaCO_3$ crystals used here are displayed in Figure 6.10, before delivery *in ovo*. For the eggshell permeation, 2000 kDa DEX^{FITC}/vaterite hybrid suspensions in PPG were deposited onto the surface of eggshell fragments; following incubation, the protein membrane was removed and placed on a glass coverslip for imaging. The images of which are displayed in Figure 6.11; only crystal sizes of 500 nm or less are able to permeate to the protein membrane, as is evident from the fluorescence image and detected fluorescence in Figure 6.11(B). Of note, no fluorescence was detected for crystal sizes above 500 nm, suggesting no DEX is released during the incubation. Indeed, this is evident from the lack of transformation from vaterite to the calcite polymorph of the 2000 kDa DEX/vaterite hybrids across a 48-hour period (Figure 5.15). Only the submicron DEX/vaterite hybrids are successfully delivered (fluorescence of 2000 kDa DEX/vaterite hybrids shown in Figure 6.11).
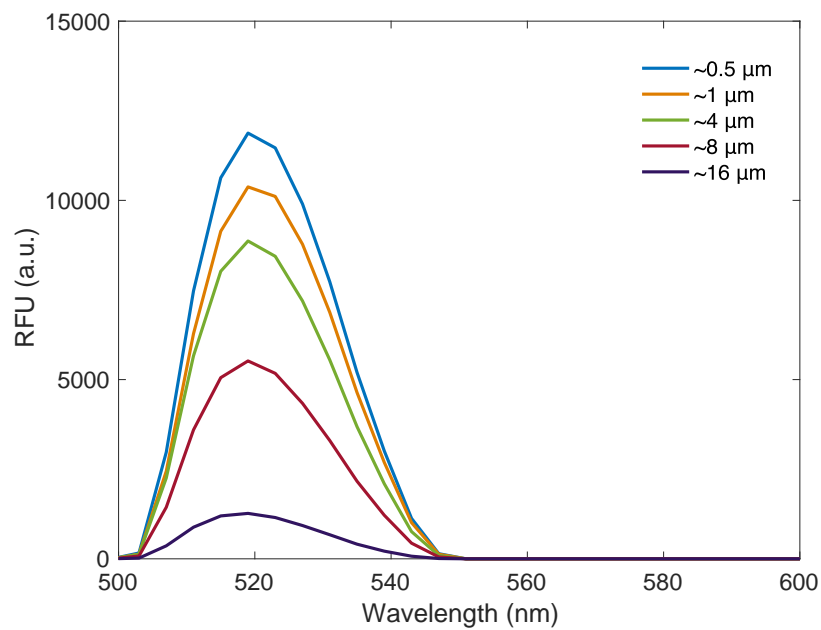
Figure 6.10: Raw fluorescence spectra (excitation wavelength 470 ± 10 nm) of 2000 kDa DEX$^{\text{FITC}}$/vaterite hybrids, with hybrid crystal diameters mentioned within the legend.
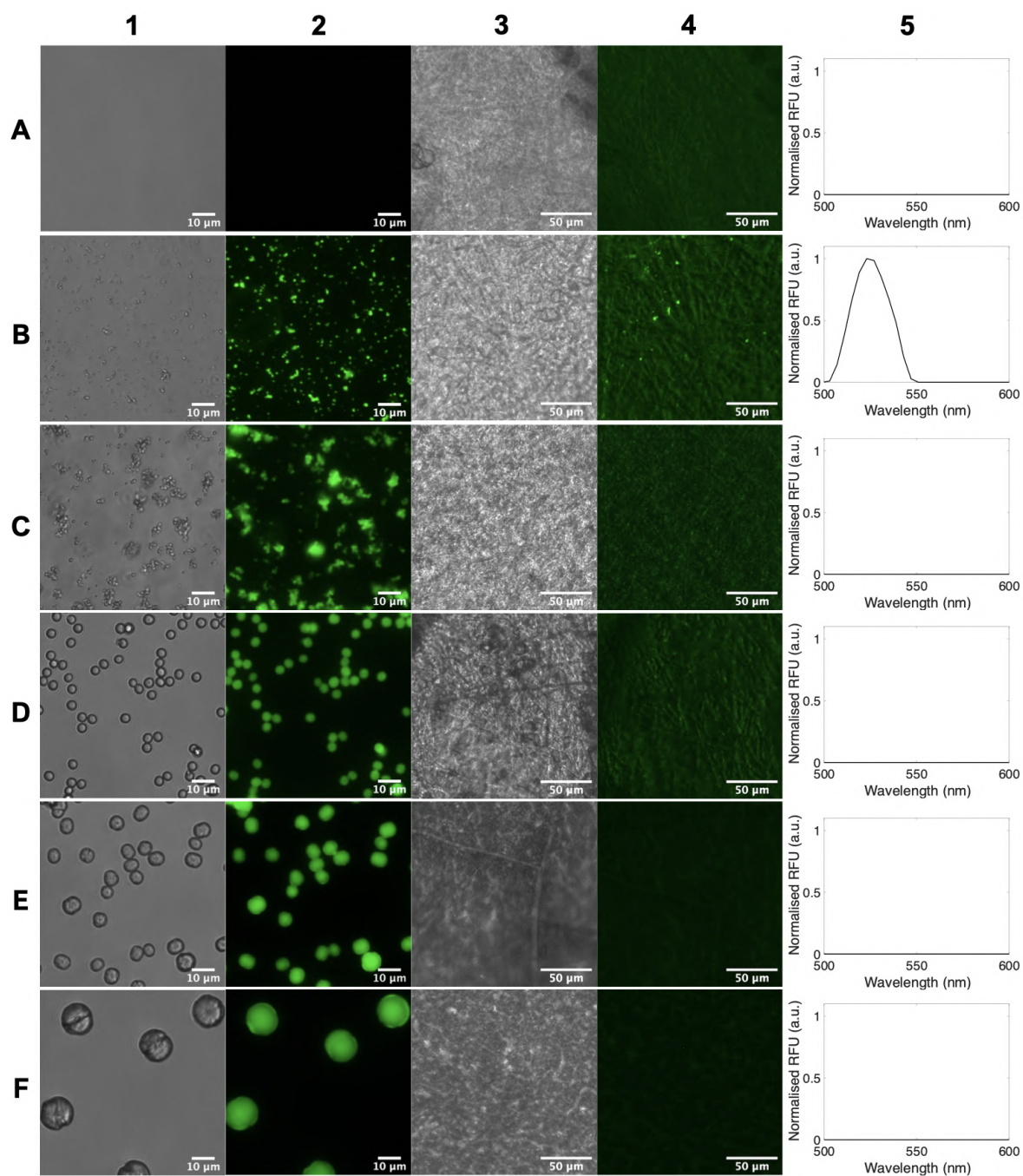
Figure 6.11: Transmittance and fluorescence images of 2000 kDa DEX$^{\text{FITC}}$/vaterite hybrids (1, 2) and inner-protein membrane (3, 4) post-incubation with hybrid-laden PPG. (5) - corresponding normalised fluorescence spectra (excitation wavelength of 470 ± 10 nm) of 2000 kDa DEX$^{\text{FITC}}$/vaterite hybrids. (A) No hybrids, (B) $\sim$500 nm, (C) $\sim$1, (D) $\sim$4, (E) $\sim$8 and (F) $\sim$16 μm sized 2000 kDa DEX$^{\text{FITC}}$/vaterite hybrids. Scalebars are (1, 2) 10 μm and (3, 4) 50 μm.

6.4 Conclusion

In this final results Chapter, the structure of the eggshell in relation to its microstructure, porosity and surface properties was explored, as well as the preliminary results of the delivery of bioactive material through a novel non-invasive *in ovo* delivery method. SEM imaging displayed the typical microstructure of the eggs used in this work, as well as the porous surface topology observed in hen eggshells. The porosity of the eggshell can be increased with the NaOCl washing of the surface, leading to the damaging of the glycoprotein-rich cuticle layer, resulting in the exposure of the pores within the $CaCO_3$-protein palisade layer beneath. Indeed, following water contact angle measurements and surface energy determination, the NaOCl wash resulted in an increase in hydrophilicity, as well as the free surface energy and polar component of the eggshell; where untreated eggshells are hydrophobic and have a higher dispersive surface energy component. The permeation of model food-grade carrier gels were tested using untreated and NaOCl-washed eggs, with a fluorescent rhodamine dye dispersed within the carrier gel. The permeation of the carrier gels strongly depended upon the polarity of the egg surface as well as the carrier gel. It was found the PPG carrier gel was able to begin permeating the eggshell at times of <1 min and did not affect the structure of the cuticle, according to SEM imaging. Bioactives dispersed within PPG (neutral DEX^{FITC}, CM- and DEAE-DEX^{FITC}, as well as DEX^{FITC}-capped AgNPs) were able to transverse and permeate the eggshell and deposit within the albumen, as was detected via fluorescence spectroscopy, and was independent of macromolecule charge. $CaCO_3$ vaterite crystals were also able to permeate the eggshell, if the crystal size was of <0.5 μm. Altogether, this Chapter presented the successful development of a carrier gel-based injection-free *in ovo* delivery system, as well as demonsrated successful delivery of various bioactives and their encapsulant, implying this method may be applied to any bioactive or nutrient for IOF.

Chapter 7

Thesis conclusions and future perspectives

7.1   Conclusions

Of note, research presented in this Chapter has been published as references (5), (8) and (10), as listed in Section 1.3.

The aim of this thesis was to develop vectors for non-invasive *in ovo* delivery, based on vaterite $CaCO_3$ crystals. Two types of vectors were developed and characterised (pure vaterite crystals and biopolymer microgels templated on the crystals), as well as the first tests for *in ovo* delivery performed.

Chapter 4 focused upon the formation of novel delivery vectors: porous vaterite $CaCO_3$ crystals and vaterite-templated biopolymer-based microgels. For this, a standard protocol for the additive-free, one-pot synthesis of vaterite $CaCO_3$ crystals of various sizes was established. The synthetic parameters were varied to achieve vaterite crystal sizes ranging from 0.5 to 20 μm. These vaterite crystals were characterised via SEM, FT-IR and BET analyses, which revealed their typical vaterite morphology and properties. Following this, 16 types of microgels consisting of biologically relevant polyelectrolytes templated upon such vaterite $CaCO_3$ were synthesised. Polycations PLL and PR are able (COL and DA are not) to form stable microgels with all tested polyanions (HS, DS, CS and HA). Microgels are prone to shrinkage upon template (vaterite) dissolution. Microgel shrinkage is driven by the local increase in ionic strength upon addition of EDTA, causing changes in charge compensation phenomena within the inter-polyelectrolyte network forming the microgels. The degree of shrinkage increased in a series of HS < DS < CS < HA, which correlates with the decrease in polyanion charge density. Via confocal and scanning electron microscopies, the internal structure of the microgels was investigated - revealing the presence of a polymer matrix within the microgel. The effect of the polymer molecular weight on the shrinkage and internal structure of microgels was explored using PLL of different molecular weights, which exhibited no influence on polymer distribution inside the microgels and a significant decrease of the shrinkage coefficients with increasing PLL molecular weight. Upon increase in the molecular weight of both the polyanion and polycation,

the microgel shrinkage is drastically increased due to lack of a polyelectrolyte matrix formed within the vaterite pores owing to the hindered diffusion of larger polymers into the vaterite pores. The adherence of microgels is driven by microgel-surface hydrophobic interactions and increases with decreasing polyanion charge density and increased multilayer water content. Depending upon the type of polycation (PR and PLL), their molecular weight, and the type of polyanion, it is possible to design microgels that hold certain properties, and tailor them in accordance with the desired application within a broad range: from shrunken (almost 2 orders of magnitude by volume) to non-shrunken (shrinkage coefficient ~ 1), varying degrees of microgel filling, and from adherent (adherence > 90%) to non-adherent (adherence closed to 0%) microgels. This Chapter revealed the clear dependencies of the biopolymer-based microgel formation, shrinkage, and internal structure on their polymer composition, which can be translated to other biopolyelectrolyte microgel and capsular systems. This is an important milestone in the further development of biopolymer-based microgels along with vaterite crystals and utilisation of the vectors in delivery applications.

The encapsulation of model food-grade macromolecule, DEX and its charged derivatives, into CaCO$_3$ vaterite crystals and microgels is explored within Chapter 5. Firstly, the influence of non-ionic DEX and its charged derivatives (DEAE-DEX and CM-DEX) on the crystallization of vaterite templates is explored. DEX is encapsulated within the vaterite crystals via co-synthesis at physiologically relevant conditions. All DEXs are loaded into the CaCO$_3$ crystals at less than 10% w/w and their content increased upon increase in DEX molecular weight. The presence of all DEXs matrix did not influence the polymorphism of the crystals and had negligible effect on the crystal size. Incorporation of non-ionic DEX, independent of DEX molecular weight, decreased the nanocrystallite size but lead to the partial blocking the crystal pores - this may influence drug release kinetics. Charged DEX increased the overall crystal porosity with no influence on the crystal size. These effects are observed regardless of the vaterite crystal size (0.5 - 20 μm). In addition, the inclusion of CM-DEX significantly slowed the vaterite-to-calcite recrystallisation process, whereas

DEAE-DEX did not affect the kinetics of recrystallisation. This may have important implications for drug delivery, where controlled loading and release are required, as well as understanding of $CaCO_3$ biomineralization. The loading of vitamin B12 into vaterite crystals via co-synthesis was demonstrated. B12 did not influence the vaterite polymorphism and morphology as shown via FT-IR and SEM analyses and can be loaded into the crystals up to 1% w/w.

Shrinkage behaviour of HA/PLL microgels was investigated upon encapsulation of both non-ionic DEX and its charged derivatives following DEX macromolecular pre-inclusion into the vaterite mesoporous matrix. Even at the low loading of macromolecules, microgel shrinkage is significantly affected and strongly depends on the nature of the DEX present. Inclusion of neutral DEX decreases the microgel shrinkage significantly, which is dependent on the mass content of DEX pre-loaded into the crystals. DEX of higher molecular weight is better retained within the microgels; this can be related to the slower diffusion of longer DEX chains out of the polymer network of the microgels. Charged DEX adopts to the polyelectrolyte chains of opposite charge, leading to increased charge compensation and allows for further rearrangement of polymer chains upon template dissolution - resulting in microgel shrinkage similar to that of pristine microgels. The encapsulation of nanoparticles is explored, utilising AgNPs with capping agents of varying nature as model nanoparticles. Encapsulation of AgNPs is driven by electrostatic interactions between the capping agent and the polyelectrolytes composing the microgel, and hence is also influenced greatly by the ionic strength of the surrounding medium.

This Chapter presented a mechanism for the crystallisation of vaterite in the presence of food-grade macromolecular DEX and small molecule vitamin B12 (via co-synthesis). Further, the first insights into the mechanisms of macromolecule entrapment within HA/PLL microgels demonstrated herein are also important for the fundamental understanding of polymer dynamics within multilayers upon shrinkage. The pathways for nanoparticle and macromolecule entrapment within the shrinkage-driven assembly of biopolymer-based HA/PLL microgels is also deciphered; an important cornerstone

in the design of these highly shrinkable polymer assembles and the development of microgel-based vectors for *in ovo* delivery.

Chapter 6 presents a newly developed approach for the non-invasive IOF of these vectors developed in Chapters 4 and 5. The permeation of food-grade carrier gels is explored in relation to the microstructure and surface properties of the eggshell. It was found that the permeation of polymer carrier gels is dependent upon the polarity of both the eggshell and the carrier gel itself. The cuticle is largely hydrophobic and dispersive in its surface free energy, hence only non-polar polymer carrier gels (i.e. only PPG out of those tested) may permeate the eggshell and serve as a medium to disperse delivery vectors. Utilising fluorescence spectroscopy, the successful delivery of FITC-labelled bioactive material, both free and encapsulated within $CaCO_3$, is exhibited, independent upon the nature of the bioactive, i.e. formal charge and size (<6 to 500 nm).

Overall, the work of this thesis presented the formation of novel delivery vectors based upon vaterite $CaCO_3$ and their templated biopolymer microgels. The mechanisms of encapsulation for both macromolecules and nanoparticles into these vectors are explored and provide key knowledge for the further utilisation of these vectors for IOF and alternate bioapplications. Preliminary studies for development of an injection-free IOF method for the successful delivery of PPG-dispersed bioactives and vectors is presented based upon spontaneous diffusion through the eggshell. Notwithstanding the work presented here, further developments are necessary for the successful employment of these vectors and IOF approach to be applied in broilers.

7.2   Future perspectives

Here, suggestions for the future direction of this work will be explored, building upon the results obtained throughout this thesis.

In order to ensure control over vector delivery and nutrient dosage, the accurate rate

of PPG permeation through the eggshell should be determined. This will provide information as to when during the egg incubation period the carrier gel may be applied. Following this, the viability of the chick embryo following PPG-based IOF should be monitored and determined throughout the incubation period, and the effect of PPG on the chick post-hatch evaluated. Furthermore, this IOF approach may be applied to eggs of other species of domestic fowl, and soft-shelled eggs of other species.

Currently, the vaterite with the necessary co-synthesised cargo is not commercially available and would need to be formulated for vector development. Indeed, vaterite produced bottom-up from $CaCl_2.2H_2O$ and Na_2CO_3 will cost between 0.2-0.4 \$ per gram of dried weight, and is a more economically viable approach due to the rare occurrence of vaterite in nature [199]. This is also necessary for the production of bioactive-laden microgels, as the encapsulation capability is dramatically increased if pre-loaded vaterite is used as the template as opposed to post-encapsulation approaches. A suitable approach for the up-scaled production of submicron vaterite $CaCO_3$ crystals ($<$ 500 nm in size) should be formulated for this, along with the co-synthesis of important nutrients required for IOF (e.g. amino acids, vitamins and nanoparticles), as well as assessment of their activity upon encapsulation. Upon scale-up, the degree of crystallinity and proportion of vaterite and calcite as a function of the bioactive content should be investigated within these scaled-up samples. X-ray diffraction (XRD) would be a suitable approach to confirm such sample properties.

Free-standing microgels may also be produced from these templates and also applied *in ovo*. Moreover, an important cornerstone for the further development of these vectors is the establishment of their degradation and release mechanisms within a suitable medium for IOF (e.g. the albumen).

The sterilisation of these vectors is also a crucial step for their future development. However, with this, the resultant physico-chemical properties of the developed materials may be affected following sterilisation. For instance, both dry- and moist-heat sterilisation approaches may significantly impact the stability and activity of the encapsulated bioactive, as these will be highly sensitive to temperature conditions. Besides

this, moist-heat sterilisation will likely result in the re-crystallisation of vaterite to calcite in the presence of water, especially at the potential increased pressure and temperature conditions used. Sample sterilisation via filtration is also not possible due to the size of the vectors developed (>200 nm). A suitable method for the sterilisation of the vector suspensions may be by irradiation, via UV or gamma radiation, for instance. Indeed, exposure to both types of radiation may impact the stability and activity of the encapsulated bioactive, however, this should be further investigated.

The adhered microgels produced here are suitable for an array of alternate bioapplications, including surface coatings for implant materials as well as tissue engineering applications. Indeed, the microgels developed here have already been applied for the functionalisation of silicone catheters [385], demonstrating promise for their further development as surface bio-functionalisation carriers. Moreover, the produced ionic DEX/vaterite hybrids have shown significant attachment to normal human dermal fibroblasts compared to pristine vaterite [386]. These data bode well for the further utilisation of these organic and inorganic carriers for an array of potential delivery applications.

References

[1] Department for Environment, Food & Rural Affairs, Latest poultry and poultry meat statistics, [online] https://www.gov.uk/government/statistics/poultry-and-poultry-meat-statistics, 2022, Accessed: 31-01-2023.

[2] M. M. Kadam, M. R. Barekatain, S. K Bhanja and P. A. Iji, *J. Sci. Food. Agr.*, 2013, **93**, 3654–3661.

[3] R. Das, P. Mishra and R. Jha, *Front. Vet. Sci.*, 2021, **8**, 754246.

[4] S. M. Roto, Y. M. Kwon and S. C. Ricke, *Front. Vet. Sci.*, 2016, **3**, 63.

[5] P. E. Givisiez, A. L. Moreira Filho, M. R. Santos, H. B. Oliveira, P. R. Ferket, C. J. Oliveira and R. D. Malheiros, *Poult. Sci.*, 2020, **99**, 6774–6782.

[6] M. Proszkowiec-Weglarz, K. B. Miska, L. E. Ellestad, L. L. Schreier, S. Kahl, N. Darwish, P. Campos and J. Shao, *BMC Microbiol.*, 2022, **22**, 206.

[7] M. Siwek, A. Slawinska, K. Stadnicka, J. Bogucka, A. Dunislawska and M. Bednarczyk, *BMC Vet. Res.*, 2018, **14**, 1–17.

[8] P. S. Wakenell, T. Bryan, J. Schaeffer, A. Avakian, C. Williams and C. Whitfill, *Avian Dis.*, 2002, **46**, 274–280.

[9] M. Alagawany and M. R. Farag, in *In Ovo Techniques and Treatments in Poultry Eggs*, Grupo Asís Biomedia SL, 2022, pp. 4–49.

[10] D. Volodkin, *Adv. Colloid Interface Sci.*, 2014, **207**, 306–324.

[11] O. Gusliakova, R. Verkhovskii, A. Abalymov, E. Lengert, A. Kozlova, V. Atkin, O. Nechaeva, A. Morrison, V. Tuchin and Y. Svenskaya, *Mater. Sci. Eng. C*, 2021, **119**, 111428.

[12] M. V. Novoselova, H. M. Loh, D. B. Trushina, A. Ketkar, T. O. Abakumova, T. S. Zatsepin, M. Kakran, A. M. Brzozowska, H. H. Lau, D. A. Gorin, M. N. Antipina and A. I. Brichkina, *ACS App. Mater. Inter.*, 2020, **12**, 5610–5623.

[13] A. S. Vikulina, A. G. Skirtach and D. Volodkin, *Langmuir*, 2019, **35**, 8565–8573.

[14] P. Toro, R. Quijada, M. Yazdani-Pedram and J. L. Arias, *Mater. Lett.*, 2007, **61**, 4347–4350.

[15] J. A. Abdalla, B. S. Thomas, R. A. Hawileh, J. Yang, B. B. Jindal and E. Ariyachandra, *Clean. Mater.*, 2022, 100061.

[16] R. Hay, B. Peng and K. Celik, *Cem. Concr. Res.*, 2023, **164**, 107040.

[17] W.-L. Tan, A. Ahmad, C. Leo and S. S. Lam, *J. CO2 Util.*, 2020, **42**, 101333.

[18] P. V. Binevski, N. G. Balabushevich, V. I. Uvarova, A. S. Vikulina and D. Volodkin, *Colloids Surf. B*, 2019, **181**, 437–449.

[19] X. Wu, S. Zhao, J. Zhang, P. Wu and C. Peng, *RSC Adv.*, 2014, **4**, 14603–14612.

[20] F. Ali, N. Bousserrhine, V. Alphonse, L. Michely and S. Belbekhouche, *Int. J. Pharm.*, 2020, **579**, 119175.

[21] A. M. Ferreira, A. Vikulina, G. W. Cave, M. Loughlin, V. Puddu and D. Volodkin, *J. Colloid Interface Sci.*, 2023, **631**, 165–180.

[22] N. G. Balabushevich, A. V. L. D. Guerenu, N. A. Feoktistova and D. Volodkin, *Phys. Chem. Chem. Phys.*, 2015, **17**, 2523–2530.

[23] N. G. Balabushevich, E. A. Kovalenko, L. N. Maltseva, L. Y. Filatova, A. M. Moysenovich, E. V. Mikhalchik, D. Volodkin and A. S. Vikulina, *Adv. Eng. Mater.*, 2022, 2101797.

[24] P. Shi, S. Luo, B. Voit, D. Appelhans and X. Zan, *J. Mater. Chem. B*, 2018, **6**, 4205–4215.

[25] L. Jeannot, M. Bell, R. Ashwell, D. Volodkin and A. S. Vikulina, *Micromachines*, 2018, **9**, 547.

[26] D. B. Trushina, R. A. Akasov, A. V. Khovankina, T. N. Borodina, T. V. Bukreeva and E. A. Markvicheva, *J. Mol. Liq.*, 2019, **284**, 215–224.

[27] O. Ersoy, D. Güler and M. Rençberoğlu, *Coatings*, 2022, **12**, 44.

[28] A. Karademir, H. Varlibaş and M. Çiçekler, *Turk. J. For.*, 2013, **14**, 48–52.

[29] Z. Hu, X. Zen, J. Gong and Y. Deng, *Colloids Surf. A: Physicochem. Eng.*, 2009, **351**, 65–70.

[30] L. Zárybnická, R. Ševčík, J. Pokornỳ, D. Machová, E. Stránská and J. Šál, *Polymers*, 2022, **14**, 199.

[31] N. Guermazi, N. Haddar, K. Elleuch and H. F. Ayedi, *Polym. Compos.*, 2016, **37**, 2171–2183.

[32] E. Batuecas, F. Liendo, T. Tommasi, S. Bensaid, F. Deorsola and D. Fino, *J. CO2 Util.*, 2021, **45**, 101446.

[33] T. Meng, Y. Qiang, A. Hu, C. Xu and L. Lin, *Constr. Build.*, 2017, **151**, 775–781.

[34] L. Brečević, V. Nöthig-Laslo, D. Kralj and S. Popović, *J. Chem. Soc., Faraday Trans.*, 1996, **92**, 1017–1022.

[35] J. Chen and L. Xiang, *Powder Technol.*, 2009, **189**, 64–69.

[36] R. Ševčík, P. Mácová, M. P. Estébanez and A. Viani, *Constr. Build.*, 2019, **228**, 116802.

[37] N. Spanos and P. G. Koutsoukos, *J. Cryst. Growth*, 1998, **191**, 783–790.

[38] P. Németh, E. Mugnaioli, M. Gemmi, G. Czuppon, A. Demény and C. Spötl, *Sci. Adv.*, 2018, **4**, eaau6178.

[39] N. Spann, E. M. Harper and D. C. Aldridge, *Sci. Nat*, 2010, **97**, 743–751.

[40] A. G. Christy, *Cryst. Growth Des.*, 2017, **17**, 3567–3578.

[41] M. Ni and B. D. Ratner, *Surf. Interface Anal*, 2008, **40**, 1356–1361.

[42] N. G. Balabushevich, E. A. Kovalenko, L. Y. Filatova, E. A. Kirzhanova, E. V. Mikhalchik, D. Volodkin and A. S. Vikulina, *Macromol. Biosci.*, 2022, **22**, 2200005.

[43] R. Ševčík, P. Šašek and A. Viani, *J. Mater. Sci.*, 2018, **53**, 4022–4033.

[44] D. B. Trushina, T. V. Bukreeva and M. N. Antipina, *Cryst. Growth Des.*, 2016, **16**, 1311–1319.

[45] Y. Mori, T. Enomae and A. Isogai, *Mater. Sci. Eng. C*, 2009, **29**, 1409–1414.

[46] P. Fadia, S. Tyagi, S. Bhagat, A. Nair, P. Panchal, H. Dave, S. Dang and S. Singh, *3 Biotech*, 2021, **11**, 1–30.

[47] A. M. Ferreira, A. S. Vikulina and D. Volodkin, *J. Control. Release*, 2020, **328**, 470–489.

[48] F. Liendo, M. Arduino, F. A. Deorsola and S. Bensaid, *Powder Technol.*, 2022, **398**, 117050.

[49] C. J. Grimes, T. Hardcastle, M. S. Manga, T. Mahmud and D. W. York, *Cryst. Growth Des.*, 2020, **20**, 5572–5582.

[50] A. U. Badnore and A. B. Pandit, *Chem. Eng. Process.: Process Intensif*, 2015, **98**, 13–21.

[51] C. Karagiozov and D. Momchilova, *Chem. Eng. Process.: Process Intensif*, 2005, **44**, 115–119.

[52] P. Bots, L. G. Benning, J. D. Rodriguez-Blanco, T. Roncal-Herrero and S. Shaw, *Cryst. Growth Des.*, 2012, **12**, 3806–3814.

[53] J. D. Rodriguez-Blanco, S. Shaw and L. G. Benning, *Nanoscale*, 2011, **3**, 265–271.

[54] N. G. Balabushevich, E. A. Kovalenko, I. M. Le-Deygen, L. Y. Filatova, D. Volodkin and A. S. Vikulina, *Mater. Des.*, 2019, **182**, 108020.

[55] A. Sarkar and S. Mahapatra, *J. Chem. Sci.*, 2012, **124**, 1399–1404.

[56] G. Choukrani, J. álvarez Freile, N. U. Avtenyuk, W. Wan, K. Zimmermann, E. Bremer and L. Dähne, *Part. Part. Syst. Charact.*, 2021, **38**, 2100012.

[57] Z. Dong, L. Feng, W. Zhu, X. Sun, M. Gao, H. Zhao, Y. Chao and Z. Liu, *Biomaterials*, 2016, **110**, 60–70.

[58] H. Wei, Q. Shen, Y. Zhao, D. jin Wang and D. fu Xu, *J. Cryst. Growth*, 2003, **250**, 516–524.

[59] M. E. shahate Ismaiel Saraya and H. H. A. L. Rokbba, *J. Nanomater.*, 2016, **4**, 44–51.

[60] Z. Zhang, D. Gao, H. Zhao, C. Xie, G. Guan, D. Wang and S.-H. Yu, *J. Phys. Chem. B*, 2006, **110**, 8613–8618.

[61] K. Naka, Y. Tanaka and Y. Chujo, *Langmuir*, 2002, **18**, 3655–3658.

[62] S. Kirboga and M. Oner, *Chem. Eng. Trans.*, 2013, **32**, 2119–2124.

[63] X. Ma, S. Yuan, L. Yang, L. Li, X. Zhang, C. Su and K. Wang, *CrystEngComm*, 2013, **15**, 8288–8299.

[64] A. R. Muslimov, D. O. Antuganov, Y. V. Tarakanchikova, M. V. Zhukov, M. A. Nadporojskii, M. V. Zyuzin and A. S. Timin, *ACS Appl. Mater. Interfaces*, 2021, **13**, 25599–25610.

[65] V. Kozlovskaya, A. Alford, M. Dolmat, M. Ducharme, R. Caviedes, L. Radford, S. E. Lapi and E. Kharlampieva, *ACS Appl. Mater. Interfaces*, 2020, **12**, 56792–56804.

[66] Y. Tarakanchikova, A. Muslimov, I. Sergeev, K. Lepik, N. Yolshin, A. Goncharenko, K. Vasilyev, I. Eliseev, A. Bukatin, V. Sergeev, S. Pavlov, A. Popov and I. Meglinski, *J. Mater. Chem. B*, 2020, 9576–9588.

[67] O. Gusliakova, E. N. Atochina-Vasserman, O. Sindeeva, S. Sindeev, S. Pinyaev, N. Pyataev, V. Revin, G. B. Sukhorukov, D. Gorin and A. J. Gow, *Front. Pharmacol.*, 2018, **9**, 559.

[68] D. V. Volodkin, N. I. Larionova and G. B. Sukhorukov, *Biomacromolecules*, 2004, **5**, 1962–1972.

[69] N. G. Balabushevich, E. A. Kovalenko, E. V. Mikhalchik, L. Y. Filatova, D. Volodkin and A. S. Vikulina, *J. Colloid Interface Sci.*, 2019, **545**, 330–339.

[70] N. A. Feoktistova, A. S. Vikulina, N. G. Balabushevich, A. G. Skirtach and D. Volodkin, *Mater. Des.*, 2020, **185**, 108223.

[71] J. Campbell, G. Kastania and D. Volodkin, *Micromachines*, 2020, **11**, 717.

[72] N. A. Feoktistova, N. G. Balabushevich, A. G. Skirtach, D. Volodkin and A. S. Vikulina, *Phys. Chem. Chem. Phys.*, 2020, **22**, 9713–9722.

[73] P. Shi, J. Qin, J. Hu, Y. Bai and X. Zan, *Colloids Surf. B*, 2019, **175**, 184–194.

[74] D. V. Volodkin, S. Schmidt, P. Fernandes, N. I. Larionova, G. B. Sukhorukov, C. Duschl, H. Möhwald and R. von Klitzing, *Adv. Funct. Mater.*, 2012, **22**, 1914–1922.

[75] S. Schmidt, K. Uhlig, C. Duschl and D. Volodkin, *Acta Biomater.*, 2014, **10**, 1423–1430.

[76] S. Schmidt and D. Volodkin, *J. Mater. Chem. B*, 2013, **1**, 1210–1218.

[77] D. Volodkin, *Colloid Polym. Sci.*, 2014, **292**, 1249–1259.

[78] M. M. Neumann and D. Volodkin, *Analyst*, 2020, **145**, 1202–1206.

[79] A. S. Vikulina, N. A. Feoktistova, N. G. Balabushevich, R. von Klitzing and D. Volodkin, *ACS Appl. Mater. Interfaces*, 2020, **12**, 57401–57409.

[80] A. Wang, Y. Cui, J. Li and J. C. van Hest, *Adv. Funct. Mater.*, 2012, **22**, 2673–2681.

[81] S. V. German, M. V. Novoselova, D. N. Bratashov, P. A. Demina, V. S. Atkin, D. V. Voronin, B. N. Khlebtsov, B. V. Parakhonskiy, G. B. Sukhorukov and D. A. Gorin, *Sci. Rep.*, 2018, **8**, 17763.

[82] P. A. Demina, D. V. Voronin, E. V. Lengert, A. M. Abramova, V. S. Atkin, B. V. Nabatov, A. P. Semenov, D. G. Shchukin and T. V. Bukreeva, *ACS Omega*, 2020, **5**, 4115–4124.

[83] A. M. Yashchenok, O. I. Gusliakova, E. V. Konovalova, M. V. Novoselova, V. O. Shipunova, T. O. Abakumova, O. I. Efimova, R. Kholodenko, A. A. Schulga, T. S. Zatsepin *et al.*, *J. Mater. Chem. B*, 2021, **9**, 8823–8831.

[84] A. S. Vikulina, N. A. Feoktistova, N. G. Balabushevich, A. G. Skirtach and D. Volodkin, *Phys. Chem. Chem. Phys.*, 2018, **20**, 8822–8831.

[85] A. Vikulina, J. Webster, D. Voronin, E. Ivanov, R. Fakhrullin, V. Vinokurov and D. Volodkin, *Mater. Des.*, 2021, **197**, 109220.

[86] N. Wada, N. Horiuchi, M. Nakamura, K. Nozaki, A. Nagai and K. Yamashita, *ACS Omega*, 2018, **3**, 16681–16692.

[87] S. Zhao, F. Caruso, L. Dahne, G. Decher, B. G. D. Geest, J. Fan, N. Feliu, Y. Gogotsi, P. T. Hammond, M. C. Hersam, A. Khademhosseini, N. Kotov, S. Leporatti, Y. Li, F. Lisdat, L. M. Liz-Marzan, S. Moya, P. Mulvaney, A. L.

Rogach, S. Roy, D. G. Shchukin, A. G. Skirtach, M. M. Stevens, G. B. Sukhorukov, P. S. Weiss, Z. Yue, D. Zhu and W. J. Parak, *ACS Nano*, 2019, **13**, 6151–6169.

[88] F. X. Xiao, M. Pagliaro, Y. J. Xu and B. Liu, *Chem. Soc. Rev.*, 2016, **45**, 3088–3121.

[89] A. Sergeeva, N. Feoktistova, V. Prokopovic, D. Gorin and D. Volodkin, *J. Adv. Mater. Interfaces*, 2015, **2**, 1500386.

[90] C. D. Easton, A. J. Bullock, G. Gigliobianco, S. L. McArthur and S. Macneil, *J. Mater. Chem. B*, 2014, **2**, 5558–5568.

[91] T. Paulraj, N. Feoktistova, N. Velk, K. Uhlig, C. Duschl and D. Volodkin, *Macromol. Rapid Commun.*, 2014, **35**, 1408–1413.

[92] N. Madaboosi, K. Uhlig, M. S. Jäger, H. Möhwald, C. Duschl and D. V. Volodkin, *Macromol. Rapid Commun.*, 2012, **33**, 1775–1779.

[93] P. Machillot, C. Quintal, F. Dalonneau, L. Hermant, P. Monnot, K. Matthews, V. Fitzpatrick, J. Liu, I. Pignot-Paintrand and C. Picart, *J. Adv. Mater.*, 2018, **30**, 1801097.

[94] A. Vaterrodt, B. Thallinger, K. Daumann, D. Koch, G. M. Guebitz and M. Ulbricht, *Langmuir*, 2016, **32**, 1347–1359.

[95] S. Srisang and N. Nasongkla, *J. Drug Deliv. Sci. Technol.*, 2019, **49**, 235–242.

[96] J. P. Govindharajulu, X. Chen, Y. Li, J. C. Rodriguez-Cabello, M. Battacharya and C. Aparicio, *Int. J. Mol. Sci.*, 2017, **18**, 369.

[97] Q. Shi, Z. Qian, D. Liu and H. Liu, *Front. Physiol.*, 2017, **8**, 574.

[98] N. G. Balabushevich, A. V. L. D. Guerenu, N. A. Feoktistova, A. G. Skirtach and D. Volodkin, *Macromol. Biosci.*, 2016, **16**, 95–105.

[99] V. Sharma and A. Sundaramurthy, *Beilstein J. Nanotechnol.*, 2020, **11**, 508–532.

[100] N. Feoktistova, J. Rose, V. Z. Prokopović, A. S. Vikulina, A. Skirtach and D. Volodkin, *Langmuir*, 2016, **32**, 4229–4238.

[101] W. Tong, X. Song and C. Gao, *Chem. Soc. Rev.*, 2012, **41**, 6103–6124.

[102] D. V. Volodkin, N. G. Balabushevitch, G. B. Sukhorukov and N. I. Larionova, *Biochem. (Mosc.)*, 2003, **68**, 236–241.

[103] N. G. Balabushevich, E. A. Sholina, E. V. Mikhalchik, L. Y. Filatova, A. S. Vikulina and D. Volodkin, *Micromachines*, 2018, **9**, 307.

[104] A. Zhuk, V. Selin, I. Zhuk, B. Belov, J. F. Ankner and S. A. Sukhishvili, *Langmuir*, 2015, **31**, 3889–3896.

[105] M. Kolasinska, R. Krastev, T. Gutberlet and P. Warszynski, *Langmuir*, 2009, **25**, 1224–1232.

[106] A. S. Vikulina and J. Campbell, *Nanomaterials*, 2021, **11**, 2502.

[107] H. Al-Khoury, E. Espinosa-Cano, M. R. Aguilar, J. S. Román, F. Syrowatka, G. Schmidt and T. Groth, *Biomacromolecules*, 2019, **20**, 4015–4025.

[108] H. Alkhoury, A. Hautmann, B. Fuhrmann, F. Syrowatka, F. Erdmann, G. Zhou, S. Stojanović, S. Najman and T. Groth, *Int. J. Mol. Sci.*, 2020, **21**, 3724.

[109] D. Guduru, M. S. Niepel, C. Gonzalez-Garcia, M. Salmeron-Sanchez and T. Groth, *Macromol. Biosci.*, 2017, **17**, 1700078.

[110] D. V. Volodkin, P. Schaaf, H. Mohwald, J. claude Voegel and V. Ball, *Soft Matter*, 2009, 1394–1405.

[111] B. V. Parakhonskiy, W. J. Parak, D. Volodkin and A. G. Skirtach, *Langmuir*, 2019, **35**, 8574–8583.

[112] M. S. Saveleva, K. Eftekhari, A. Abalymov, T. E. Douglas, D. Volodkin, B. V. Parakhonskiy and A. G. Skirtach, *Front. Chem.*, 2019, **7**, 179.

[113] A. G. Skirtach, D. V. Volodkin and H. Möhwald, *ChemPhysChem*, 2010, **11**, 822–829.

[114] D. Köhler, N. Madaboosi, M. Delcea, S. Schmidt, B. G. D. Geest, D. V. Volodkin, H. Möhwald and A. G. Skirtach, *J. Adv. Mater.*, 2012, **24**, 1095–1100.

[115] I. Y. Stetciura, A. V. Markin, A. N. Ponomarev, A. V. Yakimansky, T. S. Demina, C. Grandfils, D. V. Volodkin and D. A. Gorin, *Langmuir*, 2013, **29**, 4140–4147.

[116] D. Volodkin, R. von Klitzing and H. Moehwald, *Polymers*, 2014, **6**, 1502–1527.

[117] V. Z. Prokopovic, C. Duschl and D. Volodkin, *Macromol. Biosci.*, 2015, **15**, 1357–1363.

[118] O. N. Oliveira, R. M. Iost, J. R. Siqueira, F. N. Crespilho and L. Caseli, *ACS App. Mater. Inter.*, 2014, **6**, 14745–14766.

[119] C. D. Bostick, S. Mukhopadhyay, I. Pecht, M. Sheves, D. Cahen and D. Lederman, *Rep. Prog. Phys.*, 2018, **81**, 026601.

[120] M. Xuan, J. Zhao, J. Shao, C. Du, W. Cui, L. Duan, W. Qi and J. Li, *J. Colloid Interface Sci.*, 2017, **487**, 107–117.

[121] Q. He, L. Duan, W. Qi, K. Wang, Y. Cui, X. Yan and J. Li, *J. Adv. Mater.*, 2008, **20**, 2933–2937.

[122] A. E. Pavlath and W. Orts, in *Edible films and coatings for food applications*, Springer, 2009, pp. 1–23.

[123] U. Voigt, V. Khrenov, K. Tauer, M. Hahn, W. Jaeger and R. V. Klitzing, *J. Condens. Matter Phys.*, 2003, **15**, 213–218.

[124] M. Schönhoff, *J. Condens. Matter Phys.*, 2003, **15**, R1781.

[125] P. Nazaran, V. Bosio, W. Jaeger, D. F. Anghel and R. V. Klitzing, *J. Phys. Chem. B*, 2007, **111**, 8572–8581.

[126] R. A. Ghostine, M. Z. Markarian and J. B. Schlenoff, *J. Am. Chem. Soc.*, 2013, **135**, 7636–7646.

[127] K. Tang and N. A. Besseling, *Soft Matter*, 2016, **12**, 1032–1040.

[128] P. Lavalle, C. Picart, J. Mutterer, C. Gergely, H. Reiss, J. C. Voegel, B. Senger and P. Schaaf, *J. Phys. Chem. B*, 2004, **108**, 635–648.

[129] V. Selin, J. F. Ankner and S. A. Sukhishvili, *Macromolecules*, 2017, **50**, 6192–6201.

[130] C. Picart, J. Mutterer, L. Richert, Y. Luo, G. D. Prestwich, P. Schaaf, J. C. Voegel and P. Lavalle, *Proc. Natl. Acad. Sci. U.S.A.*, 2002, **99**, 12531–12535.

[131] D. Alkekhia and A. Shukla, *J. Biomed. Mater. Res.*, 2019, **107**, 1324–1339.

[132] Y. E. Ghoussoub, M. Zerball, H. M. Fares, J. F. Ankner, R. V. Klitzing and J. B. Schlenoff, *Soft Matter*, 2018, **14**, 1699–1708.

[133] L. Richert, A. J. Engler, D. E. Discher and C. Picart, *Biomacromolecules*, 2004, **5**, 1908–1916.

[134] J. B. R. Neto, T. B. Taketa, R. A. Bataglioli, S. B. Pimentel, D. M. Santos, A. Fiamingo, C. A. Costa, S. P. Campana-Filho, H. F. Carvalho and M. M. Beppu, *Appl. Surf. Sci.*, 2019, **486**, 508–518.

[135] E. Diamanti, N. Muzzio, D. Gregurec, J. Irigoyen, M. Pasquale, O. Azzaroni, M. Brinkmann and S. E. Moya, *Colloids Surf. B*, 2016, **145**, 328–337.

[136] J. M. Silva, A. R. C. Duarte, C. A. Custódio, P. Sher, A. I. Neto, A. C. Pinho, J. Fonseca, R. L. Reis and J. F. Mano, *Adv. Healthc. Mater.*, 2014, **3**, 433–440.

[137] J. Fu, J. Ji, W. Yuan and J. Shen, *Biomaterials*, 2005, **26**, 6684–6692.

[138] A. Barrantes, J. Wengenroth, T. Arnebrant and H. vard J. Haugen, *J. Colloid Interface Sci.*, 2017, **485**, 288–295.

References

[139] M. Sousa, F. Cleymand and J. Mano, *Biomed. Mater.*, 2016, **11**, 035008.

[140] F. Gaudière, S. Morin-Grognet, L. Bidault, P. Lembré, E. Pauthe, J. P. Vannier, H. Atmani, G. Ladam and B. Labat, *Biomacromolecules*, 2014, **15**, 1602–1611.

[141] Z. Song, J. Yin, K. Luo, Y. Zheng, Y. Yang, Q. Li, S. Yan and X. Chen, *Macromol. Biosci.*, 2009, **9**, 268–278.

[142] M. Lundin, E. Blomberg and R. D. Tilton, *Langmuir*, 2010, **26**, 3242–3251.

[143] A. Mutschler, C. Betscha, V. Ball, B. Senger, N. E. Vrana, F. Boulmedais, A. Schroder, P. Schaaf and P. Lavalle, *Chem. Mater.*, 2017, **29**, 3195–3201.

[144] N. Laugel, C. Betscha, M. Winterhalter, J. C. Voegel, P. Schaaf and V. Ball, *J. Phys. Chem. B*, 2006, **110**, 19443–19449.

[145] E. Hübsch, V. Ball, B. Senger, G. Decher, J. C. Voegel and P. Schaaf, *Langmuir*, 2004, **20**, 1980–1985.

[146] T. Radeva, K. Kamburova and I. Petkanchin, *J. Colloid Interface Sci.*, 2006, **298**, 59–65.

[147] J. A. Johansson, T. Halthur, M. Herranen, L. Söderberg, U. Elofsson and J. Hilborn, *Biomacromolecules*, 2005, **6**, 1353–1359.

[148] D. Volodkin and R. V. Klitzing, *Curr. Opin. Colloid Interface Sci.*, 2014, **19**, 25–31.

[149] D. T. Haynie, E. Cho and P. Waduge, *Langmuir*, 2011, **27**, 5700–5704.

[150] M. Salomäki, I. A. Vinokurov and J. Kankare, *Langmuir*, 2005, **21**, 11232–11240.

[151] C. Porcel, P. Lavalle, G. Decher, B. Senger, J. C. Voegel and P. Schaaf, *Langmuir*, 2007, **23**, 1898–1904.

[152] C. Porcel, P. Lavalle, V. Ball, G. Decher, B. Senger, J. C. Voegel and P. Schaaf, *Langmuir*, 2006, **22**, 4376–4383.

[153] A. S. Vikulina, Y. G. Anissimov, P. Singh, V. Z. Prokopović, K. Uhlig, M. S. Jaeger, R. V. Klitzing, C. Duschl and D. Volodkin, *Phys. Chem. Chem. Phys.*, 2016, **18**, 7866–7874.

[154] W. Yuan, H. Dong, C. M. Li, X. Cui, L. Yu, Z. Lu and Q. Zhou, *Langmuir*, 2007, **23**, 13046–13052.

[155] P. Bieker and M. Schonhoff, *Macromolecules*, 2010, **43**, 5052–5059.

[156] S. Salem, M. Müller, B. Torger, A. Janke, K. J. Eichhorn, B. Voit and D. Appelhans, *Macromol. Chem. Phys.*, 2015, **216**, 182–195.

[157] L. Shen, P. Chaudouet, J. Ji and C. Picart, *Biomacromolecules*, 2011, **12**, 1322–1331.

[158] S. E. Burke and C. J. Barrett, *Biomacromolecules*, 2003, **4**, 1773–1783.

[159] A. Barrantes, O. Santos, J. Sotres and T. Arnebrant, *J. Colloid Interface Sci.*, 2012, **388**, 191–200.

[160] S. Boddohi, C. E. Killingsworth and M. J. Kipper, *Biomacromolecules*, 2008, **9**, 2021–2028.

[161] M. Lundin, F. Solaqa, E. Thormann, L. MacAkova and E. Blomberg, *Langmuir*, 2011, **27**, 7537–7548.

[162] L. Richert, P. Lavalle, E. Payan, X. Z. Shu, G. D. Prestwich, J. F. Stoltz, P. Schaaf, J. C. Voegel and C. Picart, *Langmuir*, 2004, **20**, 448–458.

[163] S. Schmidt and D. Volodkin, *J. Mater. Chem. B*, 2013, **1**, 1210–1218.

[164] S. Abreu, J. A. Carvalho, A. C. Tedesco, M. B. Junior and A. R. Simioni, *J. Mater. Res.*, 2019, **34**, 1353–1362.

[165] I. Marchenko, T. Borodina, D. Trushina, I. Rassokhina, V. Shirinian, I. Zavarzin, A. Gogin, T. Bukreeva, I. Marchenko, T. Borodina, D. Trushina and I. Rassokhina, *J. Microencapsul.*, 2019, **35**, 657–666.

[166] A. Rodríguez-Ramos, L. Marín-Caba, N. Iturrioz-Rodríguez, E. Padín-González, L. García-Hevia, T. M. Oliveira, M. A. Corea-Duarte and M. L. Fanarraga, *Int. J. Mol. Sci.*, 2020, **21**, 9573.

[167] R. R. Castillo, D. Lozano and M. Vallet-Regi, *Pharmaceutics*, 2020, **12**, 432.

[168] N. A. Nasab, H. H. Kumleh, M. Beygzadeh, S. Teimourian and M. Kazemzad, *Artif. Cells Nanomed. Biotechnol.*, 2018, **46**, 75–81.

[169] A. D. Trofimov, A. A. Ivanova, M. V. Zyuzin and A. S. Timin, *Pharmaceutics*, 2018, **10**, 167.

[170] F. Caruso, *Chem. Eur. J.*, 2000, **6**, 413–419.

[171] S. Ye, C. Wang, X. Liu and Z. Tong, *J. Biomater. Sci. Polym. Ed.*, 2005, **16**, 909–923.

[172] N. G. Balabushevich and N. I. Larionova, *J. Microencapsul.*, 2009, **26**, 571–579.

[173] R. Georgieva, S. Moya, E. Donath and H. Baumer, *Langmuir*, 2004, **20**, 1895–1900.

[174] I. Estrela-lopis, S. Leporatti, E. Typlt, D. Clemens and E. Donath, *Langmuir*, 2007, **23**, 7209–7215.

[175] B. Neu, A. Voigt, R. Mitlöhner, S. Leporatti, C. Y. Gao, E. Donath, H. Kiesewetter, H. Möhwald, H. J. Meiselman and H. Bäumler, *J. Microencapsul.*, 2001, **18**, 385–395.

[176] F. L. Lederer, T. J. Günther, U. Weinert, J. Raff and K. Pollmann, *Microb. Cell Factories*, 2012, **11**, 1–10.

[177] D. V. Volodkin, A. I. Petrov, M. Prevot and G. B. Sukhorukov, *Langmuir*, 2004, **20**, 3398–3406.

[178] C. Gao, S. Moya, H. Lichtenfeld, A. Casoli, H. Fiedler, E. Donath and H. Möhwald, *Macromol. Mater. Eng*, 2001, **286**, 355–361.

[179] N. G. Balabushevich, O. P. Tiourina, D. V. Volodkin, N. I. Larionova and G. B. Sukhorukov, *Biomacromolecules*, 2003, **4**, 1191–1197.

[180] S. Ye, C. Wang, X. Liu, Z. Tong, B. Ren and F. Zeng, *J. Control. Release*, 2006, **112**, 79–87.

[181] C. Schüler and F. Caruso, *Biomacromolecules*, 2001, **2**, 921–926.

[182] A. C. Pinheiro, A. I. Bourbon, M. A. Cerqueira, élia Maricato, C. Nunes, M. A. Coimbra and A. A. Vicente, *Carbohydr. Polym.*, 2015, **115**, 1–9.

[183] B. V. Parakhonskiy, A. M. Yashchenok, M. Konrad and A. G. Skirtach, *Adv. Colloid Interface Sci.*, 2014, **207**, 253–264.

[184] Y. Itoh, M. Matsusaki, T. Kida and M. Akashi, *Biomacromolecules*, 2008, **9**, 2202–2206.

[185] F. Ji, J. Li, Z. Qin, B. Yang, E. Zhang, D. Dong, J. Wang, Y. Wen and F. Yao, *Carbohydr. Polym.*, 2017, **177**, 86–96.

[186] O. Mansour, T. Peker, S. Hamadi and S. Belbekhouche, *Eur. Polym. J.*, 2019, **120**, 109248.

[187] K. Radhakrishnan, M. B. Thomas, S. Pulakkat, D. P. Gnanadhas, D. Chakravortty and A. M. Raichur, *J. Nanopart. Res.*, 2015, **17**, 341.

[188] T. Imoto, T. Kida, M. Matsusaki and M. Akashi, *Macromol. Biosci.*, 2010, **10**, 271–277.

[189] O. P. Tiourina and G. B. Sukhorukov, *Int. J. Pharm.*, 2002, **242**, 155–161.

[190] L. Yuxi, Y. Jing, Z. Ziqi, L. Junjie, Z. Rui and Y. Fanglian, *J. Colloid Interface Sci.*, 2012, **379**, 130–140.

[191] Y. Itoh, M. Matsusaki, T. Kida and M. Akashi, *Chem. Lett.*, 2004, **33**, 1552–1553.

[192] D. P. Gnanadhas, M. B. Thomas, M. Elango, A. M. Raichur and D. Chakravortty, *J. Antimicrob. Chemother.*, 2013, **68**, 2576–2586.

References

[193] M. B. Thomas, K. Radhakrishnan, D. P. Gnanadhas, D. Chakravortty and A. M. Raichur, *Int. J. Nanomed.*, 2013, **8**, 267–273.

[194] S. Yan, J. Zhu, Z. Wang, J. Yin, Y. Zheng and X. Chen, *Eur. J. Pharm. Biopharm.*, 2011, **78**, 336–345.

[195] B. Han, S. Baiyong, Z. Wang, M. Shi, H. Li, C. Peng, Q. Zhao and C. Gao, *Polym. Adv. Technol.*, 2008, **19**, 36–46.

[196] T. V. Bukreeva, I. V. Marchenko, T. N. Borodina, I. V. Degtev, S. L. Sitnikov, Y. V. Moiseeva, N. V. Gulyaeva and M. V. Kovalchuk, *Dokl. Phys. Chem.*, 2011, **440**, 165–167.

[197] T. N. Borodina, D. B. Trushina, I. V. Marchenko and T. V. Bukreeva, *BioNanoScience*, 2016, **6**, 261–268.

[198] D. Konopacka-Lyskawa, *Crystals*, 2019, **9**, 223.

[199] A. Vikulina, D. Voronin, R. Fakhrullin, V. Vinokurov and D. Volodkin, *New J. Chem.*, 2020, **44**, 5638–5655.

[200] Z. She, M. N. Antipina, J. Li and G. B. Sukhorukov, *Biomacromolecules*, 2010, **11**, 1241–1247.

[201] D. G. Shchukin, A. A. Patel, G. B. Sukhorukov and Y. M. Lvov, *J. Am. Chem. Soc.*, 2004, **126**, 3374–3375.

[202] Q. Zhao and B. Li, *Nanomedicine*, 2008, **4**, 302–310.

[203] K. Radhakrishnan, J. Tripathy and A. M. Raichur, *Chem. Commun.*, 2013, **49**, 5390–5392.

[204] B. G. D. Geest, R. E. Vandenbroucke, A. M. Guenther, G. B. Sukhorukov, W. E. Hennink, N. N. Sanders, J. Demeester and S. C. D. Smedt, *J. Adv. Mater.*, 2006, **18**, 1005–1009.

[205] Z. She, C. Wang, J. Li, G. B. Sukhorukov and M. N. Antipina, *Biomacromolecules*, 2012, **13**, 2174–2180.

[206] V. Strehlow, J. Lessig, M. Göse and U. Reibetanz, *J. Mater. Chem. B*, 2013, **1**, 3633–3643.

[207] Y. Jin, W. Liu, J. Wang, J. Fang and H. Gao, *Colloids Surf. A: Physicochem. Eng.*, 2009, **342**, 40–45.

[208] A. Szarpak, D. Cui, F. Dubreuil, B. G. D. Geest, L. J. D. Cock, C. Picart and R. Auzély-Velty, *Biomacromolecules*, 2010, **11**, 713–720.

[209] F. Sousa, O. Kreft, G. B. Sukhorukov, H. Möhwald and V. Kokol, *J. Microencapsul.*, 2014, **31**, 270–276.

[210] J. xiao Chen, Y. Liang, W. Liu, J. Huang and J. hua Chen, *Int. J. Biol. Macromol.*, 2014, **69**, 554–560.

[211] L. Sun, X. Xiong, Q. Zou, P. Ouyang and R. Krastev, *J. Appl. Polym. Sci.*, 2017, **134**, 44916.

[212] L. J. D. Cock, O. D. Wever, S. V. Vlierberghe, E. Vanderleyden, P. Dubruel, F. D. Vos, C. Vervaet, J. P. Remon and B. G. D. Geest, *Soft Matter*, 2012, **8**, 1146–1154.

[213] L. J. D. Cock, J. Lenoir, S. D. Koker, V. Vermeersch, A. G. Skirtach, P. Dubruel, E. Adriaens, C. Vervaet, J. P. Remon and B. G. D. Geest, *Biomaterials*, 2011, **32**, 1967–1977.

[214] Q. Zhao, B. Han, Z. Wang, C. Gao, C. Peng and J. Shen, *Nanomedicine*, 2007, **3**, 63–74.

[215] S. Roy, N. M. Elbaz, W. J. Parak and N. Feliu, *ACS Appl. Bio Mater.*, 2019, **2**, 3245–3256.

[216] R. R. Costa, A. Girotti, M. Santos, F. J. Arias, J. F. Mano and J. C. Rodríguez-cabello, *Acta Biomater.*, 2014, **10**, 2653–2662.

[217] H. Hong, R. Murney, N. L. Yakovlev, M. V. Novoselova, S. Hui, N. Roy, H. Singh, G. B. Sukhorukov, B. Haigh and M. V. Kiryukhin, *J. Colloid Interface Sci.*, 2017, **505**, 332–340.

[218] E. Kilic, M. V. Novoselova, S. H. Lim, N. A. Pyataev, S. I. Pinyaev, O. A. Kulikov, O. A. Sindeeva, O. A. Mayorova, R. Murney, M. N. Antipina *et al.*, *Sci. Rep.*, 2017, **7**, 1–10.

[219] M. V. Novoselova, D. V. Voronin, T. O. Abakumova, P. A. Demina, A. V. Petrov, V. V. Petrov, T. S. Zatsepin and G. B. Sukhorukov, *Colloids Surf. B*, 2019, **181**, 680–687.

[220] W. Tong, C. Gao and H. Möhwald, *Colloid Polym. Sci.*, 2008, **286**, 1103–1109.

[221] L. Duan, Q. He, X. Yan, Y. Cui, K. Wang and J. Li, *Colloid Polym. Sci.*, 2007, **354**, 357–362.

[222] T. Borodina, E. Markvicheva, S. Kunizhev, G. B. Sukhorukov and O. Kreft, *Macromol. Mater. Eng*, 2007, **28**, 1894–1899.

[223] W. Huang, T. Zhang, P. Shi, D. Yang and S. Luo, *Colloids Surf. B*, 2019, **177**, 178–187.

[224] A. Yu, Y. Wang, E. Barlow and F. Caruso, *J. Adv. Mater.*, 2005, **17**, 1737–1741.

[225] S. Zhang, M. Xing and B. Li, *ACS Appl. Mater. Interfaces*, 2018, **10**, 44267–44278.

[226] W.-C. Liao, C.-H. Lu, R. Hartmann, F. Wang, Y. S. Sohn, W. J. Parak and I. Willner, *ACS Nano*, 2015, **9**, 9078–9086.

[227] A. Fujii, T. Maruyama, Y. Ohmukai, E. Kamio, T. Sotani and H. Matsuyama, *Colloids Surf. A: Physicochem. Eng.*, 2010, **356**, 126–133.

[228] A. Fujii, Y. Ohmukai, T. Maruyama, T. Sotani and H. Matsuyama, *Colloids Surf. A: Physicochem. Eng.*, 2011, **384**, 529–535.

[229] D. Zhao, C. qun Wang, R. xi Zhuo and S. xue Cheng, *Colloids Surf. B*, 2014, **118**, 111–116.

[230] P. Zhao, S. Wu, Y. Cheng, J. You, Y. Chen, M. Li, C. He, X. Zhang, T. Yang, Y. Lu, R. J. Lee, X. He and G. Xiang, *Nanomedicine*, 2017, **13**, 2507–2516.

[231] Y. I. Svenskaya, H. Fattah, O. A. Inozemtseva, A. G. Ivanova, S. N. Shtykov, D. A. Gorin and B. V. Parakhonskiy, *Cryst. Growth Des.*, 2018, **18**, 331–337.

[232] L. V. der Meeren, J. Li, M. Konrad, A. G. Skirtach, D. Volodkin and B. V. Parakhonskiy, *Macromol. Biosci.*, 2020, **20**, 2000081.

[233] K. Köhler, D. G. Shchukin, H. Möhwald and G. B. Sukhorukov, *J. Phys. Chem. B*, 2005, **109**, 18250–18259.

[234] D. B. Trushina, T. V. Bukreeva, T. N. Borodina, D. D. Belova, S. Belyakov and M. N. Antipina, *Colloids Surf. B*, 2018, **170**, 312–321.

[235] D. B. Trushina, A. S. Burova, T. N. Borodina, M. A. Soldatov, T. Y. Klochko and T. V. Bukreeva, *Colloid J.*, 2018, **80**, 710–715.

[236] E. Rideau, R. Dimova, P. Schwille, F. R. Wurm and K. Landfester, *Chem. Soc. Rev.*, 2018, **47**, 8527–8610.

[237] C. Has and P. Sunthar, *J. Liposome Res.*, 2020, **30**, 336–365.

[238] A. Mateos-maroto, I. A.-N. nez, F. Ortega, R. Rubio and E. Guzmán, *Polymers*, 2021, **13**, 1221.

[239] M. K. Riaz, M. A. Riaz, X. Zhang, C. Lin, K. H. Wong, X. Chen, G. Z. Id, A. Lu and Z. Yang, *Int. J. Mol. Sci.*, 2018, **19**, 195.

[240] C. Weber, M. Voigt, J. Simon, A. kathrin Danner, H. Frey, V. Mailänder, M. Helm, S. Morsbach and K. Landfester, *Biomacromolecules*, 2019, **20**, 2989–2999.

[241] P. Vabbilisetty and X. long Sun, *Org. Biomol. Chem.*, 2014, **12**, 1237–1244.

[242] D. Volodkin, H. Mohwald, J. C. Voegel and V. Ball, *J. Control. Release*, 2007, **117**, 111–120.

[243] D. Volodkin, V. Ball, P. Schaaf, J. C. Voegel and H. Mohwald, *Biochim. Biophys. Acta*, 2007, **1768**, 280–290.

[244] W. Liu, J. Liu, W. Liu, T. Li and C. Liu, *J. Agric. Food Chem.*, 2013, **61**, 4133–4144.

[245] A. Eivazi, B. Medronho, B. Lindman and M. Norgren, *Polymers*, 2021, **13**, 1–10.

[246] F. Hermal, B. Frisch, A. Specht, L. Bourel-bonnet and B. Heurtault, *Int. J. Pharm.*, 2020, **586**, 119568.

[247] S. Madrigal-carballo, S. Lim, G. Rodriguez, A. O. Vila, C. G. Krueger, S. Gunasekaran and J. D. Reed, *J. Funct. Foods*, 2010, **2**, 99–106.

[248] W. Liu, Y. Kong, P. Tu, J. Lu, C. Liu, W. Liu, J. Han and J. Liu, *Food Funct.*, 2017, **8**, 1688–1697.

[249] F. Cuomo, F. Lopez, A. Ceglie, L. Maiuro and G. Miguel, *Soft Matter*, 2012, 4415–4420.

[250] F. Cuomo, F. Lopez and M. G. Miguel, *Langmuir*, 2010, **26**, 10555–10560.

[251] M. Bédard, B. G. D. Geest, M. Helmuth, G. B. Sukhorukov and A. G. Skirtach, *Soft Matter*, 2009, **5**, 3927–3931.

[252] B. G. D. Geest, C. Déjugnat, M. Prevot, G. B. Sukhorukov, J. Demeester and S. C. D. Smedt, *Adv. Funct. Mater.*, 2007, **17**, 531–537.

[253] H. Lee, Y. Jeong and T. G. Park, *Biomacromolecules*, 2007, **8**, 3705–3711.

[254] A. M. Díez-Pascual and P. S. Shuttleworth, *Materials*, 2014, **7**, 7472–7512.

[255] S. Moya, L. Dähne, A. Voigt, S. Leporatti, E. Donath and H. Möhwald, *Colloids Surf. A: Physicochem. Eng.*, 2001, **183-185**, 27–40.

[256] M. Y. Yitayew and M. Tabrizian, *MRS Adv.*, 2020, **5**, 2401–2407.

[257] A. C. Santos, P. Pattekari, S. Jesus, F. Veiga, Y. Lvov and A. J. Ribeiro, *ACS App. Mater. Inter.*, 2015, **7**, 11972–11983.

[258] A. Agarwal, Y. Lvov, R. Sawant and V. Torchilin, *J. Control. Release*, 2008, **128**, 255–260.

[259] B. Du, G. Shen, D. Wang, L. Pang, Z. Chen and Z. Liu, *Drug Deliv.*, 2013, 7544.

[260] A. C. Santos, M. Caldas, P. Pattekari, C. F. Ribeiro, A. J. Ribeiro, Y. Lvov and F. Veiga, in *Design and development of new nanocarriers*, Elsevier, 2018, pp. 595–635.

[261] P. Khadka, J. Ro, H. Kim, I. Kim, J. Tae, H. Kim, J. Min, G. Yun and J. Lee, *Asian J. Pharm.*, 2014, **9**, 304–316.

[262] K. Kamburova, K. Mitarova and T. Radeva, *Colloids Surf. A: Physicochem. Eng.*, 2017, **519**, 199–204.

[263] X. Wang and J. Zhao, *J. Agric. Food Chem.*, 2013, **61**, 3789–3796.

[264] D. B. Shenoy and G. B. Sukhorukov, *Eur. J. Pharm. Biopharm.*, 2004, **58**, 521–527.

[265] F. Caruso, D. Trau, H. Mo, R. Renneberg, H. Möhwald and R. Renneberg, *Langmuir*, 2000, **16**, 1485–1488.

[266] N. G. Balabushevitch, G. B. Sukhorukov, N. A. Moroz, D. V. Volodkin, N. I. Larionova, E. Donath and H. Mohwald, *Biotechnol. Bioeng.*, 2001, **76**, 207–213.

References

[267] Y. Ohta and M. Kidd, *Poult. Sci.*, 2001, **80**, 1425–1429.

[268] Z. Uni and P. Ferket, *Enhancement of Development of Oviparous Species by In Ovo Feeding*, U.S. Patent 6,592,878 B2, Jul. 15, 2003.

[269] K.-J. Huang, C.-H. Li, P.-K. Tsai, C.-C. Lai, Y.-R. Kuo, M.-K. Hsieh and C.-W. Cheng, *Vet. Sci.*, 2022, **9**, 147.

[270] W. Zhai, P. Gerard, R. Pulikanti and E. Peebles, *Poult. Sci.*, 2011, **90**, 2134–2143.

[271] W. Zhai, D. Rowe and E. Peebles, *Poult. Sci.*, 2011, **90**, 1295–1301.

[272] M. Naeem Asa, M. Chamani, S. N. Mousavi, A.-A. Sadeghi and F. Foroudi, *Ital. J. Anim. Sci.*, 2022, **21**, 749–763.

[273] P. Retes, A. Clemente, D. Neves, M. Espósito, L. Makiyama, R. Alvarenga, L. Pereira and M. Zangeronimo, *J. Anim. Physiol. Anim. Nutr.*, 2018, **102**, 361–369.

[274] S. Li, L. Zhi, Y. Liu, J. Shen, L. Liu, J. Yao and X. Yang, *Br. J. Nutr.*, 2016, **115**, 411–421.

[275] S. Liang, X. Liu, J. Zhao, R. Liu, X. Huang, Y. Liu, X. Yang and X. Yang, *Poult. Sci.*, 2022, **101**, 101935.

[276] S. Nouri, J. G. Ghalehkandi, S. Hassanpour and H. Aghdam-Shahryar, *Int. J. Pept.*, 2018, **24**, 463–470.

[277] Z. Ahmad, M. Xie, Y. Wu and S. Hou, *Animals*, 2019, **9**, 633.

[278] B. Teymouri, J. Ghiasi Ghalehkandi, S. Hassanpour and H. Aghdam-Shahryar, *Int. J. Pept.*, 2020, **26**, 381–387.

[279] V. Tufarelli, F. Ghane, H. R. Shahbazi, M. Slozhenkina, I. Gorlov, F. M. Viktoronova, A. Seidavi and V. Laudadio, *Poult. Sci. J.*, 2022, **78**, 125–138.

[280] T. Van Hieu, B. Guntoro, N. H. Qui, N. T. K. Quyen and F. A. Al Hafiz, *Vet. World*, 2022, **15**, 685.

[281] A. Ipek, Ü. Sahan and B. Yilmaz, *Arch. für Geflugelkunde*, 2004, **68**, 132–135.

[282] H. Zhang, K. Elliott, O. Durojaye, S. Fatemi and E. Peebles, *Poult. Sci.*, 2018, **97**, 1941–1947.

[283] A. Mousstaaid, S. A. Fatemi, K. E. Elliott, A. H. Alqhtani and E. D. Peebles, *Animals*, 2022, **12**, 1020.

[284] T. Gao, M. Zhao, Y. Li, L. Zhang, J. Li, L. Yu, F. Gao and G. Zhou, *J. Anim. Physiol. Anim. Nutr.*, 2018, **102**, e166–e175.

[285] T. Gao, M. Zhao, L. Zhang, J. Li, L. Yu, P. Lv, F. Gao and G. Zhou, *J. Anim. Sci.*, 2017, **95**, 3079–3092.

[286] T. Gao, M. Zhao, L. Zhang, J. Li, L. Yu, P. Lv, F. Gao and G. Zhou, *Anim. Feed Sci.*, 2017, **225**, 8–19.

[287] L. Yu, T. Gao, M. Zhao, P. Lv, L. Zhang, J. Li, Y. Jiang, F. Gao and G. Zhou, *Poult. Sci.*, 2018, **97**, 140–148.

[288] İ. Coşkun, G. Erener, A. Şahin, U. Karadavut, A. Altop and A. A. Okur, *Turkish JAF Sci. Tech.*, 2014, **2**, 47–50.

[289] H. A. Elwan, S. S. Elnesr, Q. Xu, C. Xie, X. Dong and X. Zou, *Animals*, 2019, **9**, 25.

[290] G. Han, Y. Cui, D. Shen, M. Li, Y. Ren, T. Bungo, V. S. Chowdhury, Y. Li and C. Li, *Front. Vet. Sci.*, 2022, 288.

[291] L. Yang, G.-Y. Tan, Y.-Q. Fu, J.-H. Feng and M.-H. Zhang, *Comp. Biochem. Physiol. Part - C: Toxicol. Pharmacol.*, 2010, **151**, 204–208.

[292] G. Han, H. Yang, Y. Wang, R. Zhang, K. Tashiro, T. Bungo, M. Furuse and V. Chowdhury, *Poult. Sci.*, 2019, **98**, 1243–1253.

[293] M. Zhu, X. Zhang, X. Dong and X. Zou, *Poult. Sci.*, 2019, **98**, 5533–5540.

[294] I. Coskun, A. Akkan and G. Erener, *Rev. Bras. Zootec.*, 2018, **47**, 20170220.

[295] M. Ebrahimi, H. Janmohammadi, H. D. Kia, G. Moghaddam, Z. Rajabi, S. A. Rafat, A. Javanmard *et al.*, *Rev. Med. Vet.*, 2017, **168**, 116–124.

[296] O. I. Ajayi, O. F. Smith, A. O. Oso and O. E. Oke, *Front. Physiol.*, 2022, **13**, 972041.

[297] J. Alabi, S. Bhanja, A. Fafiolu, O. Oluwatosin, O. Onagbesan, M. Mehra and A. Goel, *Indian J. Anim. Sci.*, 2020, **90**, 1628–1637.

[298] M. Kadam, S. Bhanja, A. Mandal, R. Thakur, P. Vasan, A. Bhattacharyya and J. Tyagi, *British Poult. Sci.*, 2008, **49**, 736–741.

[299] S. Tahmasebi and M. Toghyani, *J. Anim. Physiol. Anim. Nutr.*, 2016, **100**, 947–956.

[300] H. A. Hassan, A. Arafat, K. Farroh, M. Bahnas, I. El-Wardany and S. S. Elnesr, *Anim. Biotechnol.*, 2022, **33**, 1134–1141.

[301] H. A. Hassan, A. R. Arafat, K. Y. Farroh, M. S. Bahnas, I. El-Wardany and S. S. Elnesr, *Anim. Biotechnol.*, 2021, 1–8.

[302] L. Yan, X. Fang, Y. Liu, M. A. Elzo, C. Zhang and H. Chen, *J. Appl. Anim.*, 2017, **45**, 60–63.

[303] L. Pineda, E. Sawosz, K. Vadalasetty and A. Chwalibog, *Anim. Feed Sci.*, 2013, **186**, 125–129.

[304] M. Grodzik, F. Sawosz, E. Sawosz, A. Hotowy, M. Wierzbicki, M. Kutwin, S. Jaworski and A. Chwalibog, *Int. J. Mol. Sci.*, 2013, **14**, 23033–23044.

[305] F. Sawosz, L. Pineda, A. Hotowy, S. Jaworski, M. Prasek, E. Sawosz and A. Chwalibog, *Arch. Anim. Nutr.*, 2013, **67**, 347–355.

[306] N. González-Ballesteros, L. Diego-González, M. Lastra-Valdor, M. Rodríguez-Argüelles, M. Grimaldi, A. Cavazza, F. Bigi and R. Simón-Vázquez, *J. Mater. Chem. B*, 2019, **7**, 4677–4691.

[307] M. Rai, A. Yadav and A. Gade, *Biotechnol. Adv.*, 2009, **27**, 76–83.

[308] A. Goel, S. K. Bhanja, M. Mehra, S. Majumdar and A. Mandal, *Arch. Anim. Nutr.*, 2017, **71**, 384–394.

[309] P. F. Surai, I. I. Kochish, V. I. Fisinin and O. A. Velichko, *Poult. Sci. J.*, 2018, **55**, 79–93.

[310] N. Ibrahim, E. Sabic, M. Wakwak, I. El-Wardany, Y. El-Homosany, N. E.-D. Mohammad *et al.*, *J. Anim. Feed Sci.*, 2020, **29**, 46–58.

[311] P. P. Joshua, C. Valli and V. Balakrishnan, *Vet. World*, 2016, **9**, 287.

[312] A. A. Mogahid, G. G. Gad, E. Abdalla and I. El-Wardany, *Arab Univ. J. Agric. Sci.*, 2018, **26**, 2369–2376.

[313] A. Patra and M. Lalhriatpuii, *Biol. Trace Elem. Res.*, 2020, **197**, 233–253.

[314] A. Matuszewski, M. Łukasiewicz, J. Niemiec, M. Kamaszewski, S. Jaworski, M. Domino, T. Jasiński, A. Chwalibog and E. Sawosz, *Animals*, 2021, **11**, 932.

[315] S. Gangadoo, D. Stanley, R. J. Hughes, R. J. Moore and J. Chapman, *Trends Food Sci. Technol.*, 2016, **58**, 115–126.

[316] Y. Shastak and M. Rodehutscord, *Poult. Sci. J.*, 2015, **71**, 125–138.

[317] C. Cheung, M. Spring and H. Liang, *Opt. Express*, 2015, **23**, 10145–10157.

[318] N. V. Vagenas, A. Gatsouli and C. G. Kontoyannis, *Talanta*, 2003, **59**, 831–836.

[319] Z. Anfar, H. A. Ahsaine, M. Zbair, A. Amedlous, A. A. E. Fakir, A. Jada and N. E. Alem, *Crit. Rev. Environ. Sci. Technol.*, 2020, **50**, 1043–1084.

[320] S. M. Bromfield, E. Wilde and D. K. Smith, *Chem. Soc. Rev.*, 2013, **42**, 9184–9195.

[321] J. Campbell, J. Abnett, G. Kastania, D. Volodkin and A. S. Vikulina, *ACS Appl. Mater. Interfaces*, 2021, **13**, 3259–3269.

[322] A. Mero and M. Campisi, *Polymers*, 2014, **6**, 346–369.

[323] A. R. Fajardo, L. C. Lopes, A. J. Valente, A. F. Rubira and E. C. Muniz, *Colloid Polym. Sci.*, 2011, **289**, 1739–1748.

[324] J. Seog, D. Dean, A. H. Plaas, S. Wong-Palms, A. J. Grodzinsky and C. Ortiz, *Macromolecules*, 2002, **35**, 5601–5615.

[325] H. M. Wang, D. Loganathan and R. J. Linhardt, *Biochem. J.*, 1991, **278**, 689–695.

[326] U. Bhaskar, A. M. Hickey, G. Li, R. V. Mundra, F. Zhang, L. Fu, C. Cai, Z. Ou, J. S. Dordick and R. J. Linhardt, *Biotechnol. Prog.*, 2015, **31**, 1348–1359.

[327] H. M. Eckenrode and H. L. Dai, *Langmuir*, 2004, **20**, 9202–9209.

[328] F. Xue, L. Liu, Y. Mi, H. Han and J. Liang, *RSC Adv.*, 2016, **6**, 10215–10220.

[329] S. Hattori, E. Adachi, T. Ebihara, T. Shirai, I. Someki and S. Irie, *J. Biochem.*, 1999, **125**, 676–684.

[330] M. Meyer, *Biomed. Eng. Online*, 2019, **18**, 1–74.

[331] M. Ambrosi, E. Fratini, P. Baglioni, C. Vannucci, A. Bartolini, A. Pintens and J. Smets, *J. Phys. Chem. C*, 2016, **120**, 13514–13522.

[332] S. She, B. Shan, Q. Li, W. Tong and C. Gao, *J. Phys. Chem. B*, 2012, **116**, 13561–13567.

[333] T. Crouzier and C. Picart, *Biomacromolecules*, 2009, **10**, 433–442.

[334] N. A. N. Hanafy, *Int. J. Biol. Macromol.*, 2021, **182**, 1981–1993.

[335] I. A. Burmistrov, M. M. Veselov, A. V. Mikheev, T. N. Borodina, T. V. Bukreeva, M. A. Chuev, S. S. Starchikov, I. S. Lyubutin, V. V. Artemov, D. N. Khmelenin *et al.*, *Pharmaceutics*, 2021, **14**, 65.

[336] K. Köhler, P. M. Biesheuvel, R. Weinkamer, H. Möhwald and G. B. Sukhorukov, *Phys. Rev. Lett.*, 2006, **97**, 188301.

[337] R. Teixeira, R. L. Reis and I. Pashkuleva, *Colloids Surf. B*, 2016, **145**, 567–575.

[338] M. Khanjani, D. J. Westenberg, A. Kumar and H. Ma, *ACS Omega*, 2021, **6**, 11988–12003.

[339] A. C. S. Jensen, S. Imberti, S. F. Parker, E. Schneck, Y. Politi, P. Fratzl, L. Bertinetti and W. J. E. M. Habraken, *J. Phys. Chem. C*, 2018, **122**, 3591–3598.

[340] J. Kontrec, D. Kralj, L. Brečević and G. Falini, *J. Cryst. Growth*, 2008, **310**, 4554–4560.

[341] Y. Ding, Y. Liu, Y. Ren, H. Yan, M. Wang, D. Wang, X. Y. Lu, B. Wang, T. Fan and H. Guo, *Powder Technol.*, 2018, **333**, 410–420.

[342] J. K. Armstrong, R. B. Wenby, H. J. Meiselman and T. C. Fisher, *Biophys. J.*, 2004, **87**, 4259–4270.

[343] H. Wen, J. Hao and S. K. Li, *J. Pharm. Sci.*, 2013, **102**, 892–903.

[344] K. Cychosz, R. Guillet-Nicolas, J. Garcia-Martinez and M. Thommes, *Chem. Soc. Rev.*, 2017, **46**, 389–414.

[345] V. V. Hardikar and E. Matijevic, *Colloids Surf. A: Physicochem. Eng.*, 2001, **186**, 23–31.

[346] B. N. Džakula, G. Falini and D. Kralj, *Croat. Chem. Acta*, 2018, **90**, 689–698.

[347] F. S. M. Tekie, M. Hajiramezanali, P. Geramifar, M. Raoufi, R. Dinarvand, M. Soleimani and F. Atyabi, *Sci. Rep.*, 2020, **10**, 9664.

References

[348] A. N. DE BELDER, in *Industrial gums*, Elsevier, 1993, pp. 399–425.

[349] K. Y. Chong, C. H. Chia, S. Zakaria and M. S. Sajab, *J. Environ. Chem. Eng.*, 2014, **2**, 2156–2161.

[350] A. Sergeeva, R. Sergeev, E. Lengert, A. Zakharevich, B. Parakhonskiy, D. Gorin, S. Sergeev and D. Volodkin, *ACS App. Mater. Inter.*, 2015, **7**, 21315–21325.

[351] A. van den Berg and S. F. Dowdy, *Curr. Opin. Biotechnol.*, 2011, **22**, 888–893.

[352] C. C. Young, A. Vedadghavami and A. G. Bajpayee, *Bioelectricity*, 2020, **2**, 68–81.

[353] J. Yang and J. Kopeček, *J. Control. Release*, 2014, **190**, 288–303.

[354] S. Zhou, W. Chen, J. Cole and G. Zhu, *Med. Drug Discov.*, 2020, **6**, 100023.

[355] P. Bélteky, A. Rónavári, N. Igaz, B. Szerencsés, I. Y. Tóth, I. Pfeiffer, M. Kiricsi and Z. Kónya, *Int. J. Nanomed.*, 2019, **14**, 667–687.

[356] M. Guilger-Casagrande and R. d. Lima, *Front. Bioeng. Biotechnol.*, 2019, **7**, 287.

[357] S. Singh, A. Bharti and V. K. Meena, *J. Mater. Sci. Mater. Electron.*, 2015, **26**, 3638–3648.

[358] H. Kaur, H. Kaur and A. Sharma, *Mater. Today: Proc.*, 2020, **37**, 3574–3576.

[359] S. Samiullah and J. R. Roberts, *Poult. Sci. J.*, 2014, **70**, 693–708.

[360] G. Kulshreshtha, C. Benavides-Reyes, A. B. Rodriguez-Navarro, T. Diep and M. T. Hincke, *Foods*, 2021, **10**, 2559.

[361] L. S. Júnior, I. Boleli, L. Ribeiro, D. Preitas and M. Macari, *Rev. Bras. Cienc. Avic.*, 2000, **2**, 177–181.

[362] X. Chen, X. Li, Z. He, Z. Hou, G. Xu, N. Yang and J. Zheng, *PLoS One*, 2019, **14**, e0220054.

[363] J. Gautron, L. Stapane, N. Le Roy, Y. Nys, A. Rodriguez-Navarro and M. Hincke, *BMC Mol. Biol.*, 2021, **22**, 1–17.

[364] A. H. Parsons, *Poult. Sci.*, 1982, **61**, 2013–2021.

[365] M. Panheleux, Y. Nys, J. Williams, J. Gautron, T. Boldicke and M. T. Hincke, *Poult. Sci.*, 2000, **79**, 580–588.

[366] Z. Liu, L. Song, F. Zhang, W. He and R. J. Linhardt, *Poult. Sci.*, 2017, **96**, 3775–3784.

[367] T. Moreau, J. Gautron, M. T. Hincke, P. Monget, S. Réhault-Godbert and N. Guyot, *Front Immunol.*, 2022, **13**, 946428.

[368] M. S. Fernandez, A. Moya, L. Lopez and J. L. Arias, *Matrix Biol.*, 2001, **19**, 793803.

[369] D. Carrino, J. Dennis, T.-M. Wu, J. Arias, M. Fernandez, J. Rodriguez, D. Fink, A. Heuer and A. Caplan, *Connect. Tissue Res.*, 1996, 325–328.

[370] K. J. Ruff, D. P. Devore, M. D. Leu and M. A. Robinson, *Clin. Interv. Aging*, 2009, 4–235.

[371] I. C. S. d. Araújo, N. S. M. Leandro, M. A. Mesquita, M. B. Café, H. H. C. Mello and E. Gonzales, *Rev. Bras. Zootec.*, 2017, **46**, 896–902.

[372] D. C. Deeming, *Avian Biol. Res.*, 2011, **4**, 224–230.

[373] E. M. Wedral, D. Vadehra and R. Baker, *J. Food Sci.*, 1971, **36**, 520–522.

[374] D. Fromm, *Poult. Sci.*, 1960, **39**, 1490–1495.

[375] A. B. Rodríguez-Navarro, N. Domínguez-Gasca, A. Muñoz and M. Ortega-Huertas, *Poult. Sci.*, 2013, **92**, 3026–3035.

[376] P. K. Sharma, N. Gupta and P. I. Dankov, *AEU - Int. J. Electron. Commun.*, 2020, **127**, 153455.

[377] H. Palacios-Jordan, A. Jané-Brunet, E. Jané-Brunet, F. Puiggròs, N. Canela and M. A. Rodríguez, *Foods*, 2022, **11**, 297.

[378] M. A. A. Fakhree, D. R. Delgado, F. Martínez and A. Jouyban, *AAPS PharmSciTech*, 2010, **11**, 1726–1729.

[379] J. Koliyoor, S. Hegde, R. Vasachar and G. Sanjeev, *J. Appl. Polym. Sci.*, 2022, **139**, 51826.

[380] R. J. Sengwa, V. Khatri and S. Sankhla, *Fluid Ph. Equilibria*, 2008, **266**, 54–58.

[381] T. Vishwam, K. S. P. S. Sarma, R. K. Murthy and S. Sastry, *Indian J. Pure Appl. Phys.s*, 2017, **55**, 403–412.

[382] S. N. Shareef, K. Chidambaram and S. K. Pasha, *Polym.-Plast. Technol. Mater.*, 2019, **58**, 1210–1225.

[383] K. Arnold, A. Herrman, L. Pratsch and K. Gawrisch, *Biochim. Biophys. Acta*, 1985, **815**, 515–518.

[384] R. J. Sengwa, *Polym. Int.*, 2004, **53**, 744–748.

[385] J. Campbell, A. Taghavi, A. Preis, S. Martin, A. G. Skirtach, J. Franke, D. Volodkin and A. Vikulina, *J. Colloid Interface Sci.*, 2022, 12–22.

[386] J. Campbell, A. M. Ferreira, L. Bowker, J. Hunt, D. Volodkin and A. Vikulina, *J. Adv. Mater. Interfaces*, 2022, **9**, 2201196.